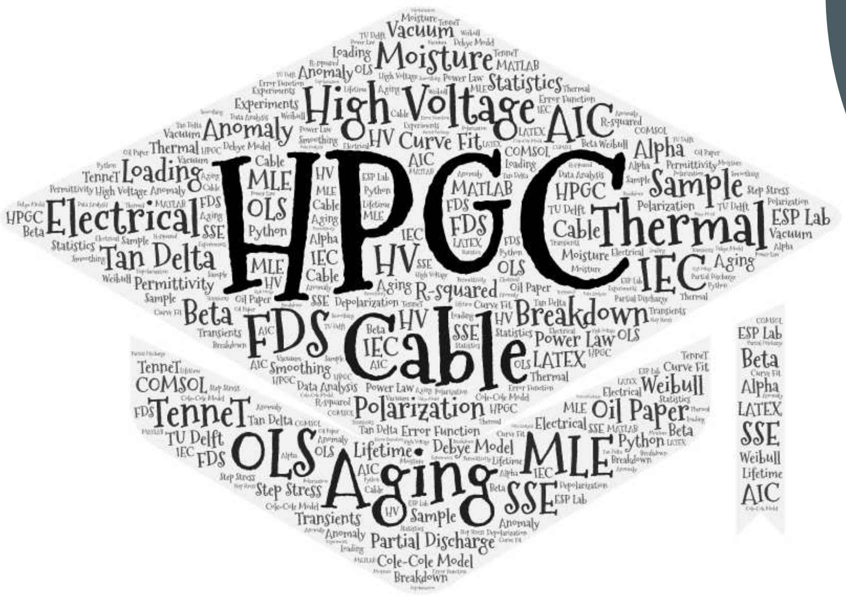

Master Thesis 2021

Aging Model and Parameter Determination for High Pressure Gas Cables at Elevated Electro-Thermal Stress

Devayan Basu (5023173)

TenneT

TU Delft

Aging Model and Parameter Determination for High Pressure Gas Cables at Elevated Electro-Thermal Stresses

by

Devayan Basu

to obtain the degree of Master of Science
at the Delft University of Technology,
to be defended publicly on Tuesday August 17, 2021 at 15:00 PM.

Student number:	5023173	
Project duration:	November 1, 2020 – August 17, 2021	
Thesis committee:	Prof. Dr. R. Ross,	TU Delft, Chair
	Dr. B. Gholizad,	TU Delft, Daily Supervisor
	Dr. J. L. Rueda Torres,	TU Delft, External Committee Member
	Dr. S. M. Gargari,	TenneT TSO, Company Supervisor

Devayan Basu
Delft, August 2021

“Our greatest weakness lies in giving up. The most certain way to succeed is always to try just one more time.”
– Thomas A. Edison

Executive Summary:

The thesis focuses on developing the aging model for High Pressure Gas Cables and to find indicators of aging when they are subjected to elevated temperatures. This research is specifically important as it will form the basis of a major replacement strategy formed by TenneT where they are prioritizing the HPGC replacement depending upon its present insulation condition. Since this plan would take substantial time, the temperature sensitivity analysis is vital. Before the completion of replacement phase of HPGC, in case of maintenance/repair/failure in a parallel line, the loading on the HPGC may increase, indirectly rising the conductor temperature, which was observed in the loading statistics of the cable in past decade. The thesis has been subdivided into three major research questions:

1) How does the insulation degrade when the field aged High Pressure Gas Cables are elevated to higher temperatures, but lower than the maximum design temperature?

2) Can diagnostic tests be developed or modified focusing on the material physics inside the insulation that can be performed on the cable alongside tan delta at 50 Hz and Partial Discharge Measurements, that is viable in field with least offline time?

3) What parameters can be extracted from measurements to develop a robust model that determines the degradation of HPG cable insulation with temperature and aging?

Initially, all the possible aging and breakdown mechanisms for oil-paper cables, different advanced multi-stress aging models, different field diagnostic tests and their respective commercial measuring equipments are discussed in the literature. Different kinds of cables are compared with GC in terms of failures/km, accessories, fault origins and other parameters. Because the tests are carried out in a controlled lab environment, it is essential to prepare the electrodes and samples well so as to replicate same situations as in field. The cable sample provided had been in service for 44 years and has been through the natural process of electro-thermal aging. The loading data for the cable was collected and IEC Standard 60287 was applied to calculate the dynamic temperature profile for more than a decade. Evaluating the temperature helped to understand how insulation aged thermally in the service.

To develop the aging model with temperature sensitivity, initially fast AC ramped breakdown tests were performed on Oil Impregnated Paper (OIP) samples. This gave an initial estimate for Breakdown Voltage(BDV) at different temperatures which enabled to design the voltage steps for long term AC step stress test. Maximum Likelihood Estimation and Least Squares were performed on Weibull Distributed Data with Power Law coded in MATLAB. It was observed that with increase in temperature the value of power ”n” in power law reduced. This way, the thermal aging influences changes of electrical life. So, the samples would breakdown faster with increased temperatures at a given field stress. This proved how sensitive the thermal stress is on aging for HPGC, answering the first research question.

Next, to estimate the degree of aging, Polarization Depolarization Current(PDC) measurement has been performed. An electronic circuit has been designed for the test which ran for a duration of 3 hours allowing polarization processes to occur inside the insulation. Extended Debye Model was applied to extract the parameters indicating aging of the insulation. It was observed that with increase in temperature, the resistances in the different branches of model reduces; whereas the capacitance increases. Also, the relaxation time reduced and the DC conductivity increased with increase in temperature and aging. This is an offline test, yet the parameters extracted help us to analyze the insulation condition.

Now, to solve the problem of long term offline test, an alternative test was researched and tested on the samples. This Frequency Domain Spectroscopy was a 6 minute test which could be performed separately or in conjunction with PDC to develop a more robust model. A frequency sweep was performed equivalent to a test of 6 minutes to obtain the real and imaginary part of capacitance. This indirectly helped to find the loss factor, tan δ, which was observed to increase with temperature. But to quantify this test with aging, Cole Cole Model was used to extract parameters which showed relaxation time and the equation constant, alpha reduces with temperature and aging. Finally, Partial Discharge (PD) characterization is performed for different temperature samples. Though further research is required in this chapter, but initial conclusions show PD activity is proportional to temperature. This answers the second and third research question, indicating a successful research output. All the conclusions obtained from individual chapters have been reported in the end along with recommendations for future work to extend it to more varieties of HPGC.

Contents

List of Abbreviations

AC	Alternating Current
AIS	Air Insulated Switchgear
BD	Breakdown
CDF	Cumulative Density Function
DC	Direct Current
D-C	Davidson Cole
DFR	Dielectric Frequency Response
DP	Degree of Polymerization
EGP	External Gas Pressure
EHV	Extra High Voltage
EPR	Ethylene Polypropylene Rubber
FDS	Frequency Domain Spectroscopy
F-K	Fuoss Kirkwood
FTIR	Fourier Transform InfraRed
GC	Gas Cables
H-N	Havriliak Negami
HPG	High Pressure Gas
HPGC	High Pressure Gas Cables
HPOF	High Pressure Oil Filled
HV	High Voltage
HVDC	High Voltage Direct Current
IPL	Inverse Power Law
LS	Least Squares
MLE	Maximum Likelihood Estimation
OIP	Oil Impregnated Paper
OLS	Ordinary Least Squares
PD	Partial Discharge
PDC	Polarization Depolarization Currents
PE	PolyEthylene
PPL	Paper Polypropylene
RVM	Residual/Recovery Voltage Measurement
SCOF	Self Contained Oil Filled
TSO	Transmission System Operators
UVH	Ultra High Voltage
XLPE	Cross Linked Poly Ethylene

1

Introduction

1.1. Motivation

From childhood, I have often been plagued by my sister, regarding which came first: the egg or the hen? Unable to present any mathematical or experimental reasoning behind this question and in a way giving up on the debate, now I have changed my focus into something that can be thoroughly researched on and provide experimental basis for the same. High Pressure Gas Cables (HPGC) had been installed about 40 years ago in the grids of the Netherlands and Germany. TenneT, the TSO of the Netherlands and parts of Germany now wants to replace these HPGC on a priority basis. But the question appeared which of the cables have aged the most. Also from a research perspective, due to repair, maintenance activity or breakdown of a parallel circuit, these cables may get overloaded, causing a rise in temperature. This was also observed in the loading data in MW during the past decade of the cable sample provided to us. So, it is important to realize the effect of temperature on aging, degradation and electrical life of the insulation. Only if a robust model is developed, can we understand which cable is closer to it's end of life. Since all the cables cannot be replaced at once; prioritizing ones which are at the very near end and in the "red zone" of lifetime should be replaced first accordingly. But making a general model is not that simple, specially when there has to be a perfect balance between the academic research and also making it as realistic to the main scenario so that it can be applied on the field cables. Thus, the focus of the thesis is on observation of the physics based processes taking place due to the effect of elevated temperatures on HPGC and the thermal-electric effect resulting in aging of insulation.

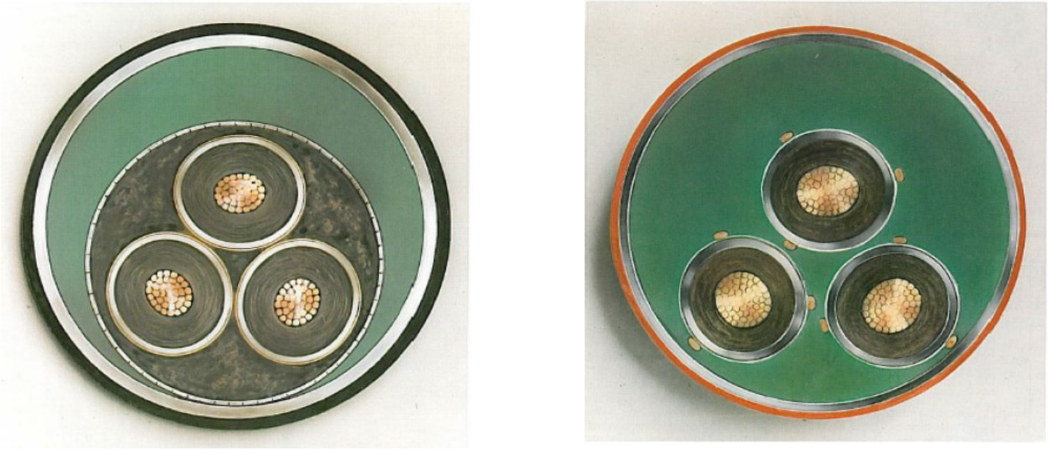

Figure 1.1: (Left) 3 Core and (Right) 1 Core Cross-Section of HPG Cable [1]

In Europe, quite a number of HPG cables are in service at High Voltage level from 110-150 kV and in Extra High Voltage Level of 220 kV. In the Netherlands, two types of External Gas Pressurized (EGP) cables have been installed in 1970 and 80's as shown in Figure 1.1: (a) Three Core Paper Insulated Lead Covered Cores with flat steel wire armouring and paper fillers, (b) Single Core Paper Insulated Lead Covered Cores with Skid Wires.

Both types of cables are put into pre installed steel pipes and the space between the cable and steel pipe is filled with Nitrogen Gas at 15 Bar pressure to compress voids in the paper and reduce partial discharge.

1.2. Scientific Gaps

With the extensive literature studied during the course of the research, the following scientific gaps were addressed which needed to be clarified with research to answer the questions by TenneT. The aging model of the HPGC with the sensitivity to thermal aging has hardly been addressed. The measurement of polarization-depolarization currents have mostly been done on transformer papers, with very limited focus on oil-paper insulation containing very viscous oil like in HPGC. It remains as an area of interest to investigate if similar trends are followed for such materials. Also, the Frequency Dielectric Spectroscopy discussed in literature mostly focused on the variation in the loss components, namely tan δ and no literature was found during the course of the research which showed how parameters can be obtained that can determine aging and degradation due to elevated thermal stress for such materials. Finally, the analysis of aging and elevated thermal stress degraded insulation parameters from different experimental procedures and combining them into a single robust model have not been used before, as observed during the literature survey phase. Thus, with all the literature gaps, it seems that if this research questions some of them, it will be possible to develop a robust model which can be used to predict degradation of dielectric material for such viscous oil paper insulation; which in turn would answer TenneT's question as to how to prioritize the replacement strategy for the most degraded HPG cables. So, in the next section, the research questions are formed which I would try to answer through the extensive research done in Chapter 4-10.

1.3. Research Questions

The focus of this thesis is to research about the effect of temperature on the insulation status of High Pressure Gas Cables and the combined electro-thermal effect on the lifetime of insulation of cables already in service to evaluate the remaining life.

Firstly, we talk about the research gap that has been there and then we address the research questions. Most of work on oil paper insulation has been carried mostly on transformer paper and transformer mineral oil [2][3][4], where majority of the samples were impregnated at lab. Lab Impregnation often rules out finer defects that arises during bulk impregnation and manufacturing at industry. During the course of research, no literature was found on the aging models of the HPG cables and papers that date back to 1950's focus on the literature of installation and design of such cables. It was until as recent as 2020 end, when researchers from Prysmian B.V. and TenneT, Van Rossum et. al. analyzed the retrofit joint for these cables. Replacement of cables can be due to various reasons, where the most prominent ones are: 1) End of Lifetime, 2) Longer Repair Time, and 3) Limitation in power rating due to aging and unknown rate of thermal degradation on the cable.

Secondly, during this course of research, not much literature was obtained regarding the observation of polarization phenomenon inside the insulation of the cables under research with elevated temperatures. Most of the literature addresses extruded cables or transformer paper and oil, which is much less viscous compared to the oil used in HPGC. Thus, the behaviour and relaxation process time would also be different, leaving us with an open question.

Thirdly, in industry, for diagnostics, the experiments are preferred to be with operation conditions. This is because, say for example during offline PD Measurement. the cable is exposed to voltages higher than nominal voltage (1.7 U_o), which may expose the already aged cables to faster aging, similar effect is observed for tanδ measurement during the frequency sweep. So if it is a prolong test, then the effect would be more detrimental to these cables. As a result under such conditions, very few parameters can be collected for further analysis about the insulation condition. Measuring tanδ at

50 Hz operating frequency and comparing over long period of time indeed gives an indication, but on basis of one parameter it is not conclusive enough about the dielectric properties. Partial Discharge has been studied over long periods of time and there has been tremendous advancements. Thus, if more parameters could be extracted from other short-duration tests, they can be studied with the PD characteristics to have a very robust model of the cable. This research at TU Delft ESP Lab in collaboration with TenneT for 10 months addresses the following questions:

1) How does the insulation degrade when the field aged High Pressure Gas Cables are elevated to higher temperatures, but lower than the maximum design temperature?

2) Can diagnostic tests be developed or modified focusing on the material physics inside the insulation that can be performed on the cable alongside tan delta at 50 Hz and Partial Discharge Measurements, that is viable in field with least offline time?

3) What parameters can be extracted from measurements to develop a robust model that determines the degradation of HPG cable insulation with thermal and electrical aging?

Regarding the temperature sensitivity of the OIP insulated HPG cables and it's aging, we have more questions left to be answered than ones that have been answered. All proposed questions have been addressed in this thesis and the answers have been discussed in Chapter 11: Conclusion with some future recommendations to elaborate the study.

1.4. Outline Of Chapters

1.4.1. Chapter 1: Introduction

Chapter 1 discusses the motivation of selecting this research topic and talks about the research gap that has been there for insulation modelling of HPGC. With all the focus mostly on oil-paper insulation in transformer, we address the questions that has been investigated through the course of the thesis to develop a robust sensitivity analysis and aging characteristics of HPGC.

1.4.2. Chapter 2: Background Knowledge

Chapter 2 discusses the state-of-art literature regarding insulation modelling. Firstly, different aging and breakdown mechanisms are discussed which occurs in solid paper insulation. Then, the different breakdown test regimes are discussed and how to apply most optimal distribution and advanced single and multi-stress models on the observed data. Thirdly, the present testing and diagnostic methods for cables are discussed along with the recent models developed from characterizing the insulation from these tests. Finally, the commercial instruments are introduced used by the leading power cable industries.

1.4.3. Chapter 3: Installed Lengths, Fault, Failure Rate, Outage Time Statistics of GC Compared to Other Types of Cables

Chapter 3 focuses on discussing the failure rate, fault origins, accessory failure and trends in the shift of material used as insulation. Different extruded, oil filled and gas filled cables have been compared on basis of these parameters.

1.4.4. Chapter 4: Electrode and Sample Preparation

Chapter 4 discusses about the preparation of electrodes in the initial section adapted to minimum oil condition. A Electrostatic COMSOL Model is developed to study the potential and field distribution and the same exact model is implemented in experiments. Finally, the chapter informs about extraction of samples from the long cable pieces which is quite different to the artificial sample preparation at laboratory.

1.4.5. Chapter 5: Operational History of the Cable

Chapter 5 focuses on the operational temperature of the cable for more than a decade. The loading profile is obtained from TenneT directly from a logger and thus it had a high quantity of bad data. The data cleaning and anomaly detection and handling has been discussed in details . Finally, IEC standards are used to convert from loading data into working temperature.

1.4.6. Chapter 6: Determination of Breakdown Voltage from Fast Ramp Stress Test

Chapter 6 introduces the first test where Fast AC Sinusoid Ramps are used to determine the breakdown voltage of oil paper samples. Three different temperatures- higher than the working temperature of the cable-have been analyzed. The BDV helps to formulate the test protocol for the next section.

1.4.7. Chapter 7: Long Term Sinusoid Step Stress Tests for Aging Model Formulation

Chapter 7 is based on the results from Chapter 6 where BDV at different temperatures were calculated which helps in developing the test protocol for AC Step Stress Tests at different temperatures. Based on breakdown data, several statistical tools are used to develop an Aging Model for the provided cable at elevated temperatures.

1.4.8. Chapter 8: Polarization and Depolarization Current Characterization

Chapter 8 introduces the realization of a dielectric as a physical model. Polarization Depolarization Current measurements are carried out using an electronic equipment developed during the research, to extract parameters that can give an indication of degradation. Several interesting conclusions were made regarding the effect of temperature on insulation which will be combined with results from next chapter to give an in-depth understanding.

1.4.9. Chapter 9: Frequency Domain Dielectric Spectroscopy Characterization

Chapter 9 focuses on Frequency Domain Dielectric Spectroscopy where advanced models are fitted on measured spectroscopy data to extract parameters which are indicative of insulation degradation due to higher temperatures. A novel method is discussed of carrying out a 6 minute offline FDS test to indicate insulation properties than conventional online 50 Hz tan delta measurement.

1.4.10. Chapter 10: Partial Discharge Characterization

Chapter 10 focuses on changes in the partial discharge patterns with increase in temperature though, further research is required in this chapter. The challenges have been overcome for the absence of bushing and the test setup is made quite robust which yielded positive results.

1.4.11. Chapter 11: Conclusion and Future Scope

Chapter 11 discusses the conclusions obtained from all the previous chapters summarized together which enables us to answer the research questions methodically. It also discusses the future research scopes that were not covered in the present research and has to be extended.

1.4.12. Chapter 12: Acknowledgement

This deserves to be a separate chapter, Chapter 12 and perhaps my favourite one in the research thesis, as it goes out to all the wonderful people who nurtured my scientific mind and helped me at every step of research, both academically as well as mental support.

2

Background Knowledge

2.1. Aging and Breakdown Mechanisms in Paper Cables

A Power Cable Network has different components from the cable itself with joints connecting it to terminations at the end of the cable connection. Each of these may have different insulating materials. Cables are mostly either Oil-Paper Insulated or made of Plastic Insulation. Joints and Terminations again can be mastic, resin, paper, oil-filled, pre-moulded and hot or cold shrink. Each of these material have different degradation processes but show similar aging identifiers and defects in the insulation. In this research, we will keep our literature and research procedure limited to Oil Impregnated Paper(OIP) Cables and analyse the faults inside the cable insulation itself. This is because the course of the research is on High Pressure Gas Cable Insulation from samples provided by TenneT.

2.1.1. Defects inside cable insulation system:

Insulation Breakdowns are caused by degradation processes due to defects created from [5]:

- Bad Design with inadequate tests during design phase,
- Damages caused during excavation,
- Normal Operational Conditions spanning over long time causing natural aging of insulation,
- Extreme elevated operational conditions with transients in system,
- Damages during transportation and installation,
- Faulty production techniques and inadequate testing during production.

For Paper Insulated Cables, the different defects for breakdown can be:

- Damages to the outer lead sheath
- Corrosion of lead sheath
- Drying out of the paper insulation
- Depolymerization of paper
- Embrittlement of insulation

In High Pressure Gas Cables (HPGC), they already have a lead pipe covering and so the possibility of water/ moisture ingress is almost impossible unless the lead sheath becomes porous, thereby problem of water trees are insignificant. But the problem of thermal-electrical aging exists referred to dry degradation developed as a result of temperature rise and heating up of cable. Figure 2.1 represents the degradation mechanisms of paper cables and how it ultimately leads to breakdown.

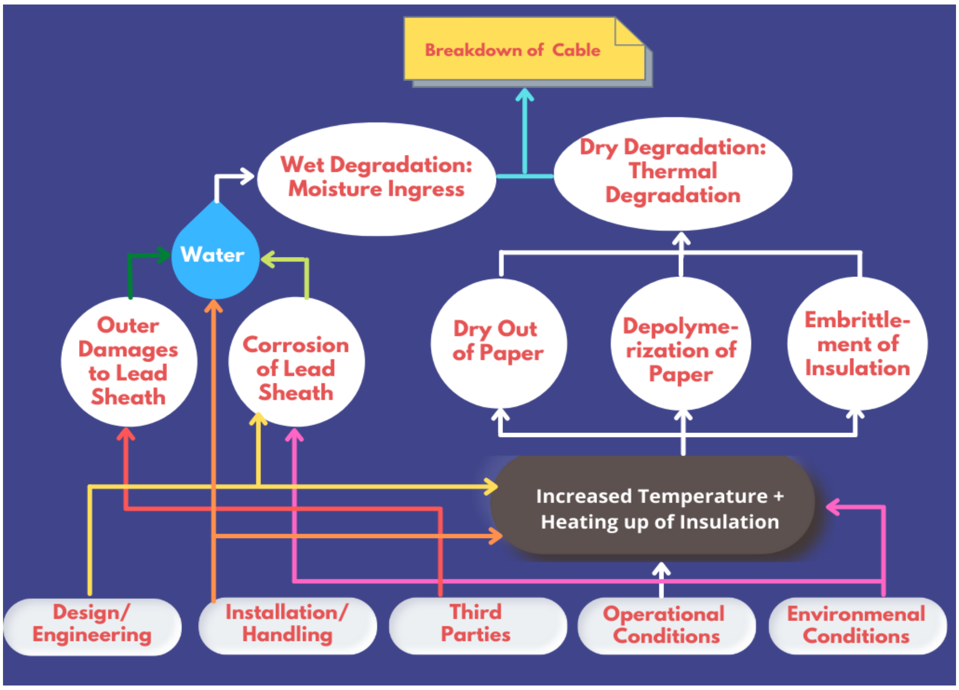

Figure 2.1: Degradation Mechanisms in Oil Paper Cables

The main natural agents of aging inside the OIP cable insulation are:

1. Thermal Effect
    - Internal (over) heating
    - External (over) heating
2. Electrical Effect
    - Partial Discharge
    - Tracking & Electrical Treeing
3. Mechanical Effect
    - Pressure Effects
    - Forces on cable system
4. Ambient Effect
    - Chemicals

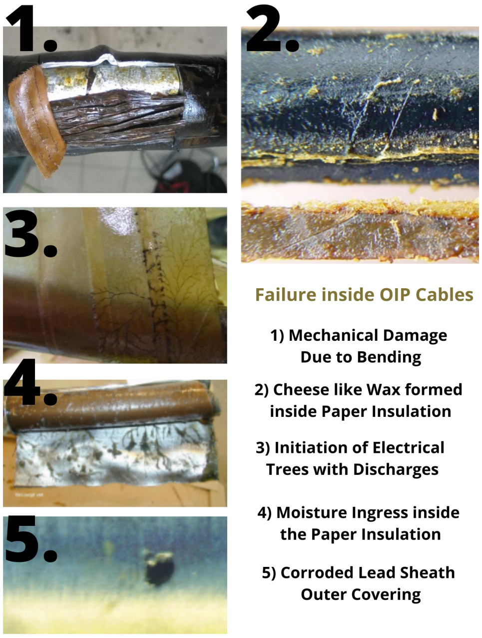

Figure 2.2: Failures in OIP Cables [5][6]

2.1.2. Practical Field Problems Leading to Aging and Breakdown for OIP Cables:

For OIP cable systems, thermal aging together with partial discharge and electrical treeing has proved to be the main aging mechanism [7][8]. Insulation Paper containing cellulose deteriorate over time causing impairment of mechanical and electrical properties. The cellulose chains break down due to aging causing reduction in mechanical strength, rendering the paper brittle [7]. Also, aging of the compounds inside the insulation layers results in a formation of wax over the paper layers and butt gaps as seen in Figure 2.2(sub-figure 2). This would not cause an immediate breakdown of insulation under normal operating conditions though. But it is instrumental in accelerating the rate of degradation of paper and compounds by elevated temperature and in presence of moisture or oxygen [9]. Besides thermal aging, this also intensifies PD activity in these voids leading to eventual breakdown. With aging, the PD activities increase further, that erodes paper layers resulting in formation of electrical trees (Figure 2.2 sub-figure 3) that propagates along the layers of the paper into the deeper layers and degrade the insulation. Though the mechanism is different compared to extruded cables, where the treeing takes place in radial direction, thus, the trees take longer time to cause an end to end breakdown since the high number of layers make it longer to propagate till it reaches the innermost layer. Yet, the inherent butt gaps present and possibility of more voids due to multiple interfaces make the oil paper cables more viable for increased PD activity over extruded ones (XLPE) which are manufactured almost without voids. In worst case scenario, for OIP cables, the electrical trees can result in a breakdown when the insulation is bridged completely. During laying of cables, they are bend underground. This may lead to mechanical damage which will expose the insulation to further degradation as shown in Figure 2.2 (sub-figure 1). Thus, to prevent the above mentioned conditions, utmost care has to be taken to monitor the cables periodically and take action in case the test results do not match the standard values.

2.1.3. Breakdown (B.D.) Mechanisms in Solid Insulation:

Breakdown mechanism in solid insulation is a complicated phenomenon that changes the insulation material into conductor locally. Under certain lab conditions, solid insulation breakdown can be analogous to gaseous breakdown. However, in practical dielectrics, partial discharge, shape of applied voltage, temperature, humidity, moisture, etc. synergistically lead to breakdown of solid insulation [10] which are summarized below:

- Intrinsic Breakdown: When the applied field is so high to provide sufficient energy to electrons to cross the band gap and move into the conduction band. On a macroscopic level, when the applied ield electric field locally exceeds the breakdown strength.
- Electrochemical Breakdown: Changes in the chemical properties of insulation (like oxidation or hydrolysis in insulation) may lead to breakdown.
- Edge Breakdown: Normally, solid insulation is surrounded by liquid or gaseous media, having lower permittivity and B.D. Strength. Thus, breakdown may occur at edge of electrode where the weaker media exists, due to field enhancement and lower B.D. strength. This B.D. Voltage is lower than real B.D. Voltage of the solid insulation mostly.
- Thermal Breakdown: Due to the flow of loss current and polarization inside the solid insulation, heat is produced increasing temperature of insulation. For solid insulation, conductivity and polarization are proportional to temperature as discussed in the course of research later. If this loss is high enough to cause thermal runaway, then it can lead to breakdown of insulation.
- Erosion Breakdown: This occurs due to partial discharge activity in solid insulation. If a cavity is present with lower permittivity compared to insulation, then it can lead to field enhancement inside the cavity. Since electric field inside cavity is higher than the solid (lower permittivity of cavity), it leads to partial discharges in the cavity. These PD activity grows with higher stresses and aging, leading to formation of electrical trees and in worst cases puncture end to end inside the insulation, causing complete breakdown.

2.2. Modelling of Failures in Paper Cables

Electric Power Transmission and distribution networks have different types of cables ranging from 50 years to 0 year old ones. Thus, with time, the electrical components are expected to age and fail. Logically thinking, we would visualize an exponential curve to fit failure data, where as time increases, failure increases and initially, it should be almost 0, due to the pristine product condition. But that is not the most practical case!

In most scenarios, the bathtub model is used, which utilizes 3 distributions leading to bath-tub under the assumptions that the three processes complete. In some literature [12], other models are also used as mentioned below:

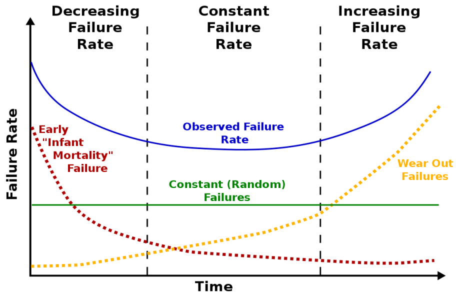

Figure 2.3: Bathtub Curve [11]

A) In the first historical data analysis method, the failure data is combined with information like age, insulation condition, etc. to make the model using a probabilistic approach [12]. A hazard rate function $\lambda(\alpha)$ is defined that describes changes in failure rate with age. Figure 2.3 represents the most commonly used model of the bathtub curve relating failure rate with time [13]. The model begins with a high failure rate referred to as the infant mortality, followed by an almost constant failure rate, which is the useful life and finally the failure rate increases again as the component reaches the end of lifetime, called wear-out phase. For the research under consideration, we are particularly interested in modelling the wear-out time and the effects of aging process on the failure rate. In the literature [12], 5 different models are evaluated to fit the failure rates during the wear-out phase:

- **Constant:** This model considers failure rate as $\lambda(\alpha) = \mu$, where μ is the mean failure rate value of all data.
- **Piece-wise constant:** Here the model is constructed by two constant lines with 2 different μ.
- **Linear:** This model is specified by a linear function with the 2 parameters: slope and intercept.
- **Piece-wise Linear:** The initial part is constant and then the failure rate grows linearly.
- **Exponential:** Here the exponential function is used with a constant in the front and a power.

Due to the constant replacement or repairing of the faulty cable section, the study showed piece-wise constant model fits the failure rate optimally as seen in Figure 2.4, with highest goodness of fit [12].

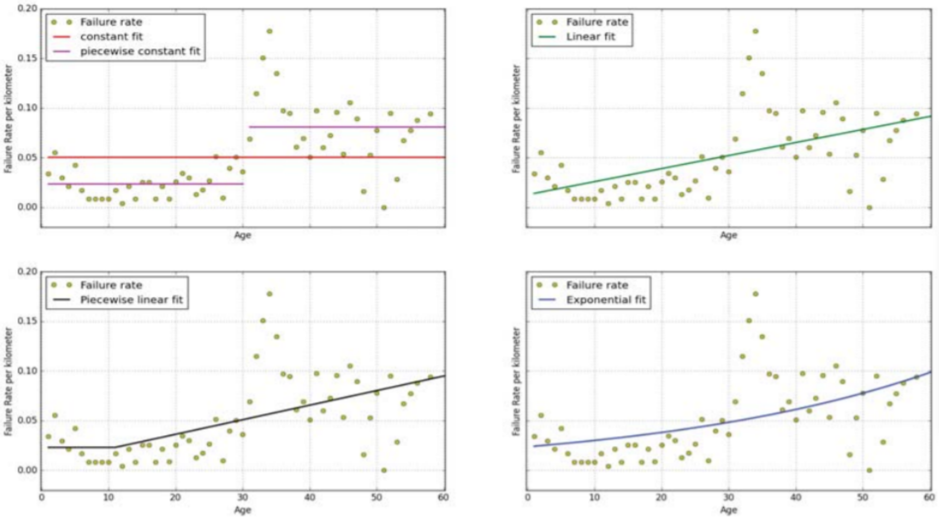

Figure 2.4: Different Rate Models Fitted to Failure Data [12]

B) In Crow-AMSAA and Reliability Growth Method [14][15]: It is used to characterize the quality development of an (often inhomogenous) population with a rather empirical method that works with a hazard rate like function (not the true hazard rate, because that is often hard to get for a population)

2.2.1. Optimal Statistical Distribution for Cable Failure:

For characterizing cable failures, the two parameter or three parameter Weibull Life Distribution is appropriate, as it considers aging mechanisms for modelling electrical insulation systems [16]. The 3 parameter model is used when there is a mechanism that causes a premature failure providing an estimate for the earliest time of failure with the threshold parameter[16]. Figure 2.5 shows the effect of the γ parameter interpreted as the threshold, shifting the distribution towards right side. The equation for the 3-parameter and 2 parameter Weibull cumulative density function, CDF, is respectively given by:

$F(t) = 1 - e^{-\left(\frac{t-\gamma}{\eta}\right)^{\beta}}$ and $F(t) = 1 - e^{-\left(\frac{t}{\eta}\right)^{\beta}}$

where α is the scale , β is the shape & γ is the threshold parameter.

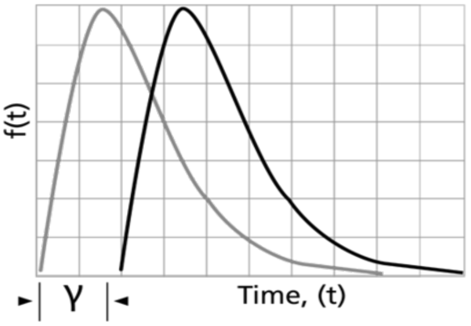

Figure 2.5: 2 vs 3 Parameter Weibull

2.2.2. Different Aging Models Under Electrical-Thermal Stress:

1) Uni-variate Models:

- **Inverse Power Law:** The Inverse Power Law Model (IPL) is most frequently used in aging studies under electrical stress. The time to breakdown (L) for this model is given by:

  $$L(V) = kV^{-n}$$

  where, V is the applied voltage, k and n are the constants [17].

- **Arrhenius Law:** The lifetime of electric insulation under thermal stress is well expressed by the Arrhenius Equation. This equation equates the chemical rate of the reaction as a function of temperature. The lifetime is given by:

  $$L(T) = Ae^{\frac{B}{T}}$$

  where T is the absolute temperature, A and B are the constants to be determined [17].

- **Exponential Law:** The exponential law is also used for lifetime calculations, given by:

  $$L(V) = ce^{-bV}$$

  where V is the applied voltage, b and c are the constants [17].

2) Multi-variate Models:

- **Combined IPL & Arrhenius Model:** The IPL model is combined with the Arrhenius relationship, to yield:

  $$L(V,T) = KV^{-n}e^{\left(\frac{B}{T}\right)}$$

  where the variables have the same meanings as previous equations [18].

- **Fallou's Model:** Fallou proposed a model based on exponential model by combining voltage and temperature by:

  $$L(V,T) = Ce^{(AV+\frac{B}{T})}$$

  where A, B, and C are electrical stress constants and must be determined experimentally from time-to-breakdown curves at constant temperatures [19].

- **Simoni's Model:** The insulation life with respect to a reference life is determined by the absence of an electrical stress and at low temperature by:

  $$L(V,T) = t_o \left[\frac{E}{E_o}\right]^{-n} e^{\left(-B\Delta\left(\frac{1}{T}\right)\right)}$$

  where t_o is the time-to-breakdown at room temperature and $V = V_o; \Delta\left(\frac{1}{T}\right) = \frac{1}{T} - \frac{1}{T_o}$, and B and n are constants which are determined experimentally [20].

- **Ramu's Model:** The Ramu's model is obtained from a multiplication of classical single-stress laws, and is given by:

  $$L(V,T) = K(T)[V]^{-n(T)} e^{\left(-B\Delta\left(\frac{1}{T}\right)\right)}$$

  where $K(T) = \exp\left(K_1 - K_2\Delta\left(\frac{1}{T}\right)\right), n(T) = e^{\left(n_1 - n_2\Delta\left(\frac{1}{T}\right)\right)}, K_1, K_2, n_1$, and n_2 are constants. $\Delta\left(\frac{1}{T}\right)$ is the same as that defined for the Simoni's model [21].

- **Montanari's Probabilistic Model:** This model relates the failure probability p to insulation life L_p. The scale parameter in the Weibull Distribution is substituted as life using the inverse power law. For a given time-to-breakdown probability p, the probabilistic model is given by:

  $$L_p(V,T) = L_s\,(V/V_s)^n\,[-\ln(1-p)]^{(1/\beta(T))}$$

  where L_p is a lifetime at probability p, L_s is a time-to-breakdown at reference voltage V_s and β is the shape parameter [22][23].

There are multiple models available, but still the question remains which one would be the best fit for the failure data. Also, the computational complexity and the limited failure data should be taken into account while modelling. So, the way to go is first collect sufficient data and then find a model that suits the data and that is preferably based on an understanding of the physics.

2.2.3. Statistical Parameter Estimation of Models:

A) Least Squares Technique (LS):

The least square basically is linear regression estimation fitting a straight line to a set of data points, estimating the parameters associated with the straight line, which are the slope and the intercept as seen in Figure 2.6. The parameters are estimated in a way that the sum of squares of errors is minimized by the following equation:

$$J = \sum_{i=1}^{N} \left(\tilde{a} + \tilde{b}x_i - y_i\right)^2 = \min(\tilde{a}, \tilde{b}) \sum_{i=1}^{N} \left(\tilde{a} + \tilde{b}x_i - y_i\right)^2$$

where $\tilde{a}$ and $\tilde{b}$ are the LS estimates of a and b, and N is the number of data points. To obtain a and b, the performance index J is differentiated with respect to a and b as shown below.

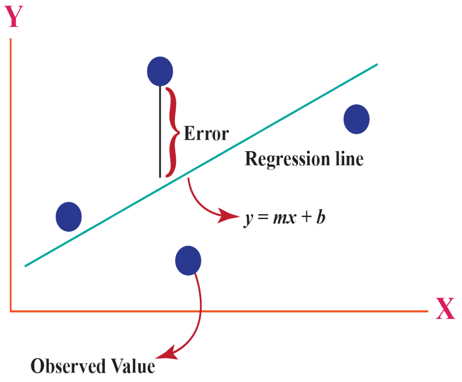

Figure 2.6: Least Square Estimation

$$\frac{\partial J}{\partial \tilde{a}} = 2\sum_{i=1}^{N} \left(\tilde{a} + \tilde{b}x_i - y_i\right)$$

$$\frac{\partial J}{\partial \tilde{b}} = 2\sum_{i=1}^{N} \left(\tilde{a} + \tilde{b}x_i - y_i\right) x_i$$

Finally, they are equated to zero to obtain the a and b estimate. This method is good for functions that can be linearized [24][25][26][27].

B) Maximum Likelihood Estimation:

The maximum likelihood estimation determines the parameters that maximize the probability of the failure data. If the likelihood function is differentiable, the derivative test for determining maxima can be applied and also the first order conditions of likelihood function can be solved analytically. If we consider Ordinary Least Squares (OLS) Estimator, it minimizes the cost function (sum of squared residues). However, in complex cases, numerical methods are required to find the maximum of the likelihood function. For a normal distribution, the Maximum Likelihood Estimation (MLE) and OLS yield the same estimate without any bias. But for Weibull or other optimal failure distributions, it tends to be slightly different.

Advantages of MLE over LS [25]:
1) The ML Estimators are consistent and asymptotically efficient. In some cases, LS can be as efficient as MLE
2) The ML Estimates tend to approach the true value of population as the size of the sample increases.
3) For Right Censored Data, they provide more information about failure.

Disadvantages of MLE over LS [25]:
1) For a small data set (<40 data points), since MLE is a biased estimator over LS, which is the best unbiased estimator, for some cases, it tends to produce a higher bias (though not significantly different and will be analyzed as a part of the research for a complicated multi-variate model).
2) Is computationally more demanding over LS which is straightforward with output parameters such as correlation coefficient and Anderson-Darling Coefficient giving the goodness of fit.

Thus, there is a trade-off and the research addresses this question of bias which might modify the parameters of the model giving inaccurate results [24][25][26][27].

2.2.4. AC Stress:

The cable under research is stressed under A.C., so the focus of interest are A.C. Stress Loadings only. D.C. stress loadings may be slightly different due to no zero-crossings [25][28]. A.C. Stress loadings can be applied several ways to accelerate aging, like:

1. Constant Stress: The most common stress type where each specimen runs at a specific level. As the stresses increase, the probability of failure increase. It is the 'best' aging method, since it is easier to maintain stress levels. They are better developed and empirically verified for most cables and also, the reliability estimations are already developed. A disadvantage is that there is no certainty of failure within a specific duration and may go for months to years, which is not optimal for lab experiments. Also, if the voltage level is too high to yield quick breakdown, then we might trigger a mechanism of failure different to the actual failure in fields. An optimal value of long step stress is still undoubtedly a preferable plan. In Figure 2.5, the left most figure shows different constant stress levels.

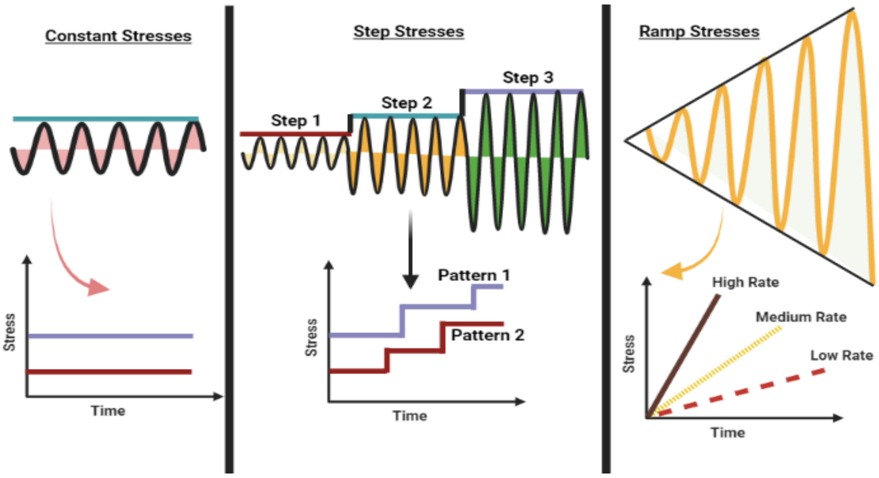

Figure 2.7: Different Kinds of Stress Loadings

2. Step Stress: A specimen in this regime is subjected to successive high levels of stress. Usually, all the specimens go through the same level of stress for similar amount of time, to maintain homogeneity in test. Also, different steps patterns are used to validate parameter estimates from different patterns. The advantages of this method is, it quickly yields failure. But quick failures can be misleading and greater failures does not guarantee accurate results, instead accuracy is sensitive to total duration of the test. The disadvantage of these kinds of stresses is reliability estimation, since most cables run at constant stresses and not stepped. Thus, the cumulative damage has to be very accurately modelled. Also, samples failing at very high stress levels may differ from those at use conditions. Yet, in a lab setting, this is one of the best loadings to obtain data within a stipulated time with a minor trade-off in accuracy. In middle of Figure 2.5, sinusoidal step stresses are shown with different patterns.

3. Ramped/ Progressive Stress: In this kind of loading, a sample undergoes a continuously increasing level of stress. Under low rate of rise of step, the samples would survive longer and vice-versa. Again, a ramp with very fast rise may not be able to reproduce the breakdown mechanism that happens in normal nominal voltage conditions. Different groups of specimens will undergo different slopes of ramp which would later help in developing the model. The disadvantages are same as Step Stress tests plus, it is also difficult to control the step stress accurately for a very long duration of time. An advantage is simpler data analytics. It also accelerates aging as in step test, but more smoothly and less risk of transients as opposed to step transitions. Figure 2.5, right side shows a ramped stress with different slopes as high, medium and low.

There are also some other types like alternate cyclic loading and random loading, but they are very seldom used for lab research purpose [25]. They are also not covered in the thesis research regime and thus, a detailed explanation is not necessary. In the most optimal situation, the test time should be as long as possible, with high number of failures. But there is always a trade-off when experimenting in the lab. In this research, the step stresses have been applied and rigorous statistical analysis has been made. Also, cumulative damage model is constructed to convert them into a constant stress discussed in Chapter 7 in details.

Thus, the key takeaways from this section can be demonstrated together as follows as shown in Figure 2.8:

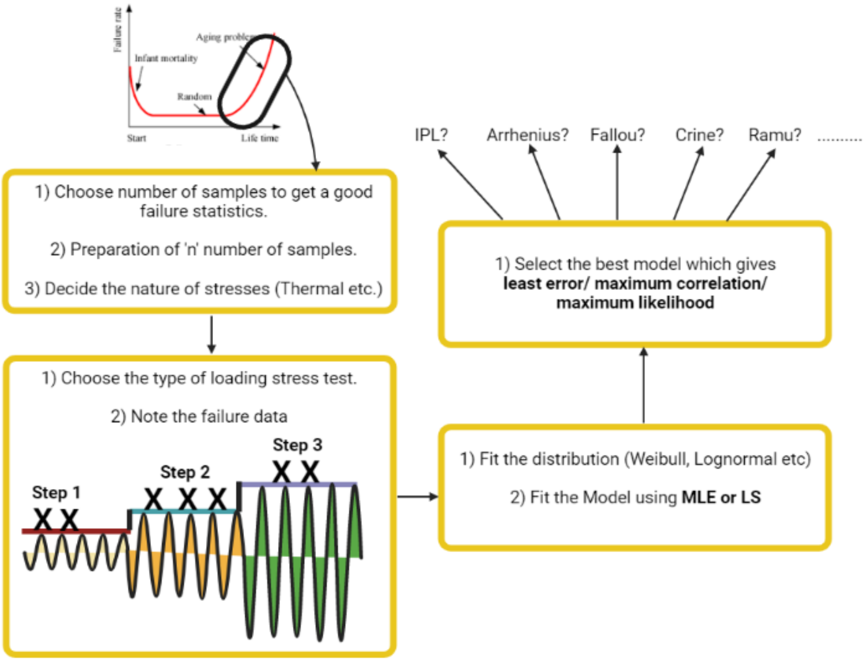

Figure 2.8: Model Fitting Algorithm starting from Stress Type

2.3. Degradation Monitoring Field Tests for Paper Cables

Multiple tests are available for testing the degradation process in OIP cables, but most of them are destructive and redundant. The most important Diagnostic tools for OIP cables are:

2.3.1. Diagnostic Test Type I:

Dielectric Frequency Response (DFR), **Polarization-Depolarization Current (PDC) measurement** coupled with **Residual Voltage Measurements (RVM)**. Online monitoring of tanδ is performed at 50 Hz and for other frequencies the cables are taken off service and monitored offline. Moisture ingress from environment and as byproduct of aging accelerates aging of cellulose, but the possibility of moisture from surroundings is almost zero for the HPG cable under research since it has a protective jacket. Karl Fischer titration can be performed to assess moisture content of paper [29]. Also, the Degree of Polymerization [30] have shown a strong negative correlation for Oil-Paper Insulation. The paper clearly indicates how the DP reduces non-linearly as the thermal aging of OIP samples increase. But these are of course destructive tests that cannot be done on full length cables. DFR is such an important measurement since it reflects the change in moisture as well as aging, temperature, structure of dielectric, acids and chemical composition [31][32][33][34]. Fourier Transform Infrared Spectroscopy (FTIR) also enables us to check the rate of degradation with aging by measuring the intensity of absorbance peak and in literature [35], it is observed that the absorbance peak of OIP samples have a tendency to decrease with aging temperature due to higher degradation rate, which is in line with the other modern literature [31][32][33]. Figure 2.9(a) show the reduction of DP with varying moisture content with increasing in aging, whereas (b) shows change in the peak absorbance with higher aging at two different temperatures of 120^{o}C & 150^{o}C. Thus, both clearly signifies how chemically the OIP samples deteriorate and is a good indication of aging.

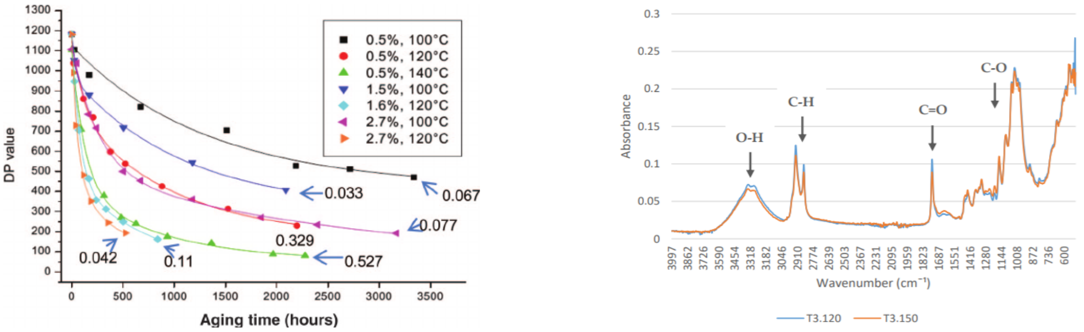

(a) Variation of DP value with Aging Time [36]

(b) Variation of Absorbance spectrum with Aging [35]

Figure 2.9: Destructive Tests for OIP Degradation Mechanism Recognition

PDC followed by Recovery voltage measurement (RVM) method is also used to examine the dielectric response, especially the deterioration or depolymerisation of paper under ageing condition. The PDC data can be interpreted computationally with most recent models (discussed in subsection 2.3.1) which involves the polarization processes and their equivalent effect on the sample parameters. An external voltage applied produces an electric field inside the paper insulation causing the dipoles to align along field direction resulting in polarization. When the cause i.e. the voltage is removed, the dipoles relax and return to original state following a time constant (R_iC_i) [38] [39]. During this dipole relaxation period, a residual voltage appears across the paper insulation as a peak as shown in Figure 2.10 with a certain $\frac{dv}{dt}$ that can be measured. RV and relaxation times are two vital indicators for assessing insulation condition since they govern the times of polarization processes.

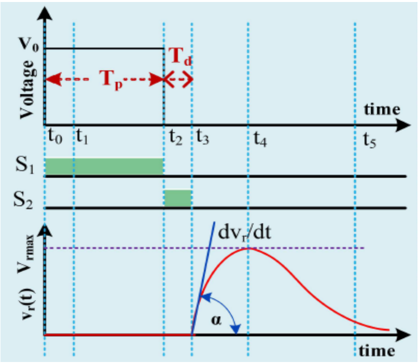

Figure 2.10: Polarization-Depolarization followed by Residual Voltage Peak [37]

After a thorough literature review, the measurement of tanδ has been divided into the voltage rating of the power supply, frequency sweep, different techniques used with FDS and their applications with state-of-the-art equipments designed for such measurements which have been discussed in details in the same chapter in Section 2.5, as shown in Figure 2.11:

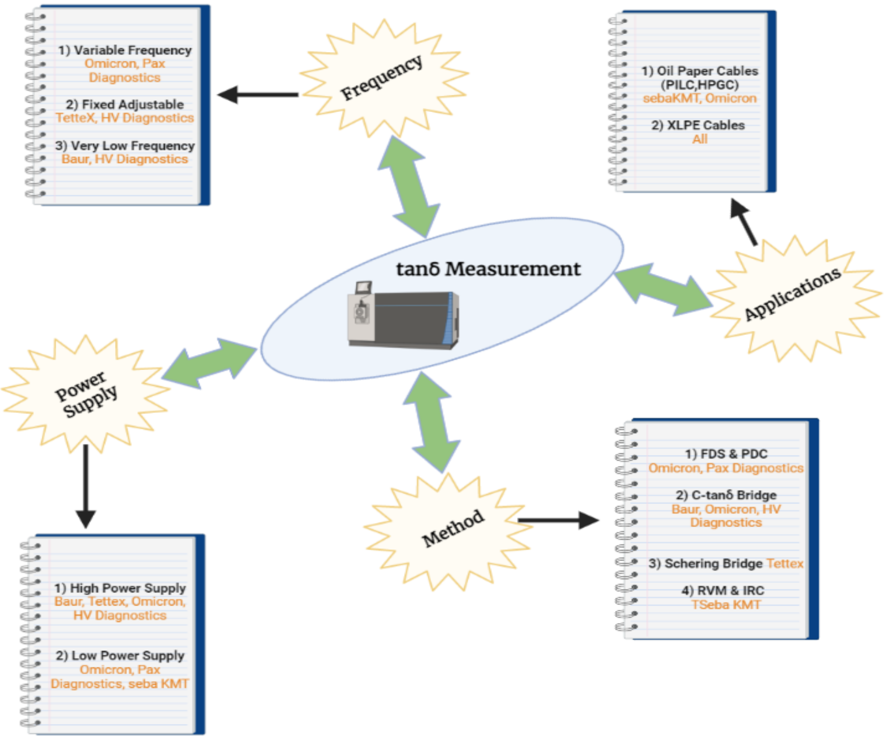

Figure 2.11: FDS Measurement Techniques

Modelling of Dielectric Response:

Several models have been developed over the years with advancements in measurements [37] and the most prominent ones have been discussed below, with a comparison in Figure 2.12(b):

1) Debye Model: The total polarization at any instant of time for paper insulation is given by

$$P_{\text{tot}}(t) = \varepsilon_0 \left[\varepsilon_\infty - 1 + \frac{\varepsilon_s - \varepsilon_\infty}{1 + j\omega\tau} \right] E_m e^{j\omega t}$$

where, $\varepsilon_s, \varepsilon_\infty$ denote the dielectric constants at DC voltage and alternating voltage with infinite frequency, $E = E_m e^{j\omega t}$ represents an alternating voltage in the exponential form.

From this the relationship between the real and imaginary permittivity of material can be derived

$$\underline{\varepsilon} = \varepsilon' - j\varepsilon'' = \varepsilon_\infty + \frac{\varepsilon_s - \varepsilon_\infty}{1 + j\omega\tau}$$

This is known as Debye Model as shown in Figure 2.12(a), which explains the behaviour of dielectrics for a wide range of frequencies [40][41]. The real and imaginary part can be evaluated as:

$$\varepsilon' = \varepsilon_\infty + \frac{\varepsilon_s - \varepsilon_\infty}{1 + (\omega\tau)^2}$$

$$\varepsilon'' = (\varepsilon_s - \varepsilon_\infty)\frac{\omega\tau}{1 + (\omega\tau)^2}$$

2) Cole-Cole (C-C) Model: All dielectrics follow Debye model however very few dielectrics agree completely with the relaxation processes in practical scenario. This is because of the simple assumptions made in Debye Model. It considers spherical molecules for any geometric configuration causing negligible field response on axis of response. In practicality, OIP has several molecular shapes

(Spheroidal or linear in the long-chain arrangements). This irregular shapes would have different responses resulting in different relaxation times. Thus, for C-C Model, the parameter ”N” is introduced contributing to the modelling process [42][43]. The model converges to Debye form if N = 0. The general form is given by:

$$\underline{\varepsilon} = \varepsilon_\infty + \frac{\varepsilon_s - \varepsilon_\infty}{1 + (j\omega\tau)^{1-N}}; \quad 0 \leq N \leq 1$$

3) Davidson-Cole (D-C) Model: The Davidson-Cole Model introduces the β-parameter, which for unity is equal to Debye Model. The D-C Model aims to explain the spatial and temporal fluctuations occurring in the dipoles [44],[45],[46]. Due to the external electric field, the molecules get disoriented creating non-uniform dipole oscillatory motion. Thus, some dipoles oscillate with higher amplitude while some with lower, contributing to dipolar modelling as follows:

$$\underline{\varepsilon} = \varepsilon_\infty + \frac{\varepsilon_s - \varepsilon_\infty}{(1 + j\omega\tau)^p} : \quad 0 \leq \beta \leq 1$$

4) Fuoss-Kirkwood (F-K) Model: The F-K Model is quantified only if it adheres to C-C relaxation processes. The distribution of relaxation time in the model is however independent of the external temperature. This enables us to derive distribution functions for long chain polymers at very high temperatures [47].

$$\varepsilon'' = (\varepsilon_s - \varepsilon_\infty)^\delta \frac{(\omega\tau)^\delta}{1 + (\omega\tau)^{2\delta}}; \quad 0 \leq \delta \leq 1$$

5) Havriliak-Negami (H-N) Model: For very complicated molecular structures, H-N proposed a generalized model, derived from C-C and D-C models, represented by:

$$\frac{\varepsilon^* - \varepsilon_\infty}{\varepsilon_s - \varepsilon_\infty} = \left[1 + (j\omega r)^{1-N}\right]^{-\beta}$$

where, α-parameter describes the connectivity of the long chains and the β-parameter indicates the insulation local density [48].

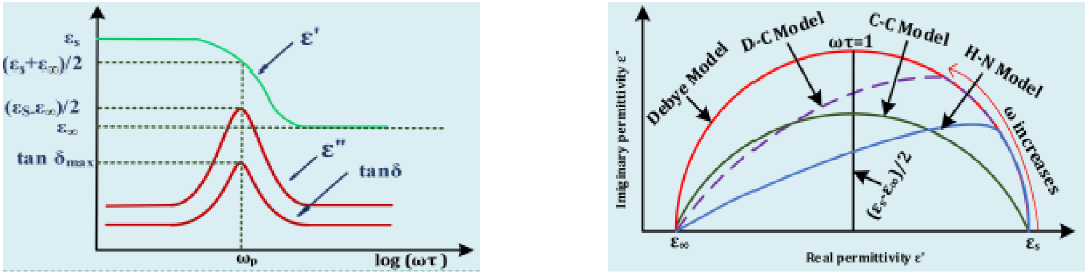

(a) Modelling of Debye Process [37]

(b) Variation of the ϵ' vs ϵ” circle for different Models [37]

Figure 2.12: Modelling of Dielectric Response

2.3.2. Diagnostic Test Type II:

Partial Discharge (PD) Measurements: Another important diagnostic tool for detecting defects and aging in paper insulation is the PD Measurement. There are basically 2 approaches: Online or Offline PD Measurements. Off-line tests are carried out on the de-energized cable from normal operation and re-energized from external source [49]. This enables to determine the PD extinction and inception voltage. On-line tests at operating conditions show the exact behaviour of PD but cannot evaluate PDEV or PDIV. There is still some relation, if PD is triggered at certain voltage and line voltage amplitude is higher than PDIV, then PD appears at the phase angle where voltage exceeds PDIV. Currently only offline methods have been standardized in IEC 60270. On-line methods like optical, acoustic and other unconventional methods do not have a benchmark to compare against.

Also, PD patterns can be represented as **time resolved data** inflicting the correlation between PD signal shape and nature of defect, which provides information about the aging. The other is the **phase resolved PD** representing the physical process at PD location. Phase resolved data are vastly used in classification since PD pulses have a strong correlation with PRPD patterns.

PD Feature Extraction: The purpose of PD feature extraction is for obtaining features from the PD data that is in close resemblance with the PD Characteristics with particular defects. Also, the dimensions of the original data set is reduced for easier processing, similar for Principal Component Analysis or t-SNE for analyzing large data sets [50]. The reduced matrix saves computation time and model complexity. The following diagram in Figure 2.13(a) shows the state-of-art used PD feature extraction techniques used both in academia as well as in industry [49].

PD Classification Methods: The PD patterns detected need to be classified into various categories with maximum accuracy. Research has been done to classify size of cavities based on PD Patterns, while some researchers focus on PD in 3-ϕ transmission lines [51]. There are majorly 4 main defects and the classification categories are cavities or voids, surface discharges, corona and treeing. The different algorithms for classification are shown below in Figure 2.13(b) .

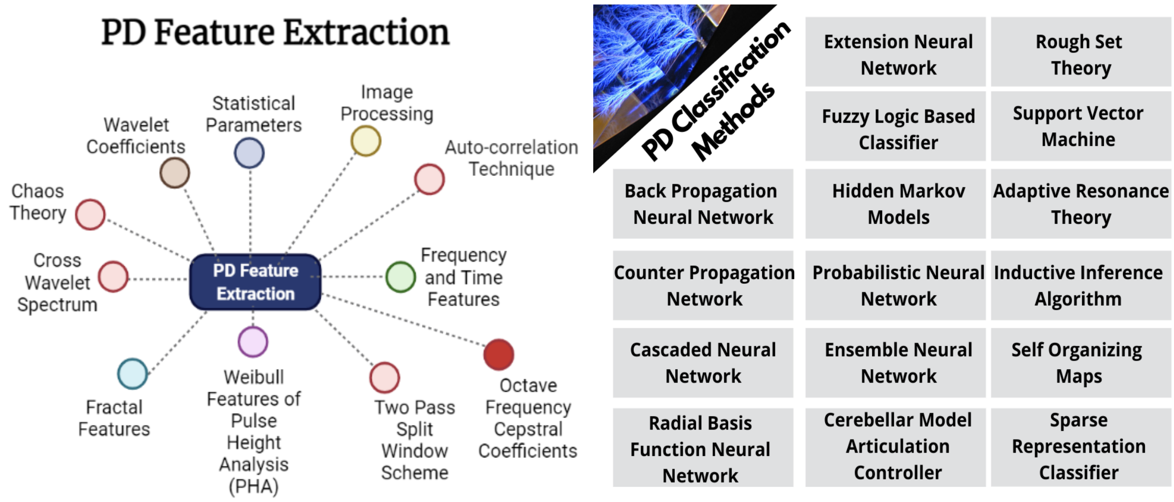

(a) Extraction of PD Features

(b) Classification Techniques of PD Patterns

Figure 2.13: Post Processing Methods of PD Patterns

2.3.3. Diagnostic Test Type III:

The rest of type and maintenance tests are represented into this category which are not essential for analyzing the aging degradation, but important for any cable [52].

- DC Sheath Test: This monitors the condition of the non-metallic outer sheath.
- Oil Analysis: Monitors the condition of oil from joints and removed cable sections for indicating aging and defects in insulation.
- G-value Measurement: Measuring the thermal resistance around the soil
- Inspection of Hydraulic System: Checks leakages, working of pressure gauges and alarm systems. Since the nitrogen is pressurized under high pressure, any leakage can distort the shape of the cable during loading, thus, it has to be monitored frequently.The shape distortion will be minimal, but pressure drop on the outside of the lead, means pressure drop on the inside and that means voids and gaps are not compressed anymore, which means PD probability is higher.
- Inspection of Earthing System: Checking the layout and resistances. Also the earth system and cross-bonding should be inspected.
- Visual Inspection of the Cable Accessories: Detection of Pollution, Aging or Damages due to Human Interference. Possible detection of jacket faults.
- Determination of the Impregnation Constant: For detecting the presence of free gas in the cable insulation

2.4. Different Polarization Mechanisms in Insulation

With advancements in commercially available test equipments, it has been possible to investigate into the physical phenomena inside the insulation. When an external field is applied, dipoles inside dielectrics get excited from their initial state as shown in Figure 2.14(a) below and the dipole moment is given by: $p = Qd$, where Q is the charge and d is the separating distance between two similar charged particles in the dipole. These excited dipoles contribute to 3 prominent types of polarization as shown in Figure 2.14(b) below:

- **Electronic Polarization:** Under external electric field, the electron cloud is displaced and results in a dipole moment. The resultant atom with respect to the nucleus is said to be electronically polarized. The magnitude of induced moment is proportional to field strength and when the field is removed, it becomes zero. Electronic polarization is very spontaneous and fast and is normally difficult to model due to the small time constant [53][54][55].
- **Ionic Polarization:** Dependent on frequency, after exposure to an external field, two opposite charged ions in a molecule gain a relative displacement leading to the formation of an ionic dipole. When the field is removed, the restoring forces convert them back to the equilibrium position. The ionic displacements follow harmonic oscillations in the infrared region of Electromagnetic Spectrum [53][55].
- **Orientation Polarization:** All physical processes can be modelled as an ionic molecule having higher electropositivity in one atom compared to the other. This molecular behaviour leads to formation of permanent dipoles even in absence of fields. The moment is defined by charge transferred from one atom to other and the inter nucleic distance [48]. The frequency dependence of orientation polarization is regarded as dipolar relaxation in dielectrics.

On the basis of concentration of bulk insulation, surface interaction and density of metal ions, they can be divided into 3 main processes:

- **Interfacial Polarization:** They are effective in inhomogenous dielectrics and occurs between the boundaries of two dielectrics with different conductivities. This polarization contributes to the anomaly in the low-frequency spectrum specially between 0.1Hz-10 Hz, known as the Maxwell-Wagner Effect [56][57][58]. This is because of accumulation of charges at the interface and this accumulated charge influences the dependency of the overall conductivity and permittivity on the mixture of their properties [58].
- **Bulk Polarization:** This is caused by hopping of charge carriers occurring in amorphous and non-conductive insulating material. Due to hopping mechanism, this polarization contributes to conduction current. Hopping regions generally extend through the material forming interconnected network allowing intermediate energy levels in forbidden gap. It is possible to observe the process of dipolar relaxation if hopping distance is smaller between two consecutive sites [59].
- **Tunneling Polarization:** This is due to the electrode/insulation interface causing tunnelling effect. With very little/absence of external field, there is tunnelling of charge carriers from electrode interface into unoccupied traps of lower energy levels. This is because there is a reverse polarity occurring in voltage resulting in inversion of space charges causing the delocalized charges to travel across the channel [60][61][62].

(a) Orientation of Dipoles

(b) Generalized Polarization Processes

Figure 2.14: Dipoles in Equilibrium and after Polarization

2.5. Commercial Diagnostic Instruments

The commercial diagnostic instruments used for field measurements are shown in Figure 2.15 and discussed below:

1) Baur VLF Diagnostic System: This covers all the main requirements while testing medium voltage cables at very low frequency. Invented in 1995, the company offers flexibility to generate excitation voltages with frequencies ranging from 0.01-0.1 Hz. Apart from primary measuring equipments, it also provides cable status evaluation, following accepted standards for installation and maintenance [63].

2) SebaKMT Diagnostic System: SebaKMT has their own cable diagnostic system (CDS) and tanδ test equipments for condition monitoring of 3-ϕ cable insulation. CDS system is a advanced technology combining isothermal relaxation currents and return voltage measurement (RVM) for analysis. It conducts the measurements with cosine wave and highly effective for detecting aging effects like humidity, moisture and effect of temperature [64].

3) Pax Diagnostics Instruments: Pax Diagnostics manufactured IDAX-206, VAX-230 instrument which has been integrated with a high voltage supply IDA 200 for assessment of insulation. The power supply has been developed by General Electric. The system works on a wide band of frequencies from 0.1μHz-1kHz calculating the capacitance and dielectric losses [65].

4) Tettex Instruments Haefely Hipotronics has manufactured three dielectric loss analyzing machines for measuring dissipation factor at very low frequencies for H.V. apparatus. The Tettex 2820, Tettex Midas 2880 and 2881 and Tettex Midas 2883 measure loss factors for rotating machines, transformers, bushings and circuit breakers at the power frequency [66].

5) HV Diagnostic Instruments: HV Diagnostics has developed a double-integrated diagnostic system, HVA28TD and HVA45TD offering both very low frequency power supply and tanδ to evaluate condition of medium voltage and extra high voltage electrical cables. They also produce stand alone tanδ measurement units like TD 30, TD 60 and TD 90 evaluating at low frequencies of 0.02 - 0.1Hz which is effective to characterize moisture or water tree degradation in cable insulation [67].

6) Omicron Instruments: They have a varied range of products like CPC 8./100 with CP TD1, MI 600 and Dirana. The CP 80/100 is a multi-functional instrument equipped with TD1 for measuring the loss factor. It is an universal system for performing tests on power transformers, machine insulation, instrument transformers and grounding systems with a frequency sweep from 15 to 400 Hz. MI 600 is also another precise analyzer with frequency range from 5 Hz to 50 kHz [68][69].

BAUR PHG 80 TD/PD

Tettex 2820

VAX 230

HVA 28TD

Omicron dirana

Figure 2.15: Commercial Diagnostic Instruments [63][65][66][67][68]

3

Installed Lengths, Fault, Failure Rate, Outage Time Statistics of GC Compared to Other Types of Cables

3.1. AC Land Cables Overview

This section describes the circuit-km of AC Land Cables in 2019 as a survey done by CIGRE B1-57 [70]. As of 2019, the maximum circuit-km is laid for the lowest voltage range of 60-109 kV for a length of 14997 units with subsequent reductions with increase in voltage levels of 110-219 kV, 220-314 kV, 315-500 kV and above 500 kV having the least circuit-km length of AC land cables. This is because the lower voltage levels have been in operation for more than 80 years and have the maximum number and length of AC cables [70]. The EHV and UHV ranges has been an outcome of recent technological advancements and thus the circuit kilometers is relatively less. The total circuit kilometer as of 2019 according to CIGRE is 29350 units. This statistics have been obtained as a result of questionnaire prepared for 59 utilities from 19 different countries worldwide and represented in Figure 3.1(a).

The data has been compared with CIGRE B1-07 data available for the year 2007 [71] as shown in Figure 3.1(b) which is more than a decade back. Statistics show that the circuit-km for each of the voltage ranges were higher as compared to 2019 data with the maximum length of 24859 units for 60-109 kV. With increase in voltage levels, the data has a same pattern of lowering of circuit km with more than 500 kV having a circuit length of 0 km. A reduction is expected due to more research on HVDC cables and overhead lines. But the large difference maybe interpreted as the diversity in the scope of the surveys and variations in the questions proposed. It is believed that the complexity of the questions in the recent 2019 survey gave rise to some disputed statistics and also the number of replies is believed to be fewer.

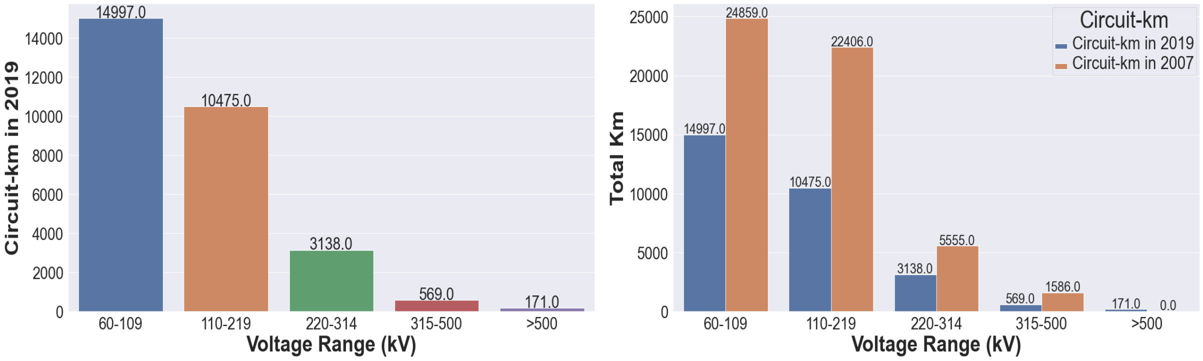

(a) Circuit-km of AC Land Cables in 2019 according to CIGRE B1-57

(b) Circuit-km of AC Land Cables in 2019 according to CIGRE B1-57 compared to CIGRE B1-07 in 2007

Figure 3.1: Circuit-km of AC Land Cables from 2007 to 2019 according to CIGRE Reports

3.2. AC Land Cables According to Different Types

The following are considered in the different types of AC Land Cables:

- **SCOF** - Self-Contained Oil-Filled cables including kraft-paper and paper-polypropylene (PPL) insulation. Flat-type cables (Mollerhoj type) are also included under SCOF cables.
- **HPOF** - High-Pressure Oil-Filled cables also known as High-Pressure Fluid-Filled (HPFF) cables
- **GC** - Gas cables, including High-Pressure Gas-Filled (HPGF) cables & Self-Contained Gas- Filled (SCGF) cables
- **EPR** - Extruded Ethylene Propylene Rubber with or without a water barrier
- **PE** - Extruded Low density thermoplastic polyethylene with / without a water barrier/laminated barrier
- **XLPE** - Extruded Cross-Linked Polyethylene with or without a water barrier/laminated barrier

The quantities of AC Land Cables in service at the end of 2015 [70] data has been collected and assessed. The maximum circuit-km length of cables has been recorded for XLPE with 12,848 units and the lowest for Polyethylene Cables according to the utility companies approached. The Gas Cables are predominantly found for voltage levels between 110-219 kV with 433 circuit-km and almost 0 for extra high voltages above 315 kV. The Gas Cables are almost only 2% in circuit-km length when compared to XLPE. This clearly signifies a shift in the technology from the Gas Compressed Cables to the XLPE based Cables. Though, the figures are very low for GC, yet proper efforts must be taken to conserve the ones in operation or to replace the ones failing due to aging. The statistics for the number of circuit km length for different types of cables at different voltage levels has been observed in Figure 3.2 and a comparison has been made.

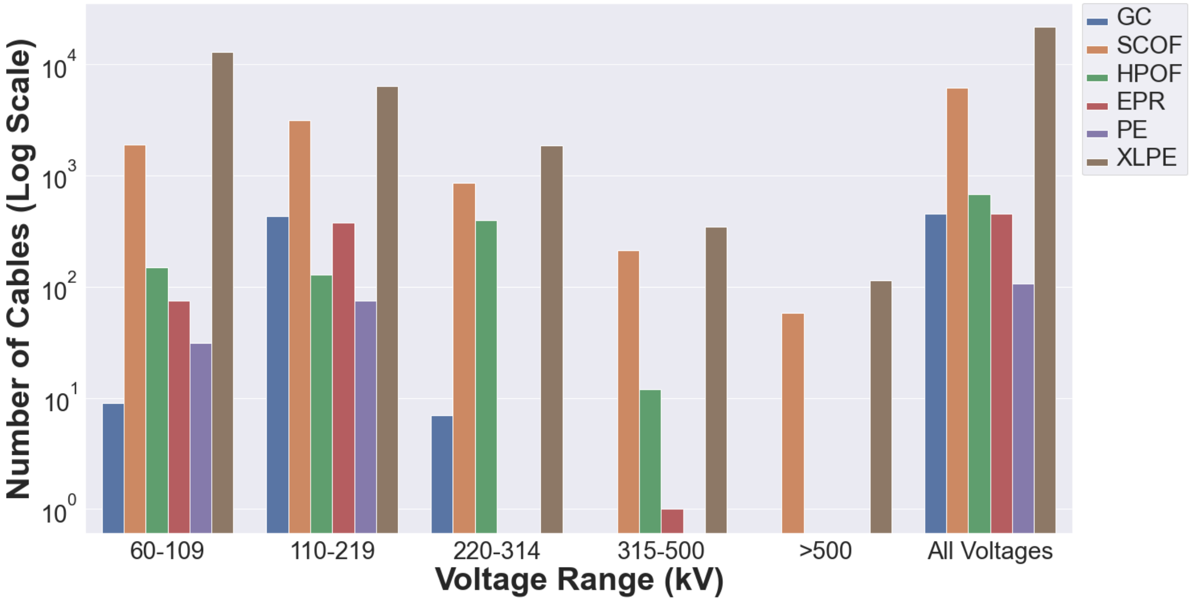

Figure 3.2: Different Types of AC Land Cables at Different Voltage Levels in the end of 2015

The number of cables installed between 2006-15 also shows a strong skew towards XLPE with 6,890 circuit-km length which dominates all other kinds of cables. Thus, the pie-chart shown in Figure 3.3(a) represents other types different to XLPE Cables. Among the other types of cables, SCOF and EPR are installed most with almost 35% each and Gas Pressure Cables are installed only 5.9%, the statistic calculated without taking into account the XLPE cables.

Since the year 2005, the following statistics is observed with the statistics for different type cables shown in Figure 3.3(a):

- 24% of all reported AC land cables have been installed since 2005.
- Almost all installed AC land cables have been XLPE cables (98%) as seen in Figure 3.3(b).
- SCOF and HPOF cables only account for 0,7% and 0,5% respectively.
- No PE cables have been installed.

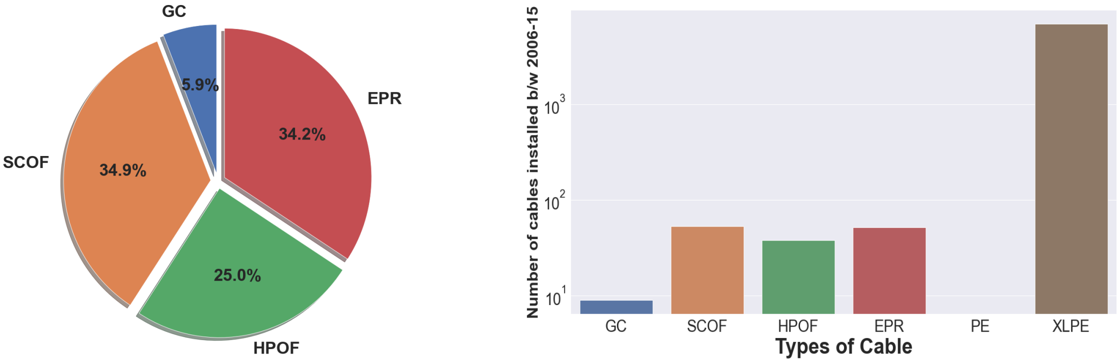

(a) Percentage of Cables installed between 2006-15 except XLPE

(b) Circuit-km of AC Land Cables installed between 2006-15

Figure 3.3: Circuit-km of AC Land Cables installed from 2006-15 according to CIGRE Report in form of Pie and Bar chart

3.3. Shift from Paper Cables to Extruded Cables

The percentage of extruded cables is higher for all the voltage levels and almost double for some. For 60-109 kV systems, the ratio of extruded to paper cables is almost 6:1 whereas for EHV systems of more than 500 kV, the ratio is 2:1. When all the voltage levels are considered the ratio is a striking 3:1. When the data is considered for installations between 2006-15, the ratio is 99:1 as seen in Figure 3.4(b) which means that there has been a complete paradigm shift from paper to extruded. But, with the rising concern over non-bio degradation of plastics,its derived products and government regulations, the focus is shifting towards biodegradable materials like P-Laser manufactured by Prysmian B.V.. The trends for different voltage levels for these two types are represented in Figure 3.4(a).

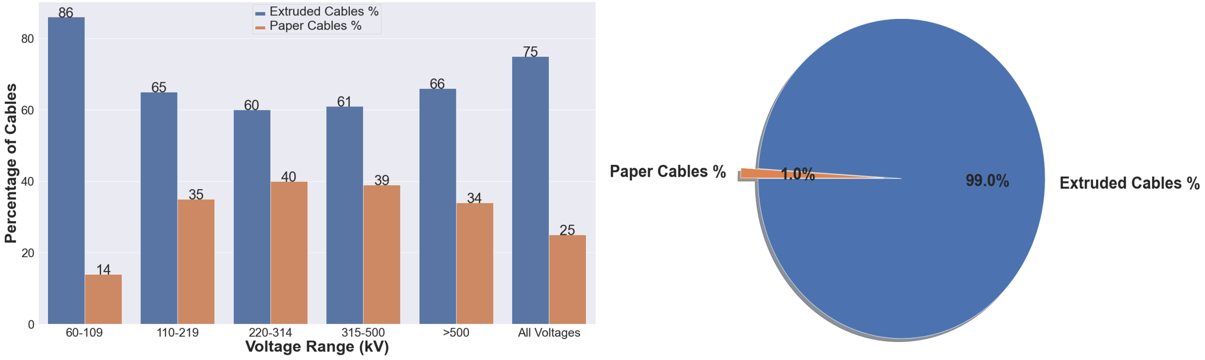

(a) Percentage of Extruded or Paper Cables in service till 2015

(b) Percentage of Extruded or Paper Cable installed between 2006-2015

Figure 3.4: Comparison between Extruded or Paper Cables

3.4. Reported Faults on Land Cable Systems

The reported faults are either Internal, External or Unknown in nature. The faulty components considered here are Cable, Joint, Termination and other miscellaneous components. Since the number of XLPE Cables are higher in number the statistics also show a higher number of failure of XLPE components between 2006-2015 [70]. Since the total number of cables, joints or terminations were not possible to calculate hence the statistics are of low significance and so we consider failure rates in the next section, which is a very crucial statistic for evaluating condition of a system. The least number of failures in components were recorded for Gas Cables mainly due to the very low number of such existing installations. Figure 3.5(a) depicts the number of failed components for each type of cable whereas Figure 3.5(b) focuses on faults for GPC.

For GC,the reported faults between 2006-15 were most predominant in the cable system with 63% and 18.2% each in termination and Joints. Thus, it is crucial to evaluate the failure in the cable mainly in the insulation owing to the higher number of reported faults.

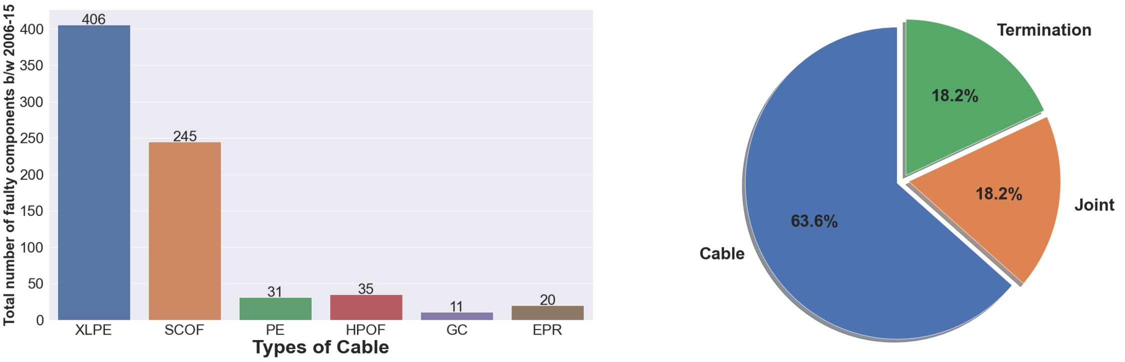

(a) Faulty Components in different cable types b/w 2006-15

(b) Reported Faults in GPC components b/w 2006-15

Figure 3.5: Failure Statistics of different cable types b/w 2006-15

3.5. Failure Rates for AC Land Cables

$$FailureRate = \frac{\sum_{i=1}^{n} N_i}{\sum_{i=1}^{n} A_i} \times 100$$

Where, Failure Rate = Number of cable failures per 100-circuit-km-years or number of component failures per 100-component-years. They are also referred to as mean failure rates.
N_i = Number of failures of the component considered during the i-th year of the period concerned
A_i = Quantity of the component in service at the end of the i-th year (circuit-km or number)

The internal and external reason of fault statistics have been represented in Fig 3.6 (a) and (b).

- The internal failure rates reflect the inherent performance of the cable system.
- GC, HPOF, EPR cable systems have double the internal failure rate compared to XLPE and SCOF, though the average age of the former types are greater than extruded cable systems.
- PE Cable systems have the highest internal fault rates over the other kinds of cables.
- It can be observed that there is no trend in failure rates correlated to increase in the voltage levels.
- For external faults,the pattern is almost similar to internal faults, except that there has been no reported failures for GC.
- PE and HPOF have the highest failure rates which is almost 4 times higher than XLPE.

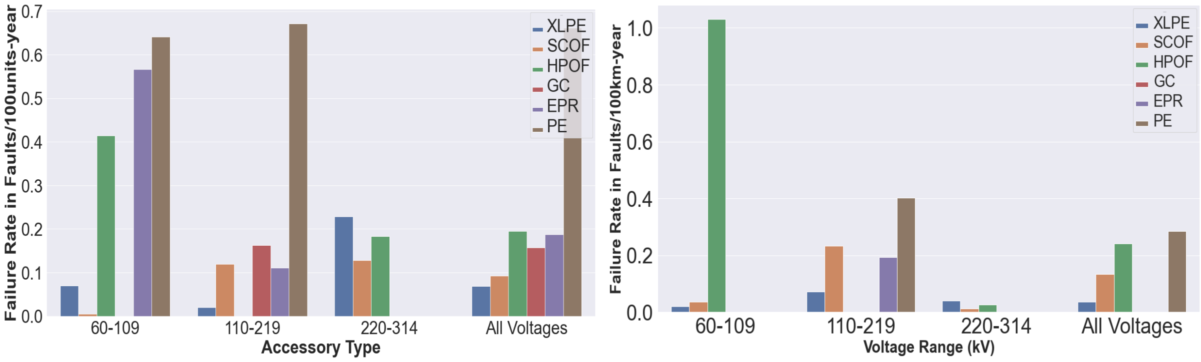

(a) Failure Rates of different AC Land Cable of Internal Origin

(b) Failure Rates of different AC Land Cable of External Origin

Figure 3.6: Failure Rates of Different AC Land Cables of Varied Origins

3.6. Failure Rate Statistics of Accessories

GC Cables have the highest joint and Air Insulated Switchgear (AIS) Termination Accessory failure rate of all types of cables.

For extruded cables, the joint failure rate is more at higher voltages whereas it is the reverse for SCOF cables.

No termination failures have been reported for HPOF and GC cables

The failure rates in GIS/ Transformer Termination is relatively smaller over Joints and AIS Termination Accessory Failure Rates. All the statistics about failure rates for different cable accessories have been shown in Figure 3.7.

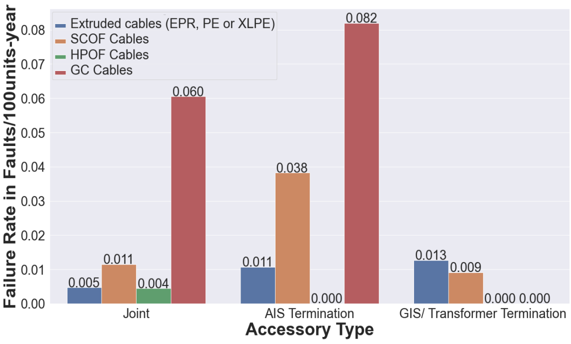

Figure 3.7: Failure Rate of Different Cable Type Accessories

3.7. Outage time for land cables

- The average outage time of GC are least with only 6 days in average for all voltage levels, though they are not installed over 220kV.
- The average outage time of HPOF is the longest. These are installed in higher voltages, and sometimes localization of faults could be more time consuming. This causes higher outage times.

Comparison of outage times for different cable Types at Different voltage levels have been shown in Figures 3.8(a) and (b).

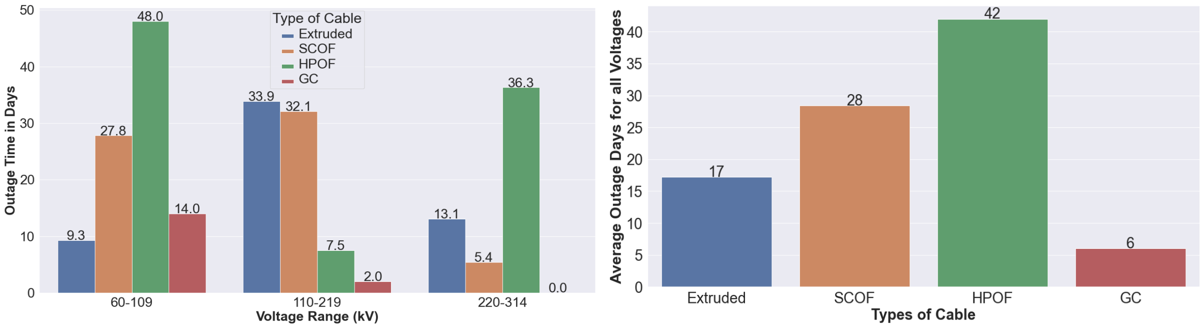

(a) Outage Times for Land Cables w.r.t Voltages

(b) Average Outing Times for Different Cable Types

Figure 3.8: Comparison of Outage Times for Different Cable Types at Different Voltage Levels

3.8. Failure Statistics for Gas Pressure Cables

For failure rates in the AC Gas Pressure Cables, the source of failure are observed to be all internal in nature according to the data. The failure rate is mostly between 110-219 kV, which is the predominant voltage level for such kind of cables. Since there are almost no GC in extra high voltage systems, hence there is no failure reported. Thus, when all the voltage levels are taken into account, the failure rate is 0.157 which is relatively on the higher side as shown in Figure 3.9.

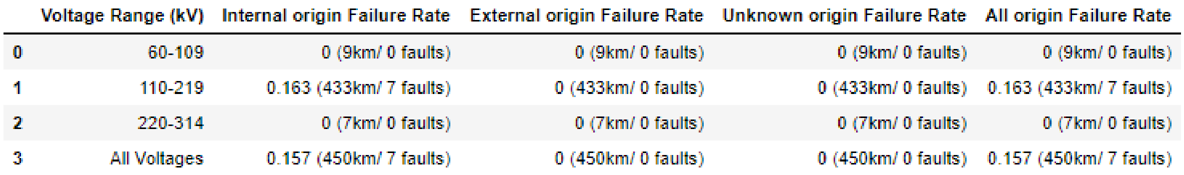

	Voltage Range (kV)	Internal origin Failure Rate	External origin Failure Rate	Unknown origin Failure Rate	All origin Failure Rate
0	60-109	0 (9km/ 0 faults)	0 (9km/ 0 faults)	0 (9km/ 0 faults)	0 (9km/ 0 faults)
1	110-219	0.163 (433km/ 7 faults)	0 (433km/ 0 faults)	0 (433km/ 0 faults)	0.163 (433km/ 7 faults)
2	220-314	0 (7km/ 0 faults)	0 (7km/ 0 faults)	0 (7km/ 0 faults)	0 (7km/ 0 faults)
3	All Voltages	0.157 (450km/ 7 faults)	0 (450km/ 0 faults)	0 (450km/ 0 faults)	0.157 (450km/ 7 faults)

Figure 3.9: Failure Rate of GC from Different Origins

For failure in the cable accessories, the failure is again predominant in the 110-219 kV range for the joints, but peculiarly there was a high amount of failure in the AIS termination where 2 faults happened in only 4 terminations. There has been no faults reported in the GIS/ Transformer Termination. Overall, the failure rate of accessories is lesser than that of cable systems when all the voltages are considered. The failure rate in the AIS termination of 0.081 is higher than that of Joints of 0.0605 as shown in Figure 3.10.

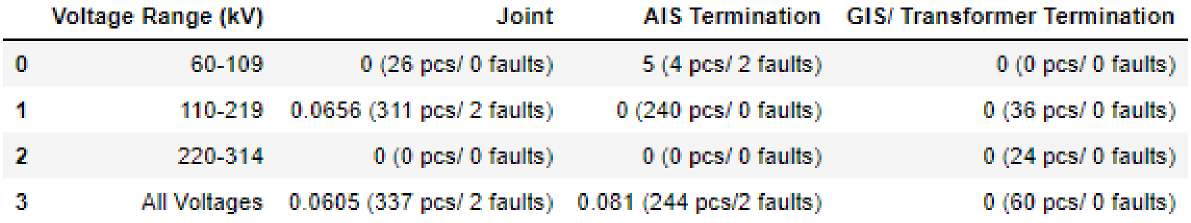

	Voltage Range (kV)	Joint	AIS Termination	GIS/ Transformer Termination
0	60-109	0 (26 pcs/ 0 faults)	5 (4 pcs/ 2 faults)	0 (0 pcs/ 0 faults)
1	110-219	0.0656 (311 pcs/ 2 faults)	0 (240 pcs/ 0 faults)	0 (36 pcs/ 0 faults)
2	220-314	0 (0 pcs/ 0 faults)	0 (0 pcs/ 0 faults)	0 (24 pcs/ 0 faults)
3	All Voltages	0.0605 (337 pcs/ 2 faults)	0.081 (244 pcs/2 faults)	0 (60 pcs/ 0 faults)

Figure 3.10: Failure Rates of GC in joints and terminations

The failure of Gas Compresses cables and their accessories have been represented and compared with other types of cables in Figure 3.11(a) and (b) respectively. The graphs show that the joints and the AIS Terminations have the maximum fault rates for Gas Cables over the other variants. The cable under study is also rated at 110 kV. Thus, the insulation and other internal parameters are being investigated in the thesis, to predict such failure in advance by calculating the remaining useful life and the aging parameters of the cable system.

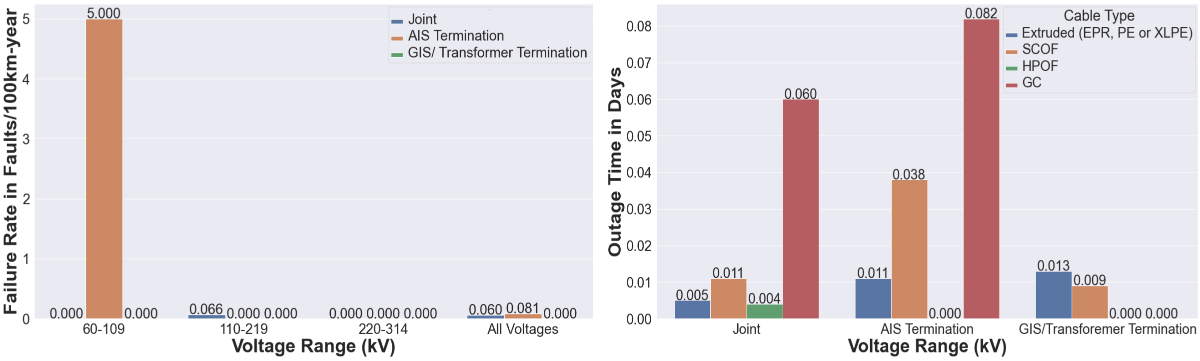

(a) Failure Rates of GC for different Voltage Levels

(b) Failure Rates of GC for different accessory types

Figure 3.11: Comparison of GC Failure Rates for Different Voltages and Accessory Types with other types

4

Electrode and Sample Preparation

For carrying out the stress tests on the Oil impregnated paper samples, the most important aspects of the experiment is to build the electrode and its support and also to prepare the samples from the cables provided by TenneT. It is made sure to choose the electrodes and samples of exactly same dimensions since changing the size can affect the breakdown voltage, as suggested in literature [72][73][74].

4.1. Electrode Preparation

The high voltage electrodes used are made of steel and are 7 cm in length and 0.5 cm in diameter as shown in figure 4.1 (a). The diameter is chosen in such a way that it is smaller than the breadth of the rectangular samples, which is almost 2 cm. Initially an electrode of diameter 1.5 cm was chosen, but during the tests it was observed that placing the sample right in the centre was a major issue. As a result, if the placement was biased towards a certain sides, discharges would occur as the H.V. electrode is placed very near to the edge of the sample, thus affecting the accuracy of the experiments. Thus, for the breakdown tests, the diameter was reduced and finally the ones with 0.5 cm were chosen for conducting the experiments. The ground electrode is also made up of steel and the dimensions are decided to make sure the samples completely fit on the electrode. They have a height of 2 cm and a diameter of 12 cm as seen in figure 4.1(b). Also, the ground electrode surface was made as smooth as possible, since initially, a small bump in the centre caused the breakdown to occur near it and biases the experiments.

(a) HV Cylindrical Electrode

(b) Polished Ground Electrode

Figure 4.1: Electrodes used for Different Tests in Research

Since, the setup is not immersed in oil during the stress experiments, there is a possibility of surface discharges during the experiments and hence to reduce them, the electrodes are casted in epoxy. The electrodes are polished to a surface roughness Ra <200 nm using the Proxxon Polishing machine suited for rough, medium and extra smooth surface profiling as shown in figure 4.2(a). Considering the dimensions of the samples, the epoxy radius is made 4.8 cm and a height of 3 cm, shown in figure 4.2(b).

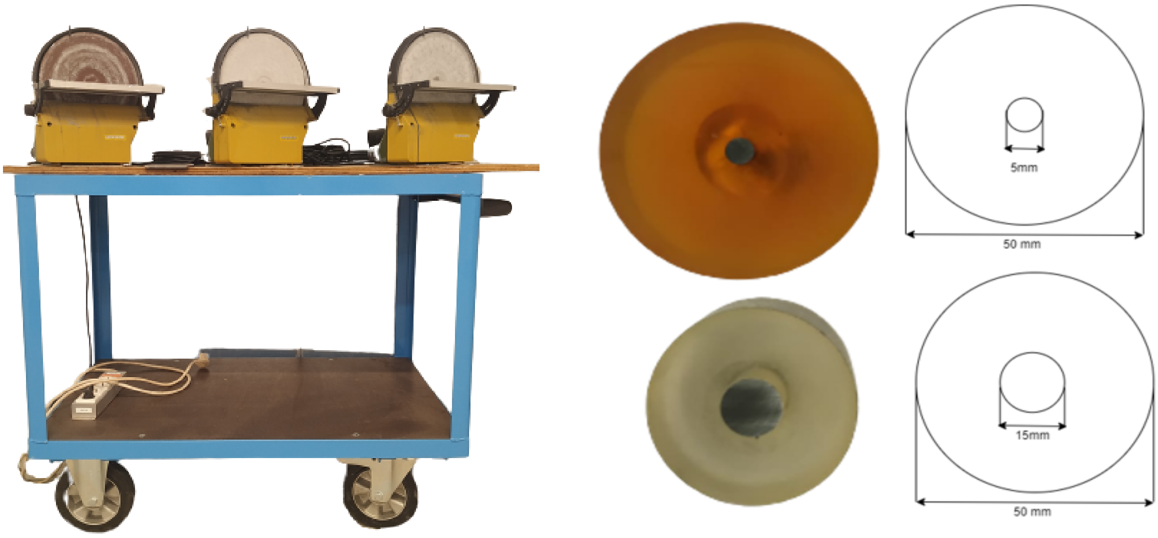

(a) Proxxon Polishing Machine for electrode surface machining

(b) Epoxy casted steel Electrodes

Figure 4.2: Electrodes and Surface Polishing Machine used during Experiments

The overall electrode arrangement is shown in figure 4.3. The corona ring, also modelled later as seen in Figure 4.7(a) is used to create uniform voltage distributions at higher fields which can be seen at the top of the electrode support. A screw is attached which can be manipulated for horizontal movement of the electrode support, made of brass.

The electrode support is connected to a spring which allows flexible movement and thus helps in accurately setting the sample on the ground electrode. In the lower region, the H.V. electrode is casted in epoxy which is placed on the samples, below which is the ground electrode, made of steel connected to the ground. The H.V. electrode is connected to a brass holder and is detachable, so that the surface can be polished after a set of samples have been tested. The setup is made on a wooden frame which is an insulator and only the brass and steel conducts when a high voltage source is connected to it. It has to be ensured that the H.V. electrode rests perfectly horizontal on the ground electrode and there is absolutely no movement when the sample is placed. Uneven surfaces may cause discharges which would affect the experiment outcomes. To analyze the electric fields and potential, a COMSOL Model has been created of the same with the exact dimensions to simulate the process. For long term tests, 6 such arrangements were prepared and mounted on a large rectangular steel board. Also, each of the samples were decoupled from each other and so they had a separate supply each.

Figure 4.3: Test Cell Setup with both Electrodes and Corona Ring as used for Experiments in Chapter 6

4.2. COMSOL Model

A COMSOL 2D Axis-symmetry model has been prepared as shown in figure 4.4(a) and the dimensions have been specified in figure 4.4(b).

The components of the COMSOL Model which is based on the design derived from the experimental setup are described as follows:

- **Corona Ring:** The role of the corona ring is to distribute the electric field gradient and lower its maximum values below the corona threshold, preventing corona discharge.
- **Electrode Supports:** These brass structures help to put pressure on the high voltage electrode to ensure proper contact with the sample and also to ensure even pressure throughout the sample.
- **Tank:** The tank isolates the sample from atmosphere and helps in maintaining the desired temperature.
- **High Voltage Electrode:** This supplies the high voltage through the sample and has to be smaller in diameter compared to the width of the sample. Is is made of steel and is 5 mm in diameter.
- **Oil Impregnated Paper:** This forms the sample for our study and is obtained from the HPGC supplied by TenneT.
- **Epoxy:** Since, there is no external oil available to submerge the samples, hence epoxy is used to reduce surface discharges by reducing the field enhancement near the edges of the H.V. electrode.
- **Ground Electrode:** This forms as a base where the sample is placed below the HV electrode. Due to a voltage gradient, eventually breakdown of paper would take place. This is made using the same material, steel, as in HV electrode and the diameter is larger compared to the length of the sample.

Note: There has to be proper clearance from the ground, walls and the ceiling of the tank when the HV is applied else, it would lead to further discharges. The insulating medium inside the tank is air which is heated up to the desired temperature.

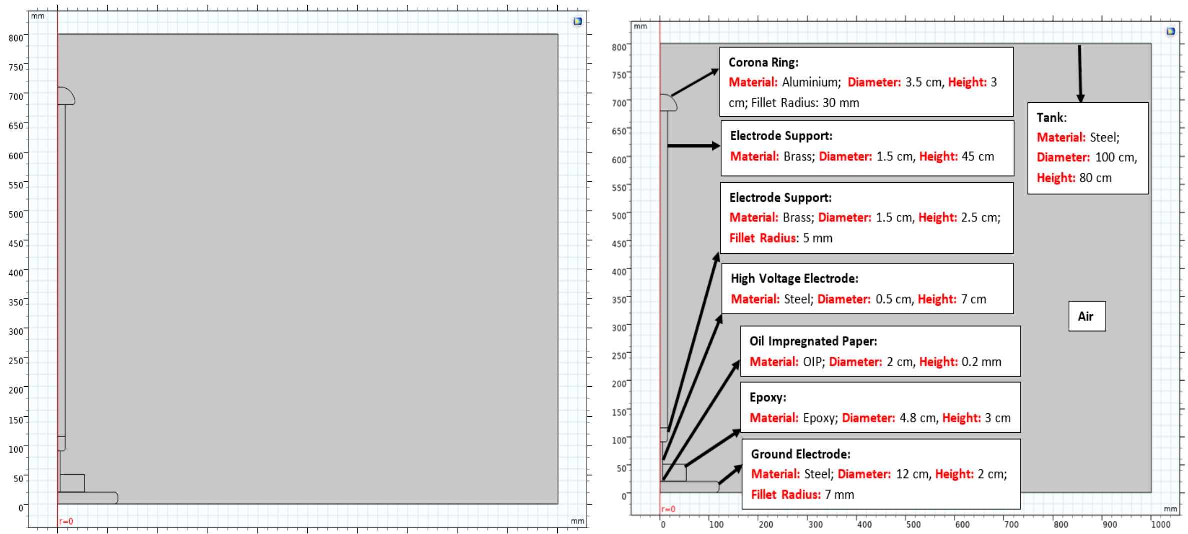

(a) 2D Axis Symmetry COMSOL Model of Test Setup for Breakdown Tests

(b) Dimensions of the components in the COMSOL Implementation

Figure 4.4: COMSOL Modelling before Experimentation Implementation

The Front view of the electrode used for the ramp voltage stress test is represented in Figure 4.5(a) and the 3D Isometric view of the electrode setup inside the tank is seen in Figure 4.5(b). As it can be observed, there is sufficient clearance from all the 4 walls of the tank.The total height of the electrode arrangement is 62.5 cm and the height of the heating oven is 80 cm. So there is a ceiling clearance of 17.5 cm which is sufficient for the applied voltage.

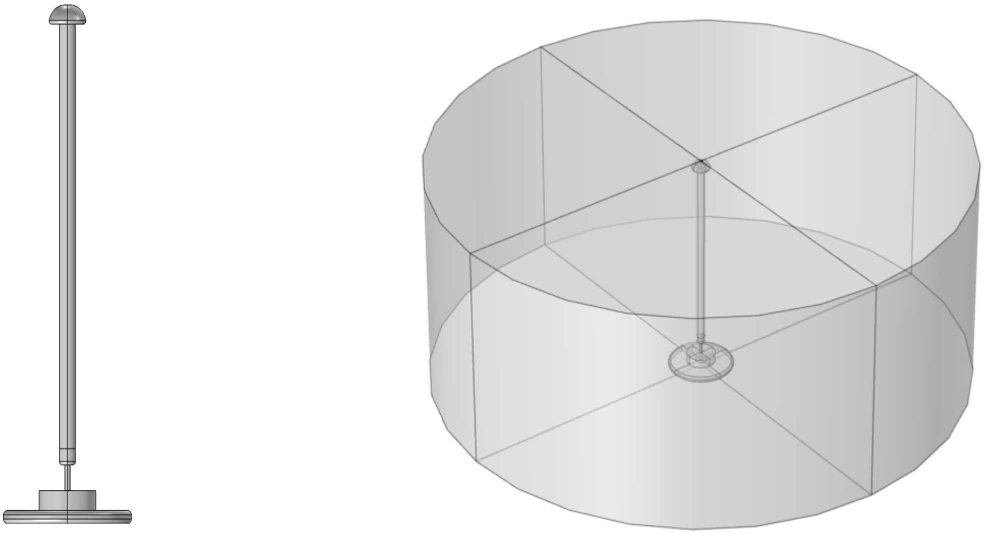

(a) Front View of Electrodes with Corona Ring in COMSOL (b) 3D Isometric View of the Structure inside the Oven

Figure 4.5: Electrode support structure front view and Isometric view inside oven

Though, in the experiments, both electrical and thermal stresses are applied, but in COMSOL Simulation, only the electrical aspect is analyzed, since we are considering constant temperatures of 45, 60 and 75°C for the sample sets. Thus, Electrostatics Physics is used with a Time-Dependent Study on the 2D Axis-Symmetry model. Since, in the first test, we are applying a reference ramped sinusoidal 50 Hz voltage of 15 kV peak (Function Name: sine) on the samples, hence the following parameters are entered in COMSOL and simulated for 1 second as shown in Figures 4.6 (a) and (b).

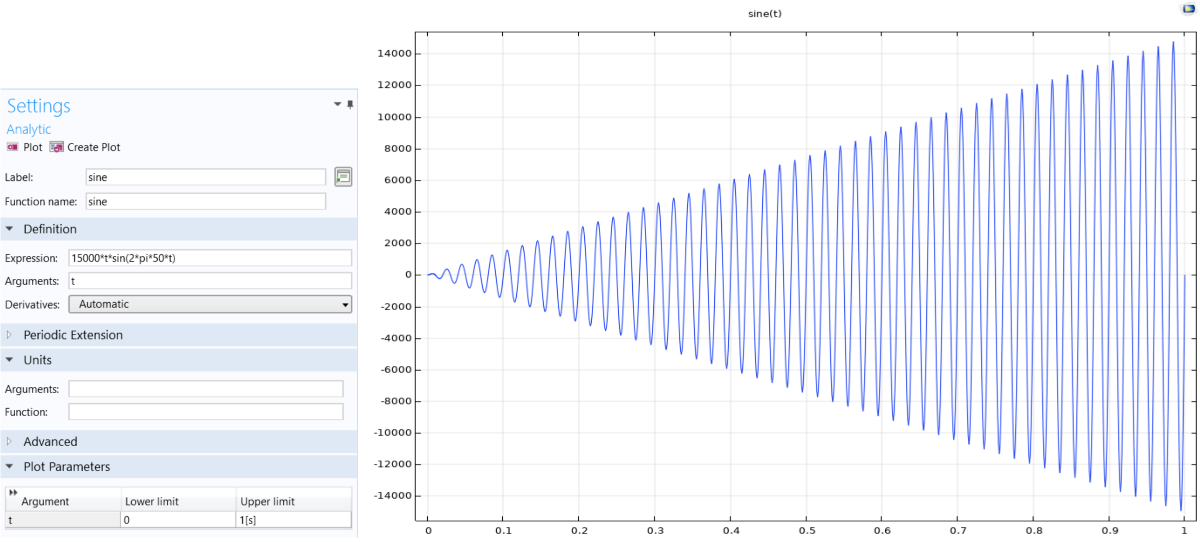

Label: sine
Function name: sine
Expression: 15000*t*sin(2*pi*50*t)
Arguments: t
Derivatives: Automatic
Arguments:
Function:

Argument	Lower limit	Upper limit
t	0	1[s]

(a) COMSOL GUI for producing AC Sinusoid Ramp

(b) Ramped Sinusoid Applied as Supply Voltage to Sample in COMSOL

Figure 4.6: Applied Voltage Stress on COMSOL Model

Electric Potential Plot: The plot in figure 4.7 (a) shows the electric potential in 2D at t = 1 sec and 4.7(b) shows the profile in 3D. The voltage is applied to the electrode support and the HV electrode and hence as we move away towards the right, the potential reduces and finally goes to 0 since the walls of the tank are grounded. The potential at the ground electrode is 0 since it is grounded.

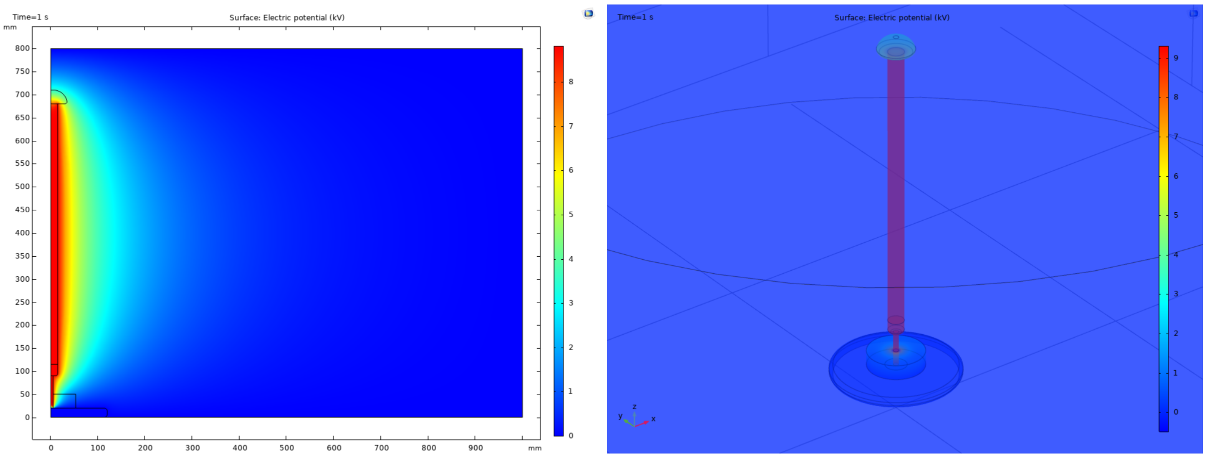

(a) Electric Potential Plot in 2D at t = 1 sec

(b) Electric Potential in 3D at t = 1 second

Figure 4.7: Variation of Electric Field in 2D and 3D across the Setup

Electric Field Plot: The plot in Figure 4.8(a) shows the electric field at t=1s in 2D. It can be observed that the maximum field is observed at the edges of the electrode, since there is an interface and sharp edge is located due to the ending of the H.V. steel electrode and the starting of the epoxy causing a field enhancement. But during experiments, the H.V. electrode is polished very well to prevent any sharp edges and casted into the epoxy. It can be observed in the later chapters that the breakdown is infact a stochastic process and takes place anywhere within the electrode. The field strength as observed in the 2D plot in Fig 4.8(b) concludes that the strength is 0 everywhere in the setup and only concentrated at the H.V. electrode as seen in the spike of 158 kV/mm where the breakdown would actually take place. These simulations help us to give an estimate as to how much the approximate field strength for the geometry used in our experiment.

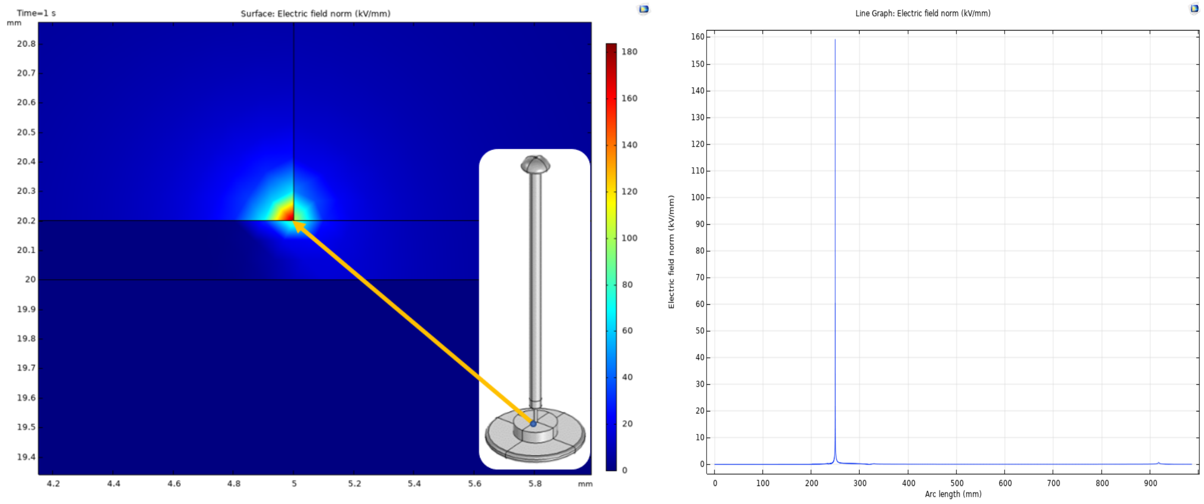

(a) Field Enhancement at Edge of HV Electrode

(b) Variation of Field Strength across the boundary of setup

Figure 4.8: Variation of Electric Field in 2D across the Boundary

Note that the thermal modelling is not taken into consideration, since the oven is kept at that specific temperature for a duration long enough to reach thermal equilibrium.

4.3. Preparing the Samples from Cable

The High Pressure Gas Cable sample as seen in Figure 4.9(a) were taken from a healthy part of the cable close to the failed section, by TenneT. They were covered by a blue plastic cover and the terminations were soldered with lead tubes after putting on heat shrink caps on the ends.The following steps were taken to extract the samples from the cables.

STEP 1: Removing the Steel Tapes around the Cable

The steel tapes around the cable was removed by hand and can be observed in Figure 4.9(b). Now the cable has the lead sheath around it and the heat shrink caps. Care must be taken to use protective gloves since the steel tapes have extremely sharp edges and can damage bare hands.

(a) Cable sections of 1.2m supplied by TenneT

(b) Steel Tapes removed from the periphery of Cable

Figure 4.9: Structure of HPGC Sample with Steel Tape Covering

STEP 2: Removing the Tar and Carbon Black near the end

The cable is mounted on a support and fixed tightly using the two supports. The tar and the carbon black has to be removed first before cutting the desired cable length to prepare the samples. These are removed with a blunt knife from the end which has to be cut open up to a length so that the next heat shrink cap can be fitted. This is done to ensure tight fitting of the caps after the cable is cut. Care must be taken to ensure not to penetrate through the lead sheath and damage the insulation inside. The mounting of the cable can be seen in figure 4.10(a) and after removing a part of the carbon black and tar, the cable can be seen as one observed in Figure 4.10(b). Basically, the lead sheath is exposed near the part which would be cut.

(a) Mounting the Cable without any Modifications

(b) Removal of Excess Tar from Outer COvering

Figure 4.10: Before and after removal of Tar from Outer Sheath

STEP 3: Cutting the desired length of Cable

Now, the cable is moved to the cutting machine, where the desired length is selected and the saw automatically cuts the portion of the cable as shown in Figure 4.11(a). This greatly reduces manual effort but it must be ensured to not place any finger near the machine while it is in the working condition. The cut part of the cable can be observed in Figure 4.11(b) which is now placed between two supports for further processing. Since, we are extracting samples, a large number of samples can be obtained from 18 cm of cable specimen.

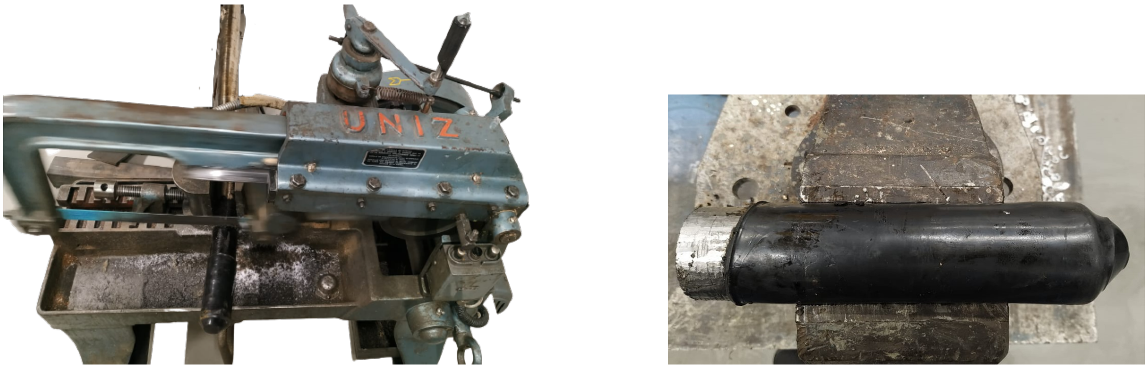

(a) Machining the large cable sample to cut 18cm specimens

(b) 18 cm cut sample of HPGC

Figure 4.11: Comparison between Extruded or Paper Cables

STEP 4: Treatment of the Cable Segments

The portion of the cable not used now has to be preserved very carefully so as to ensure no penetration of moisture as that would affect the outcomes of the experiment. Thus, a new heat shrink cap is placed on the cut end and the heat is finely distributed so as to have a tight even grip near the end as observed in Figure 4.12. Care must be taken not to overheat cap as it tends to melt if too much heat is applied.
The small part of the cable to be used for experiments is now mounted on the supports as seen in Figure 4.13(a) to remove the lead sheath around it. The covering is very firm and thus the following procedure was undertaken to open it. Firstly, two cuts were made at a distance of 10 mm with a very sharp knife. Then one end of the cut edges are pushed by tweezers and opened just like that of a tuna can as seen in Figure 4.13(b). This effectively removes a rectangular lead section and the rest can be easily opened with brute force.

Figure 4.12: Fitting of Heat Shrink Caps

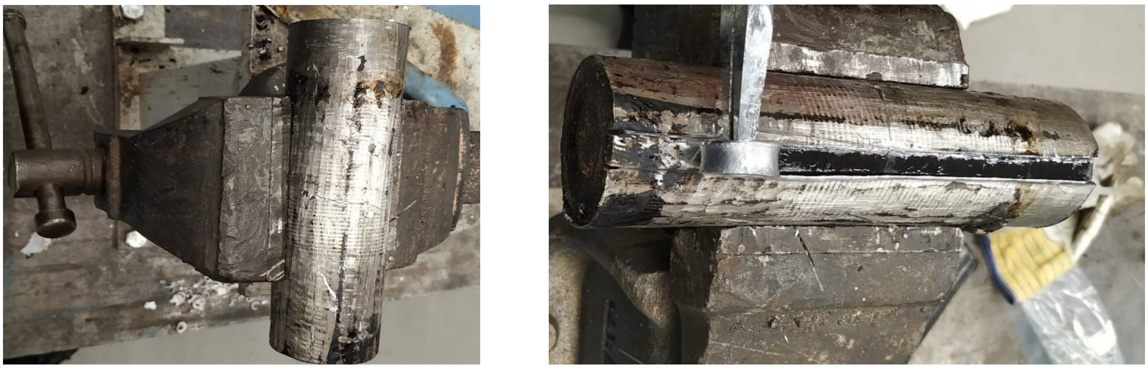

(a) Mounting of cut specimen and removal of heat shrink cap

(b) Removal of outer lead sheath for insulation extraction

Figure 4.13: Processing of the cut specimens to extract insulation

STEP 5: Cable Segments Before Storage

Now, the unused portion is carefully covered with heat shrink tape from the side it was cut. With this protection, there is almost no probability of moisture penetration as seen in Figure 4.14(a). It is now put into a plastic cover and stored at room temperature of about 18°C.

The small portion is now removed from the lead sheath as observed in Figure 4.14(b) and can be seen to be covered with a layer of carbon black paper impregnated with oil. The lead sheath and the carbon paper are removed and it is then stored as discussed in Step 6.

(a) Closing the terminations of the large sample with heat shrink caps (b) Extraction of Insulation from cut specimen

Figure 4.14: Post Treatment of the two parts after Machining

STEP 6: Storing the small cable sample

The most important aspect of the experiment is to mimic the conditions as that of the original field conditions. Thus, it has to be ensured that the moisture content does not vary in the samples. Thus, they are stored in the vacuum chamber as observed in Figure 4.15(a) and the vacuum is created by the suction pump connected to it as seen in Figure 4.15(b). The reading in the pressure meter is taken as close to 0 cm Hg so as to ensure there is least air inside. Also, after every 1 month the samples are changed and replaced by freshly cut ones from the bigger cable following the steps mentioned above. In the end, the oil papers are removed layer by layer and cut into rectangular pieces with scissors and stored in air tight jars and placed inside the same vacuum chamber.

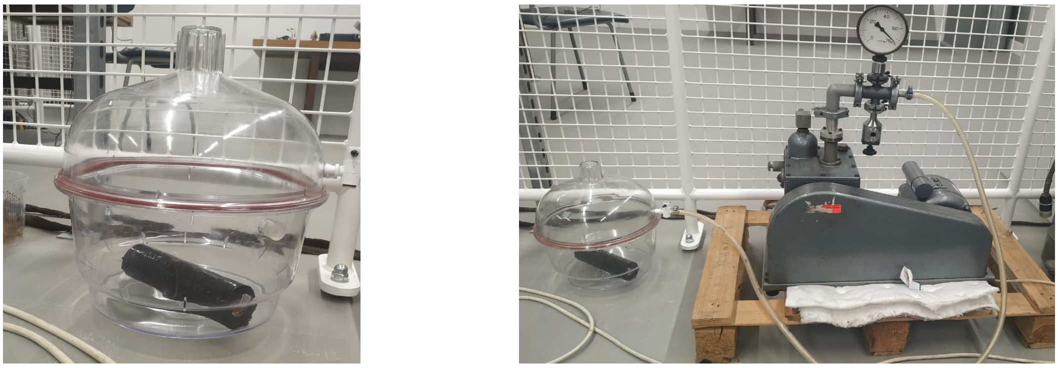

(a) Storage of Samples in Vacuum Chambers (b) Vacuum Chamber connected with Suction Pump

Figure 4.15: Storage of Extracted Insulation for Future Tests

Thus, a detailed procedure has been discussed in form of the 6 steps to extract the paper samples from the cable specimen as well as how to carefully protect it from atmospheric conditions and storage.

5

Operational History of the Cable

The flowchart below represents the loading profile analysis and calculating the dynamic temperature of the HPG cable. Each step is in details explained in this section and finally the working temperature conditions is plotted which enables us to estimate how much the temperature can be risen from the existing conditions to the permissible limits. This analysis was done since there was no temperature sensor attached to record the temperatures.

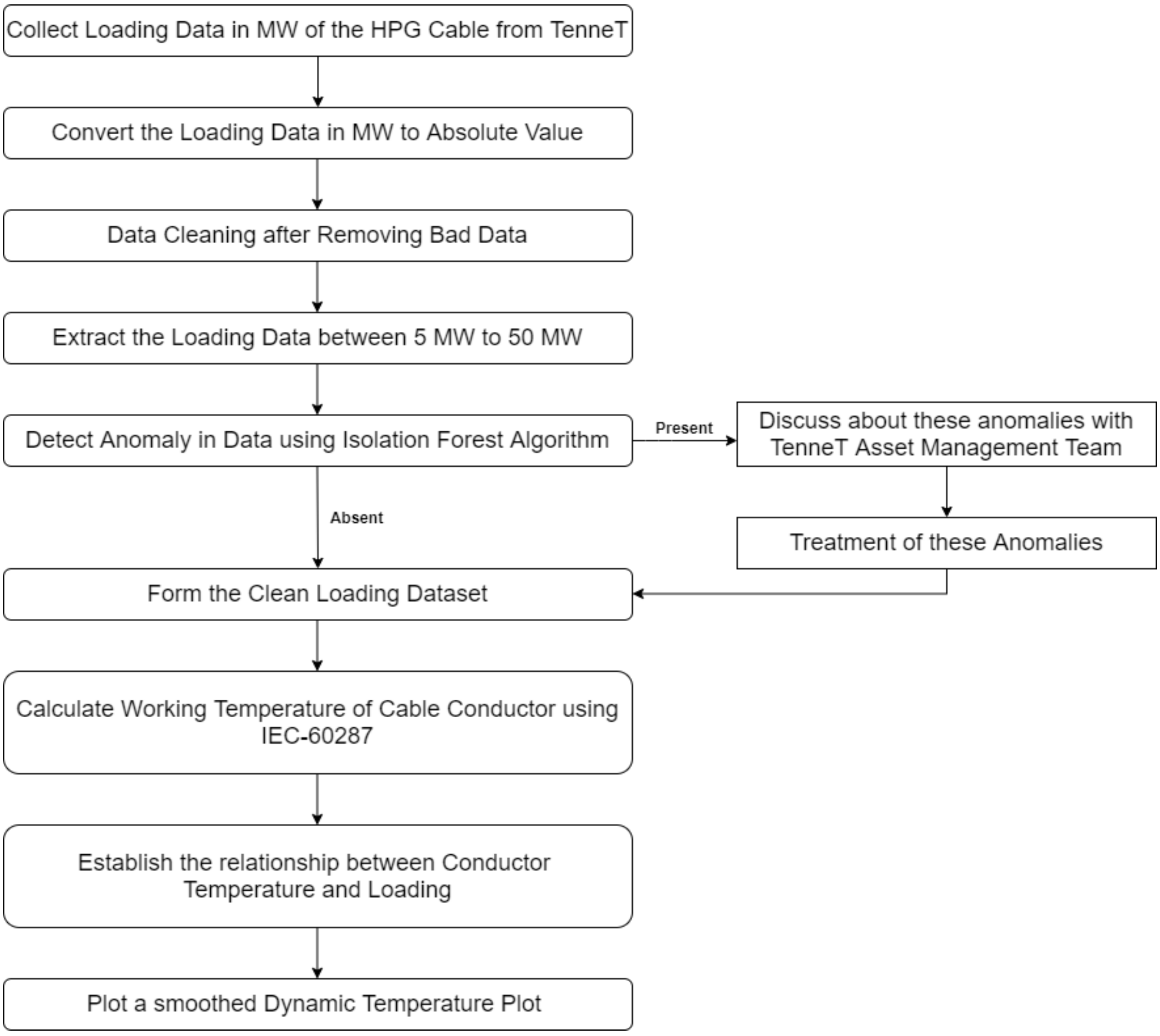

Flow of Research in Chapter 5:

The loading data in MW is collected for 6 years at an interval of 5 minutes for the HPGC sample supplied by TenneT.

Because of the bidirectional flow of current, the value of power can be observed to be of both polarity. So, the loading data is converted to the absolute value.

The data is observed to contain spikes, multiple times higher than the designed voltage, due to error in measurement by the data logger or sensors. This data has to be cleaned, so the following procedure is followed.

It is observed that beyond 50 MW, majority loading magnitudes were higher than the designed limits. So, they were eliminated and capped at 50 MW. In the lower region, no stretches of prolonged 0 MW was observed, which indicates the cable was not put out of operation or offline, and the sudden zeros also indicated faulty measurements. So, the lower value was capped to 5 MW, values were either suddenly 0 or much higher than 5 MW. So, the operational limit was chosen between 5 and 50 MW.

Now, after the first step of cleaning, the question remains if there is any sudden spike within this bounds, which is normally not expected during field operations; though short period spikes may occur. So, to detect any anomalous data, Isolation Forest Algorithm was applied to the previously cleaned dataset. It was observed that the spikes were in groups for short durations and hardly any of them occurred as single spike. So, there was no prominent anomalies detected and this forms the basis of the cleaned dataset.

Now, the work remains to convert the loading into operational temperature. So, IEC 60287 was applied considering the geometry of the cable, establishing a relationship between loading and conductor temperature.

Since the trend and seasonality are of importance to analyze the dynamic cable temperature, so a smoothing method was undertaken. Therefore, by evaluating the working temperature, it was possible to analyze in what steps the temperature can be elevated up to the permissible temperature.

Cable Specifications:

- Insulation Type: Oil Impregnated Paper (OIP) Insulation
- Nominal Line Voltage: 110 kV
- Nominal Line Current: 570 A
- Nominal Power: 108 MW
- Maximum Designed Temperature: 75^{o}C

5.1. Smoothing Techniques in Time Series Data Processing:

Smoothing techniques used in time series data pre-processing removes noise from data set allowing the trends and important patterns to be reflected. In this chapter, we are also interesting in understanding the trend of change of temperature profile and calculating the mean operating temperature, and not the minute changes or noises.

The four major smoothing techniques are:

- **Moving Average Smoothing:** It is a simple and common method of smoothing time series data where the time series are derived from the average of last 'kth' elements of the series. The value of k depends on how smooth the time series we want to visualize without loss of trend and seasonality. This means the smaller the k, the more is the variation. The larger k gets, the smoother the data becomes [75]. It is given by:

$$S_t = \frac{(X_{t-k} + X_{t-k+1} + X_{t-k+2} + \dots\dots + X_t)}{k}$$

  where, S_t is the smoothed observation at time index 't' and X is the observation number.

- **Exponential Smoothing:** It is a Weighted Moving Average technique in which moving average of the past observations are weighed equally. The smoothing is done by assigning weights that decrease exponentially, to the past observations. It is expressed by a recursive formula due to the multiplication of (1-α) to the previous expected value of S_{t-1}, and that is why it gets it's name[76]. It is expressed as:

$$S_0 = X_0; S_t = \alpha * X_t + (1-\alpha) * S_{t-1}; \{t > 0, 0 < \alpha < 1\}$$

  where, S and X have the same representations and α is called the data smoothing factor (0<α<1)

- **Double Exponential Smoothing:** Single Smoothing does not perform very well when there is a trend. This is improved by introducing a similar second equation with constant β. It is mostly applied when the time series have trend but no seasonality[77][78].It is given by:

$$\begin{gathered} S_0 = X_0; B_0 = X_1 - X_0 \\ S_t = \alpha * X_t + (1-\alpha) * (S_{t-1} + B_{t-1}) \\ B_t = \beta * (S_t - S_{t-1}) + (1-\beta) * B_{t-1} \\ \alpha, \beta \in (0,1) \end{gathered}$$

  where S,X,α have the same representations, β represents the trend smoothing factor (0<β<1) and B represents the Trend Factor.

- **Triple Exponential Smoothing:** Also known as the Holt-Winter's Exponential Smoothing, it handles trend and seasonality typically well. By adding the seasonality smoothing, we introduce the third parameter γ and is represented by[77][78]:

$$\begin{gathered} S_0, F_0 = X_0; B_0 = \frac{\sum_{i=0}^{L-1} (X_{L+i} - X_i)}{L^2} \\ S_t = \alpha * \left(X_t - C_{t\%L}\right) + (1-\alpha) * (S_{t-1} + \phi * B_{t-1}) \\ B_t = \beta * (S_t - S_{t-1}) + (1-\beta) * \phi * B_{t-1} \\ C_{t\%L} = \gamma * (X_t - S_t) + (1-\gamma) * C_{t\%L} \\ \alpha, \beta, \gamma \in (0,1) \end{gathered}$$

  where S,X,α,β have the same meanings, γ represents the seasonal trend smoothing factor (0<γ<1), ϕ represents damped smoothing factor and C represents the seasonal index.

Why Choose Moving Average Algorithm in this Chapter? For our application, initial Explanatory Data Analysis (EDA) revealed that there is not much fast changing trend or seasonality in data and also we are not interested in a forecasting method, but strictly a smoothing tool by eliminating the high frequency noises. Due to the simplicity of the Moving Average Algorithm simplicity and ability to be less prone to false outlying signals make it an automatic choice for this specific application.

5.2. Loading Conditions of the Cable

The loading data for the provided cable is supplied by TenneT which spans from 1st October 2013 to 31st December 2019, which is roughly 6 years of data in an interval of every 5 minutes. The statistics about the data without any data cleaning is evaluated in Table 5.1 as shown below and the plot for the Change in Loading in MW vs Time is depicted in Figure 5.1. Since the period is 6 years long, hence the variation in loading for during a day and for a span of a week has been represented in Figures 5.2 (a) and 5.2(b). For the weekly analysis of the loading, the variation was mostly between 12 to 17 MW, similar to a 5 MW change on 12^{th} October 2013, which means the temperature of the conductor was almost the same throughout the day. For the weekly data between 1st October 2013 to 7th October 2013, there is more variation as the loading changes between 10 to 24 MW, equivalent to a 14 MW change, which comparatively less loading on 2 days compared to other 5 days. It can also be considered that there might be no bad data as the loading cycle is very uniform over the week and less deviations during the daily cycle.

Table 5.1: Table showing statistical parameters of loading conditions without Data Cleaning c

Data Count	Mean	Std. Dev.	Min. Loading	Max Loading	25%	50%	75%
6,56,162	15.02	111.77	-55,507.42	15,843.89	11.16	14.32	19.72

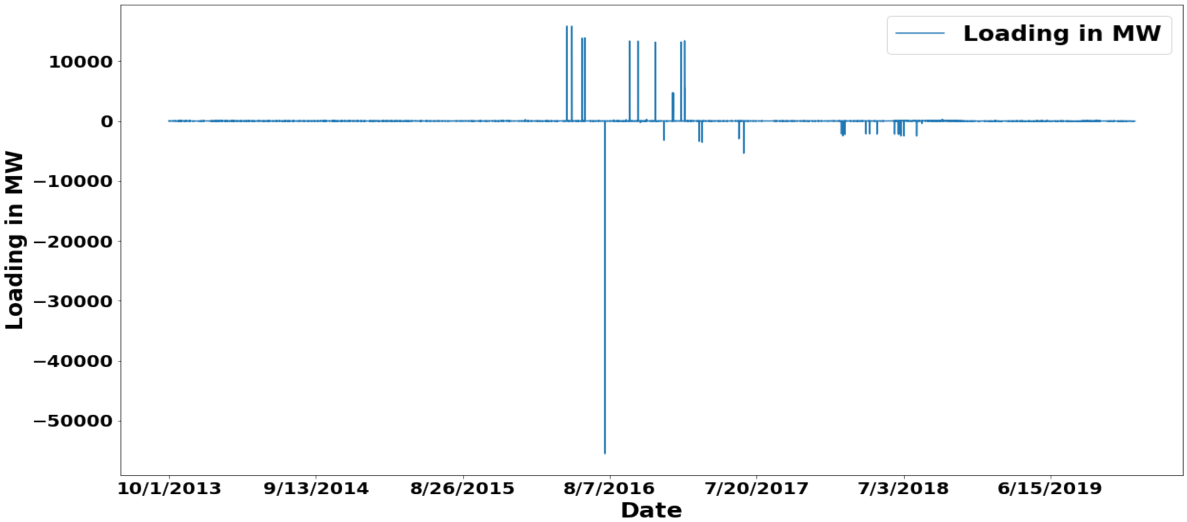

Figure 5.1: Change in Loading in MW vs Time for Raw Data observed for the Provided Cable

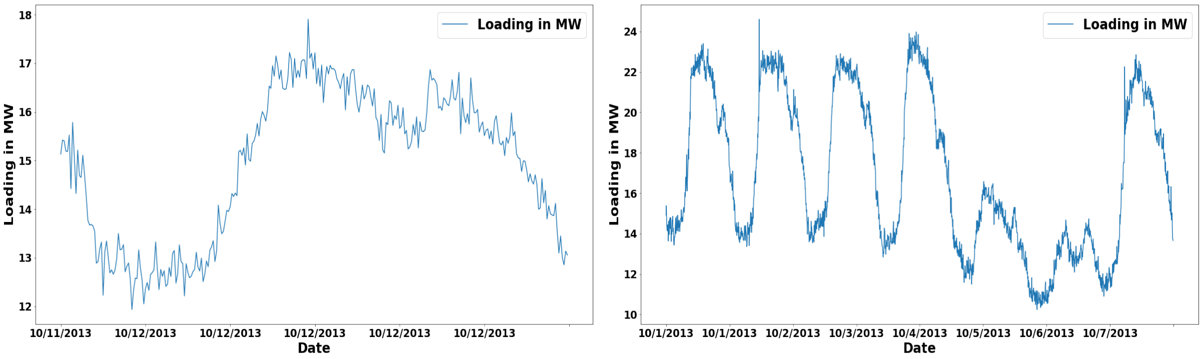

(a) Variation of Loading in a Day

(b) Variation of Loading in a Week

Figure 5.2: Daily and Weekly Trends in Change of Loading in MW

From the statistics in Table 5.1, there are 656162 data counts with a mean of 15.02 MW but the standard deviation is almost 8 times that of the mean, which means the data is very scattered, which should not be an optimum scenario for the cable loading. Upon inspection, the maximum and minimum values are nearly 15 GW and -55 GW. But the nominal power rating of the cable is 108 MW. So, this absurd value cannot be true measurement or transient, instead it is an error in the monitoring device. This clearly signifies there is a lot of bad data and thus it has to be processed before analysis. The mean is nearly 15 MW and above 50 MW, most of the data points were observed at very high values more than the design loading, which cannot be the case based on operational loading over the past decade, indicating outliers and observed due to errors in data logging. Similar situation was observed below -30 MW where most data points lied far off indicating bad data. So, all data above 50 MW and below -30 MW are capped as observed in Figure 5.3, which is more of a viable scenario for loading such a cable. Now, the negative sign is due to the flow of the current in the opposite direction hence, the modulus value of the loading is being used for analysis of the conductor temperature. Also, there were certain periods when the loading was 0, which refers to loss of connection with the data logger or maybe during transients, thus these data were also removed and the range of data was taken from 5 MW to 50 MW in absolute value as shown in Figure 5.4.

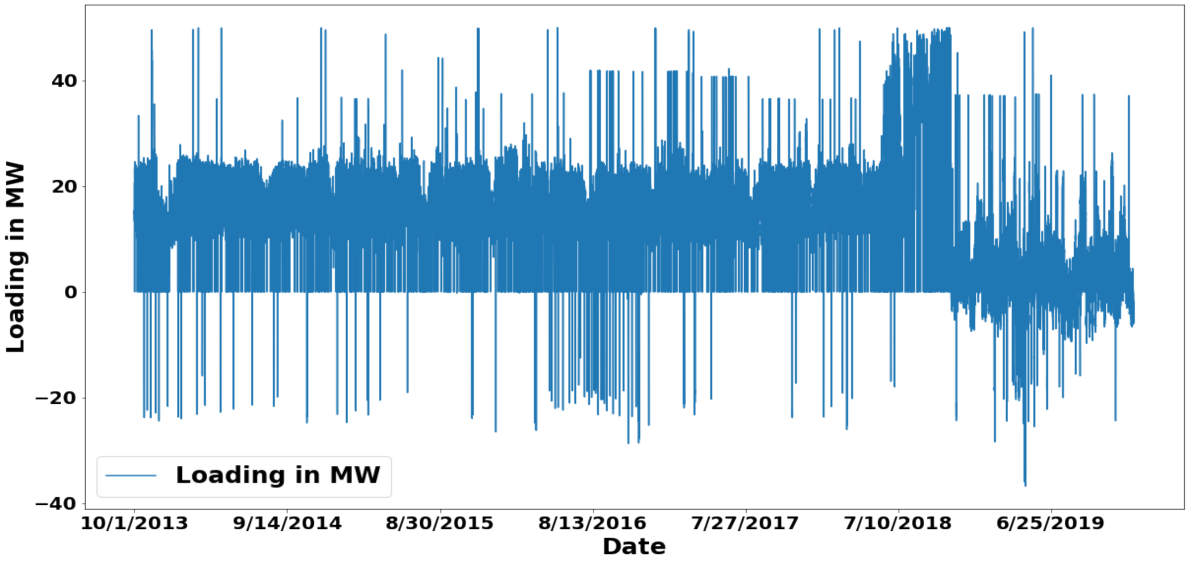

Figure 5.3: Loading Profile after limiting the value from -30 MW< P < 50 MW

The statistics for data after cleaning now lies between 5 MW and 50 MW and enumerated in Table 5.2.

Table 5.2: Table showing the change in statistical parameters after limiting loading between 5 to 50 MW (units in MW)

Data Count	Mean	Std. Dev.	Min Loading	Max Loading	25%	50%	75%
5,63,441	17.13	7.11	5.00	49.99	12.68	15.21	20.55

It can be observed in Table 5.2 that after data cleaning, the mean now increases to 17.13 MW than the previous case. Also, since the bad data were eliminated, the number of value points have reduced but still significantly high enough for analysis. The most interesting change from the former case is that now the standard deviation is significantly smaller than the mean, which means we are considering a compact data set now which should be the case for loading a cable in a practical scenario. Now, after the loading profile is passed through a rolling window in the Moving Average Algorithm [75] to remove the high frequency elements. This is a very effective method specially in Time Series Analysis specifically in our application as discussed in Section 5.1. The mean of the smoothed loading profile is around 17 MW with a peak of 35 MW in October 2018 as shown in Figure 5.5.

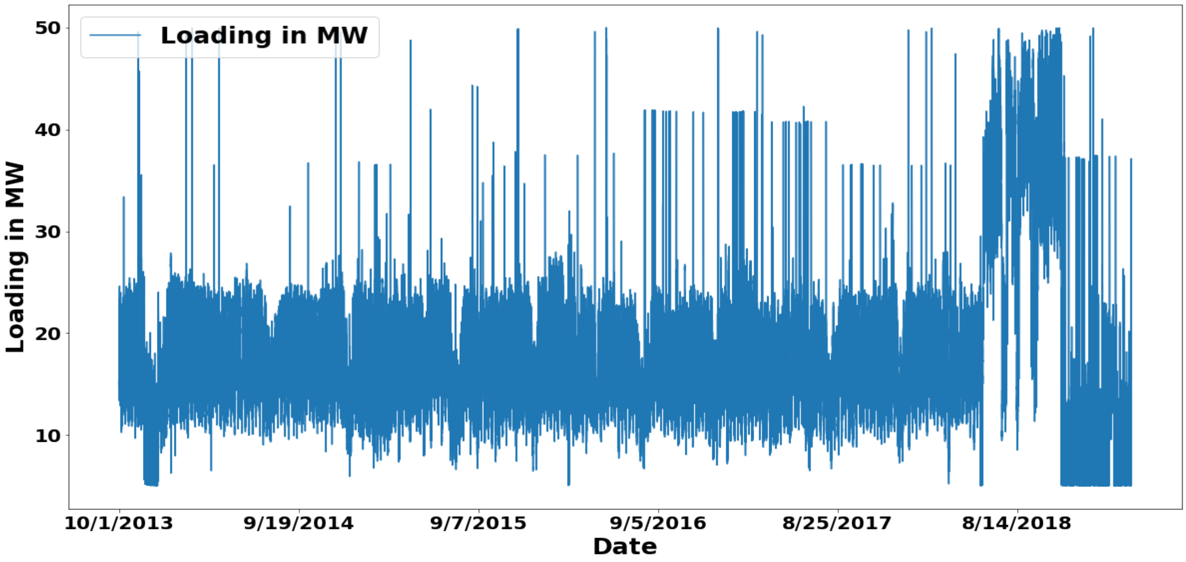

Figure 5.4: Loading Profile representing magnitude from 5 to 50 MW

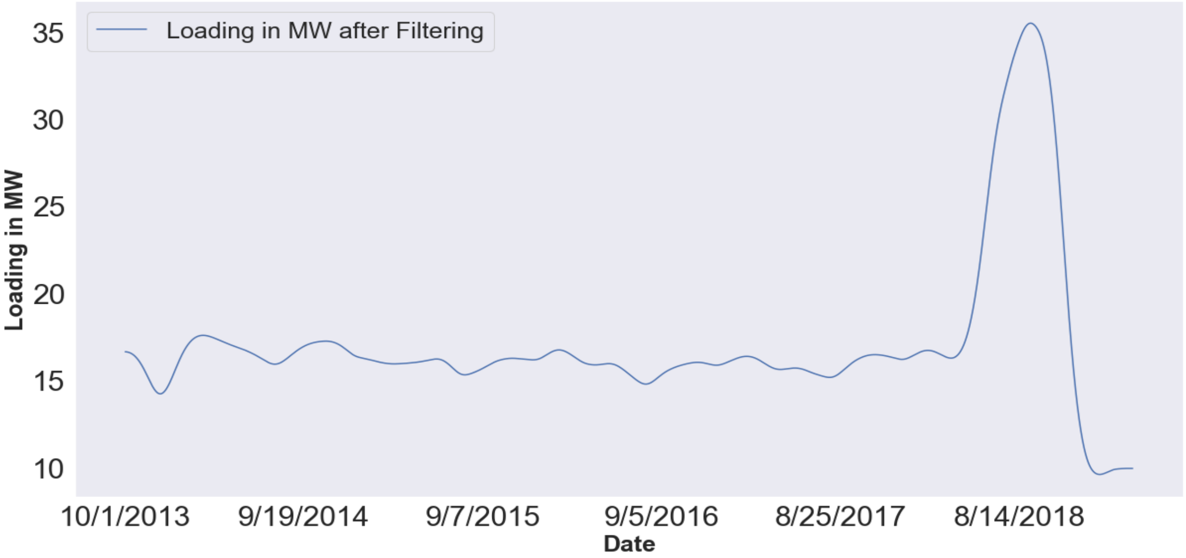

Figure 5.5: Loading Profile capturing the trend after application of Moving Average Algorithm

5.3. Anomaly Detection Algorithms in Time Series Data

It is also known as outlier detection that determines the types of anomalous data found in the set and capture details about their occurrences. Following are the most popular anomaly detection methods in time series data:

- **K-Means Algorithm:** It is a clustering algorithm that creates ’k’ similar clusters of data points and the data that fall outside the clusters are considered to be ’potential anomalies’. The optimal number of clusters are determined by an iterative process called the elbow method [79].
- **Isolation Forest Algorithm:** This detects anomalies purely based on the assumption that anomalies are data points that are few and unique. The method is discussed in details in Section 5.4 since we would be using for Anomaly Detection for our cleaned dataset[80].
- **Support Vector Machine Algorithm:** SVM is a supervised learning method but OneClassSVM identifies anomalies by treating it as an unsupervised problem that learns a decision function for

detection of anomaly[81].

- **Gaussian Distribution:** This is particularly effective when our data are normally distributed. But anomalies are normally not distributed normally and thus they stand out of the normal data set indicting an outlier [82].
- **Predictive Confidence Level Approach:** Building a predictive model with historic data helps us to estimate the overall trend, seasonality and cyclicity pattern of time series. Popular time series modelling methods like ARIMA, SARIMA, GARCH, VAR or LSTM can be used to make the predictive model. It helps in finding local outliers but the main disadvantage is this method is based on the efficiency of the predictive model. Less accurate models would give false positives or false negatives during anomaly detection which is not desirable. Thus, if the data are significantly different from the prediction model, it is considered as anomaly. Obviously, if the prediction model is trustworthy and remains applicable. If the situation changes, the data may change and the prediction model may no longer apply.[83]
- **Statistical Profiling Approach:** Generating a statistical model or profile of the given data set is very useful to force a controlled outcome. The statistical parameters can be calculated to provide an upper and lower bound and anything that falls beyond the range is an anomaly. this is specifically useful for volatile data, but it fails to detect local outliers which reduces the efficiency of this method[84].
- **Clustering Based Supervised Approach :** Unsupervised learning is very effcient in anomaly detection as it does not require labelled data. The most difficult part of this method is defining the number of clusters, which is the basic input requirement for such algorithms.But with advancement of technology, recently an algorithm called Density Based Spatial Clustering of Applications with Noise (DBSCAN) is developed that does not require initial cluster specifications.We need to specify minimum number of points in clusters and distance between the clusters from domain knowledge[85].

Why Isolation Forest is used for Anomaly Detection for our dataset?

Isolation forest is an unsupervised learning that detects anomalies quite fast and requires much less memory compared to the other methods. It is specifically effective when the anomalies are very different which is the case in our dataset when we have sudden spikes between two data loading logs indicating some error in the logger during logging data. Also, we have a very large dataset and the computation time was quite small(<1 hr) for detection of anomalies that make it a simple yet efficient choice.

5.4. Anomaly Detection in our Cleaned Dataset

The most simple anomaly detection method is a Box plot [86] representing the median value between the First Quartile(Q1) and 3rd Quartile(Q3), but it is not fitted for time series data, as in this case. The maximum and the minimum values are determined by first calculating the interquartile range which is IQR = Q3 - Q1, and then (Q1-1.5*IQR) and (Q3+1.5*IQR) represents the minimum and maximum values which are referred to as 'inliers'. Any value lesser than the minimum or larger than the maximum are referred to as 'outliers'. The theory discussed above is well represented in the Figure 5.6(a). For the given data after cleaning, it can be observed that the maximum value is near to 32 MW and values above it are referred to as outliers. There is no value below the minimum as observed in Figure 5.6(b) but quite some above the maximum, indicating the mean is skewed towards the minimum value due to the nature of the data set. But this, cannot be used effectively for a time series data analysis and more in-depth algorithm has to be used to detect the anomalies and so Isolation Forest is used to mark the anomalies.

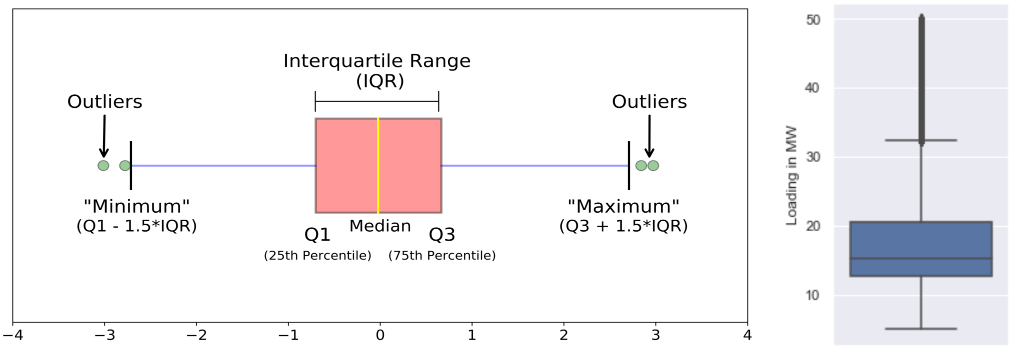

(a) Representation of Box Plot showing Different Regions

(b) Box Plot of Cleaned Data

Figure 5.6: Box Plot Representation and its application on given data

Isolation Forest Algorithm:

The algorithm first "isolates" the anomalies by creating decision trees over random attributes as shown in Figure 5.7. The random partitioning produces shorter paths for anomalies since:

- **fewer instances (of anomalies) result in smaller partitions**
- **distinguishable attribute values are more likely to be separated in early partitioning**

Thus, a forest of random trees produce shorter path lengths for certain points and these are very likely to be "anomalies" [80].

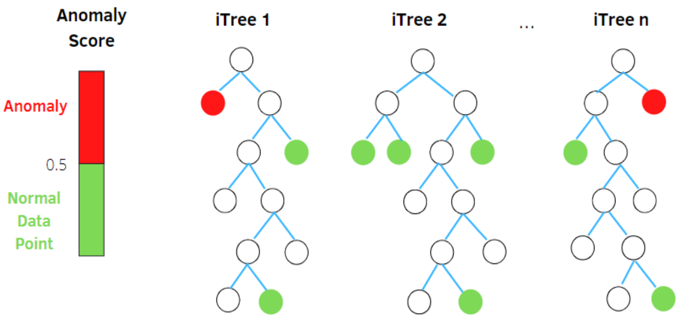

Figure 5.7: Isolation Forest Algorithm Working

Isolation Forest algorithm scores its data points/instances and quantify the confidence the algorithm has on its potential anomalies. The generated anomaly score has to be bounded and comparable. The anomaly score is a function of path length defined as: Path Length h(x) of a point x is the number of edges x traverses from the root node.
For a tree of height n, we define c(n) which is average of path length h(x) for given n, to normalize h(x).

$$c(n) = 2H_{n-1} - \frac{2(n-1)}{n}$$

where H(i) is the Harmonic number, estimated by $\log(i)$ + 0.5772156649 (Euler-Mascheroni constant).
Now, the anomaly score of an instance x is defined as [80]:

$$s(x,n) = 2^{-\frac{E(h(x))}{c(n)}}$$

where E(h(x)) is the average path length (average of h(x)) from a collection of isolation trees.
From the scoring function defined above, we could deduce that if:

- **the score is very close to 1, then they are definitely anomalies**,
- **the score is much smaller than 0.5, then they are safe to be regarded as normal instances**,
- **all the instances return around 0.5, then the sample does not have any distinct anomaly**.

For the loading dataset of the cable, the Isolation Forest Algorithm is implemented to check the anomalies in loading so that they can be dealt accordingly. From the histogram bin in Figure 5.8, the red regions represent ”Outliers” and the blue region represents ”Inliers” according to the Isolation Forest Algorithm. While implementing it in Python, the outlier fraction was chosen as 0.01 which is roughly 5,634 points. This value is chosen as we have already done some pre-processing earlier to eliminate the highly spurious values. These anomalies have been then plotted on the time scale itself represented by red dots in Figure 5.9. As expected the higher values could depict some anomalies but in the lower values of loading, no such anomaly is detected. Upon discussion with TenneT experts, it was found that loading can sometimes rise high over a period and also, during temperature calculation, since we would use a filter, the very high frequency components would get eliminated anyways. The anomalies were analyzed to check if there was any sudden increment which would mean malfunctioning during collection of data by the data logger. Thus, it was observed that the red anomalous data obtained in Figure 5.9 were not singlet points but appear as clusters for short durations. This indicates there were some transients for certain durations, so they are part of the loading dataset. If there was a certain spike which was very short lived, only then it would indicate some errors in data logging.

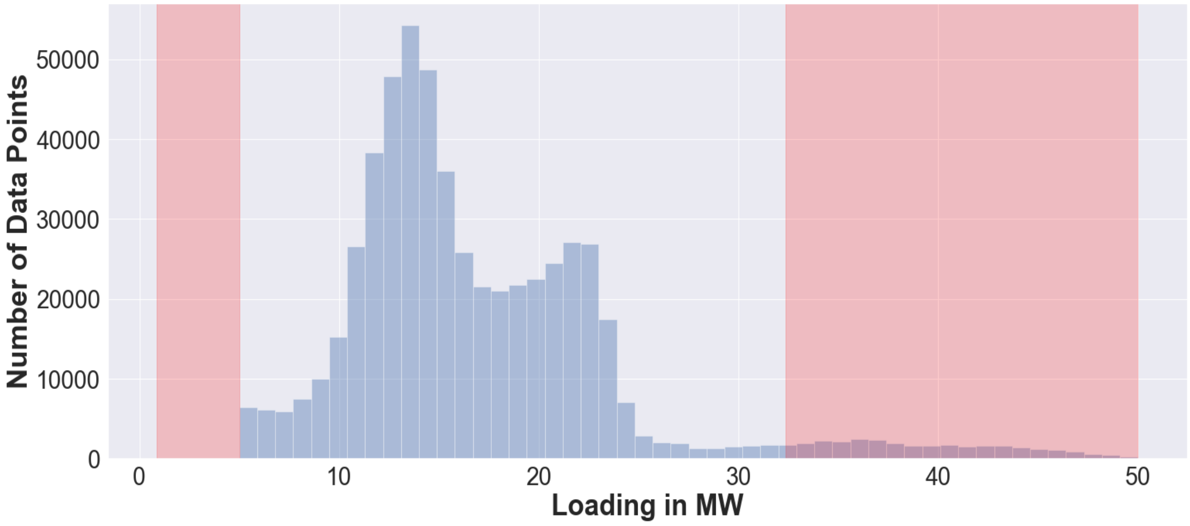

Figure 5.8: Histogram Bin of Cleaned Loading Data

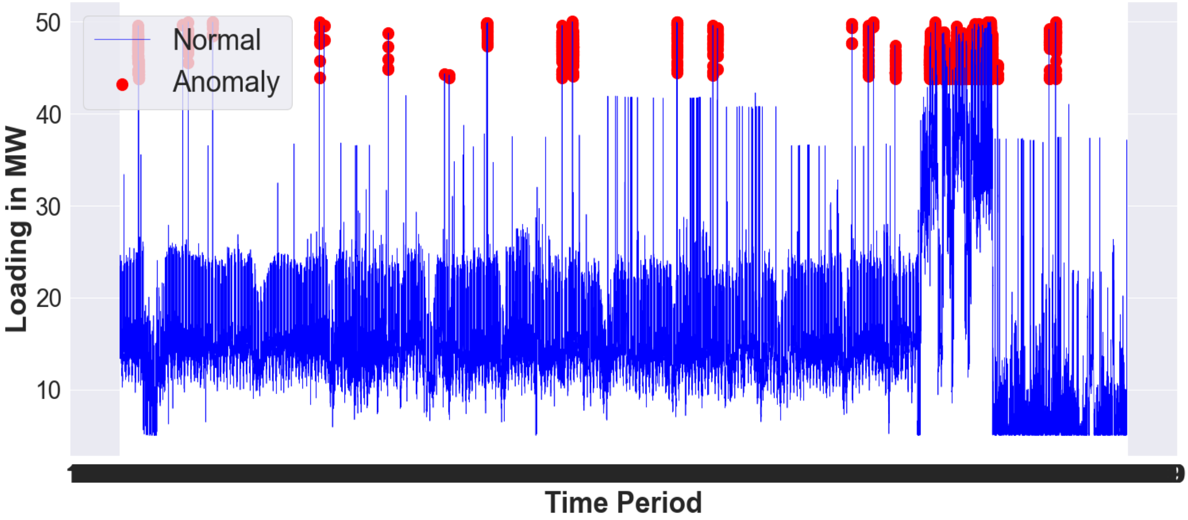

Figure 5.9: Red Dots representing Anomalies detected by Isolation Forest

5.5. Calculating Temperature from Cable Loading

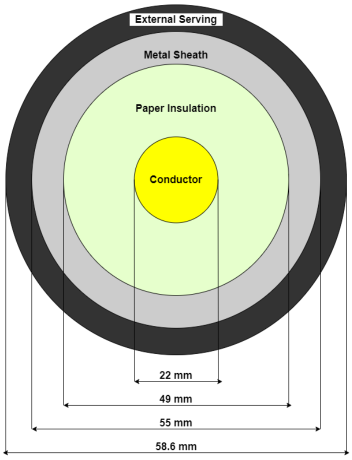

Figure 5.10: Supplied HPG Cable Dimensions with marked components

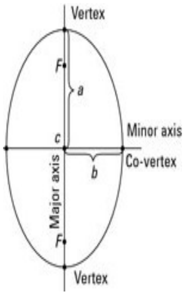

Figure 5.11: Elliptic Conductor

Diameter of Elliptic Conductor:

From Figure 5.11, the larger diameter is the major axis (2b) and the smaller diameter is the minor axis (2a).Thus, formula for the equivalent diameter of an ellipse is given by:

$$
\begin{aligned}
D_{eq} &= \frac{2 * MajorAxis + MinorAxis}{3} \\
&= \frac{2 * 2.3 + 2}{3} \\
&= 2.2cm
\end{aligned}
$$

Figure 5.12(a) represents the cross sectional view of the HPG cable designed in AUTOCAD and (b) shows the Trefoil Formation of the cables buried at an distance of 1 m from surface of land. The void as seen is filled by high pressure Nitrogen Gas. The calculations used in the subsequent steps consider the cable to be within pipe structure, 3 phase, 3 single core cables laid in Trefoil Formation which is the case as that in real life scenario.

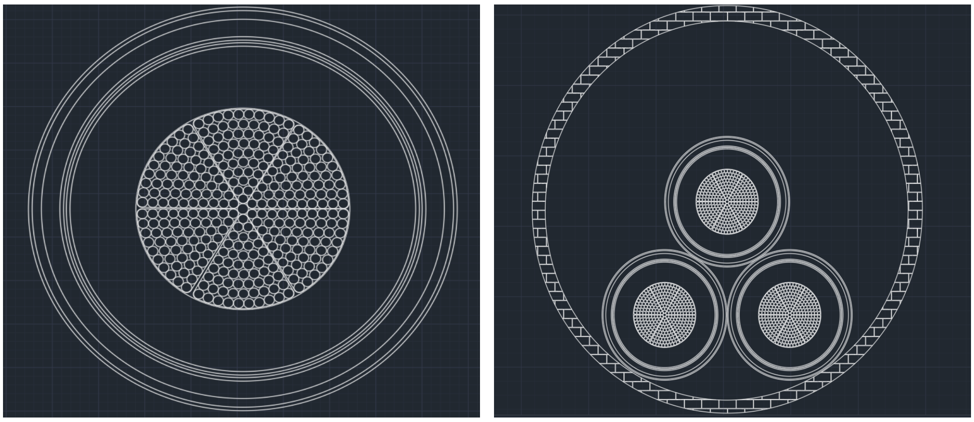

(a) Cross Sectional view of the HPGC cable designed in AUTOCAD

(b) Trefoil Formation of the Cables in AUTOCAD

Figure 5.12: AUTOCAD Design of Single HPGC cable vs Trefoil Formation of 3-phase cables

Parameters:

The following calculation to calculate the working temperature of the cable conductor has been done in accordance with IEC 60287-1-1 and IEC 60287-2-1 [87][88].

ρ_{Cu} = $1.68 * 10^{-8}\ \Omega m$
α_{Cu20} = $3.86 * 10^{-3}$ /^{o}C
σ_{Cu} = $5.95 * 10^{7}\ /\Omega m$
l = 1 m, considering per unit length of cable
$\theta = 75^{o}C$
R = 11 mm

The area of the copper conductor is given by,

$$\begin{aligned} A_{Cu} &= \pi * R^2 \\ &= \pi * (11 * 10^{-3})^2 m^2 \end{aligned} \tag{5.1}$$

Therefore, Conductor Resistance per unit length,

$$R_o = \frac{\rho_{Cu} * l}{A_{Cu}} \quad = 4.42 * 10^5 \Omega/m \tag{5.2}$$

The D.C. Resistance can be calculated as following [87],

$$\begin{aligned} R_{dc} &= R_o(1 + \alpha_{20}(\theta - 20)) \\ &= 4.42 * 10^5 * (1 + 3.86 * 10^{-3} * (75 - 20)) \\ &= 5.358 * 10^{-5} \Omega/m \end{aligned} \tag{5.3}$$

Now, for an A.C. 3-phase Cable, the D.C. resistance is very different to A.C. Resistance due to Skin Effect and Proximity Effect [89].

1) Effect of Proximity Effect for 3 single core Cables:

x_p = argument of a Bessel function used to calculate proximity effect
y_p = proximity effect factor
k_p = factor used in calculating xp (proximity effect). This factor is obtained from Table 2 of IEC 60287-1-1 and for round stranded conductors it is 1.
f = Operating Frequency = 50 Hz

Now, to calculate x_s[87]:

$$x_p^2 = \frac{8\pi f}{R_{dc}} * 10^{-7} * k_p \tag{5.4}$$

$$= 2.345$$

Therefore, x_p = 1.53

Now, to calculate y_p, since 0<x_p<=2.8, hence we can utilize the following formula [87]:

$$y_p = \frac{x_p^4}{192 + 0.8x_p^4} * (\frac{d_c}{s})^2 * [0.312 * (\frac{d_c}{s})^2 + \frac{1.18}{0.27 + \frac{x_p^4}{192+0.8x_p^4}}]$$

$$= \frac{5.4798}{196.3839} * (\frac{22}{58.6})^2 * [0.312 * (\frac{22}{58.6})^2 + \frac{1.18}{0.27 + \frac{5.4798}{196.3839}}] \tag{5.5}$$

$$= 0.01575$$

2) Effect of Skin Effect for 3 single core cable:

x_s = argument of a Bessel function used to calculate skin effect
y_s = skin effect factor
k_s = factor used in calculating x_s (skin effect). This factor is obtained from Table 2 of IEC 60287-1-1 and for round stranded conductors it is 1.
f= Operating Frequency = 50 Hz

Now, to calculate x_s[87]:

$$x_s^2 = \frac{8\pi f}{R_{dc}} * 10^{-7} * k_s \tag{5.6}$$

$$= 2.345$$

Therefore, x_s = 1.53

Now, to calculate y_s, since 0<x_s<=2.8, hence we can utilize the following formula[87]:

$$y_s = \frac{x_s^4}{192 + 0.8x_s^4}$$

$$= \frac{1.53^4}{192 + 0.8 * 1.53^4} \tag{5.7}$$

$$= 0.0279$$

Calculating the R_{ac}:

For pipe-type cables, the skin and proximity effects are multiplied by a factor of 1.5, so the formula comes out to be [87]:

$$R_{ac} = R_{dc} * (1 + 1.5 * (y_s + y_p))$$

$$= 5.358 * 10^{-5} * (1 + 1.5 * (0.0279 + 0.01575)) \tag{5.8}$$

$$= 5.70 * 10^{-5} \Omega/m$$

Calculating the Dielectric Losses:

The dielectric loss is voltage dependent and thus only becomes important at voltage levels related to the insulation material being used.

The dielectric loss per unit length in each phase is given by [87]:

$$W_d = \omega C V_o^2 tan\delta \tag{5.9}$$

where ω = 2πf;
C is the capacitance per unit length (F/m);
U_o is the voltage to earth (V).

Now, to calculate the Capacitance, C[87]:

$$\begin{aligned} C &= \frac{\epsilon_r}{18ln(\frac{D_i}{d_c})} \\ &= \frac{3.6 * 10^{-9}}{18ln(\frac{49}{22})} \\ &= 2.4976 * 10^{-10} F/m \end{aligned} \tag{5.10}$$

From the IEC standard, for moderately aged oil paper cables, the average tanδ value is roughly 0.004. Thus, the dielectric loss is:

$$\begin{aligned} W_d &= \omega C V_o^2 tan\delta \\ &= 100\pi * 2.4976 * 10^{-10} * [\frac{110}{\sqrt{3}} * 10^3]^2 * 0.004 \\ &= 1.2659 W/m \end{aligned} \tag{5.11}$$

Thermal resistance of the constituent parts of a cable, T1, T2,T3 and T4:

1) Thermal resistance between one conductor and sheath T1:

The thermal resistance between one conductor and sheath T1 for single core cables is given by [88]:

$$\begin{aligned} T_1 &= \frac{\rho_T}{2\pi} ln[1 + \frac{2t_1}{D_c}] \\ &= \frac{2.5}{2\pi} ln[1 + \frac{2 * 13.5}{22}] \\ &= 0.3186 mK/W \end{aligned} \tag{5.12}$$

2) Thermal resistance between sheath and armour T2:

Since there is no armour for the HPG cable, hence there is no thermal model for this region. Hence, T_2 = 0.

3) Thermal resistance of outer covering (serving) T3:

The external servings are generally in the form of concentric layers and the thermal resistance T3 is given by[88]:

$$T_3^* = \frac{\rho_T}{2\pi} ln[1 + \frac{2t_3}{D_a}]$$

$$= \frac{0.1}{2\pi} ln[1 + \frac{2 * 1.8}{55}] \tag{5.13}$$

$$= 10^{-3} mK/W$$

Now, for piped cables, the value is 1.6 times, thus $T_3 = 1.6 * 10^{-3}$ = 1.615*10^{-3} mK/W

4) External thermal resistance T4:

Three single-core cables, trefoil formation: For this configuration, L is measured to the centre of the trefoil group and D_e is the diameter of one cable. T4 is the external thermal resistance of any one of the cables and the configuration may be with the apex either at the top or at the bottom of the group. The thermal temperature is given by [88]:

$$T_4 = \frac{1.5\rho_T}{\pi}[ln(2u) - 0.630] \tag{5.14}$$

Now, the value of u is calculated as[88]:

$$\begin{aligned} u &= \frac{2L}{D_e} \\ &= \frac{2 * 1000}{58.6} \\ &= 34.13 \end{aligned} \tag{5.15}$$

For the soil in Netherlands, the value of resistivity (ρ_T) is almost 1. Thus, the thermal temperature is given by:

$$\begin{aligned} T_4 &= \frac{1.5\rho_T}{\pi}[ln(2u) - 0.630] \\ &= \frac{1.5 * 1}{\pi}[ln(2 * 34.13) - 0.630] \\ &= 1.716 mK/W \end{aligned} \tag{5.16}$$

Calculation of ratio of losses in the cable:

In trefoil formation with sheaths bonded at both ends, the circulating currents in cable is given by[87]:

$$\lambda_1' = \frac{R_s}{R_{ac}}[\frac{1}{1 + (\frac{R_s}{X})^2}] \tag{5.17}$$

where, X is evaluated by the following formula[87]:

$$\begin{aligned} X &= 2\omega ln(\frac{2s}{d}) \\ &= 100\pi ln(\frac{2 * 58.6}{55} * 10^{-7}) \\ &= 4.754 * 10^{-5} \Omega/m \end{aligned} \tag{5.18}$$

To find R_s of the metal lead sheath,

$$\begin{aligned} R_{so} &= \frac{\rho_{lead}}{a_s} \\ &= \frac{22 * 10^{-8}}{\pi * (27.5^2 - 24.5^2) * 10^{-6}} \\ &= 4.48 * 10^{-4} \end{aligned} \tag{5.19}$$

Now, to calculate the metal sheath resistance[87],

$$\begin{aligned} R_s &= R_{so} * (1 + \alpha * (\theta - 20)) \\ &= 4.489 * 10^{-4}(1 + 39 * 10^{-4} * (75 - 20)) \\ &= 5.452 * 10^{-4}\Omega/m \end{aligned} \tag{5.20}$$

Thus, the circulating currents in that cable can be calculated as:

$$\begin{aligned} \lambda_1^{'} &= \frac{R_s}{R_{ac}}[\frac{1}{1 + (\frac{R_s}{X})^2}] \\ &= \frac{5.452 * 10^{-4}}{5.70 * 10^{-5}}[\frac{1}{1 + (\frac{5.452*10^{-4}}{4.754*10^{-5}})^2}] \\ &= 0.0789 \end{aligned} \tag{5.21}$$

Now, the eddy current losses neglected, except for cables having Milliken conductors as specified in the IEC Standard, Pg 18, Subsection 2.3.1 [87], which leads us to:

$$\lambda_1^{''} = 0 \tag{5.22}$$

Now, ratio of losses in the metal sheath to total losses in all conductors in that cable[87], $\lambda_1 = \lambda_1^{'} + \lambda_1^{''}$, Since, the second part is zero, we have $\lambda_1 = \lambda_1^{'}$.

Thus,

$$\lambda_1 = 0.0736 \tag{5.23}$$

Now, λ_2 is the ratio of losses in the armouring to total losses in all conductors in that cable. Since, we have an unarmoured cable, thus λ_2=0.
Calculating the current flowing through the conductor in terms of loading (P) and considering a nominal power factor of 0.92 (it varies 0.9-0.94 as discussed by TenneT cable specialist):

$$\begin{aligned} I &= \frac{P * 10^6}{\sqrt{3} * 10^3 * 110 * 0.92} \\ &= 5.705PA \end{aligned} \tag{5.24}$$

The permissible current rating of an A.C. cable can be derived from the expression for the temperature rise above ambient temperature can be expressed as[87]:

$$\begin{aligned} \theta_{cond} = \ & I^2[R_{ac}T_1 + nR_{ac}(1 + \lambda_1)T_2 + nR_{ac}(1 + \lambda_1 + \lambda_2)(T_3 + T_4)] \\ & + W_d[0.5T_1 + n(T_2 + T_3 + T_4)] + \theta_{ambient} \end{aligned} \tag{5.25}$$

$$\begin{aligned} \theta_{cond} = \ & (5.705P)^2[(5.7 * 10^{-5} * 0.3186) + (3 * 5.7 * 10^{-5}(1 + 0.0789) * 0) \\ & + (3 * 5.7 * 10^{-5}(1 + 0.0789 + 0)(1.615 * 10^{-3} + 1.716)) \\ & + 1.2659[(0.5 * 0.3186) + (3 * (1.615 * 10-3 + 1.716))] + 20 \\ & = 0.0109P^2 + 26.73 \end{aligned} \tag{5.26}$$

Thus, the relationship between the conductor temperature and loading has been established as: $\theta_{cond} = 0.0109P^2 + 26.73$. From the loading profile after cleaning the data, the dynamic temperature can now be plotted to estimate the working temperature of the cable conductor as shown in Figure 5.13.

The statistics for data about the conductor temperature before processing is enumerated in Table 5.3.

Table 5.3: Table showing the statistical parameters for conductor temperature before smoothing (Units in MW)

Data Count	Mean	Std. Dev.	Min. Loading	Max. Loading	25%	50%	75%
563441.0	30.48	3.70	27.00	53.97	28.48	29.25	31.33

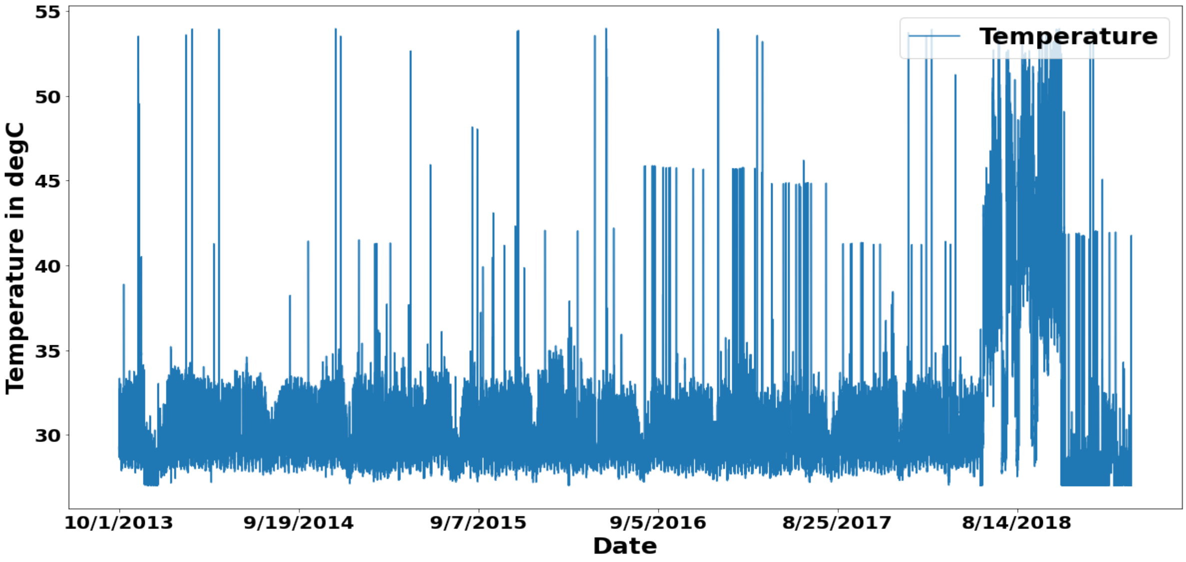

Figure 5.13: Working Temperature of the Cable Conductor before smoothing

The statistics about the temperature profile can be seen to have 563441 rows, with a mean of 30.48^{o}C with a standard deviation of $\pm$ 3.71^{o}C. Since the cable was lightly loaded which is far away from its loading limits, the temperatures are also way below the permissible limits. The minimum temperature is very close to the mean as shown in Figure 5.14(a) indicating that it is the normal operating temperature.The box plot shows most of the data is very less scattered as seen from the Q1 and Q3 being close to each other. There are indeed some data greater than 2.5 time the IQR due to the parallel circuit switch off period. During this period, when one of the lines was removed and this cable was overloaded, the temperature is higher reaching a maximum of 53.98^{o}C. Thus, under any circumstances, the temperature is below 75^{o}C which is the permissible value [90]. That is why it is under research as to what will happen if the cable temperature is pushed higher up to its designed limits?

The variation of conductor temperature with loading is observed in Figure 5.14(b). The curve is parabolic in nature, due to the squared power dependence on the loading term with a constant term due to the ambient temperature and the loss factors contributing to the temperature rise equalling 26.73^{o}C.The loading is varied from 0 to 50 MW since that is the region of interest with respect to the cable. The temperature profile as shown in Figure 5.13 is computed with a Moving Average Algorithm with 5000 width of rolling window in python to obtain a smoother curve to understand the temperature variation in a smoothed curve and plotted in Figure 5.15.

5.6. Decisions from Chapter 5

The operational temperature for this cable based on analysis of loading in MW indicates it was close to 30^{o}C. So, for elevated temperature investigation in the subsequent chapters, the selected temperatures are 45, 60 and 75 ^{o}C, which is the maximum designed temperature of HPGC. Though there are more failure mechanisms in addition to thermal degradation, the replacement strategy for the HPGC cables for TenneT is mainly focused on insulation degradation based on temperature.

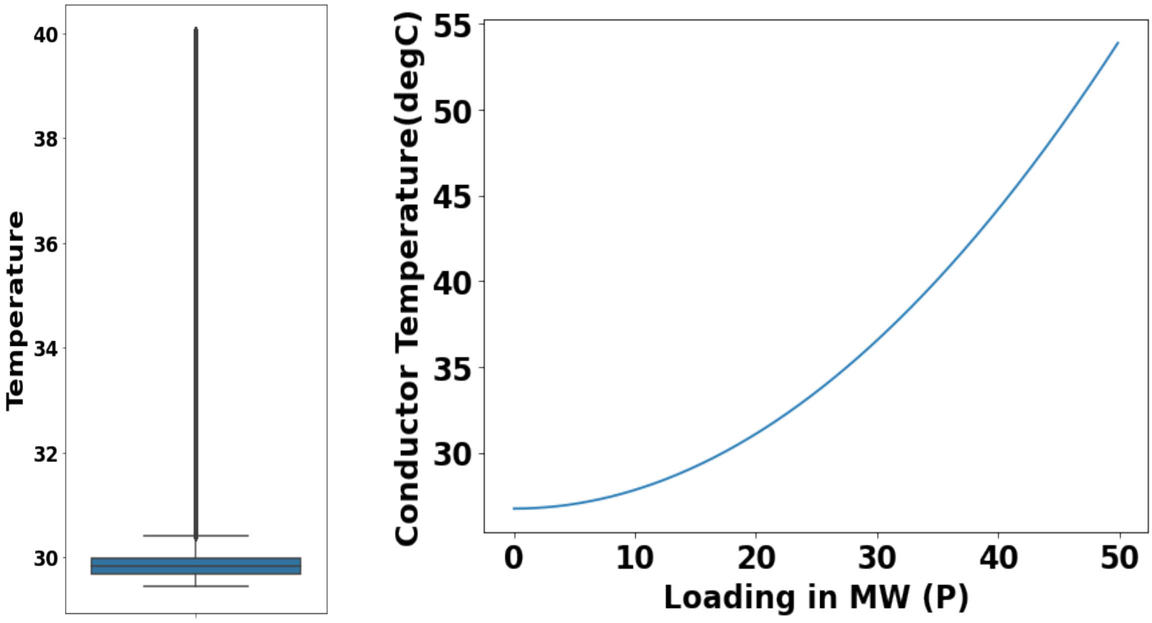

(a) Box Plot of Conductor Temperature

(b) Variation of Cable Conductor Temperature with Loading (MW)

Figure 5.14: Statistics of Conductor Temperature and its variation with Loading

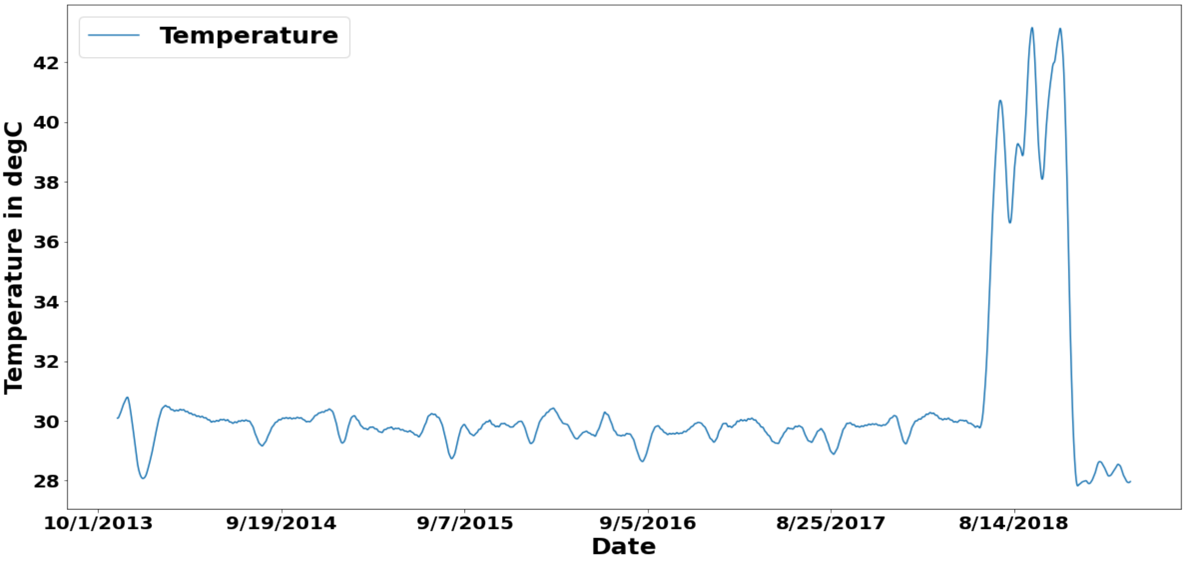

Figure 5.15: Moving Average Based Smoothed Plot of Conductor Temperature

6

Determination of Breakdown Voltage from Fast Ramp Stress Test

In this chapter, we will focus on determining the breakdown strength of samples at different temperatures. Accordingly, the voltage levels would be set for the long term step stress test discussed in Chapter 7. The algorithm followed for this Fast Ramped Sinusoidal Stress Test has been discussed and then the number of layers and the breakdown strengths have been determined as seen below.

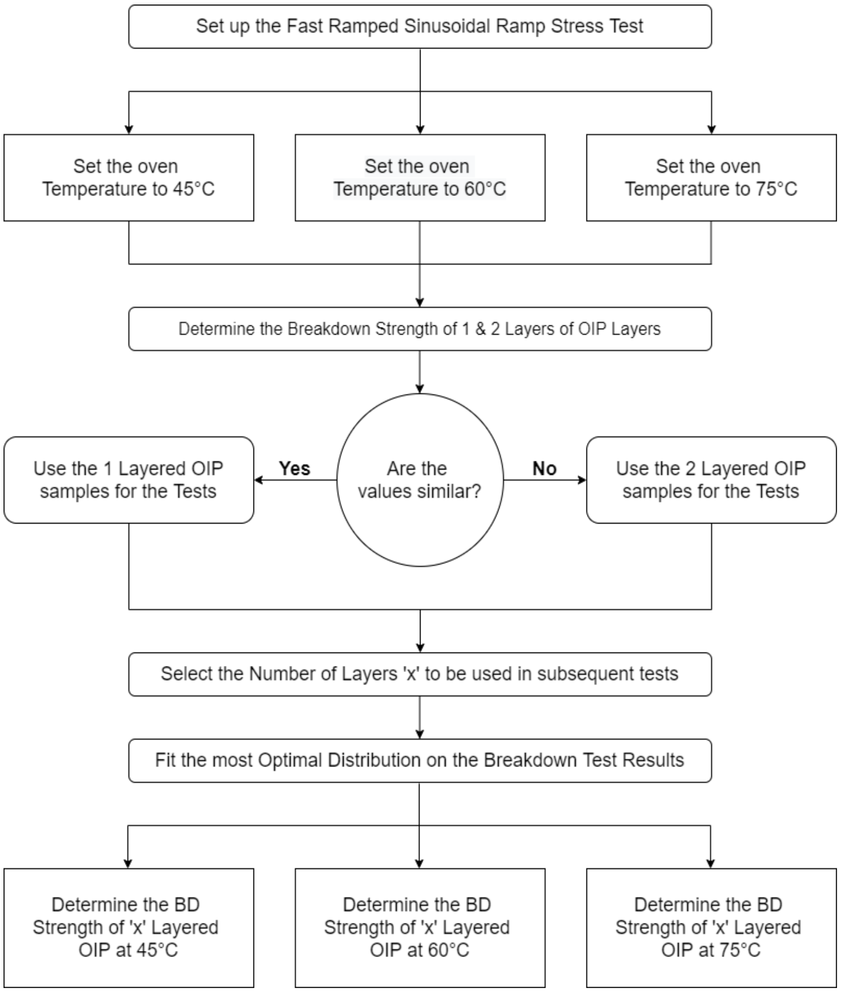

Flow of Research in Chapter 6:

This chapter focuses on deciding the type of sample that resembles the same physics based processes as in the cable insulation. Finally, the breakdown voltages for the three temperatures decided in Chapter 5 is determined. This would form the basis of the tests in Chapter 7. So, Fast Ramped Sinusoid Ramp Test is set up and breakdown of samples is carried out at 3 temperatures for different layers of OIP samples. Rigorous statistical methods are applied to validate the number of layers to be selected for the subsequent experiments. Also, the insulation has layers of three different thickness and so the selection procedure is also discussed in details. With the selected layers, the BDV for the different temperatures are obtained. This voltage is chosen by fitting the data to wide range of distributions and selecting the best one in accordance with the best goodness of fit score and referring to the literature. Due to the fast nature of the test, the samples did not have adequate time to reach thermal equilibrium and so the BDV are rough estimates, which is sufficient for designing the long term experiments in Chapter 7.

6.1. Experimental Setup for Fast Ramp Stress Test

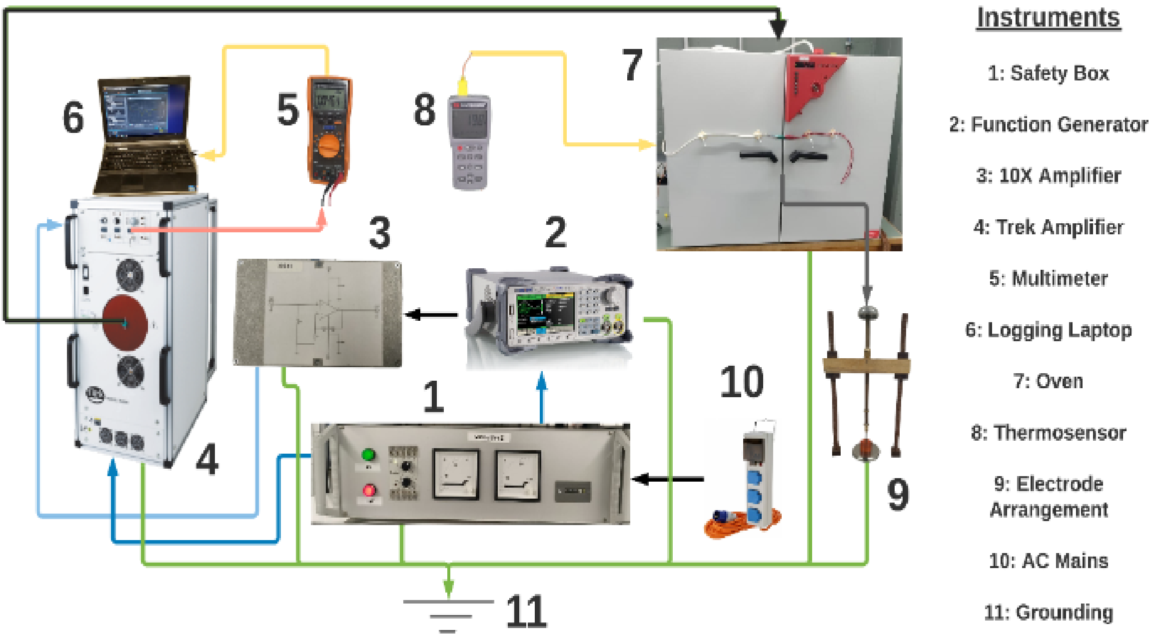

Figure 6.1: Diagrammatic Representation of the test setup for Fast AC Sinusoid Ramp Test

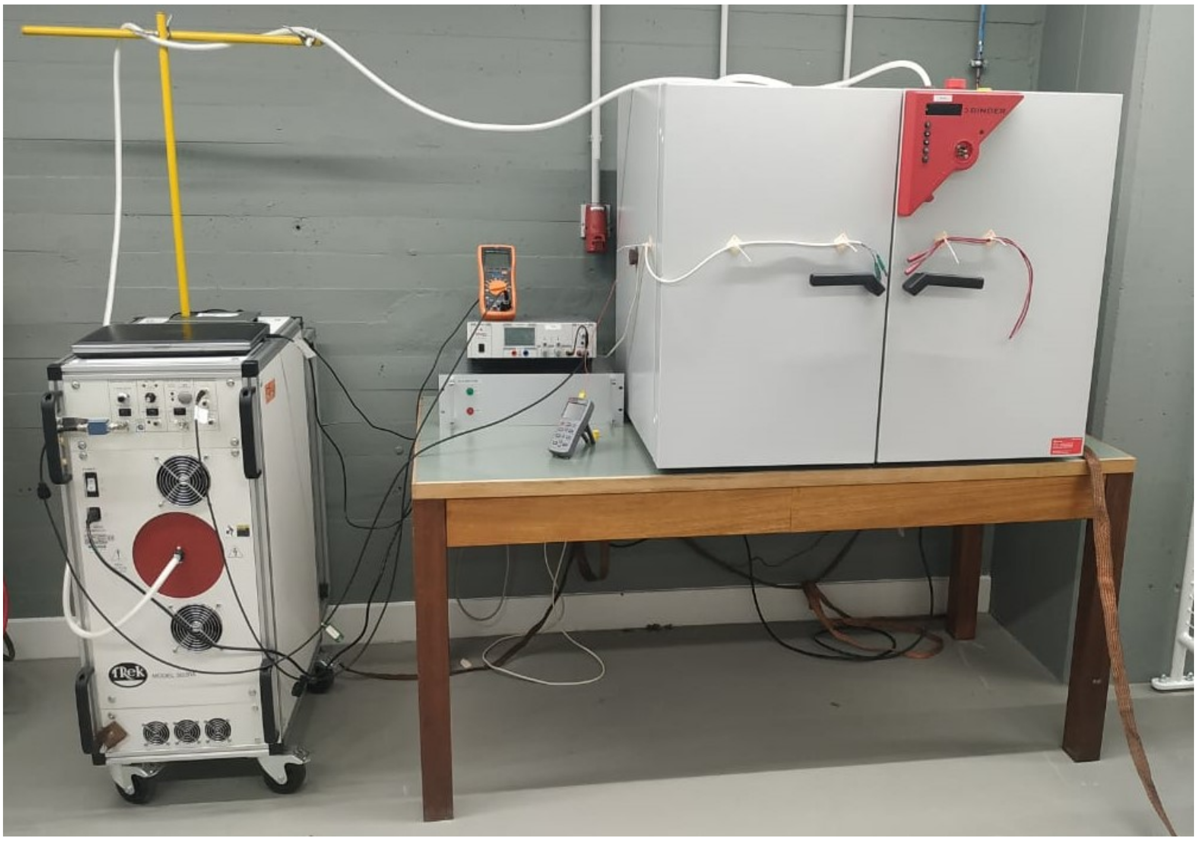

Figure 6.2: Experimental Implementation of Fast AC Sinusoid Ramp Test

Building up the Experiment

Figures 5.1 and 5.2 represents the line diagram and the actual setup for the Fast Ramped Sinusoid Tests. In the single line connection diagram, the wires connected from the same instrument are represented with similar colour. The setup has been explained in details as following:

Step 0: The samples are pre treated after they are removed from the conductor. The inner layers used for the experiments are cut into equal rectangular strips and then stored at 75 ^{o}C for 5 days in a different heating oven to remove any moisture that might have penetrated during the opening of the cable. Then the samples are transferred into the oven where the experiments are being carried out.

Step 1: The safety box, supplied from the Mains is connected to the Trek Amplifier, Oven and the Function Generator, so that all of the appliances are switched off in case of any short circuit. The safety box basically consists of a relay which has a current setting and trips if the current is exceeded.

Step 2: The Function Generator Tektronix AFG3252C is used to generate the ramped sinusoid signal which is fed into the amplifier box having a 10X amplification factor. The amplifier is used else, the maximum voltage reached by the resultant equipment would not be enough to break down the OIP.

Note 1: The signal generator was set to 0.5-1.5 V$_{p-p}$, 50 Hz operating frequency, Upward Ramp, 2 mHz sampling frequency and 100% Ramp Rate. This would result in a increasing ramped sinusoid with a slope of 26.5 V/s for a time period of 500 seconds resulting in a maximum voltage of 13.25 kV (stops if the sample breaks down before 13.25 kV).

Step 3: The output from the OP-AMP is now fed into the Trek Amplifier Model 30/20A having an amplification factor of 3000. The Trek is fitted with a Zener Diode which goes into breakdown region in Reverse Bias Mode, shown in Figure 6.3 as soon as the voltage exceeds 25 kV since the Trek can sustain up to 30 kV. Thus, the 5 kV is kept as a buffer for protection purpose. For the experiments performed for 1 layer and 2 layers of OIP, 25kV was sufficient for the breakdown. The Trek works on a voltage threshold such that if the voltage falls below a trip limit, then the TREK is switched off in case of a breakdown in the OIP insulation. This is because a breakdown in the sample would mean the H.V. electrode is shorted to the ground electrode, greatly reducing the voltage difference, triggering the Trek to shut off. A Multimeter, KEYSIGHT U1282A was connected from the Low voltage (Before Amplification) Output of the Trek which in turn was connected to a data logger, a Lenovo Laptop, collecting data using an interface software. The sampling rate of the logger was 1 sec, giving us enough accuracy in measurement.

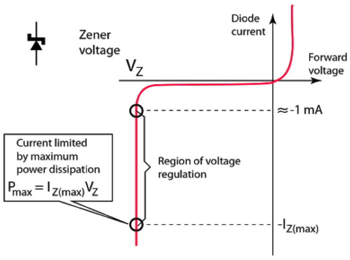

Figure 6.3: Working of a Zener Diode

Step 4: This Amplified Output from the Trek is now transmitted by a shielded wire into the Oven which has been set into a preset temperature. A thermo-sensor is connected to a thermo-couple to record the temperature inside the oven, to ensure high accuracy while evaluating the breakdown results.

Note 2: The thermo-sensor needs to be disconnected before the breakdown tests as some signal gets transmitted which triggers a beeping sound in the device, which might lead to damage.

Step 5: Finally, the electrode setup is constructed inside the oven, where the paper samples are placed between the H.V. and the ground electrode and the breakdown tests are performed.

Note 3: All the equipments are ensured first to be properly grounded before the experiments are performed. Also, the experiments were carried inside a cage and the oven was tied with safety leads connected to the safety box. Which means if the leads are opened anytime during the experiments, that would disconnect the trek and the equipment is safe to handle.

6.2. Dimensions of the OIP Samples

Figure 6.4: Micrometer for Measurement

The OIP samples are measured using a micrometer having a precision of 3 places in decimal (least count of 0.001 mm) as observed in Figure 6.4. It must be ensured that the zero error is corrected before each sample is measured. 20 samples have been measured in each case for 1 layer which are used for the ramped test and 8 samples for 2 layers of inner insulation. Their mean is taken as the average thickness for that layer of paper and represented in Figures 6.5 and 6.6. A comparative analysis has been demonstrated in figure 6.7 showing the increment in the thickness of paper as we move away from the conductor. As mentioned earlier, the cable has 3 layers of insulation, represented as the outer layer with maximum thickness, the middle layer and the inner layer with minimum thickness closest to the conductor.

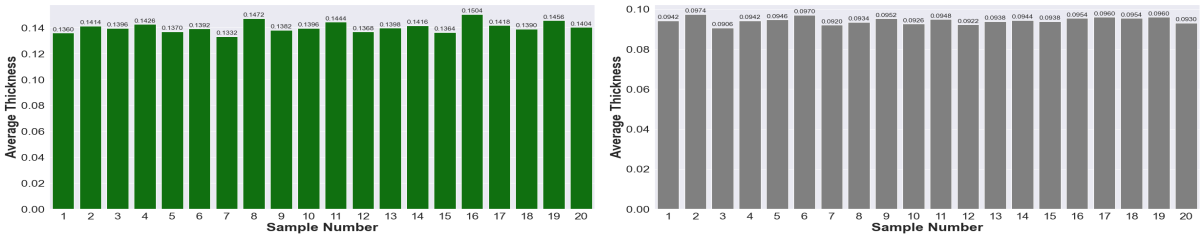

Case A: 1 Layer Outer Sample

Case B: 1 Layer Middle Sample

Figure 6.5: Variation of thickness for single layer outer and middle sample

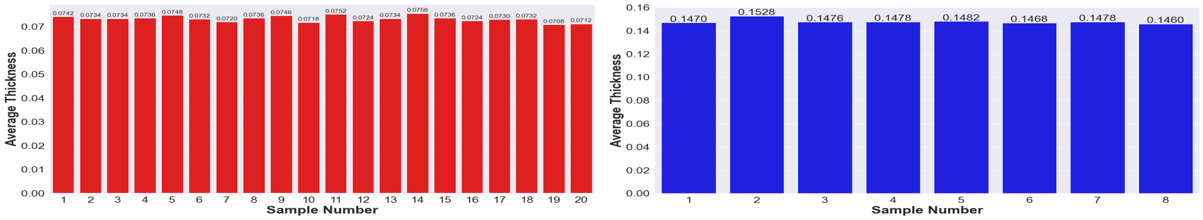

Case C: 1 Layer Inner Sample

Case D: 2 Layers Inner Sample

Figure 6.6: Variation of thickness for 1 vs 2 layer inner sample

Calculations of Mean Thickness:

A) 1 Layer Inner: **0.073 ± 0.001 mm**

B) 1 Layer Middle: **0.094 ± 0.001 mm**

C) 1 Layer Outer: **0.141 ± 0.004 mm**

D) 2 Layers Inner: **0.148 ± 0.002 mm**

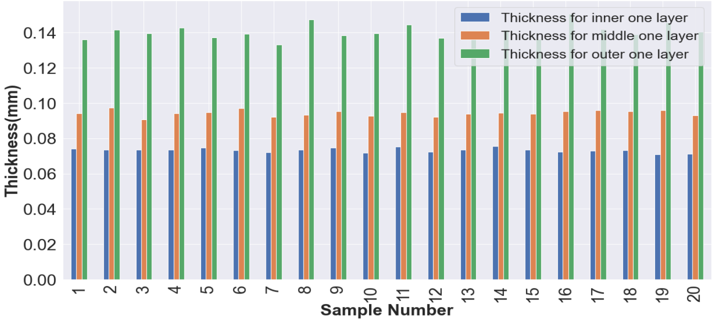

Figure 6.7: Variation of thickness of paper from inner to outer for 1 layer

The thinnest layer of insulation is wound close to the conductor since thinner insulation has lower thermal capacity. The cable conductor is exposed to maximum temperature rise and thus the layers near it should cool down faster compared to the outer layers. Thus, as we move away from the cable the thickness increases and they have lower rate of cooling. Thus, by adjusting the width, it is possible to have an even rate of cooling than having different layers of same thickness. Hence, the OIP cables are produced with 3 layers of different dimensions[91][92].

6.3. Breakdown Results for 45^{o}C Samples

6.3.1. Single Layered Inner OIP Samples:

The fast ramped sinusoidal breakdown tests has been carried on the single layered oil paper insulation as shown in Figure 6.10(b) at 45^{o}C. A total of 20 samples have been used and the breakdown statistics can be observed in Figure 6.8 and the distribution is observed in the violin plot in Figure 6.9 which is a symmetrical plot depicting the distribution.The box plot reads that the median breakdown voltage is at 10.05 kV and the range is quite condensed with a value of 2.817 kV$_{p-p}$.There is no data which lies 1.5 times the IQR which means the distribution is devoid of outliers, thereby indicating robust results.

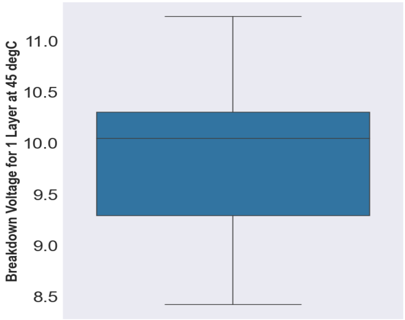

Figure 6.8: Box Plot of BD data for 1 layer inner

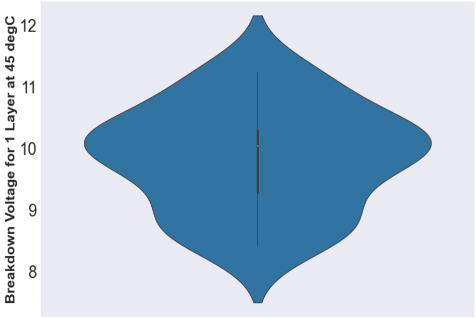

Figure 6.9: Violin Plot of BD data for 1 layer inner

The violin plot shows that most breakdowns have occurred near 10 kV which follows from the box plot and relatively very few samples on the extreme points.Now, after obtaining the data, the next objective is to fit the best distribution, for which Weibull, Lognormal, Exponential and Logistic distribution is fitted. The parameter which evaluates the best model is the Anderson-Darling Coefficient, the lower the coefficient is, the better is the fitting. It is observed that Exponential does not fit the distribution at all and Lognormal has higher coefficient too. The best fit are Logistic and Weibull with a minor difference of 0.01. Now for failure data, Weibull distribution is more suited and thus, now the task is to obtain if 2-parameter or 3-parameter Weibull is more suited. The figure 6.10(a) has been computed in the MINITAB 17 software to evaluate the coefficients of each distribution.

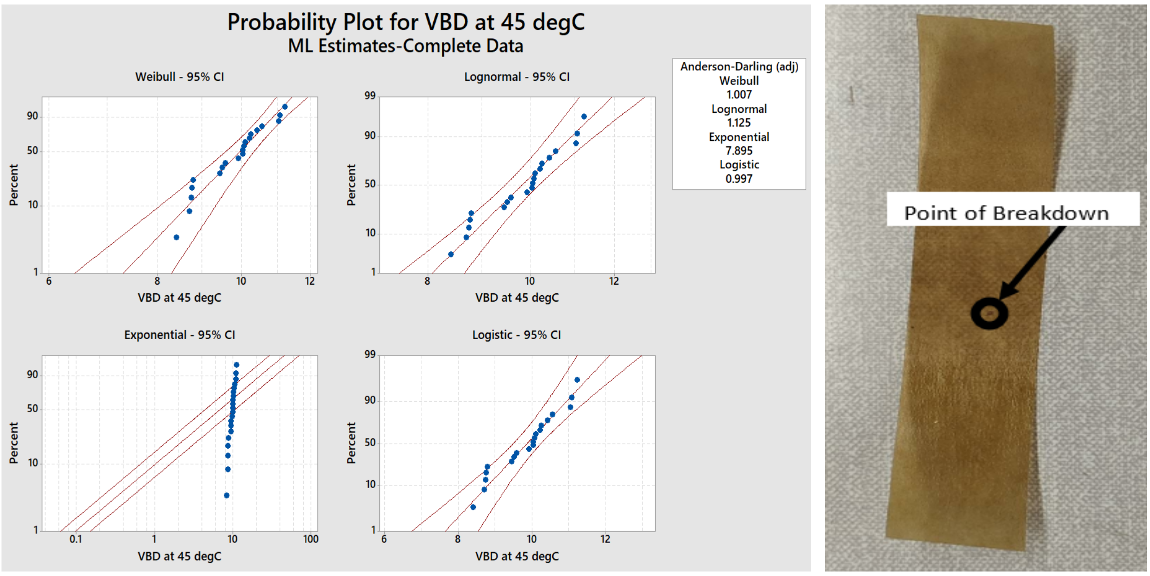

(a) MINITAB Fitting of BD Data with different distributions

(b) Sample Point of Breakdown

Figure 6.10: Sample Breakdown and fitting of Data

The 3-parameter Weibull fit shows some erroneous results since the scale parameter, which signifies breakdown voltage is well below the threshold of 7.56 kV and the median value of 9.86 kV. Also, from the 95% confidence interval as shown in Figure 6.11(a), it can be observed that the boundaries are distorted thereby, indicating it is not a good fit. Now, for 2-parameter Weibull which drops the threshold parameter, it can be observed from Figure 6.11(b) that the scale is close to the median value, which is expected. Also, the 95% confidence interval shows a closed curve, thereby indicating that the 2-parameter Weibull is the most appropriate fit for this data.

At 45^{o}C, the 2-parameter Weibull shows the best fit with breakdown voltage as 10.227 kV_{p-p} for a single layer of oil impregnated paper sample.

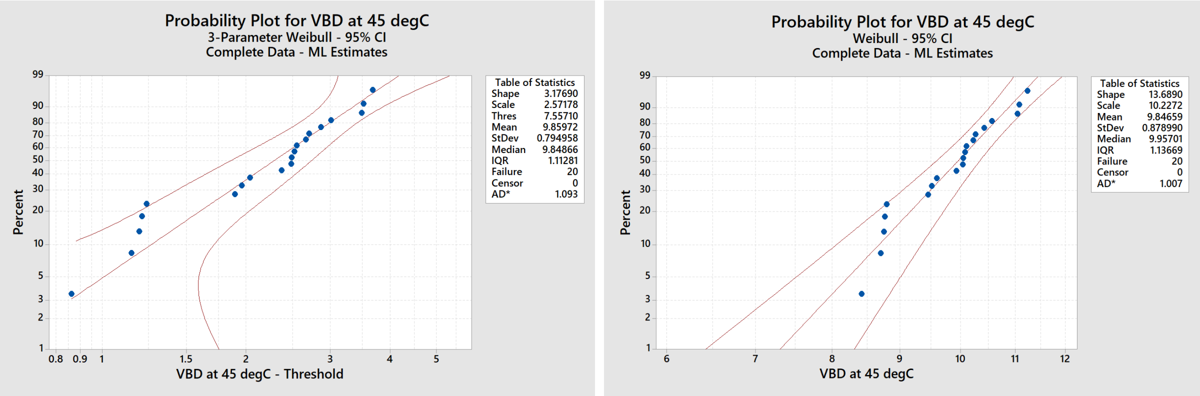

(a) Fitting of 3 parameter Weibull on the BD Data

(b) Fitting of 2 parameter Weibull on the BD Data

Figure 6.11: Comparison of goodness of fit between 2 and 3 parameter Weibull

An insight into the survival and hazard functions for 2-parameter Weibull Distribution has been made in Figure 6.12.

The Survival Function:
Let's assume that T is a continuous random variable with probability density function (p.d.f.) $f(t)$ and cumulative distribution function (c.d.f.) [93][94]:

$$F(t) = \Pr\{T < t\},$$

giving the probability that the event has occurred by duration t. It will often be convenient to work with the complement of the c.d.f, the survival function [94]:

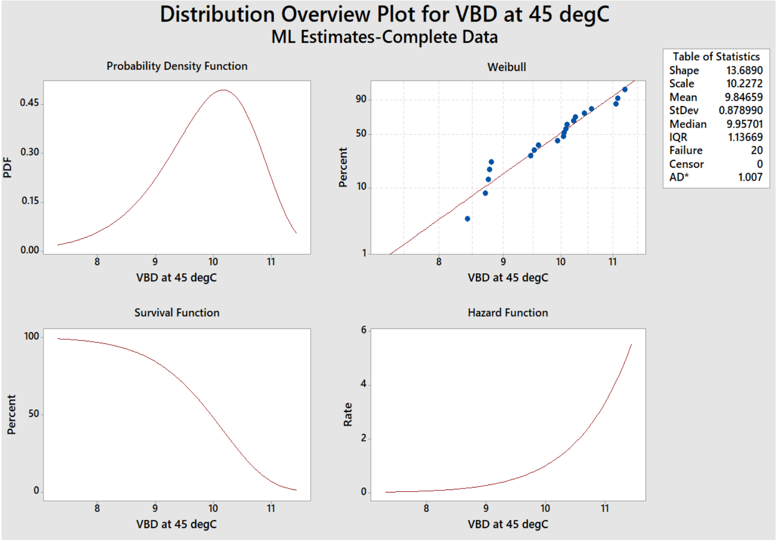

Figure 6.12: Survival and Hazard Function Estimation for 2 parameter Weibull

$$S(t) = \Pr\{T \geq t\} = 1 - F(t) = \int_t^{\infty} f(x)dx \tag{6.1}$$

which gives the probability of being alive just before duration t, or more generally, the probability that the event of interest has not occurred by duration t.

Inference from the graph:

It is observed that as the Breakdown Voltage increases, the survival rate decreases as sigmoid. This is as expected since higher the stress, more would be the probability of breakdown. An example interpretation of the graph would indicate that below 8 kV, it is almost 100% sure of the survival and above 11 kV, it is 100% sure of breakdown.

The Hazard Function:
An alternative characterization of the distribution of T is given by the hazard function, or instantaneous rate of occurrence of the event, defined as[94],

$$\lambda(t) = \lim_{dt0} \frac{\Pr\{t \leq T < t + dt \mid T \geq t\}}{dt} \tag{6.2}$$

The numerator of this expression is the conditional probability that the event will occur in the interval $[t, t+dt)$ given that it has not occurred before, and the denominator is the width of the interval. Dividing one by the other rate of event occurrence per unit of time. Taking the limit as the width of the interval goes down to zero, we obtain an instantaneous rate of occurrence.
The conditional probability in the numerator may be written as the ratio of the joint probability that T is in the interval $[t, t + dt)$ and $T > t$ (which is, of course, the same as the probability that t is in the interval), to the probability of the condition $T \geq t$. The former may be written as $f(t)dt$ for small dt, while the latter is $S(t)$ by definition. Dividing by dt and passing to the limit gives the useful result[94]

$$\lambda(t) = \frac{f(t)}{S(t)} \tag{6.3}$$

which is defined as the rate of occurrence of the event at duration t equals the density of events at t, divided by the probability of surviving to that duration without experiencing the event. Note from Equation 6.1 that $-f(t)$ is the derivative of $S(t)$. This suggests rewriting Equation 6.3 as $\lambda(t) = -\frac{d}{dt} \log S(t)$. Now if we now integrate from 0 to t and introduce the boundary condition $S(0) = 1$ (since the event is sure not to have occurred by duration 0), we can solve the above expression to obtain a formula for the probability of surviving to duration t as a function of the hazard at all durations up to t[94]:

$$S(t) = \exp\left\{-\int_0^t \lambda(x)dx\right\} \tag{6.4}$$

This expression should be familiar to demographers. The integral in curly brackets in this equation is called the cumulative hazard (or cumulative risk)[94]

$$\Lambda(t) = \int_0^t \lambda(x)dx \tag{6.5}$$

Inference from the graph:

The hazard function shows a parabolic rise with increase in voltage, which is as expected, since the hazard rate is proportional to the stress level raised to a power. Thus, near 11 kV, which is near the scale parameter indicating the breakdown, the hazard rate is maximum. In time, hazard rate gradually becomes infinite with increasing stress.

6.3.2. Double Layered Inner OIP Samples:

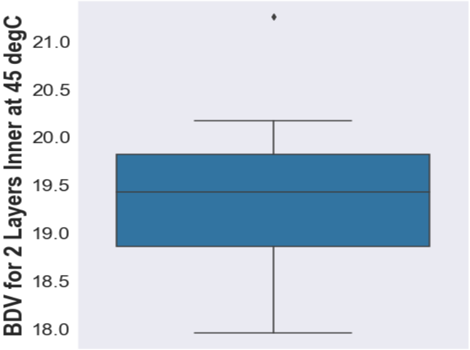

Figure 6.13: Box Plot for BD Data of 2 Layer

The fast ramped sinusoidal breakdown tests has been carried on the doubled layered oil paper insulation as shown in Figure 6.15(b) now at 45^{o}C. A total of 9 samples have been used and the breakdown statistics can be observed in Figure 6.13 and the distribution is observed in the violin plot in Figure 6.14 which is a symmetrical plot depicting the distribution.The box plot reads that the median breakdown voltage is at 19.43 kV and the range is quite condensed with a value of 2.5 kV$_{p-p}$, which is comparable to that of 1 layered dispersion.There is no data which lies 1.5 times the IQR which means the distribution is devoid of outliers, thereby indicating robust results as in previous case.

Note: For doubled layer case, 20 samples had been used, but there is a problem of void between the two layers when they are pushed with one another, thereby the breakdown results are erroneous for the other 11 cases, where or some the breakdown happened through the surface of the paper and reached the edge of the paper. Thus, the 9 successful breakdowns have been used and the 11 samples where the breakdown happened through surface have not been registered.

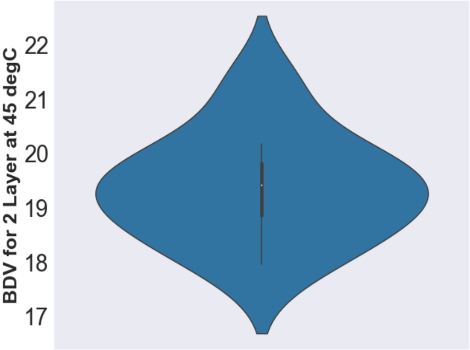

Figure 6.14: Violin Plot for BD Data of 2 Layer

The violin plot in Fig 6.14 shows that most breakdowns have occurred near 19 kV which follows from the box plot and relatively very few samples on the extreme points.Now, after obtaining the data, the next objective is to fit the best distribution, for which Weibull, Lognormal, Exponential and Logistic distribution is fitted. The parameter which evaluates the best model is the Anderson-Darling Coefficient, the lower the coefficient is, the better is the fitting. It is observed that Exponential does not fit the distribution at all. The best fits are Logistic, Lognormal and Weibull with a minor difference of 0.1. From the previous case it is observed that the Anderson-Darling coefficients have increased significantly, indicating slight reduction in fitting as seen in Figure 6.15(a). Now for failure data, Weibull distribution is more suited and thus again, now the task is to obtain if 2-parameter or 3-parameter Weibull is more suited.

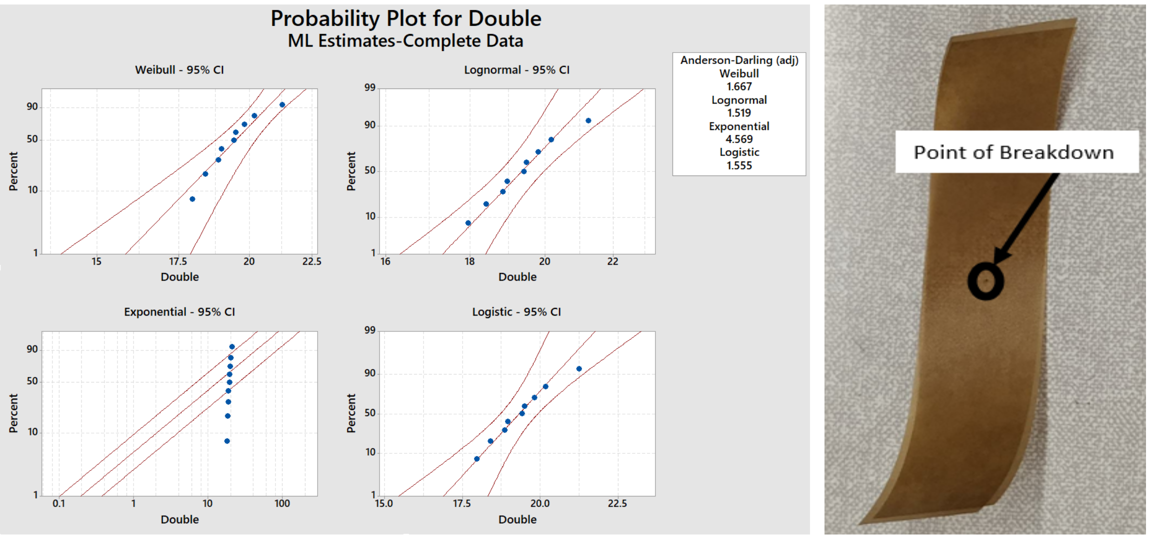

(a) Fitting of Distributions on BD Data of 2 Layer Inner Samples

(b) Double Layer OIP Breakdown

Figure 6.15: BD in 2 Layer Samples and the Optimal Distribution Fitting

The 3-parameter Weibull fit shows some erroneous results since the scale parameter, which signifies breakdown voltage is well below the threshold of 17.71kV and the median value of 19.24 kV. Also, from the 95% confidence interval as shown in Figure 6.16(a), it can be observed that the boundaries are distorted thereby, indicating it is not a good fit. Now, for 2-parameter Weibull which drops the threshold parameter, it can be observed from Figure 6.16(b) that the scale is close to the median value, which is expected. Also, the 95% confidence interval shows a closed curve, thereby indicating that the 2-parameter Weibull is the most appropriate fit for this data.

At 45^{o}C, the 2-parameter Weibull shows the best fit with breakdown voltage as 19.836 kV_{p-p} for a double layers of oil impregnated paper sample.

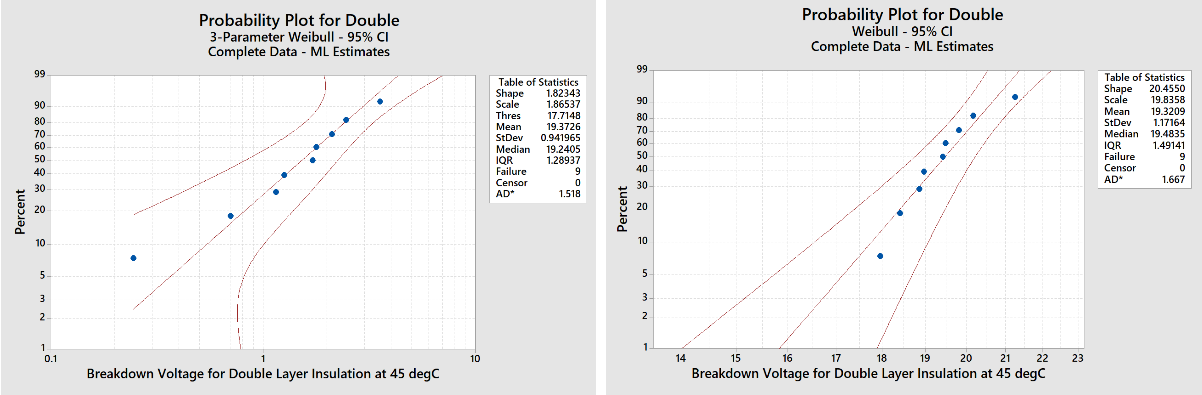

(a) 3 parameter Weibull fit for 2 layer inner samples

(b) 3 parameter Weibull fit for 2 layer inner samples

Figure 6.16: Comparison between 2 vs 3 Parameter Weibull Distribution Fitting

Selection b/w 2 layers vs 1 layer Inner OIP Sample (Section 6.3.1 vs 6.3.2):

A simple approach for selection would be to calculate the Electric Field for both the types by dividing the respective Breakdown Voltages by the Mean Insulation Thickness as observed in Section 6.2. This gives us the Electric Field of 139.582 kV/mm for 1 layer and 134.026 kV/mm for 2 layers. Though the values are very close to each other, there needs to be a more robust statistic to indicate that the Electric Field Distributions are identical. The Kernel Density Estimate[95] of the Electric Fields for both the cases have been plotted in Figure 6.17 which indicates that both are overlapping. Obviously, they cannot be superimposing one another as different phenomenon is expected to occur as we increase the thickness. But the main intention is to observe if the distributions are similar, so that a single layer would suffice with lower input voltage applied as stress. Thus, a quantifiable test needs to be done to find the similarity of the 2 distributions, which is not very clear from visual inspection of KDE's. Thus, the Kolmogorov-Smirnov (KS) Test[96] is undertaken to observe if the distributions are identical. Thus, the following null and alternate hypothesis is modelled and the algorithm is coded in python to obtain the KS Statistic and the p-value. The output from the code is observed in Figure 6.18.

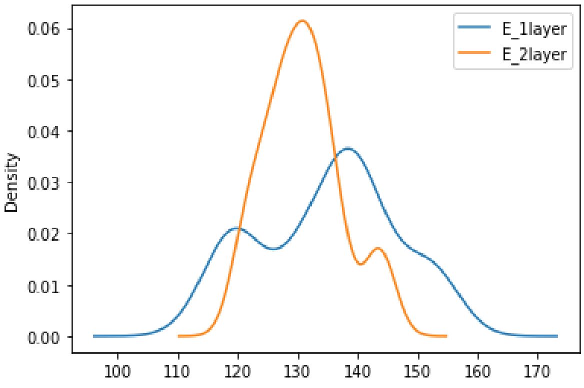

Figure 6.17: Kernel Density Estimation for 1 and 2 layer inner samples

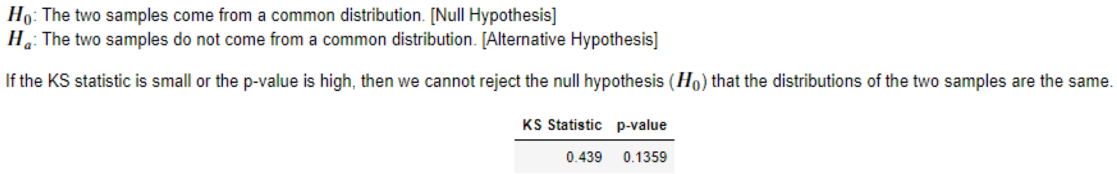

H_0: The two samples come from a common distribution. [Null Hypothesis]
H_a: The two samples do not come from a common distribution. [Alternative Hypothesis]

If the KS statistic is small or the p-value is high, then we cannot reject the null hypothesis (H_0) that the distributions of the two samples are the same.

KS Statistic	p-value
0.439	0.1359

Figure 6.18: Output from KS statistic Evaluation

In hypothesis testing, we quantify the significance level called α depending on which we fail to reject (mind it not accept!) or reject the null hypothesis. As a rule of thumb, taking alpha =0.1, we obtain the p-value as 0.136. We observe that p is slightly greater than α but there is not a high deviation though (only 0.136). So, it can be deduced that the distributions are slightly different but we can not reject the null hypothesis that both samples come from a similar distribution. Thus, this is a quantitative analysis to deduce the similarity. Thus, we will use 1 layer of OIP samples in the subsequent tests.

Summarizing Why We Would Use 1 Layer OIP:

- Breakdown stress for 1 Layer Inner is 139.582 kV/mm. Breakdown stress for 2 Layer Inner is 134.026 kV/mm. This is observed by fitting 2 parameter Weibull distribution and using the scale parameter. The beta parameter is also similar in both cases indicating similar breakdown mechanism is taking place.
- The Distribution of Breakdown Electric Field is similar to that of 1 layer as confirmed by the KS Test.
- Experiments can be performed with lower voltage levels for single layer as compared to 2 layers, which is readily available in the lab.
- Issue of voids present between the two layers of paper, often causing breakdowns at unexpected voltages and giving errors in data.

Note: Maybe if we used multiple layers like 10-12 layers, a different phenomenon may be observed, but it is not possible to provide such high voltage levels in the laboratory equipments available in the Faraday Cage. But with fewer layers, it can be concluded that the observations are similar as discussed in this Chapter. Also, since the number of samples tested for 1 layer was more than 2 layer, so the observed scatter is more maybe due to this reason.

6.4. Breakdown Results for 60^{o}C Samples

In this section, we discuss the breakdown strength for Inner, Middle and Outer Layers to validate if the breakdown Electric Field Stress is similar.

6.4.1. Breakdown for 1 Layer Outer, Middle & Inner Layers for 60^{o}C Samples

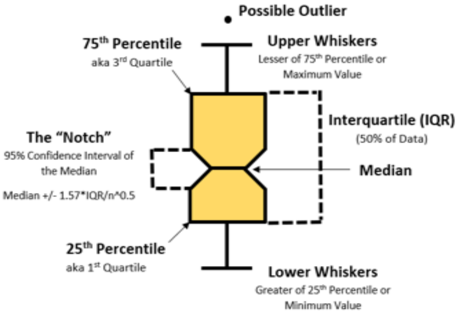

Figure 6.19: Notched Boxplot

The breakdown voltages for Outer, Middle and Inner Layers have been plotted for 20 samples each in form of box plots in Figure 6.20(a),(b) and (c).Since the inner layer has the lowest thickness, hence the breakdown voltage is comparatively lower to the middle and the outer layer with the maximum thickness. The range of BD voltage from outer to inner is quite small from 2.404 kV, 2.042 kV and 1.26 kV. This indicates much less scatter. But the important breakdown parameter is the Breakdown field, which is computed by dividing each of the voltages by their respective thickness as calculated in Section 6.2. The question remains whether the breakdown fields come from the same sample population or different. As we should expect them to come from different populations, since the breakdown mechanisms would be different for the papers with different thickness. The way to find it is by plotting a notched box plot for the BD Fields and to see if the notched region overlap or not. The notched boxplot is explained clearly in Figure 6.19. The extra parameter is the notch which is calculated as Median +/- 1.58*IQR/$n^{0.5}$. Now, if this region overlaps majorly between two populations, then it indicates that they are from similar populations else different. When plotting the Fields in Figure 6.21, it is observed that the notches do not overlap significantly (except for the slight overlap between middle and outer), indicating they are from significantly different populations. Thus, now the question arises which layer to consider since the breakdown fields are quite different for the 3 layers as observed from the notched boxplot. This is true for 45 and 75 ^{o}C as well but the analysis has been shown for 60^{o}C here.

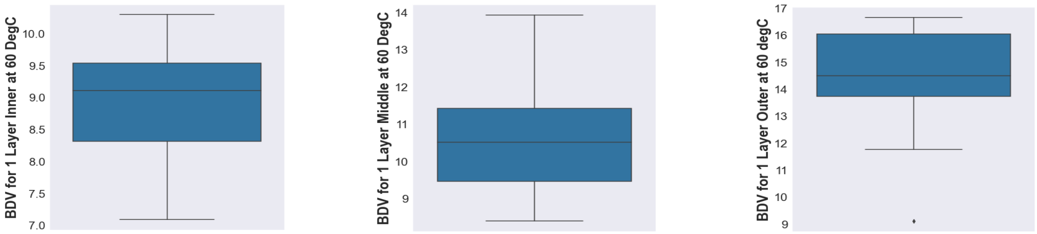

(a) BD Data Boxplot for Inner

(b) BD Data Boxplot for Middle

(c) BD Data Boxplot for Outer

Figure 6.20: Comparison between Outer, Middle and Inner Layer Breakdown Values

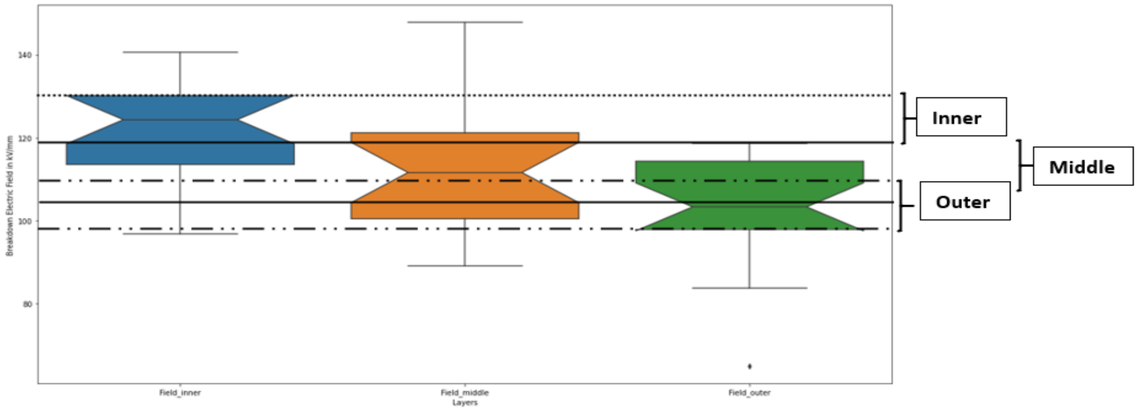

Figure 6.21: Notched Boxplot comparing Breakdown Fields for Inner, Middle and Outer Layers

The Weibull distribution is fitted for Inner, Middle and Outer for 1 layer of OIP as shown in Fig 6.24 (a), (b) and (c) and the B.D. Voltage and Fields obtained from the scale parameter of Weibull have been tabulated in Figure 6.22. It can be observed that the Inner Layer has the maximum breakdown Field. This is because thinner layers contain less impurities and voids in insulation and so they have a higher BD voltage capability. The Breakdown strength reduces as we move out from Inner to Outer Layers as shown in the trend in Figure 6.23 with almost an uniform reduction. Thus, the inner layer is placed close to the conductor such that it can handle higher electro-thermal stress. Thus, we choose the inner layer for our analysis in the subsequent research. As discussed for 45^{o}C, over selection of 1 or 2 layer, the same analysis is performed for 60^{o}C for cross-validation.

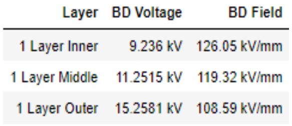

Layer	BD Voltage	BD Field
1 Layer Inner	9.236 kV	126.05 kV/mm
1 Layer Middle	11.2515 kV	119.32 kV/mm
1 Layer Outer	15.2581 kV	108.59 kV/mm

Figure 6.22: BD Voltage and Field

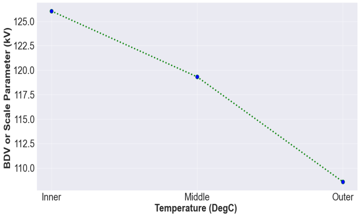

Figure 6.23: BDS with thickness

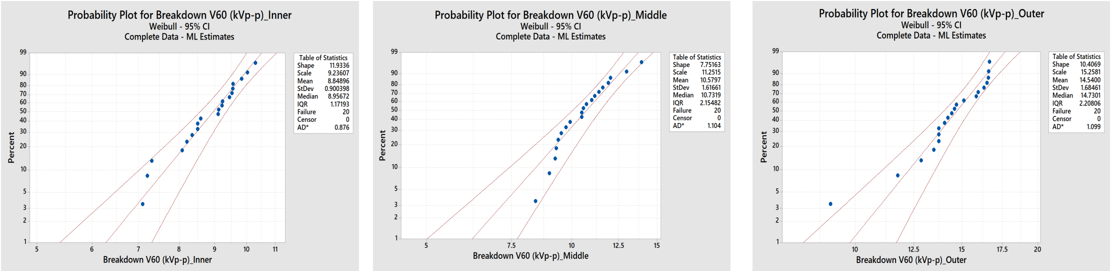

(a) Weibull Distribution fitted to BD data of Inner Sample

(b) Weibull Distribution fitted to BD data of Middle Sample

(c) Weibull Distribution fitted to BD data of Inner Sample

Figure 6.24: Comparison between Weibull Distributions for Inner, Middle and Outer Layers

6.4.2. Breakdown Test for 1 or 2 Layers for 60^{o}C Samples

The Breakdown Test was carried at 60^{o}C for 2 layers and the Weibull Distribution was fitted. As expected, the hazard rate increases as the voltage increases and the survival rate reduces drastically as voltage increases. From the scale parameter it is observed to be 19.2144 kV, corresponding to 129.82 kV/mm as breakdown field. Thus, for 1 layer the BD Strength is 128.05 kV/mm and for 2 layers it is 129.82 kV/mm with a minor difference of 1.77 kV/mm. This, again validates that the single layer OIP insulation would suffice for the subsequent tests.

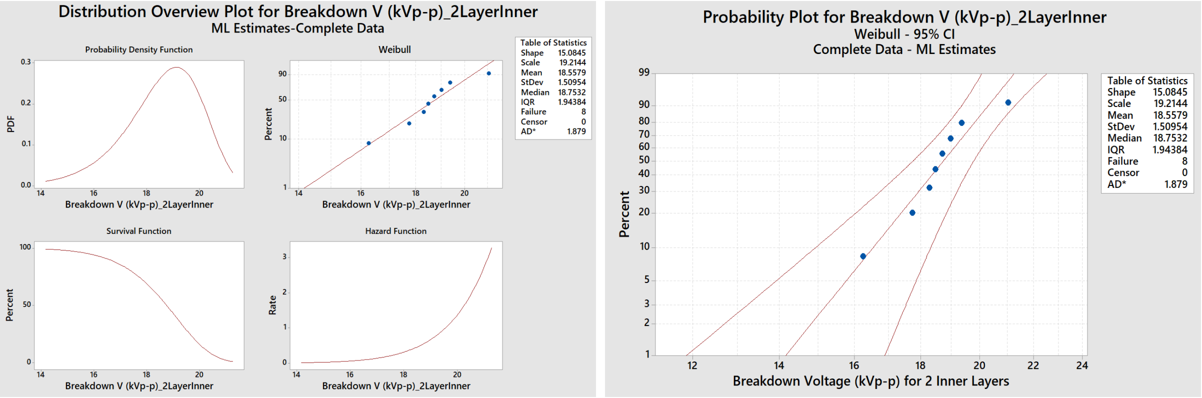

(a) Hazard and Survival function for 2 Layer sample

(b) 2 parameter Weibull fitted to 2 Layer BD Data

Figure 6.25: Statistics and Distribution fitted to 2 Layer Samples at 60^{o}C

Two important questions have been answered with experiments and explained here,first which layer should be selected for the rest of the experiments out of Inner, Middle or Outer Layer; second, how many insulation layers should be used: one or two layers. From the explanation above it is evident that the inner layer seems to experience higher stresses and probability of failure is higher. Also, BD strength of single and double layer insulation is quite similar. With double layer samples, there is possibility of excess voids between the layers of insulation which makes the experimental results biased or unsuccessful. Therefore, in this research, inner layer of insulation and single layer samples have been used in the subsequent experiments.

6.5. Breakdown Results for 75^{o}C Samples

The number of samples tested at 75^{o}C were 15 in number and the first 5 were used as test samples. This is because at 75^{o}C, the coefficient of thermal expansion for steel and epoxy is quite different owing to the different material characteristics, causing uneven surface on the electrode, which was not observed at lower temperatures. Thus, the electrode was extracted at high temperature, polished instantly and used for the tests. In that way, the expansions remained even for steel and epoxy at that specific temperature and the test results were more accurate. This led to 5 unintended failures due to uneven expansion which were left out of the statistics. The scatter is pretty low (1.42 kV) as observed from the box plot in Figure 6.26 and the distribution is observed in the symmetrical violin plot in Figure 6.27. Similar routine as used for other temperatures were followed by fitting the best fit distribution, showing exponential as the worst fit and Weibull and Log-logistic as the best indicated by the Anderson Darling Coefficient. Since, there is no substantial difference between the two and Weibull is known to best fit breakdown data, hence 2 parameter Weibull is fitted as shown in Figure 6.29(b). The hazard rate and survival function follows similar trend as lower temperatures which increases and decreases with voltage respectively. The scale parameter of 8.89 kV indicates the breakdown voltage at 75^{o}C, corresponding to a field strength of 121.35 kV/mm for 1 Layer. The shape parameter is also similar as to the other 2 temperature levels. The inner, middle and outer layer alongside 1 vs 2 layers showed similar trend as previous temperatures and thus has not been explained again.

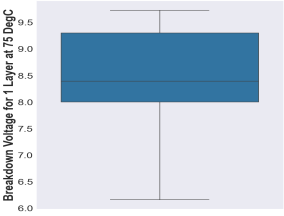

Figure 6.26: Box Plot of BD Data

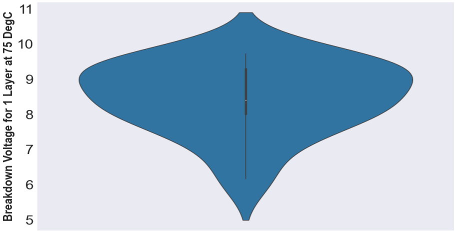

Figure 6.27: Violin Plot of BD Data

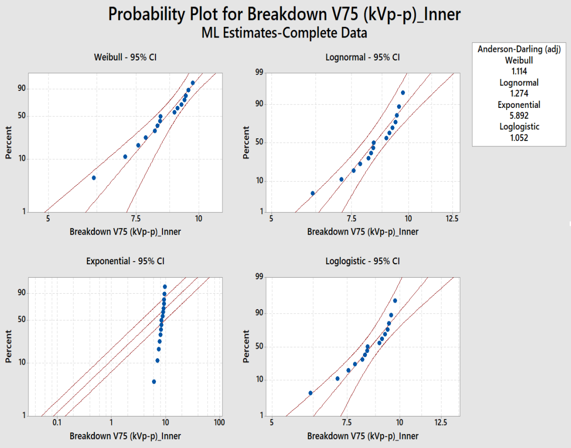

Figure 6.28: Distribution Fitting on BD Data

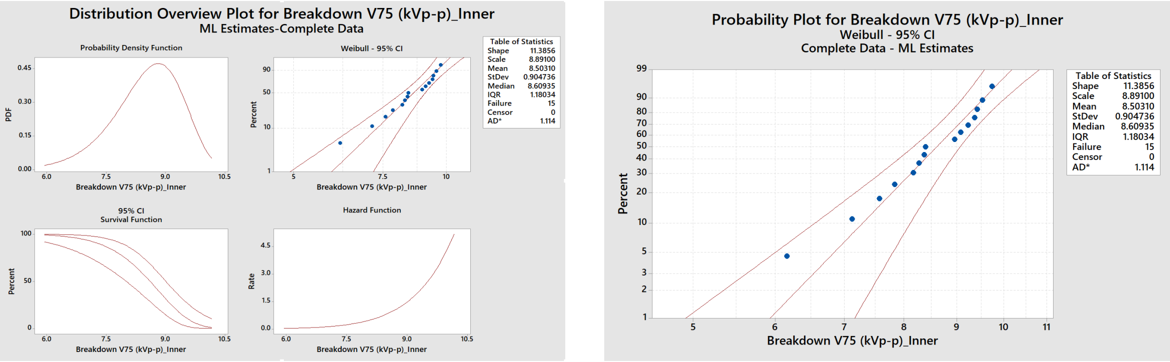

(a) Hazard and Survival functions for 1 layer BD Data

(b) 2 parameter Weibull Distribution fitted to BD Data

Figure 6.29: Statistics and Distribution fitted to 1 Layer Samples at 75^{o}C

6.6. Comparison of Breakdown Results for 45, 60 and 75^{o}C

A comparison has been made based on the fast breakdown tests with increase in temperature. Since now we are applying two stresses in form of electrical and thermal, it can be observed that as we increase the temperature, the breakdown field goes down, also as observed in Fig 6.30. For 1 layer of insulation, when the temperature stress is higher, it is observed that the voltage stress is lower to cause breakdown in sample. The reason why with 15^{o}C rise each time, the change is not linear has been explained in the next section with appropriate chemical equations. The trend in scale parameter with increase in temperature is parabolic as seen in Fig 6.31. Whereas, the shape parameter (β) is observed to be almost constant as observed in Fig 6.32. This shows homogeneity and accuracy in the measurements and also we can compare similar β values as it represents a certain wear-out phase in the life of the insulation. If we had different β for different temperature, it would signify we are comparing at different regions in the wear out phase of insulation, which is not of much significance. This trend in the parameters of 2-parameter Weibull Distribution is directly reflected in Fig 6.33(a), where similar β results in almost parallel lines and with increase in temperature the lines shift towards left indicating reduction in α or breakdown voltage. The Anderson-Darling Coefficients of near 1.0 represents the distribution is quite an optimum fit, as discussed before already. Comparing the Survival and Hazard Function in Figure 6.33(b) now gives more insight than individually analyzing. For, survival function, if we take a vertical line anywhere, say at 9 kV, the chances of survival for lower temperature is more than at higher temperature. Thus, with increase in temperature, the hazard function trend goes down. Initially, almost for all temperatures and at very low voltage levels, chances of survival is same and near 100% after which they diverge according to the trend and then converge to 0 again at very high voltages at which all samples at all temperatures are expected to fail. For the hazard function, at a constant voltage, the hazard rate for 45^{o}C is lesser than the other higher temperatures since we are applying lesser stress. At low voltages the hazard is almost 0 for all temperatures after which they diverge according to the trend (minimum for 45^{o}C and maximum for 75^{o}C). Thus, now the breakdown voltages at different temperature forms the basis to design the steps for long term step stress on the insulation to calculate the lifetime parameters.

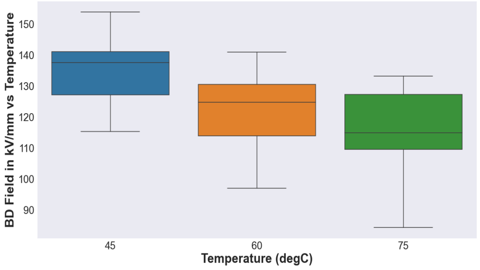

Figure 6.30: BD Strength at 3 Temperatures

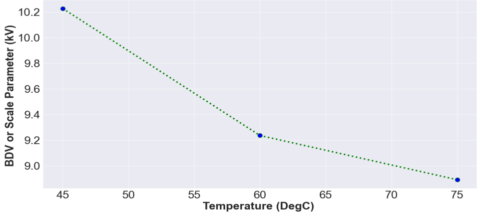

Figure 6.31: BD Voltage/ α at 3 Temperatures

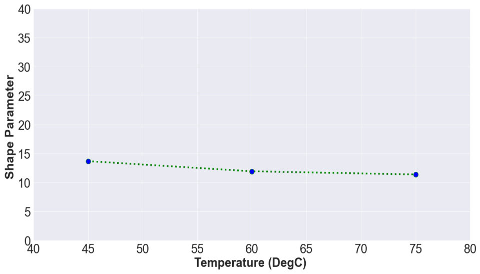

Figure 6.32: β variation with Temperature

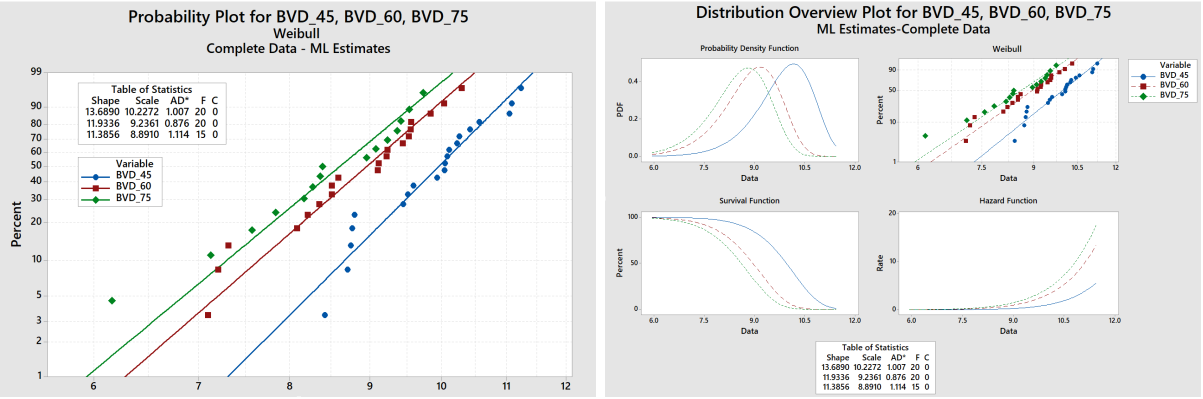

(a) 2 parameter Weibull fit for BD data at Different Temperature

(b) Hazard and Survival Functions for BD data at Different Temperature

Figure 6.33: Comparison between Distribution Parameters for 3 Different Temperatures

7

Long Term Sinusoid Step Stress Test for Aging Model Formulation

Chapter 7 describes the Sinusoid Step Stress Test for long term breakdown analysis to obtain aging model estimates using Maximum Likelihood and Least Squares. Finally, the aging model is constructed from the breakdown data as shown by the flowchart below.

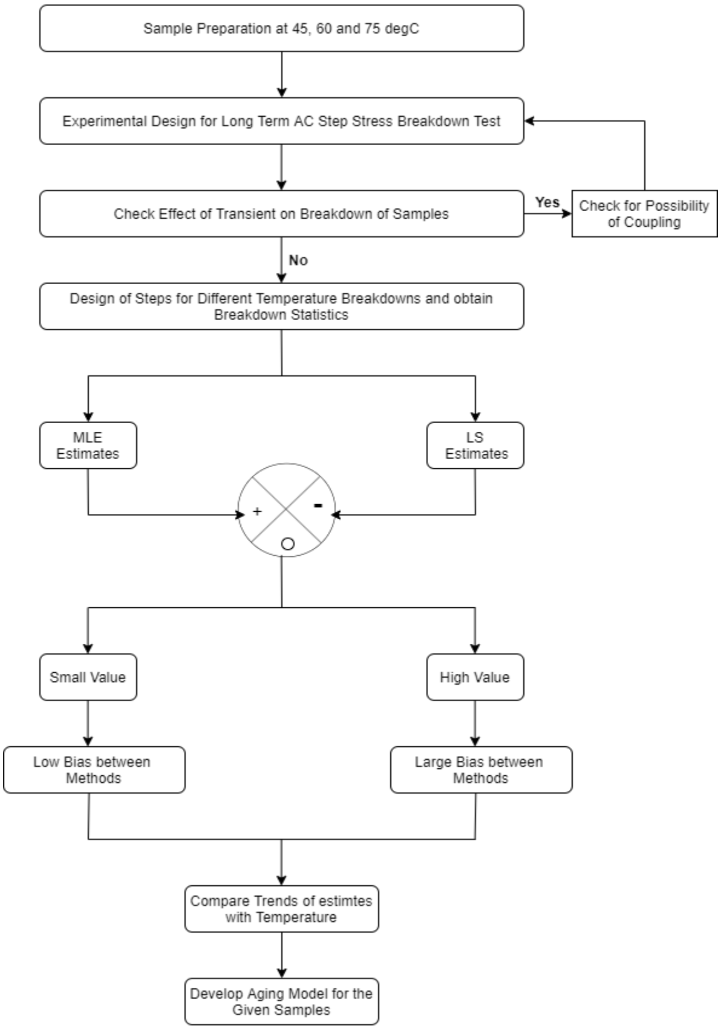

Flow of Research in Chapter 7:

This chapter first discusses the preparation of the samples at the three temperatures for the long term tests. After preparation, the experimental setup is made for Long Term Sinusoid AC Step Stress Test to develop an aging model. The setup was thoroughly checked for any transients arising due to breakdown of one sample and affecting the healthy ones. So, all of them were decoupled from the source and the randomness pattern of the breakdown was observed for different temperatures. Once it was verified that the breakdowns were not biased with numerous initial dummy tests, the main tests were carried out. Firstly, the steps were designed with the maximum value going till the breakdown voltage at that temperature obtained from the fast tests in Chapter 6. Different types of step patterns were also applied to check its effect on failure data. The data was fitted on a 2-Parameter Weibull Distribution with Inverse Power Law Model. The estimates of the resultant was obtained using the Maximum Likelihood Method. The estimates were also verified using the Ordinary Least Squares Method to check if there is any significant bias between the two methods. Since the two estimates were very close, hence the aging model was developed for different temperatures. Once, the model is made, now the question remains how to check the condition of the insulation with increase in temperature and rate of aging.

7.1. Experimental Setup for Long Term Breakdown Test

This section describes the experimental setup for long term tests on the OIP samples which have been prepared at different temperatures for fixed duration of time. The setup has been discussed in details in Subsection 7.1.1 which the following Figures 7.1-7.5 showing the experimental setup in an over all view, the safety boxes for protection of the system, the low voltage and the high voltage sides of the setup and finally the arrangement of the electrode-sample setup inside the oven maintained at the specific temperature.

Figure 7.1: Experimental Implementation of Long Term Breakdown Test

Figure 7.2: Safety Box Arrangement with PXI and Oscilloscope Setup

Figure 7.3: Low Voltage Side of Breakdown Test Setup

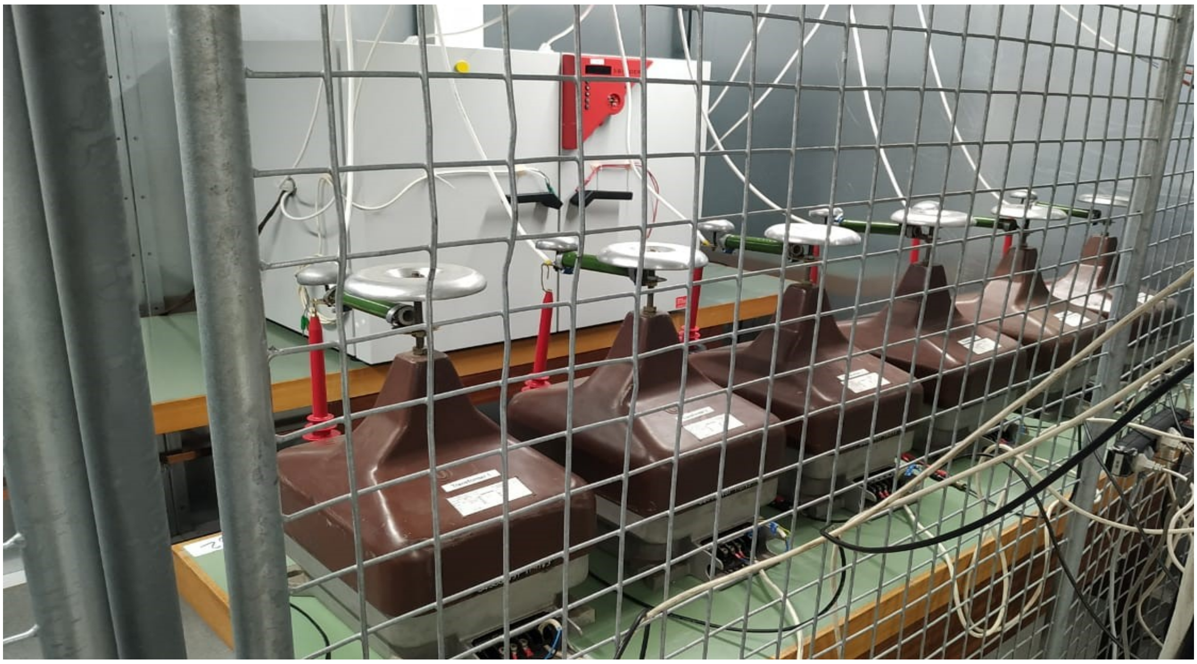

Figure 7.4: High Voltage Side of Breakdown Test Setup

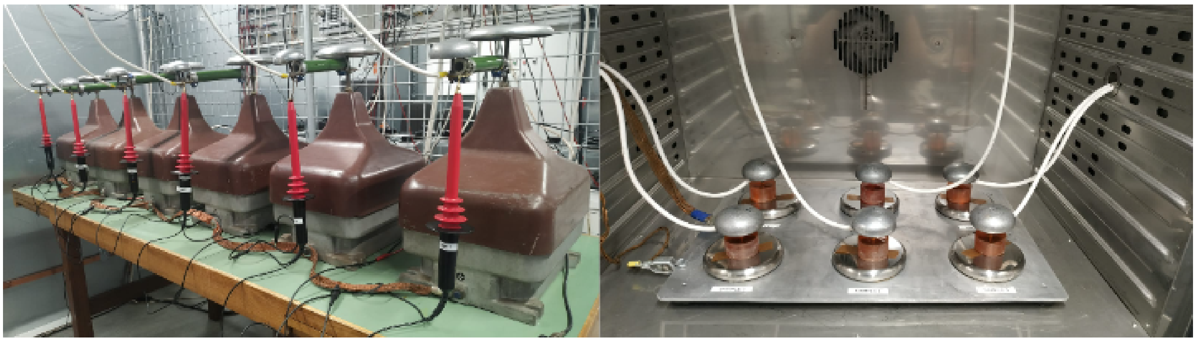

Figure 7.5: (a) HV Probe Arrangement on Transformers, (b) Electrode Arrangement inside Oven

7.1.1. Description of Experimental Setup

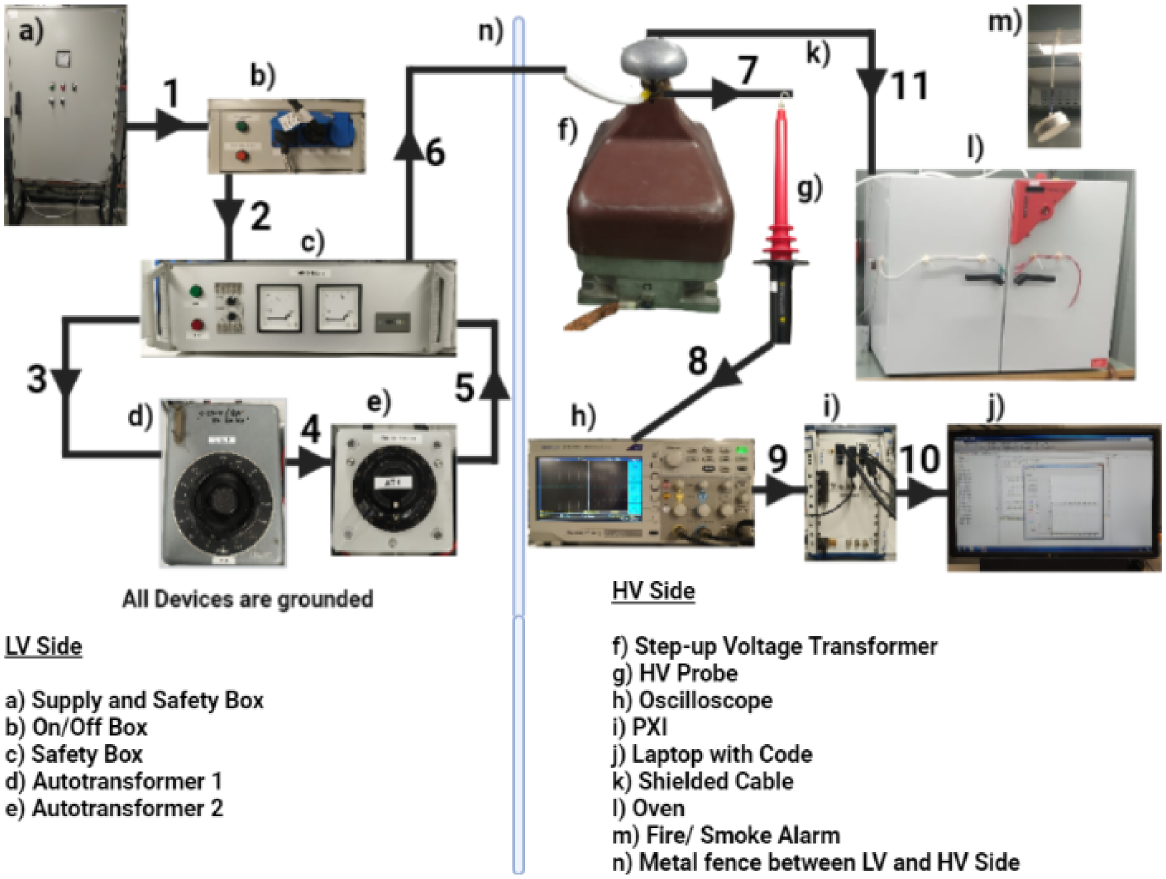

Figure 7.6: Schematic Diagram for Long Term Step Stress Test for 1 Sample (6 like these in parallel)

Figure 7.6 represents the schematic diagram for long term step stress test for 1 samples as 6 such are put in parallel from components c-k and inserted into the oven with 6 electrodes (Figure 7.5 (b)). Figures 7.2-7.4 shows the parallel arrangement of equipments for 6 samples (6 safety box, 12 autotransformers, 6 step up transformers, 6 HV Probes, 6 shielded cables inside the oven into 6 electrodes). This was needed because initially one such setup as seen in Figure 7.6 was used to supply 6 samples and it was observed that there was a lot of transients due to breakdown of one sample induced on other healthy samples, causing their premature breakdowns. Thus to reduce the probability of any transients, the whole setup was decoupled for 6 samples so that even if there are transients during breakdown (which is obvious), it does not propagate to other samples. This effect after improvement has been studied in Subsection 7.1.2 where it has been observed that the duration of transients reduced greatly from previous case and they do not affect each other, making the test results very reliable.

Low Voltage Side:

Firstly, 220 V is supplied by the supply and Safety Box which maintains a constant input voltage with safety equipments that trip during faults. It is connected to the On/Off Box and switching this off disconnects the whole circuit. In case of any anomaly during experiment, since I can only access the LV Side, hence turning it off acts as a safety manual protection. It is connected to safety boxes which basically trips if the current is above a certain threshold and thus, when the sample breaks, the safety box trips. It has a timer inside which clocks the time interval from switching on and off and basically gives us the time to breakdown. But this has not been used for timing calculation since sometimes even after breakdown, the box did not trip during the dummy test runs since the current did not reach the threshold. I will later discuss in this section itself how the time to breakdown is evaluated. Each safety box is connected to 2 Variacs which are basically auto-transformers. We use 2 such so as to have a very sensitive measurement since initially using one Variac was increasing the voltage at a much faster rate which is undesirable if the rate is too high during change from one slope to the other, specially at higher voltages close to breakdown. Thus, 2 Variacs now gave more control over the voltage change and the voltage rise was much slower for equivalent rotation of the Variac knob. These instruments constitute the low voltage side which is accessible to me for increasing the voltage for each step and to switch off the circuit during any unseen circumstances.

High Voltage side:

There is a metal fence between the LV and HV side and the actuation is done such that when the door is closed, the whole circuit has power else, it is disconnected from the On/Off Box. Even opening the fence during measurements switch off the circuit immediately and acts as a protection from touching the HV components. In the HV side, the safety box is connected to the step up voltage transformer with step up ratio of $34500/\sqrt{3} : 110/\sqrt{3}$. A HV probe is connected to the transformer which has a ratio by which the voltage is reduced. The calibration of all 6 HV Probes are done with a known voltage to find the accurate amplification factor. The probe is connected to an oscilloscope that displays the output, which is connected to a PXI which in turn is connected to a laptop used for logging the measured data. A MATLAB Code has been prepared with all the HV Probe values inserted to observe the HV steps and log the data. The GUI is seen to have different calibration factors for different probes which was calculated before for different voltages and a best fit line was fitted whose slope represented the most optimal amplification factor for that probe. The data is stored every 30 mins so that there is no chance of data loss even if the laptop crashes. The GUI of the MATLAB Interface can be seen in Figure 7.7 where the sinusoid voltage signal is observed in the upper pane and there is a sampling rate of 2s for the sine signal, giving a constant amplitude voltage waveform. The 2 second is chosen because of the delay in communication between the oscilloscope and the PXI which is little over 1.5 s. When a sample breaks, the voltage comes to zero and thus, this enables us to calculate the time to breakdown with a standard deviation of 2 seconds (sampling time) which is more accurate than the safety box tripping, which often did not trip because of the current not going above set limit. The transformer output is now connected by shielded cables and inserted into the oven prepared at a certain temperature and connected to the electrode as shown in Figure 7.5(b). 6 transformers with 6 cables are inserted inside the oven through different holes so as to ensure maximum distance between the cables, so that the signals do not interfere. There is also a fire/smoke detector installed over the oven which is triggered as soon as there is any smoke arising due to short circuit or failure in any component. As a result, a very robust setup has been developed so as to ensure most accurate breakdown readings with maximum safety for the equipments. Figure 7.2 and 7.3 represents the LV side where the voltage is increased after certain durations following a step pattern. Figure 7.4 shows the HV side separated by the fence and 7.5(a) shows the HV probes attached to the transformers for voltage measurement. The whole experiment has been done inside a Faraday Cage so that there is no external interference and also all the equipments are grounded properly and double checked before starting the experiment. It has also been ensured that the Variacs are always at the 0 position before starting the experiment for each temperature test. In the end of the long term breakdown experiment spanning more than a week, the ground and epoxy casted HV electrodes are polished well because of the carbonization spots from the breakdown of samples.

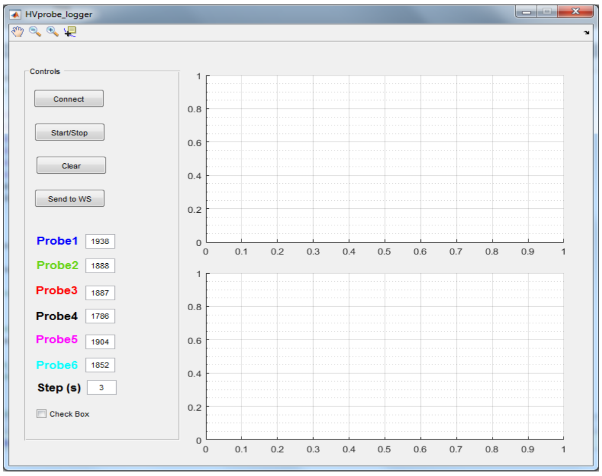

Probe1 1938
Probe2 1888
Probe3 1887
Probe4 1786
Probe5 1904
Probe6 1852
Step (s) 3
☐ Check Box

Figure 7.7: MATLAB GUI for Communication with Oscilloscope

Note: During voltage increment, the knob is rotated as slowly as possible to ensure a smooth transition from one level to the other and ensure uniform rates throughout and the change reflected in the MATLAB output is observed carefully.

7.1.2. Effect of Transients and Setup Defects on Breakdown of Samples

One of the major factors biasing the long term step stress tests is the transients that are transferred on to the rest of samples when one of the samples breakdown. To explain clearly, if the different samples are not electrically decoupled from each other, then due to breakdown of the sample, an electrical transient is created with magnitude 3-4 times higher the operating voltage magnitude, which propagates to the other samples and causes premature breakdown on healthy samples under test. This biases the experiment as a result of which the data and statistics obtained is not accurate. Initially the test setup was not decoupled and similar phenomenon was observed. But then all the samples were separately supplied by individual Variacs and connected with shielded wire and the following observations were noted:

- Except for sample number 2, all other samples broke down without a voltage transients
- Similar trends were observed for 45^{o}C and 75^{o}C, where there were 1 and 2 transients respectively, and again the magnitude was very less and did not bias the experiment.
- There is absolutely no correlation with higher temperature and higher transients as all of them were less than 3-4 times the operating value.

To ensure, that all the samples are perfectly decoupled, all the samples in the beginning of the main long term tests were kept very close to the breakdown voltage as determined from the fast ramp tests in Chapter 6. Then for each one, the voltage was increased in a steep slope until breakdown. It was still noticed that there was no effect on the other samples (no voltage rise or transient based breakdowns). Figures 7.10 represent the transients caused due to breakdown of the sample

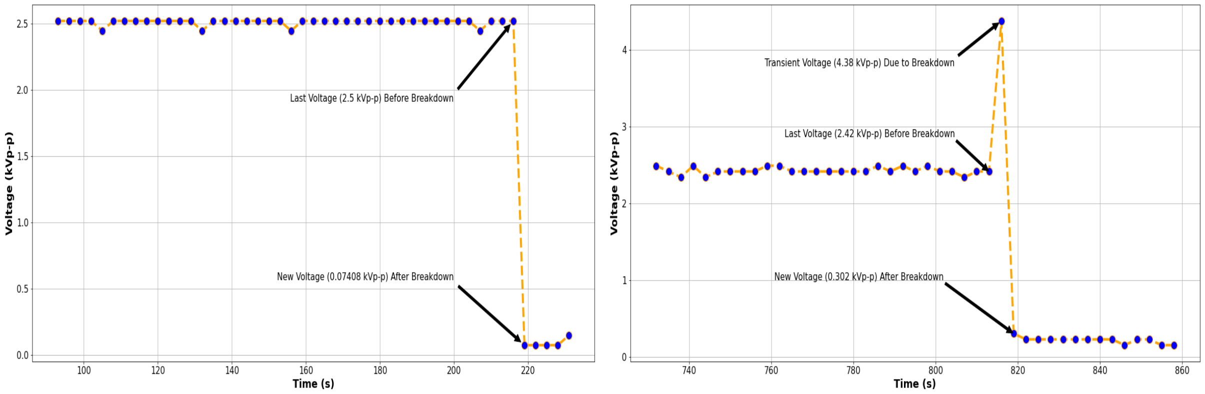

(a) Transients from Breakdown of Sample 1

(b) Transients from Breakdown of Sample 2

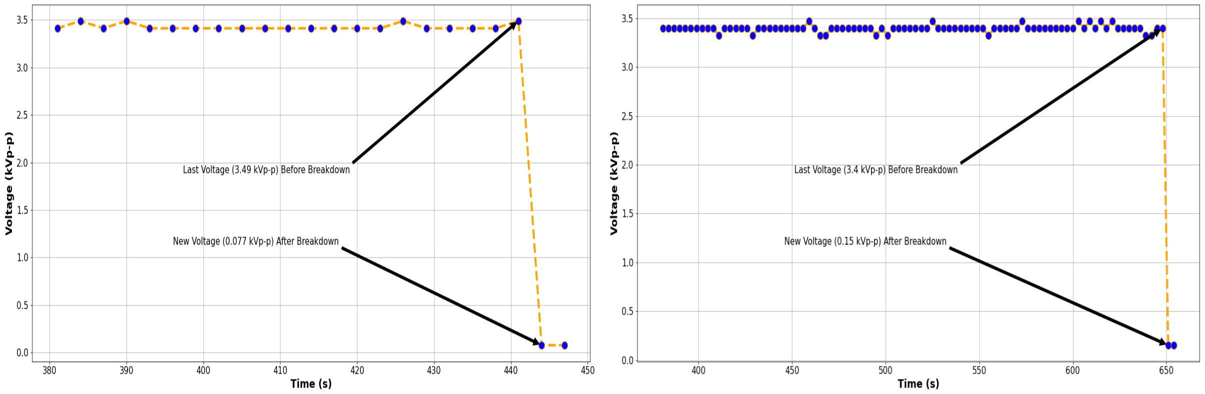

(a) Transients from Breakdown of Sample 3

(b) Transients from Breakdown of Sample 4

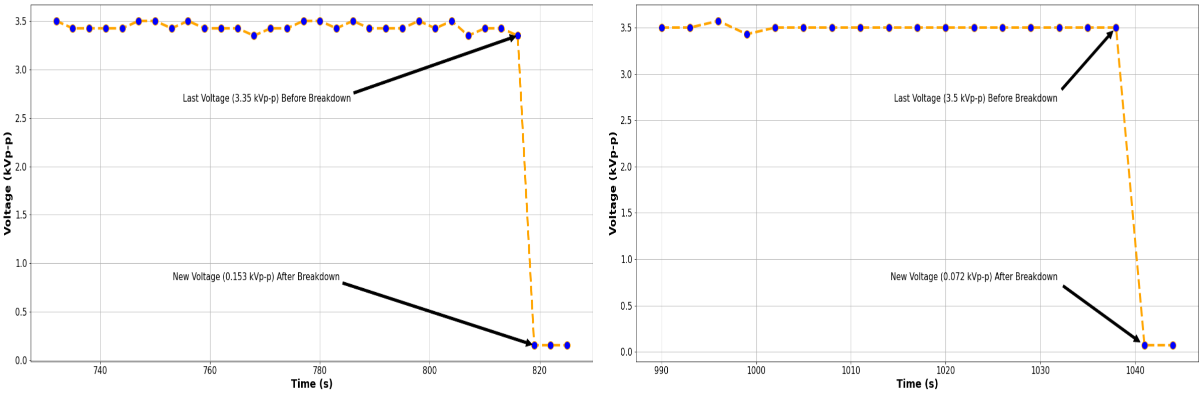

(a) Transients from Breakdown of Sample 5

(b) Transients from Breakdown of Sample 6

Figure 7.10: Comparison of the transient peaks during BD of 6 samples

Setup Based Defect Investigation

The next challenge was to investigate the if the breakdown was influenced by the defects in the setup. This means if there was any anomaly on the surface of the high voltage or ground electrode which would create a field enhancement and create premature breakdowns biasing the experiments. Also, it was investigated if there was any co-relation between the sequence of breakdowns in the different batches for different temperatures. Thus, all the sequences are taken and flattened into a 1-D array and then a two hypothesis is defined to check the randomness in the event.

The first step in the runs test is to count the number of runs in the data sequence. There are several ways to define runs, however, in all cases the formulation must produce a dichotomous sequence of values. In our case, the values above the median are treated as positive and values below the median as negative. A run is defined as a series of consecutive positive or negative values.

Applying Runs Test [97]:

☐ The first step in applying this test is to formulate the null and alternate hypothesis.

H_{null} : The sequence was produced in a random manner
H_{alt} : The sequence was not produced in a random manner

☐ Calculate the test statistic, Z as:

$$Z = \frac{R-R'}{s_R}$$

R = The number of observed runs

R′ = The number of expected runs, given as:

$$R' = \frac{2n_1n_2}{n_1+n_2} + 1$$

S_R = Standard Deviation of the number of runs [97]

$$s_R^2 = \frac{2n_1n_2(2n_1n_2-n_1-n_2)}{(n_1+n_2)^2(n_1+n_2-1)}$$

Where n_1 and n_2 are the number of positive and negative values in the series

☐ Compare the value of the calculated Z-statistic with Z_{critical} for a given level of confidence (Z critical $= 1.96$ for confidence level of 95%). The null hypothesis is rejected i.e. the numbers are declared not to be random, if $|Z| > Z_{\text{critical}}$.

Thus, if there is a substantial difference between R and $R^{'}$ then the Z statistic would be higher and would mean the numbers are not that random that is there is an effect of the electrode defect. The code was made in Python and the sequence was inserted, giving following output in Figure 7.11.

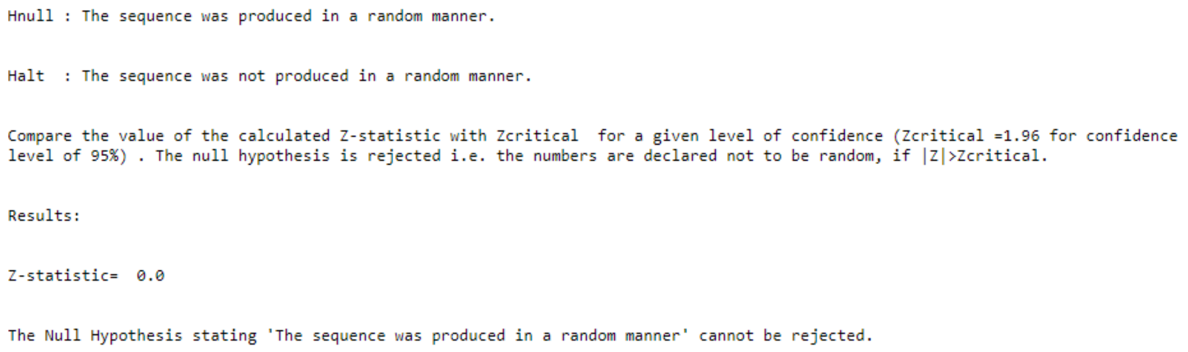

```
Hnull : The sequence was produced in a random manner.


Halt  : The sequence was not produced in a random manner.


Compare the value of the calculated Z-statistic with Zcritical  for a given level of confidence (Zcritical =1.96 for confidence
level of 95%) . The null hypothesis is rejected i.e. the numbers are declared not to be random, if |Z|>Zcritical.


Results:


Z-statistic=  0.0


The Null Hypothesis stating 'The sequence was produced in a random manner' cannot be rejected.
```

Figure 7.11: Test of Randomness for Sample Breakdown Sequence

Thus, a value of Z = 0 means, the null hypothesis cannot be rejected and that they may be produced in a random order. Thus, this verifies that there has been no added bias in experiment designing. Now, the long term tests have been carried out at different temperatures which has been discussed in the following subsections.

7.2. Pre-Treatment of Samples and Electrodes:

Sample Treatment:

For each set of temperatures, 12 samples are cut into equal rectangular pieces (6 are kept as buffer in case of unforeseen circumstances) and put in the respective temperatures of 45, 60 and 75 ^{o}C for 7 days to condition them and remove any extra moisture ingressed during cutting of cables. Also, the period is chosen such that it does not cause additional thermal aging to the already service aged insulation [98]. Thus, similar treatment would ensure the samples have similar very low percentage of moisture which otherwise would yield anomalous results in the breakdown tests. Before the long term tests are started the oven is maintained at that temperature and the samples are transferred there minimizing contact with air.

Electrode Treatment:

The oven is set to the specific temperature and the expansions for steel and epoxy occurs unevenly. Then they are instantly transferred to the polishing machine and machined at that temperature and put back into the oven. This ensures no protruding edges and a smooth surface. Also, the ground electrode is polished with fine sand paper for 5-7 mins to remove any carbonization from the previous tests.The temperature is allowed to set at the desired value and measured with the thermosensor. Then the samples are transferred and the tests are run.

Post Examination of Samples & Electrodes after Breakdown Test:

The samples and H.V. electrodes are examined very carefully after the tests to detect the point of contact. It is ensured that all the breakdowns take place inside the HV electrode and not at the very edge, which may indicate some form of field enhancement or breakdown due to partial discharge. Out of all the samples, majority of breakdowns take place inside the periphery of the H.V. electrode and a very few near the edges. But none of them broke down exactly on the edge, indicating no such anomalous field enhancements. Also, the puncture size obtained in each case is very fine due to the tripping of the safety boxes as soon as the current goes below the threshold.

7.3. Sample Calculation to Find Initial Estimates:

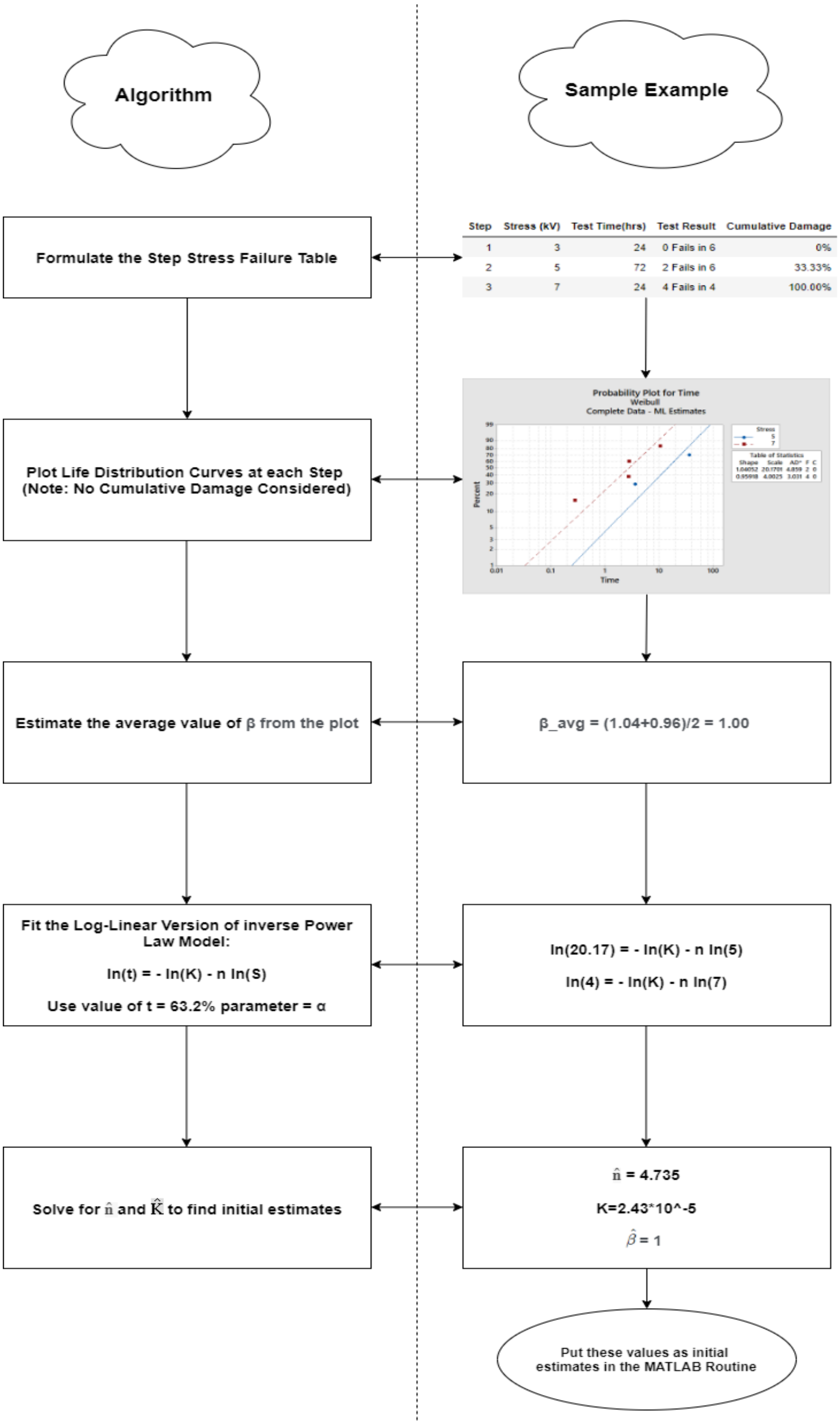

Step	Stress (kV)	Test Time(hrs)	Test Result	Cumulative Damage
1	3	24	0 Fails in 6	0%
2	5	72	2 Fails in 6	33.33%
3	7	24	4 Fails in 4	100.00%

Shape	Scale	AD*	F	C
1.04052	20.1701	4.859	2	0
0.95918	4.0025	3.031	4	0

The values for the 3 estimates are thus calculated using the algorithm above at each temperature with some approximations made, when we have just one sample breaking down at one step, since in that case it is not possible to have a Weibull Fit for one data point. In that case, the other steps are combined with values from literature to get a more accurate estimate. The values after substituting in MATLAB Code is evaluated in the next subsections.

7.3.1. Application of MLE with Weibull

POWER LIFE-STRESS WITH WEIBULL LIFE MODEL:

When a Weibull distribution describes the life at each accelerated stress level, the Weibull scale parameter α, which corresponds to 63.2% of life, may be chosen as the characteristic value for life in the power life-stress with the Weibull life distribution [99].

$$\alpha = L(S) = \frac{1}{KS^n} \tag{7.1}$$

where, α is the scale parameter, L(s) represents the time to breakdown for the insulation, K is the constant of proportionality in power law, S is the voltage stress and n is the power in power law.

Therefore, the conditional power life-stress with the Weibull distribution representing the time-to failure is given by[99]:

$$f(t,S) = \frac{\beta t^{\beta-1}}{\left(\frac{1}{KS^n}\right)^{\beta}} * e^{-\left(\frac{t}{\frac{1}{KS^n}}\right)^{\beta}} \tag{7.2}$$

$$= \beta KS^n \left(KS^n t\right)^{\beta-1} e^{-\left(KS^n t\right)^{\beta}} \tag{7.3}$$

where, β is the shape parameter from Weibull Distribution.
The expressions for mean and reliability functions derived from the model are[99]:

$$\mu = \frac{1}{KS^n}\Gamma\left(\frac{1}{\beta} + 1\right) \tag{7.4}$$

$$R(t,S) = e^{-\left(KS^n t\right)^{\beta}} \tag{7.5}$$

where, Γ represents the Gamma Function such that

$$\Gamma(n) = (n-1)!$$

Derived by Daniel Bernoulli, for complex numbers with a positive real part, the gamma function is defined by a convergent improper integral:

$$\Gamma(z) = \int_0^{\infty} x^{z-1} e^{-x} dx, \quad \Re(z) > 0$$

Note from above, β is positive by definition, then reliability increases as stress decreases. Also, the corresponding hazard rate function is

$$\lambda(t,S) = \frac{f(t,S)}{R(t,S)} = \beta KS^n \left(KS^n t\right)^{\beta-1} \tag{7.6}$$

The Power-Weibull log-likelihood function for complete and right censored data is[99]:

$$\Lambda = \sum_{i=1}^{N_c} n_i \cdot \ln\left[f\left(t_i, S_i; \beta, K, n\right)\right] + \sum_{j=1}^{N_r} n_j \cdot \ln\left[F\left(t_j, S_j; \beta, K, n\right)\right] \tag{7.7}$$

where, N_c is the number of samples which constitute the complete failure data set and N_r represents the right censored data which have been separately treated in two parts in the likelihood function.
When combined with the time to failure for complete data set as represented in Equation 7.3 and Reliability function in Equation 7.5 for right censored data, the likelihood function can be represented as follows:

$$\Lambda = \sum_{i=1}^{N_c} n_i \cdot \ln\left[\beta KS_i^n \left(KS_i^n t_i\right)^{\beta-1} e^{-\left(KS_i^n t_i\right)^{\beta}}\right] - \sum_{j=1}^{N_r} n_j \cdot \left(KS_j^n t_j\right)^{\beta} \tag{7.8}$$

The MLE solution for parameter estimates $\widetilde{\beta}$, $\widetilde{K}$, $\widetilde{n}$ will be obtained by solving for β, K, and n such that:

$$\frac{\partial \Lambda}{\partial \beta} = 0 \tag{7.9}$$

$$\frac{\partial \Lambda}{\partial K} = 0 \tag{7.10}$$

$$\frac{\partial \Lambda}{\partial n} = 0 \tag{7.11}$$

Putting in the expression from Equation 7.8, and differentiating with respect to the variables, the following equations are obtained[99]:

$$\frac{\partial \Lambda}{\partial \beta} = \frac{1}{\beta}\sum_{i=1}^{N_c} n_i + \sum_{i=1}^{N_c} n_i \ln\left(KS_i^n t_i\right) - \sum_{i=1}^{N_c} n_i \left(KS_i^n t_i\right)^{\beta} \ln\left(KS_i^n t_i\right) - \sum_{j=1}^{N_r} n_j \left(KS_j^n t_j\right)^{\beta} \ln\left(KS_j^n t_j\right) = 0 \tag{7.12}$$

$$\frac{\partial \Lambda}{\partial K} = \frac{\beta}{K}\sum_{i=1}^{N_c} n_i - \frac{\beta}{K}\sum_{i=1}^{N_c} n_i \left(KS_i^n t_i\right)^{\beta} - \frac{\beta}{K}\sum_{i=1}^{N_r} n_j \left(KS_j^n t_j\right)^{\beta} = 0 \tag{7.13}$$

$$\frac{\partial \Lambda}{\partial n} = \beta \sum_{i=1}^{N_c} n_i \ln\left(S_i\right) - \beta \sum_{i=1}^{N_c} n_i \cdot \ln\left(S_i\right)\left(KS_i^n t_i\right)^{\beta} - \beta \sum_{i=1}^{N_r} n_j \cdot \ln\left(S_j\right)\left(KS_j^n t_j\right)^{\beta} = 0 \tag{7.14}$$

From Equations 7.12, 7.13,7.14, we have three equations to solve for three unknowns. This procedure is coded in MATLAB and the derivatives are obtained from Wolfram[100].

7.3.2. Long Term Step Stress Breakdown Tests at 45^{o}C

The samples used have been pre-treated as mentioned earlier in section 7.1 and the same procedure is maintained at all temperatures so that the results are not biased by any external effects. The breakdown voltage determined at 45^{o}C from the Fast Ramped Breakdown Tests was 10.22 kV. Thus, the steps have been designed in such a way that the samples breakdown within 8 days and the rate of rise of voltage is not too steep. The following procedure is maintained for each temperature test:

- The oven is kept at the test temperature for 2 days before the test is started so that all the components including the ground and H.V. electrodes already reach the temperature.
- After each set of breakdown tests at that temperature, the ground and H.V. electrode is polished to remove any carbon present due to breakdown.
- Each broken sample is analyzed to check that the breakdowns happened within the area of the H.V. electrode and not due to some surface discharge bridging the 2 electrodes.In all cases, the breakdowns were observed to be scattered all around the electrode and a very few were near the edges. Also, it must be ensured that the HV Electrode is placed exactly at the centre of the sample. Putting the electrodes too close to the edge of the sample may trigger discharges, which have been observed while running preliminary dummy tests.
- For temperatures higher than 50^{o}C, proper protection gloves have to be used as a safety precaution while handling the samples at such elevated temperatures.

Design of the Steps:

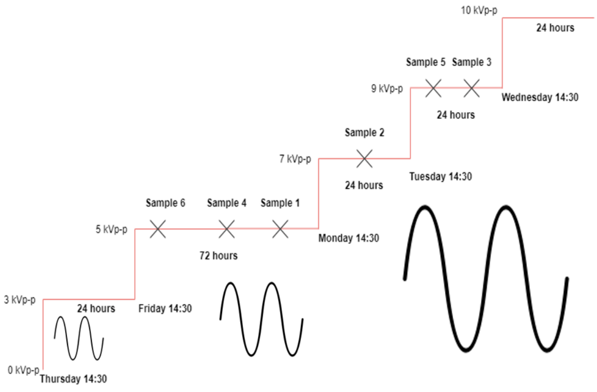

Figure 7.12: Steps Designed for 45^{o}C

The design of the step will be discussed for one temperature since similar methodology is used for other temperatures as well. The first step is set to be approximately 30% the breakdown voltage since it is expected that all the samples should survive the first step but at the same time it should accumulate damage in form of aging. Lower magnitude of steps will not cause any damage and higher values might lead to breakdown, so it will not be possible to understand if there was already some pre-existing fault in the sample.Thus, some additional experiments helped to verify that 30% of the BDV is very optimum for the first step and if any sample fails during this time, then it would be replaced and the test should be re-run. But this condition did not arise for any temperature. The next step is considerably the longer one representing the normal working condition of the cable, where the stress is almost constant for the majority of the lifetime. This step is 3 times the initial step time and it is expected that samples should start failing from now on wards. The cumulative damage from step 1 and 2 should be sufficient to breakdown a few. The ones which survive are now exposed to 1 kVp (2 kV$_{p-p}$) increment in voltage for the same time as step 1 and this step continues till we reach the breakdown voltage. The last step is kept more as a buffer since it is expected that all the samples should breakdown before the last step (which was the case for all temperatures). This is because the samples acquire cumulative damage that actually causes breakdown at lower magnitudes than constant magnitude voltage stress tests. So, for this temperature since BDV was 10.22 kV$_{p-p}$, the last designed step is 10 kV$_{p-p}$. As expected, all 6 samples failed before the last step as observed in Figure 7.12.

The sinusoids in Fig 6.5 represents that we are applying sinusoidal constant voltage steps for the defined time and not D.C. voltages since we are dealing with AC Cables for the research. The Breakdown under D.C. and A.C. stress is quite different and we can expect different physics to happen thereby causing different breakdown time.

Test Results for 45^{o}C:

The test has been carried out at 45^{o}C for 6 OIP samples. From Table 7.1, it can be observed that 5 steps have been used for the test varying from 3 kV$_{p-p}$ to 10 kV$_{p-p}$. The time for all the steps are 24 hours except for the longer 2nd step for 72 hours. For this temperature it was observed that no samples failed in Step 1, which is designed in such a way. 3 samples failed in step 2 due to the accumulated damage, with 1 failing in the next step and finally the last 2 failed in the second last step at 9 kV giving a good scatter to obtain the statistics.

Step Number	Stress Level (Vp-p)	Test Time (Hrs)	Failure Data
1	3000	24	0 in 6 Failed
2	5000	72	3 in 6 Failed
3	7000	24	1 in 3 Failed
4	9000	24	2 in 2 Failed
5	10000	24	0 in 0 Failed

Table 7.1: Long Term Test Failure Data at 45^{o}C

The time to failure at each voltage is calculated after importing the MATLAB files from the PXI and carefully analyzed. These values are then fed into the code prepared for Maximum Likelihood Estimation applied to Weibull Distribution for Inverse Power Law Life Characteristics. The initial estimates are decided as discussed in the previous subsection and arrived to beta = 2.5, K-parameter = 1*10^{-13} and n-parameter = 15. The initial estimates on first glance seems quite within the range as mentioned in literature for long term constant stress tests. Now, the initial estimates alter due to the different iterations and finally converge to the values as obtained in Table 7.2 and their variation from the initial estimates are graphically plotted in Figures 7.13(a),(b) and 7.14(a).It can be observed that there is not much difference from the initial estimates from which it can be inferred that we are optimizing in the Global Minima for the MLE. Also, the obtained value for n and beta looks reliable according to studies done in past using constant stress tests. An example computation has been demonstrated in Figure 7.14(b), where first few iterations has been shown. Basically, the most important parameter is the trust region radius. With each iteration it is observed that the radius gradually reduces and in the i^{th} iteration when it is less than a specific epsilon, the loop is terminated and the most optimal solution is printed. It should be noted that the most optimal solution may not exactly lead to the function to 0 (roots) but may be very close to it.

Beta-Parameter	K-Parameter	n-Parameter
1.543	6.8E-12	13.6062

Table 7.2: MLE Parameters at 45^{o}C

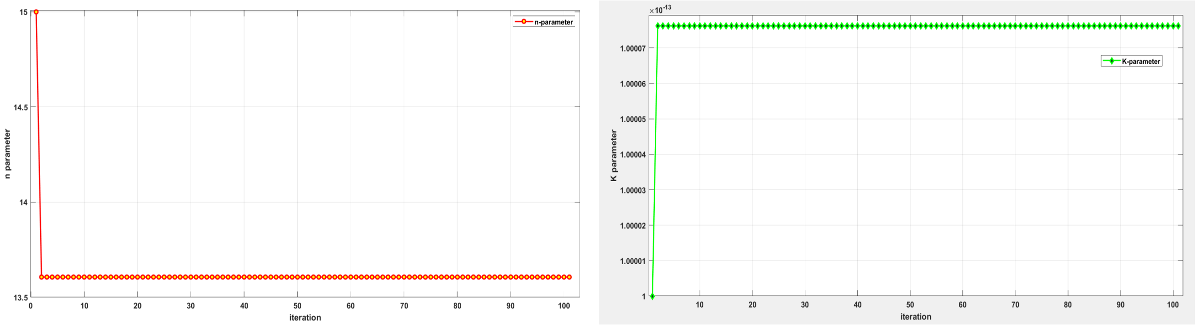

(a) Variation of n parameter

(b) Variation of K parameter

Figure 7.13: Iteration of MLE Parameters n and K at 45^{o}C

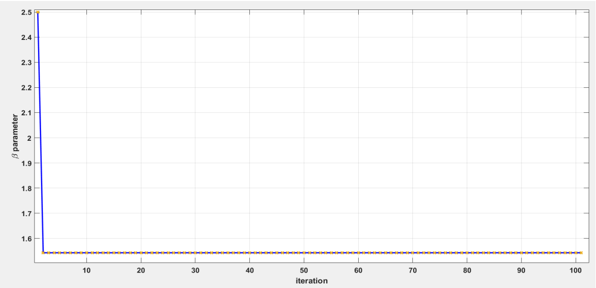

(a) Variation of β parameter

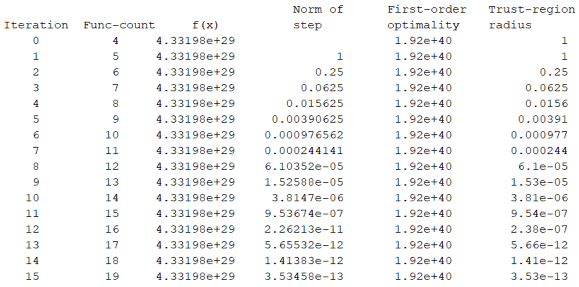

```
                                           Norm of      First-order   Trust-region
Iteration  Func-count     f(x)             step         optimality    radius
    0           4     4.33198e+29                        1.92e+40              1
    1           5     4.33198e+29               1        1.92e+40              1
    2           6     4.33198e+29            0.25        1.92e+40           0.25
    3           7     4.33198e+29          0.0625        1.92e+40         0.0625
    4           8     4.33198e+29        0.015625        1.92e+40         0.0156
    5           9     4.33198e+29      0.00390625        1.92e+40        0.00391
    6          10     4.33198e+29     0.000976562        1.92e+40       0.000977
    7          11     4.33198e+29     0.000244141        1.92e+40       0.000244
    8          12     4.33198e+29     6.10352e-05        1.92e+40        6.1e-05
    9          13     4.33198e+29     1.52588e-05        1.92e+40       1.53e-05
   10          14     4.33198e+29      3.8147e-06        1.92e+40       3.81e-06
   11          15     4.33198e+29     9.53674e-07        1.92e+40       9.54e-07
   12          16     4.33198e+29     2.26213e-11        1.92e+40       2.38e-07
   13          17     4.33198e+29     5.65532e-12        1.92e+40       5.66e-12
   14          18     4.33198e+29     1.41383e-12        1.92e+40       1.41e-12
   15          19     4.33198e+29     3.53458e-13        1.92e+40       3.53e-13
```

(b) Sample Computation for convergence

Figure 7.14: Iteration of MLE Parameter β and the backend computation process

Test Results for 60^{o}C:

The test has been carried out at 60^{o} for 6 OIP samples similarly. The same methodology has been used to design the steps. From the fast ramp stress tests, it is observed that the BDV at 60^{o}C is 9.24 kV. The time for each step is exactly similar as before, except in this case the maximum designed last step is 9 kV as shown in Figure 7.15(a). The failure data has been reported in Table 7.3. As discussed previously, there were no failures in the first step. But due to cumulative damage, there were 2 failures in step 2 and in the third step of 7 kV, all the remaining 4 samples failed. Thus, the scatter in the breakdown data is much smaller in this case compared to the latter.

Step Number	Stress Level (V_{p-p})	Test Time (Hrs)	Failure Data
1	3000	24	0 in 6 Failed
2	5000	72	2 in 6 Failed
3	7000	24	4 in 4 Failed
4	9000	24	0 in 0 Failed

Table 7.3: Long Term Test Failure Data at 60^{o}C

The time to failure are again fed in the MATLAB code with the initial estimates calculated from each damage steps which were obtained to be beta = 8, K-parameter = $1*10^{-11}$ & n-parameter = 10. Due to the low scatter, the initial estimate of beta was a still off, but surprisingly, the MLE Code converges to the accurate value of beta. The rest parameters seem quite a sensible guess and the obtained values have been reported in the Table 7.4. The change in all the parameters with increase in iteration is observed in Figures 7.15(b),7.16(a) and 7.16(b). The values obtained again, seem to be quite feasible when compared with the literature of constant stresses. A detailed comparison would be made at the end of the section to quantify the change in parameters with temperature.

Beta-Parameter	K-Parameter	n-Parameter
1.4665	6.18E-10	10.8074

Table 7.4: MLE Parameters at 60^{o}C

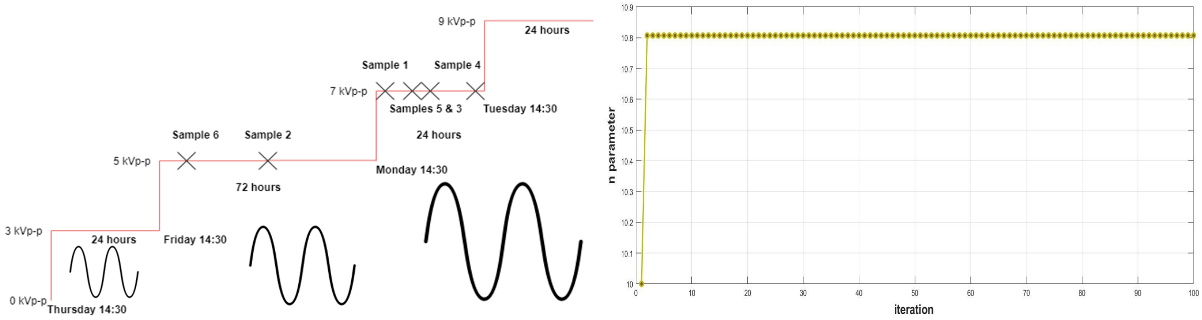

(a) Designed Steps for 60^{o}C

(b) Variation of n parameter

Figure 7.15: Design of steps and obtaining the MLE Parameter n

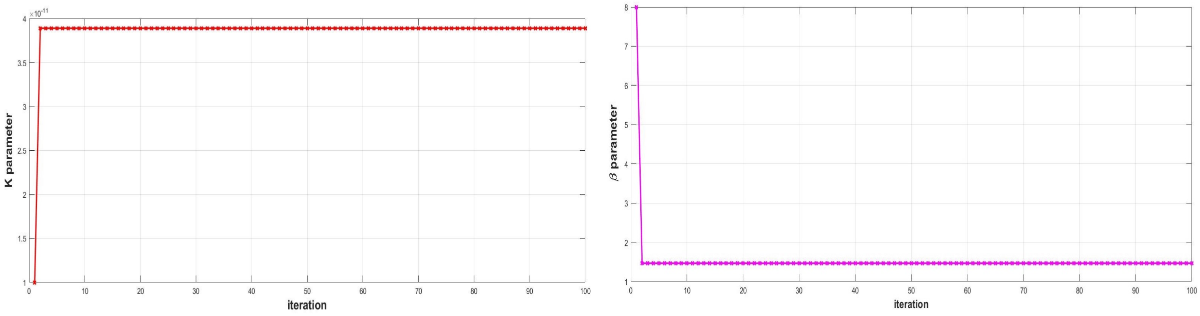

(a) Variation of K parameter

(b) Variation of β parameter

Figure 7.16: Iteration of MLE Parameters K and β

Test Results for 75^{o}C:

The test has been carried out at 75^o for 6 OIP samples similarly on the similarly pre-treated samples with same treatment to the electrodes as discussed for 60^o.

Application of Different Step Lengths:

A different methodology has been used now to investigate the effect of step size on breakdown values. So for this temperature both the previously designed step and the new step sizes are used to validate the effect. As seen in Figure 7.17(a), the new step heights are now smaller with finer adjustment in increment from:

3 kV->5kV->6kV->7kV->8kV->8.5kV

The Breakdown data has been represented in Table 7.5 and as it can be observed, for finer steps, the scatter is a bit more than the previous cases. This is because the cumulative damage is lower in each step than longer steps and thus, the breakdown data is accordingly varied. The time for each step is kept fixed nonetheless with second step being the largest for 72 hours and the rest at 24 hours. There are 3 failures in step 2, with 1 failure each in Steps 3,4 & 5.

Step Number	Stress Level (V$_{p-p}$)	Test Time (Hrs)	Failure Data
1	3000	24	0 in 6 Failed
2	5000	72	3 in 6 Failed
3	6000	24	1 in 3 Failed
4	7000	24	1 in 2 Failed
5	8000	24	1 in 1 Failed
6	8500	24	0 in 0 Failed

Table 7.5: Long Term Test Failure Data at 75^{o}C

The maximum voltage level is set to 8.5 kV$_{p-p}$ since the B.D.V obtained during the Fast Ramped Test is 8.89 kV$_{p-p}$. The initial estimate from the mathematical calculations bring us to the following values of beta = 1.5, K-parameter = 1*10^{-11} & n-parameter = 8, which are again quite calculated initial guesses in accordance to literature. The final estimates obtained from MATLAB is seen in Table 7.6 and the convergence is demonstrated in Figures 7.17(b), 7.18(a) and 7.18(b).

Beta-Parameter	K-Parameter	n-Parameter
1.5014	6.27E-8	7.3815

Table 7.6: MLE Parameters at 75^{o}C

Conclusions from Different Steps:

It is observed that the parameters obtained from the different steps (2 types) are very similar and thus, the average value for all the parameters have been recorded in Figure 7.21. The difference between these values and the different step values is less than 1.5% for each parameter.Thus, the method is not sensitive to step changes and thus, does not add bias to the estimates. The next subsection now compares the change in parameters to investigate if temperature has any significant effect on lifetime.

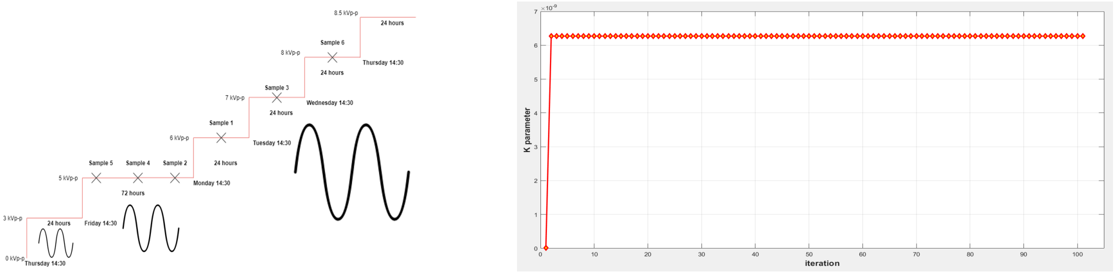

(a) Designed steps for 75^{o}C

(b) Variation of K parameter with iteration

Figure 7.17: Designed steps for 75^{o}C and corresponding K variation from MLE

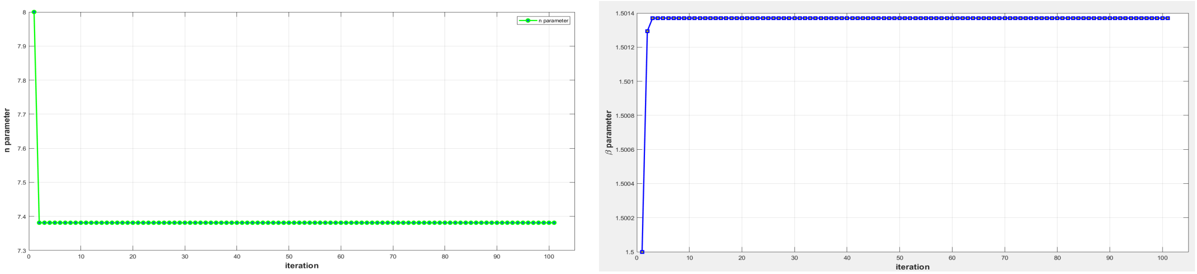

(a) Variation of n parameter with iteration

(b) Variation of □parameter with iteration

Figure 7.18: Variation of n and β parameters with iteration

7.3.3. Comparison of Aging Model Parameters for 45^o, 60^o and 75^{o}C

From the comparative analysis of the breakdown tests, the following observations can be drawn:

- The beta parameter remains almost constant for all the temperatures with an average value of 1.504 [98]. This indicates we are comparing samples with similar failure rate behaviours at different temperatures. Different values of beta would mean there may be another process initiated, other than the one under study. So, beta should remain constant if a process is not altered but being accelerated.
- The value of n as observed in Fig 7.19(a) shows a non-linear downward trend [98]. The reason for the non-linearity is due to the difference in the breakdown voltage indirectly affecting the power law model as discussed with chemical equations later in Section 7.3.
- The rate of change of K, the constant in the power law equation, $L(S) = \frac{1}{KS^n}$ varies more rapidly with a monotonic increase as seen in Fig 7.19(b) where the y axis is in logarithmic scale[98],[101].
- Since the temperature is changed, α=$\frac{1}{KS^n}$ also changes. α is observed to decrease with increase in temperature, which is justified as lifetime should reduce with thermal degradation.

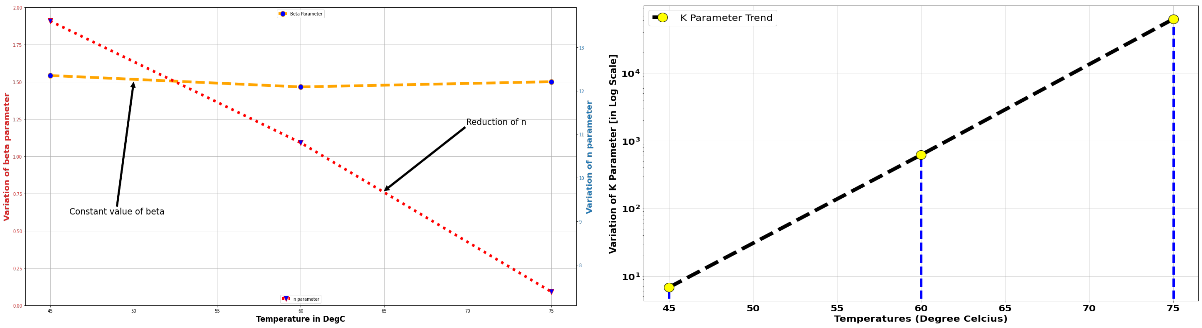

(a) Variation of n and β parameters with temperature (b) Variation of log K parameter with temperature

Figure 7.19: Variation of MLE Parameters with increase in Temperature

The values have been obtained for 3 temperatures from the laboratory experiments. It can be extended, for different temperature ranges as well according to the field measurements. Thus, for each temperature, we can find a duplet of n, beta parameter (though it does not change) from Fig 7.20(a) and a duplet of K & n from Fig 7.20(b) which would enable us to define the Power Law for each temperature set.The contours have been generated using MINITAB software where we have 2 regressors and 1 prediction variable, which is the temperature. A model would be developed end of this chapter and validated for a temperature different to the 3 used in the experiments.

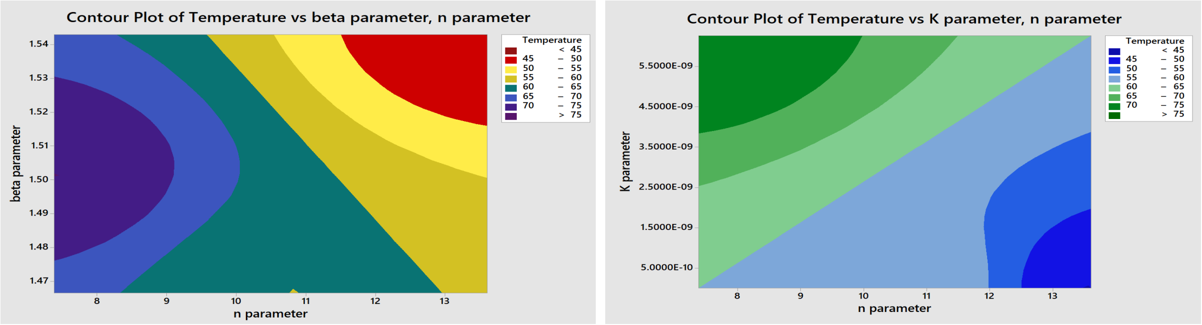

(a) Contour plot of n vs β parameter with Temperature (b) Contour plot of n vs K parameter with Temperature

Figure 7.20: Variation of the MLE estimated parameters with Temperature

7.4. Possible Reasons for Non-Linearity in BDV with Temperature

7.4.1. Oxidation of Cellulose at Elevated Temperatures:

The typical raw material for paper insulation in cables is electrical grade softwood Kraft pulp consisting of approximately 85% cellulose, 10% hemicelluloses, and 5% residual lignin [102]. It is good for impregnation, and is easy to be moulded, and wrapped around a conductor. The paper is constituted mostly by cellulose fibres whose structure can be observed in Fig 7.21 [103].

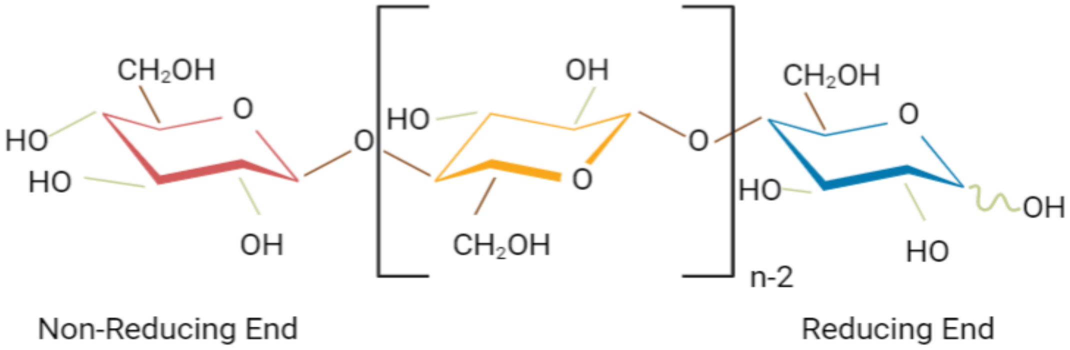

Figure 7.21: Chained Structure of Cellulose

A critical requirement of insulator paper pulps is a very low content of main and transition metal ions to assure low conductivity, i.e., good insulation properties, as well as satisfying aging performance under elevated temperatures. Transition metal ions are more critical than main group metal ions, because they are known to trigger oxidative cellulose degradation by catalyzing the formation of hydroxyl radicals, other reactive oxygen species and hydroxyl anions in the presence of oxygen and water. Even though engineers do their utmost to exclude water, oxygen, and metal ions from the system, these elements will always be present in traces ready to start the vicious circle of paper degradation. Also, the oil used for impregnation is susceptible to various degradation factors that can influence its dielectric strength. The most significant ones are:

- Oxidation
- Moisture
- Dissolved Gases

Due to temperature, it is possible to get rid of moisture as a result of pre-treatment and also since we are carrying out the experiments in minimum oil situation, the amount of dissolved gas would be really low. But, due to temperature, the biggest threat is oxidation, which indirectly impacts the breakdown voltage due to chemical changes. Oxidation of cellulose causes introduction of carbonyl groups (keto groups: C2, C3, aldehyde function: C6) and carboxyl groups (C6) [104] along the cellulose chain which can be traced very well throughout paper ageing experiments by means of Fourier transformed infrared spectroscopy and ultraviolet-visible spectroscopy[105]. The keto groups entail decreased thermal stability because they render the structure more prone to aldol-type condensation reactions. Most importantly, they introduce a pronounced instability towards alkali (hydroxyl anions) and constitute “hot spots” along the cellulose chain where cleavage is to occur. Small amounts of such oxidized groups are found well distributed over the cellulose polymer introduced by pulping processes or due to thermally induced partial dehydration.

The first step of an alkali-induced degradation is the nucleophile attack of the hydroxide ion (OH^-) at the carbonyl carbon (low electron density) initiating β-alkoxy elimination, which causes cleavage of the cellulose backbone already at low alkalinity (pH 9 and above) and promoted by increased temperature as observed in Fig 7.22.

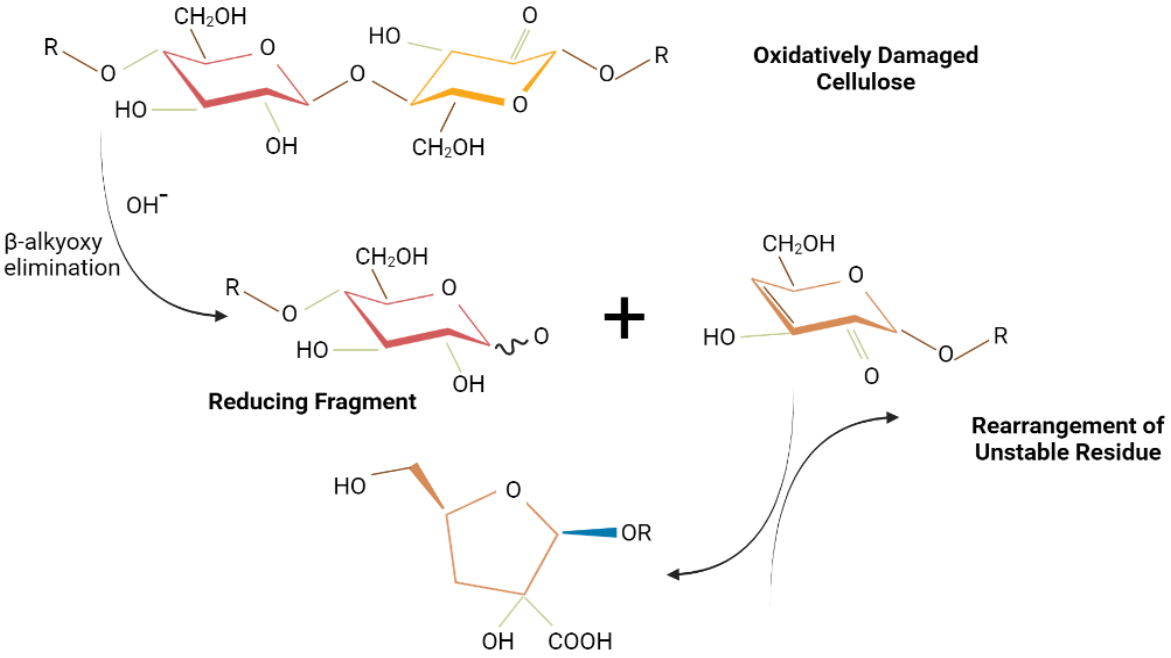

Figure 7.22: Cleavage of Cellulose at High Temperatures

This alkali induced degradation paves the way for subsequent acid-catalyzed hydrolysis of cellulose [**?**]. This reaction, which would cause only "normal" chain shortening by hydrolytic cleavage of a glycosidic bond, can cause production of additional acids under thermal conditions and thus become an auto catalytic process, observed in Figure 7.23.

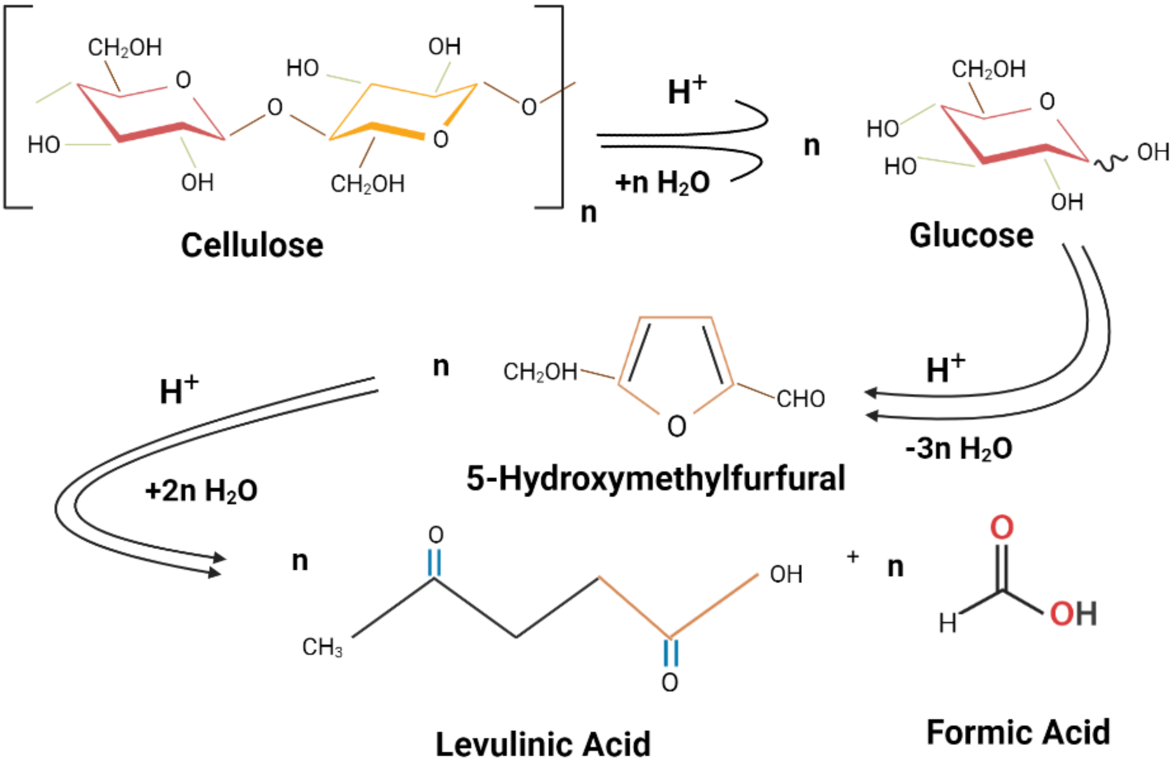

Figure 7.23: Acid Catalyzed Hydrolysis of Cellulose

To summarize, due to present of small amounts of OH^- ions, alkali induced degradation starts leading to oxidatively damaged cellulose to be reduced to an unstable residue. The rate of the reaction is highly temperature dependent which determines the oxidative state of the cellulose. Thus, with proportional increase in temperature, there is no proportional degradation in the chemical properties. Infact, there are complex organic reactions determining the oxidation of cellulose, which in turn affects the breakdown strength of the paper insulation. Also, this alkali promoted oxidative process might trigger acid catalyzed hydrolysis of cellulose which can lead to even more stochastic behaviour in breakdown due to temperature. Thus, proportional temperature increment does not guarantee proportional reduction in breakdown voltage, owing to the chemical reactions taking place inside the OIP insulation

In contrast to alkali-promoted oxidative degradation (β-alkoxy elimination), acid-catalyzed hydrolysis is not suppressed by its own degradation products. On the contrary, in the presence of water and within the normal working temperature range of the High Pressure Gas Cable, the carboxylic acids eventually formed by cellulose hydrolysis will further accelerate chain scission, rendering the process autocatalytic. The formation of Levulinic acid and Formic acid within working temperature (<75^{o}C) greatly affects breakdown strength [106].

7.4.2. Effect of Cellulose Chain Movements with Elevated Temperature:

Studies have proved a strong correlation between elevated temperatures and movement in the cellulose chain. The more intense the chain movement in insulation paper cellulose, the worse its mechanical performance, which leads to a poor thermal stability. The intensity of the chain movement can be analyzed by the mean square displacement (MSD). The MSD describes the overall movement of the molecular chain centroid, and can be calculated as [107]:

$$\mathrm{MSD} = \left\langle \left| \vec{r}_i(t) - \vec{r}_i(0) \right|^2 \right\rangle$$

where $\vec{r}_i(t)$ and $\vec{r}_i(0)$ represent molecular or atomic position vectors at time t and initial time i, respectively, and <> represents the ensemble average. Thus, The chain movement is the direct embodiment of the thermal movement ability of the insulation paper cellulose chain. The more intense the chain movement is, the worse the mechanical performance will be, which leads to a poor thermal stability as seen in Figure 7.24.

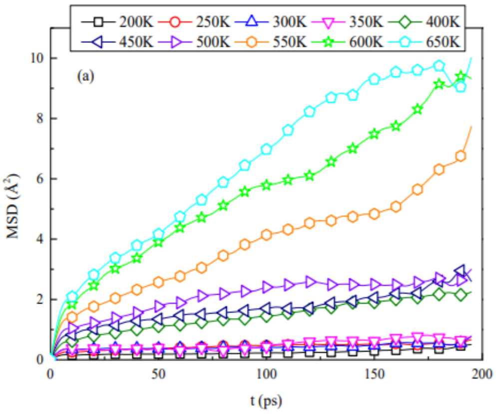

Figure 7.24: Effect of Chain Movements with Increase in Temperature

7.4.3. Effect on Degree of Polymerization with Elevated Temperature:

For new oil-impregnated paper insulation, the Degree of Polymerization value is between 1000 and 1200. The cable sample used in this research has been in service for 44 years thereby receiving high electro-thermal stresses. Continuous exposure of the insulation to the temperature, causes the cellulose chains breaking, and that results in the decrease of the DP level. The rate of the DP decrease is temperature dependent as described by the Arrhenius law and further, is proportional to the square of the DP value:

$$\frac{dDP(t)}{dt} = -k(t)\,[DP\,(t_0)]^2$$

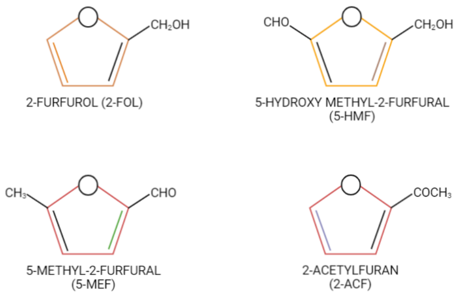

Figure 7.25: Degree of Polymerization with Temperature

Where: $k(t)$ is the Arrhenius reaction rate, $DP(t)$ is the DP value at time (t). Therefore, the mean value of the DP in the paper after time t will become [108]:

$$DP(t) = \frac{DP\,(t_0)}{1 + DP\,(t_0)\int_{t_0}^{t} k(t)dt}$$

The degradation of the cellulose chains brings the presence of water, acids and gases in the oil. Moreover the furanic compounds as shown in Fig 7.25 and alcohols can be found as the byproducts of the decomposition[109]. These byproducts increase the conductivity and the dissipation factor (or tanδ) of the insulation, what finally increases the level of thermal aging[110].

7.4.4. Gases from Cellulose Degradation at Elevated Temperatures

Thermal degradation in form of heat is detrimental to the cellulose and the heat can break glycosidic bonds and opens the glucose rings. Thus, cleavage takes place between two consecutive structures and leads to the generation of water, carbon monoxide, carbon dioxide and traces of other gases[111]. This breakage basically weakens the paper along with the dissolved gases leading to weak spots and breakdown occurs as seen in Figure 7.26.

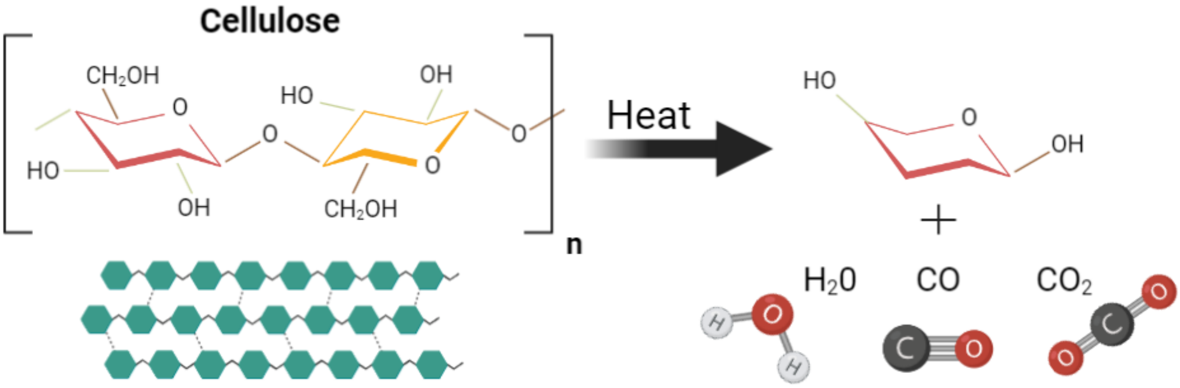

Figure 7.26: Evolution of Gases from Cellulose Degradation at High Temperature

Thus, oxidation of cellulose, rapid chain movements, reduction in the degree of polymerization (DP) together with the cellulose reduction and emission of byproduct gases cumulatively contribute in weakening the spots. Also, sometimes, there are some intrinsic voids present during the manufacturing processes and due to elevated temperatures, they become weaker and breakdown may also take place there.

7.5. Verification of MLE Estimates with Least Squares Estimation

The power law is expressed as $L(s) = \frac{1}{KS^n}$, sometimes $\frac{1}{K}$ is also expressed as D_{tot} and thus, the empirical formula can be re-written as[112]:

$$D_{tot} = L(s).S^n \tag{7.15}$$

where, p is the power and D_{tot} is the damage or aging dose. The dimension of D_{tot} is time multiplied by the stress dimension to a power p. So, a dimensionless expression of relative aging dose $D_{\%}$ is introduced given as[112]:

$$\frac{L(s).S^n}{D_{tot}} = D_{\%} = 1 \tag{7.16}$$

This expresses that when the aging time t of the asset reaches its lifetime L(s), the relative aging dose $D_{\%}$ becomes 1 and the asset fails. If the aging history period θ is sum of k periods θ_j with load S_j, where j=1,2,......,k, then $D_{\%}$ is written as[112]:

$$\frac{\sum_{j=1}^{k} \theta_j \cdot \left(S_j\right)^n}{D_{tot}} = D_{\%}\left((\theta_1 S_1), \dots, (\theta_k, S_k)\right) \leq 1 \tag{7.17}$$

In integral form the relative ageing dose of an asset with varying stress and ageing history time $\theta \leq L(s)$ is written as:

$$\frac{\int_0^{\theta} (S(t))^n dt}{D_{tot}} = D_{\%}(\theta; S(t)) \leq 1$$

Again, it should be noted that the asset fails at $D_{\%} = 1$ (or 100% relative damage dose) in the power law model and that $D_{\%}(\theta)$ strongly depends on the stress profile $S(t)$.

The power law is often used to translate the lifetimes τ_i from one stress level to another. If two stress levels S_1 and S_2 are considered and the power law is assumed to apply, then Equation 7.15 with constant D_{tot} links lifetimes and stresses[112]:

$$L(s)_1 \cdot {S_1}^n = D_{tot} = L(s)_2 \cdot {S_2}^n \tag{7.18}$$

This can be rewritten as:

$$L(s)_1 = L(s)_2 \cdot \left(\frac{S_2}{S_1}\right)^n \tag{7.19}$$

Using Equations 7.17 and 7.19, the equivalent time for each failure in a step stress test can be evaluated and brought back to a constant stress value with an equivalent time at that stress. The equivalent time is given by[112]:

$$\theta_{eq} = \frac{\sum_{j=0}^{k} \theta_j \cdot \left(B_j\right)^n}{\left(B_0\right)^n} \tag{7.20}$$

where, θ_j from j= 0 to (k-1) is the time in each step that the sample survived. When j = k, it represents the step when it failed and thus only the survival time is considered. B_0 is the base constant step stress in which the equivalent time is converted.

For this research, each sample failure time is converted into a base stress level and the equivalent time are calculated. Then, least squares algorithm is used as explained in [112].

The Least Squares Method would be shown in details for T=60^{o}C, where all the samples are converted from the step regime as shown in Figure 7.19(a) into a constant voltage of 3kV$_{p-p}$. Now in Equation 7.20, the value of n is varied from 6 to 12, to obtain the equivalent breakdown times at 3kV$_{p-p}$ as shown in Figure 7.28.

Example Calculation: For n=6 corresponding to the steps for 60^{o}C long term test (Fig 7.27), the equivalent breakdown times for each samples have been calculated at 3kV$_{p-p}$:

1) For Sample 1:
$32*(5/3)^6 + 24 = 710$ s
2) For Sample 2:
$36.12*(5/3)^6 + 24 = 798$ s
3) For Sample 3:
$0.278*(7/3)^6 + 72*(5/3)^6 + 24 = 1612$ s
4) For Sample 4:
$2.71*(7/3)^6 + 72*(5/3)^6 + 24 = 2005$ s
5) For Sample 5:
$2.97*(7/3)^6 + 72*(5/3)^6 + 24 = 2046$ s
6) For Sample 6:
$10.54*(7/3)^6 + 72*(5/3)^6 + 24 = 3268$ s

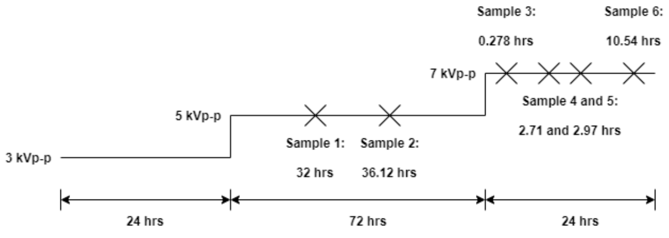

Figure 7.27: Long Term Step Stress Test at T=60^{o}C

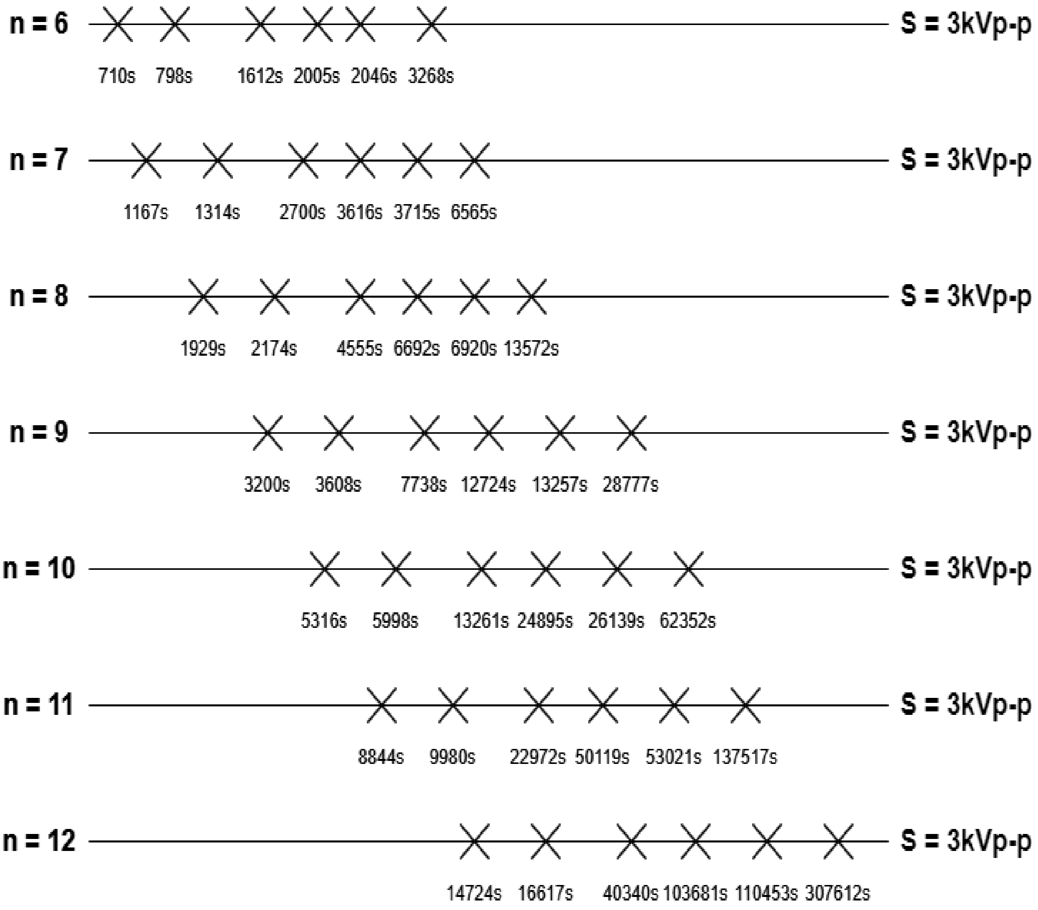

Figure 7.28: Variation of Breakdown Times converted to Constant Stress with different n

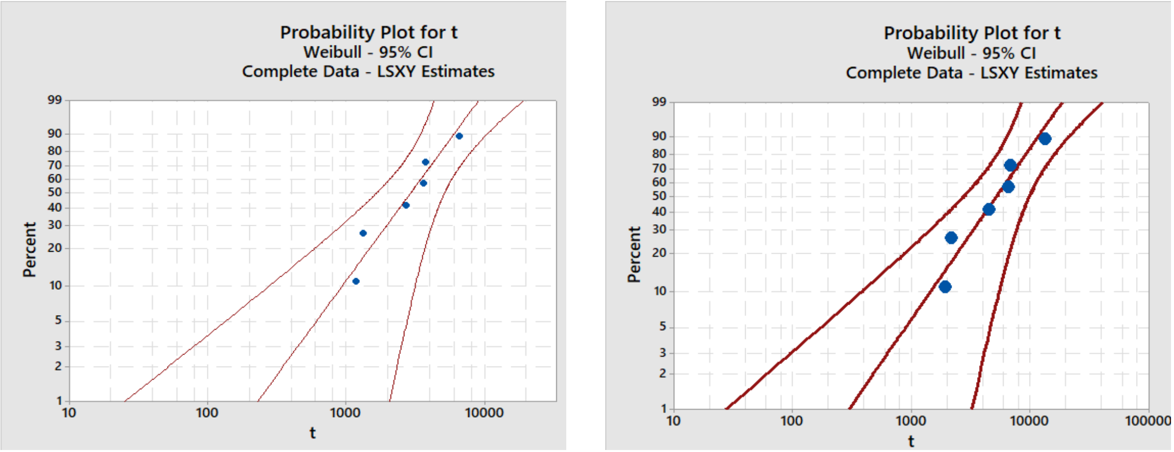

(a) n = 7, 2-parameter Weibull Fit

(b) n = 8, 2-parameter Weibull Fit

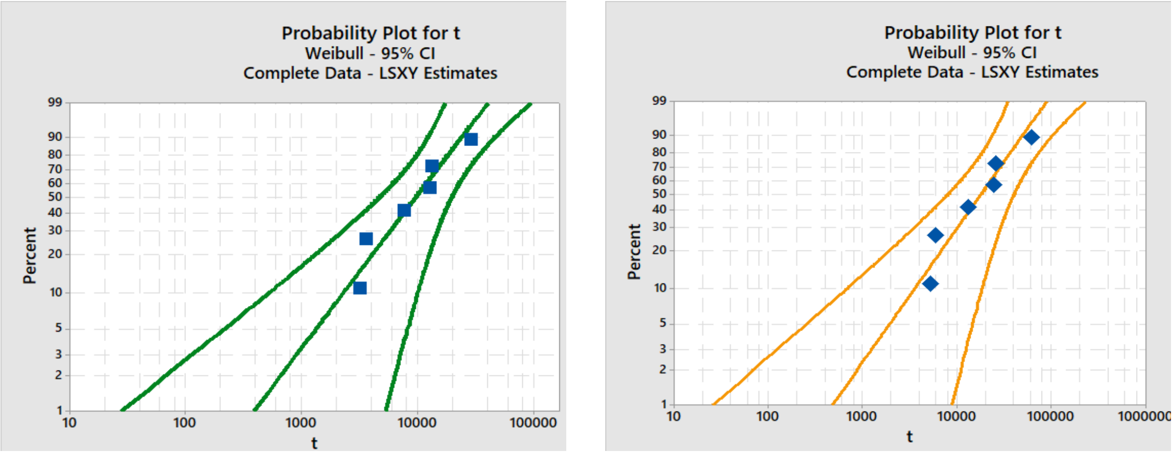

(c) n = 9, 2-parameter Weibull Fit

(d) n = 10, 2-parameter Weibull Fit

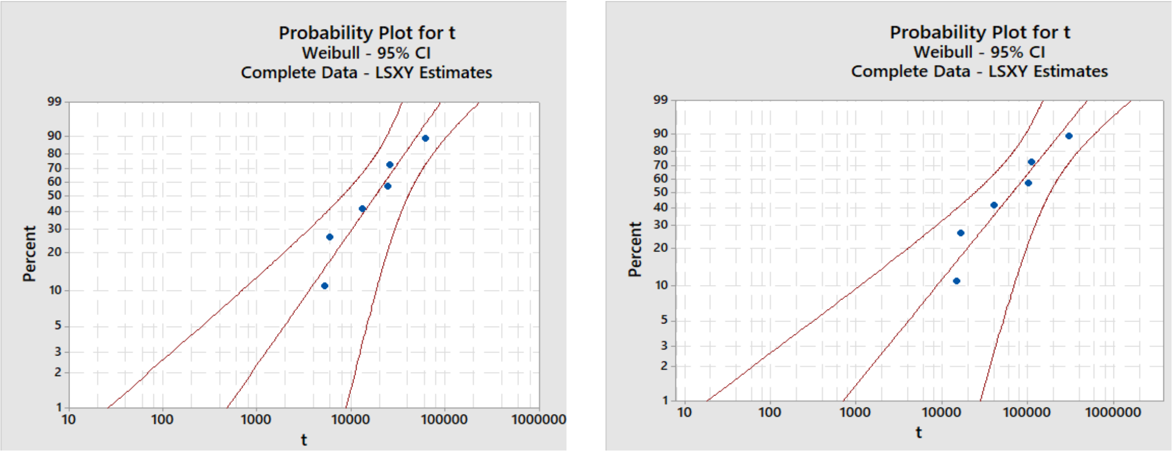

(e) n = 11, 2-parameter Weibull Fit

(f) n = 12, 2-parameter Weibull Fit

Figure 7.29: Variation of n-parameter to find best fitting Power Law Model

The 2-parameter Weibull Fit using Least Squares visually show how good the fit is for the range of n as shown in Figure 7.29. The statistics for each fit has been represented in Table 7.7.

Power n	α	β	AD Coefficient	Correlation Coefficient
7	1985	1.86	2.105	0.96
8	3611.77	1.66	2.109	0.961
9	6711.48	1.48	2.121	0.96
10	12732	1.32	2.134	0.958
11	24643	1.17	2.144	0.956
12	97668	0.94	2.151	0.952

Table 7.7: Goodness of fit for LS with variation in n

Lower is the AD Coefficient and higher is the Correlation Coefficient, better is the fitting of the data in the distribution. But, for a wide range of n it is seen that the coefficients are already much better and do not vary much.

It can be observed that as n increases, α increases and β reduces. This is because from the power law, inverse of n is the power and for lower temperatures, the value of n was higher. This means, for a fixed field stress, it will take longer to breakdown and thus, the value of alpha increases and the line becomes flatter, reducing beta.

α	β
0.8	-0.999

Table 7.8: Correlation of n with α and β

Table 7.8 clearly indicates a strong positive correlation of n with α and a perfect negative correlation with β [113]. Analyzing the α and β value with ML would give an indication how close the estimates are from both methods. From MLE, at 60^{o}C step stress test, the β was 1.46, n was 10.807 and K-parameter was 6.18*10^{-10}.

Thus, from $\alpha = L(s) = \frac{1}{KS^n}$, which gives α = 11292 s. From Table 7.7, for LS at n = 10, the value of α is 12732 sec which is very close. This indicates the value of n is slightly lower than 10.8 obtained from MLE but close to 10.

Also, from the Least Squares, we see that for n=10, the value of alpha and beta are very close with a Standard Deviation of less than 10% for all the variables. Also in LS, for n = 10, the AD and Correlation Coefficients are very optimal.

So, it can be verified that the values obtained from both LS and MLE are very close to each other and thus there is a very minute bias between the two methods, of 10.8/10 = 1.08, which is negligible. For other temperatures, the variable variation were less than 10% and exact similar method was used for the calculation. Therefore the values obtained from the MLE MATLAB code have been verified with LS Method.

7.6. Model Determining Power Law Parameters at All Temperatures:

7.6.1. Determining the n-parameter:

The variation of n parameter as observed before varies non linearly, thus a code has been created to fit the best polynomial so as to minimize the error residues. The observed parameters are reported as a perfect R-squared value = 1 and SSE = 2.288*10^{-29}. After substituting the coefficients, the dependence of n on T is obtained as:

$$n = 18.24 - 0.04026T - 0.001394T^2 \tag{7.21}$$

The parabolic curve fitting can be observed in Figure 7.30:

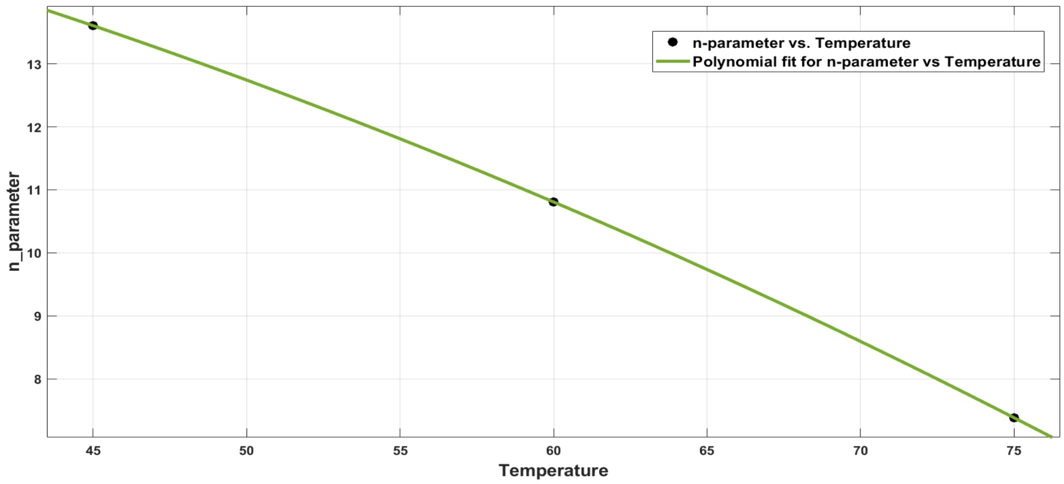

Figure 7.30: Variation of n-parameter Vs Temperature Model

7.6.2. Determining the K-parameter:

It is observed that an exponential function fits the points with minimum error and maximum goodness of fit. The observed parameters are reported as a perfect R-squared value = 1 and very low SSE.The dependence of log K on T (in ^{o}C) is demonstrated by the following mathematical formula:

$$\log K = 0.3043T - 39.43 \tag{7.22}$$

The linear curve fitting can be observed in Figure 7.31:

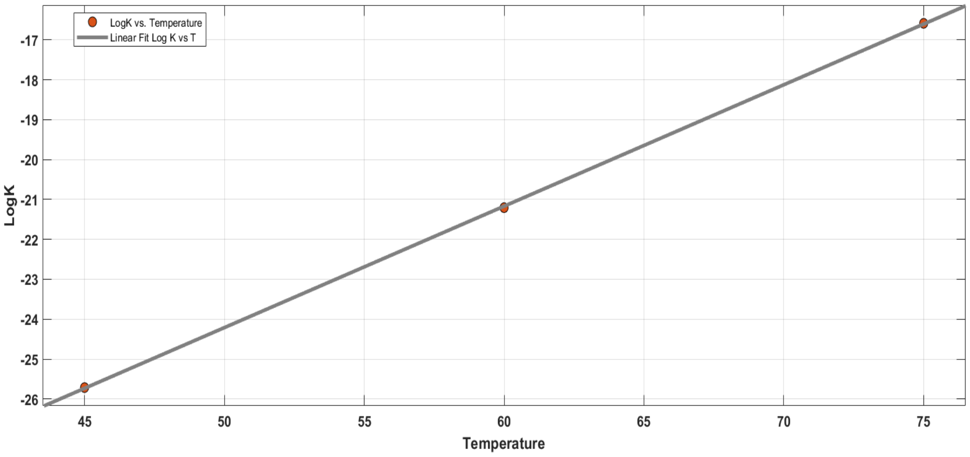

Figure 7.31: Variation of K-parameter vs Temperature Model

7.6.3. Determining the beta parameter:

The β parameter is observed to be almost constant for all temperatures as seen in Figure 6.18 (a). Thus, taking the average of all the values would be the best statistic measure to determine the parameter.

$$\beta_{avg} = \frac{1.543 + 1.4665 + 1.5014}{3} = 1.5036 \tag{7.23}$$

Thus, for any temperature, the value of β = 1.5036 can be used as the standard value.

7.7. Conclusion

- Thermal degradation decreases electrical life (time-to-breakdown) of the insulation at given electrical stress level. This has been observed from the Fast Ramped Tests and also validated in the Long Term Step Stress Tests.
- The slope n of the life-line decreases when thermal degradation of the oil-impregnated paper insulation increases. In this way, the influence of thermal aging on the electrical life of the insulation is described quantitatively.
- The rate of fall of n parameter is parabolic in nature with increase in temperatures, thus indicating, shorter life time if we push the cables towards the permissible thermal limits.
- There is a strong correlation between n, α and β as observed from the Least Square Analysis.
- The estimates from both MLE and LS are very similar with very low bias. So, even though MLE is a biased estimator, the difference is not significant for the given breakdown values.

8

Polarization Depolarization Current Characterization

This chapter discusses the implementation of PDC measuring electronic circuit. The polarization and depolarization currents are measured to obtain material characteristics and are used to fit the Extended Debye Model. The equivalent parameters obtained from the model compared to evaluate the change in trends with varying temperature and increase in aging. These characteristics are coupled with parameters from other experiments for temperature sensitivity analysis and aging based degradation.

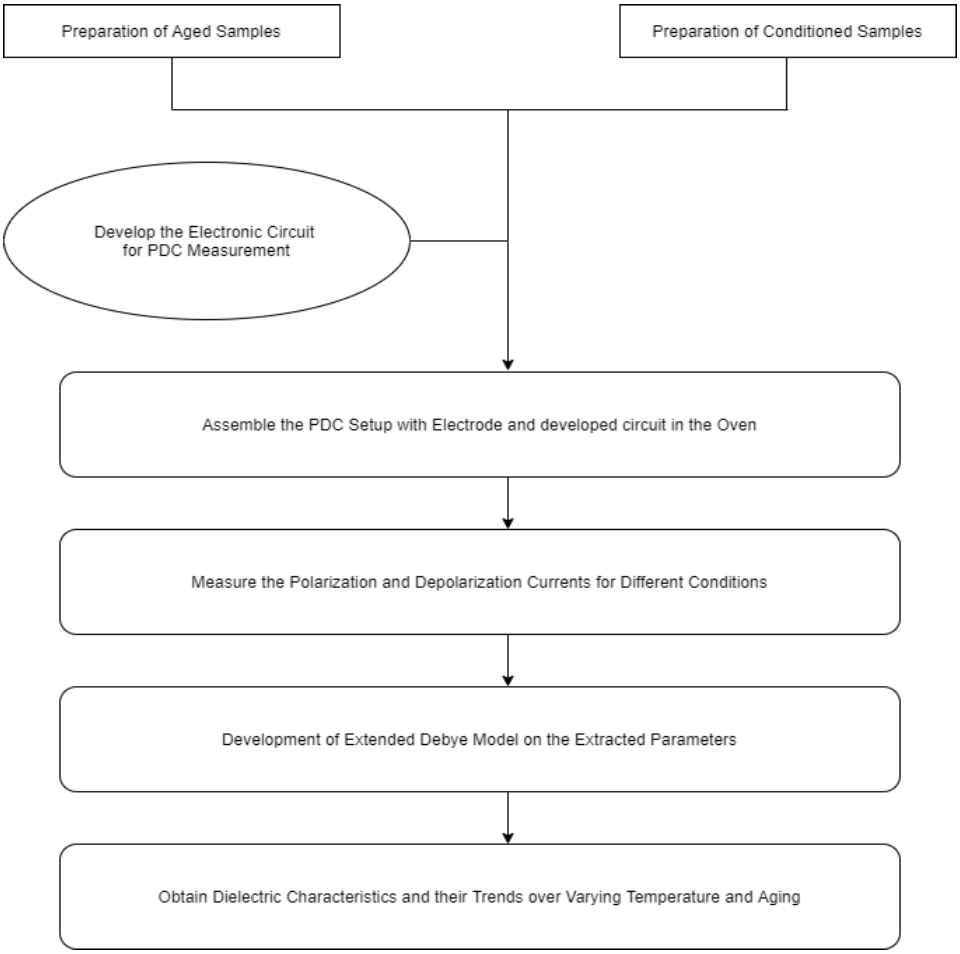

Flow of Research in Chapter 8:

Chapter 8 discusses the indicators of elevated temperature and aging for the OIP insulation under study. So, two types of samples re prepared: one type is aged and the other is conditioned in the three temperatures. Next, an PCB was designed to develop an electronic circuit to measure Polarization-Depolarization Currents for the two types of samples at three temperatures. Extended Debye Model was developed to fit the currents. An intense study has been performed to find optimal modelling of the dielectric corresponding to the different polarization processes taking place inside it. Finally, indicators were extracted from the model which showed degradation of parameters with higher temperature and aging. The duration of the test is around three hours and so the next question remains if a short duration measurement can be performed. Also, additional parameters would help to build a more robust model to indicate aging and elevated temperature which will be discussed in Chapter 9.

8.1. Polarization Depolarization Current Setup:

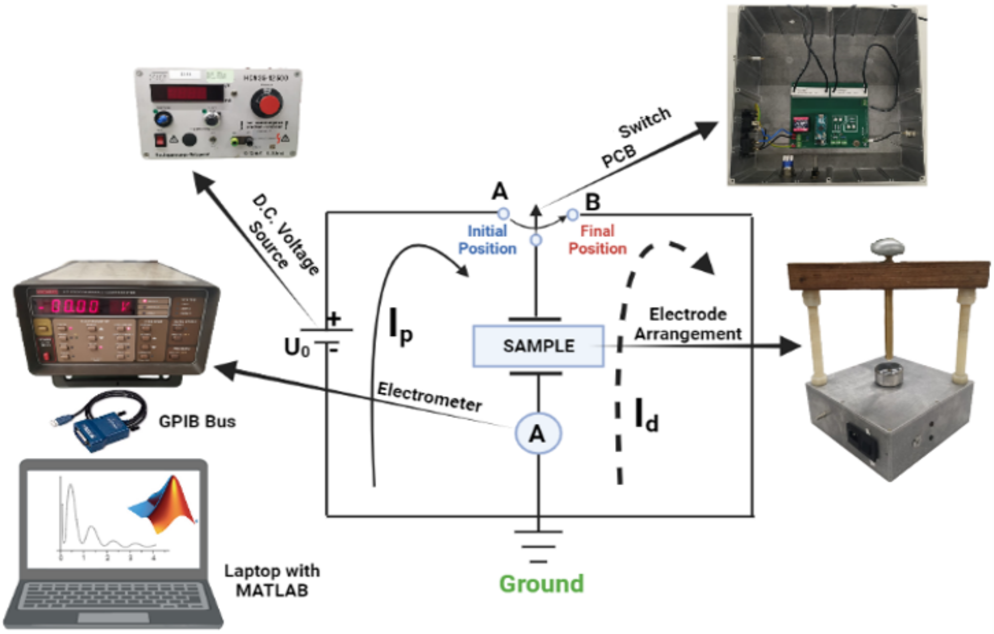

Figure 8.1: Schematic Diagram of PDC Measurement

Figures 8.1 and 8.2 represents the schematic and experimental PDC setup respectively. A D.C. voltage source is used to supply 1 kV during the polarization process. It should be noted that the field is not too high such that it can initiate electrical aging during that time [114]. The polarization process is carried out for $t_p = 5000s$ and then the depolarization process is carried out for $t_d = 5000s$ as in Figure 8.3(b), thus for each sample, the whole process takes close to 3 hours. The electrometer used for measurement of current is Keithley 617 Programmable Electrometer, which can measure as low as 10^{-15}A. The instrument is warmed up for 3 hours before the test and the zero correction is checked before running the test, so as to ensure there is no zero error. The electrometer is connected with a GPIB Bus from NI Instruments into a Laptop, where a MATLAB Script has been prepared to establish communication between the Programmable Instrument and MATLAB to log the current values. The Graphic Interface is seen in Figure 8.3(a) where, firstly, we have to detect the driver, input the Board Index and Pin Address, set the step size, which is 1 in this case and then connect the instrument.

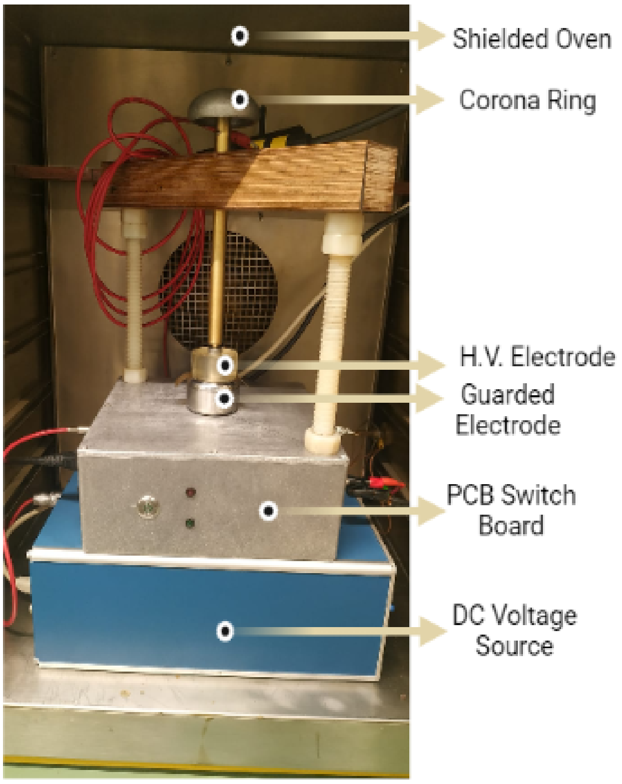

Figure 8.2: Experimental Setup of PDC Measurement

The ground electrode is guarded in nature so that the leakage currents are not measured and one gets the current that only passes through the insulation without fringing, giving very accurate readings.

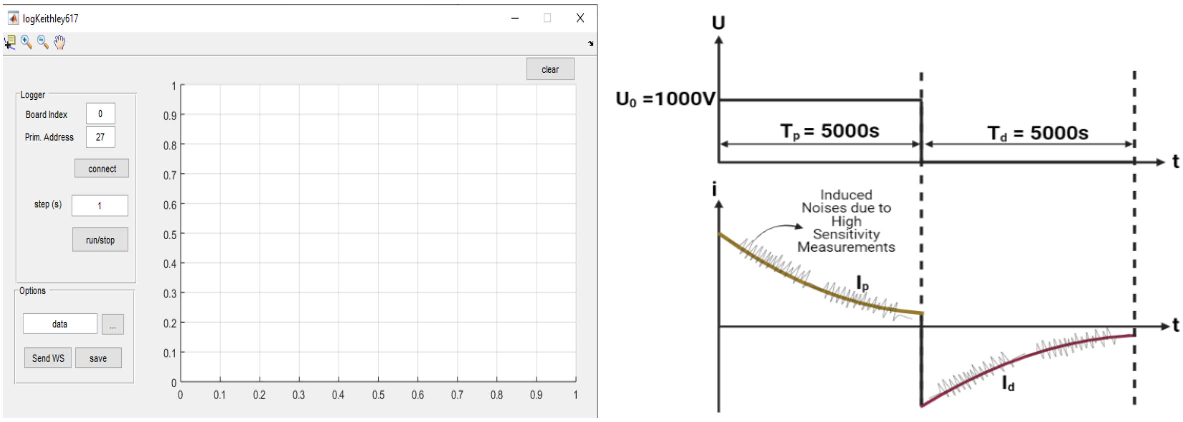
Board Index 0
Prim. Address 27
step (s) 1
data

(a) GUI of the MATLAB Developed PDC Communication Code

(b) Flow of Polarization-Depolarization Current for 1.5 hrs each

Figure 8.3: PDC Measurement Specifications

Working of Designed Circuit:

With respect to Figure 8.4, firstly, the circuit is powered from Tb2 through 220 V A.C. Mains, which is fed into the Traco Power AC to DC Converter. This is because the Reed Relays and Arduino needs a DC Power Supply of 5V. Thus, it steps down 220 V A.C. to 5V D.C.

In Figure 8.1, the loop where I_p flows is referred to as Loop 1 and where I_d flows is called Loop 2. The Switch is initially in Position A for Loop 1 and Switched to Position B for Loop2.

Working of Loop 1 (Polarization Current): From Figure 8.4, Pin 13 of the Arduino Micro is connected to the paralleled NPN Transistor 1 and 2. Two Transistors are used since the current rating of the Reed Relay is higher than one NPN, thus 2 are used in parallel to increase the current capability. This is followed in the 2^{nd} Loop as well. Now the collector of the NPN is connected to the energizing coil of the Reed Relay 1. A diode is used in parallel to a resistor since, during switching, there can be a voltage surge, causing a current to flow and damage the circuit. Thus, the arrangement takes care of the protection. The Arduino Micro is fitted with a switch connected between Pin 10 and +5V. During 0<t_p<5000s, the Arduino is coded such that it communicates HIGH State to pin 13, connected to NPN 1 and 2 and the Reed Relay 1. Thus, the collector junction becomes forward biased putting the transistor in the Saturation Region. The Red LED connected to Ts1, starts glowing indicating that the first stage has started. Also, a delay of 10 seconds is provided to the Arduino. This is because, the whole setup is shielded inside an oven, connected to a safety box. Until the oven doors are closed, the safety box prevents application of high voltage to the system. If the Arduino starts immediately, it would not be possible to track the first few seconds of the polarization phase. The delay provides enough time to close the oven doors and apply HV. During this phase, the current is transferred to the electrometer for reading.

Working of Loop 2 (Depolarization Current): The Pin 14 is connected to NPN Transistors 3 and 4 which is in turn connected to Reed Relay 2. The same protection arrangement is designed for the 2^{nd} Loop. During 5000<t_d<10000, the Pin 13 is made LOW and Pin 14 goes to HIGH State, triggering the collector junction of NPN 3 and 4 to Forward Biased Mode. This, switching operation takes place in 3 milliseconds and also, there is no problem of bouncing debouncing as in a mechanical relay over a Reed Relay. Also, Cynergy3 Reed Relays are optimal for H.V. Switching at very fast operation times making it a good design choice. Thus, the Relay 2 operates during the next phase and a Green LED connected to Ts2 indicates the operation. After the coded stipulated time, the Arduino stops sending signal.

All the individual components are checked to be grounded well. Also, since the current is in the tune of Pico or hundreds of Femto Amperes, hence the sensitivity in the order of magnitude may sometime cause slight noises during the polarization and Depolarization currents as shown in Figure 8.3(b). Figure 8.4 represents the circuit diagram of the PDC setup and Figure 8.5 shows the lab implementation of the setup with all the parts marked in details. The analysis of the measurements as discussed in this chapter (Section 8.3) validates that the design has been correctly made. The components are fitted into a metal shielded box and made into a compact instrument which can be used for future measurements.

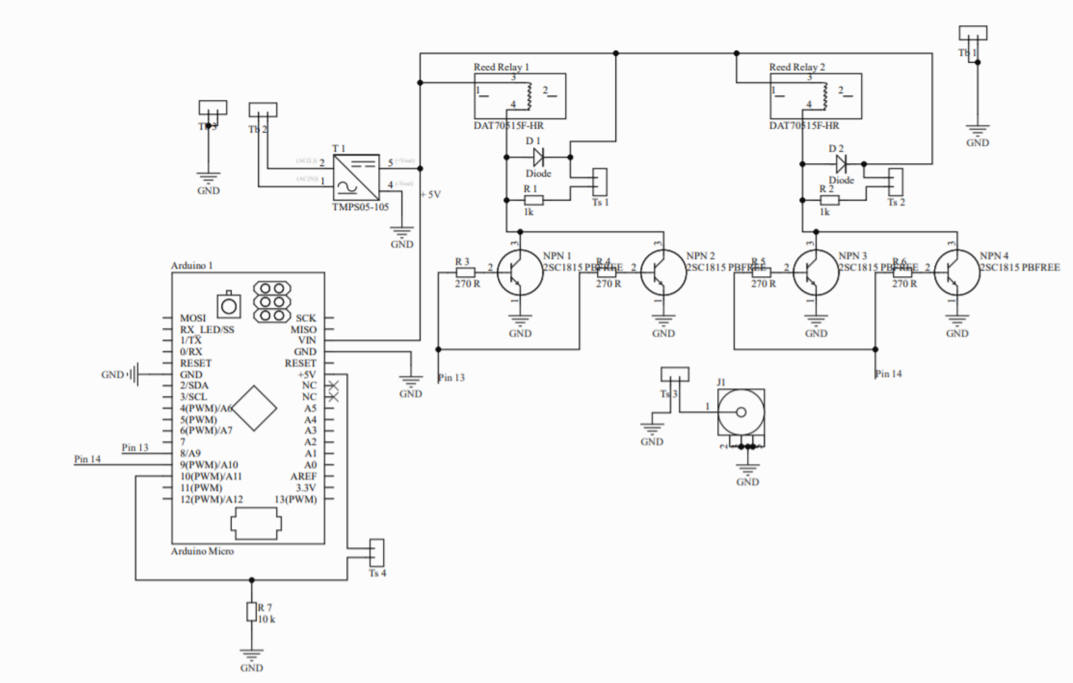

Figure 8.4: Pin Diagram of the Switching Circuit Developed

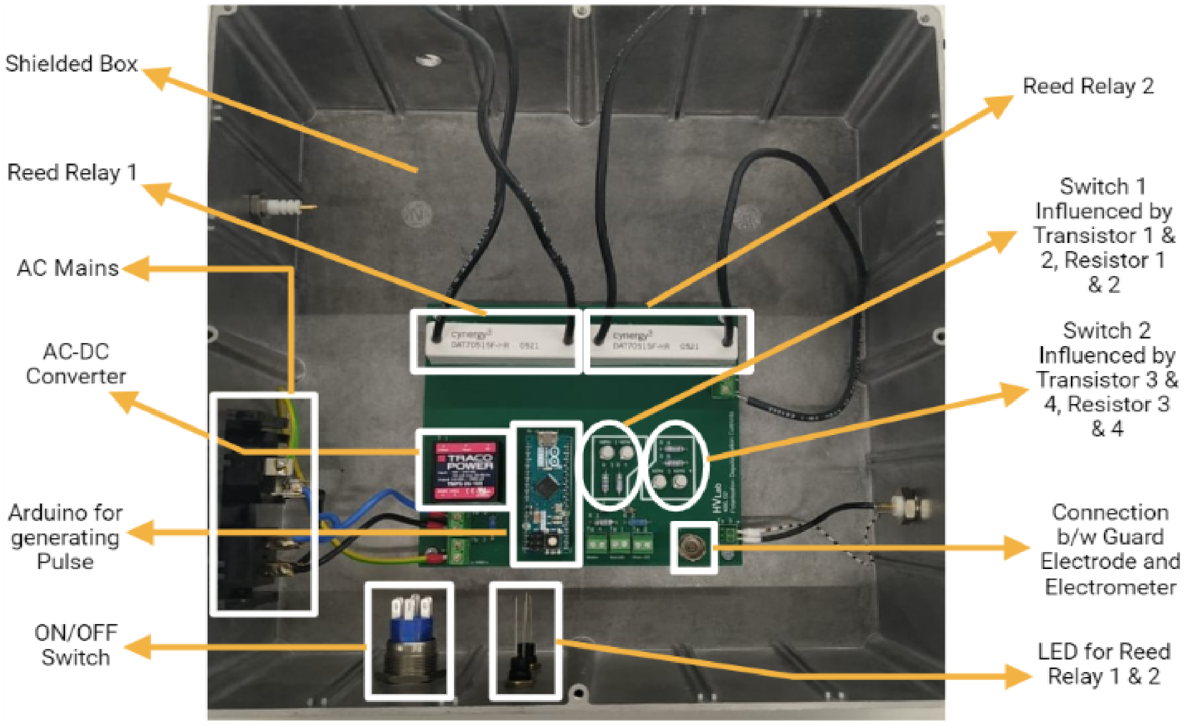

Figure 8.5: Circuit Implementation of Switching Circuit for PDC Measurement

8.2. Physics Based and Mathematical Analysis of PDC

Treatment of samples:

For each set of temperature, 5 samples are prepared out of which 3 are used for each temperature. The measurement procedure and post processing has been addressed later in this chapter.

Type 1: Aged Samples: The samples are first kept at 75^oC for 1 week to remove the moisture and then they are kept for 14 days at the specific temperatures of 45^oC, 60^oC and 75^oC. Thus, they undergo a total of around 500 hours of aging. The regime is strictly maintained for all the samples to ensure similar aging conditions so that they can be compared.

Type 2: Conditioned Samples: These samples are kept at 75^oC for 1 week to remove any moisture and maintain equal levels for each one. Then they are kept at 45^oC, 50^oC, 60^oC and 75^oC for 4 more days to condition them. It is expected that 11 days of elevated temperature would condition the samples but not age them as high as 21 days aged samples [115]. This is done to compare the sudden temperature rise due to dynamic line ratings which may not necessarily age the insulation in the short run. But in the long run, repeated temperature rise would definitely age them as simulated with the Type 1 samples [116].

8.2.1. Mathematical Modelling of PDC:

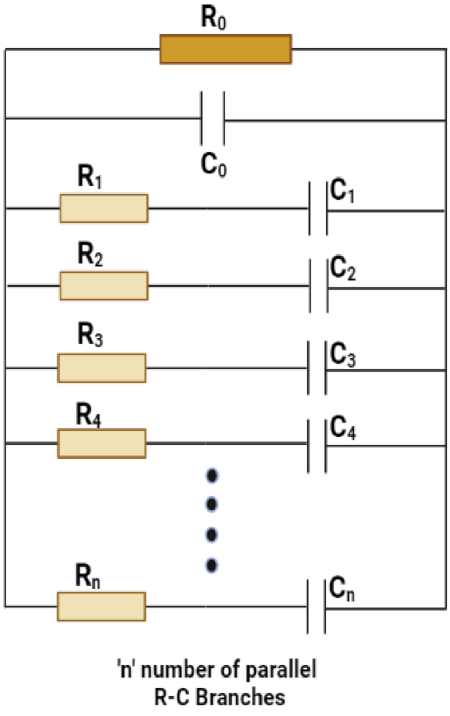

Figure 8.6: Parallel RC realization of Insulation

An insulation can be modelled as a capacitor with parallel resistor, C_0 and R_0. First of all, a DC voltage U_0 is applied on the specimen for a period of t_p, in order to make all the polarization process complete [114]. In the presence of an electric field, the corresponding current, called polarization current is developed due to the tendency of dipoles to align in the direction of the field. When the field is removed, the dipoles relax and return to the original state. In a polymer dielectric, with cellulose being the primary polymer in OIP insulation, every polar group can have a different configuration of neighboring molecules. Thus, the response time of the groups after the application of an electric field may differ from one to another. This polarization current can be divided into two parts, the first part is conductive current, due to the intrinsic conductivity of the specimen; the other part is caused by polarization process, including electronic polarization, dipolar polarization and interfacial polarization which last for t_p,which has been discussed in details during the literature study [117][118]. After that, the switch is off, and the external voltage is removed. The specimen is short circuited and discharge to ground. The depolarization current is recorded during a period of t_d, which contain no conductive current anymore. Taking influence of power source into consideration, the polarization current and first 10 seconds of depolarization current are usually neglected since there are some transients. Thus, each polarization branch can be modelled by the Extended Debye Model as a series Capacitor and a Resistor [119]. Depending on the number of polarization events, the insulation has same number of parallel branches as shown in Figure 8.6 with the primary insulation resistance and capacitance and parallel polarization branches [118][120]. Now, the question remains how many branches to consider, since a very low number would not adequately cover all polarization processes and high number of branches might not have significant physics based interpretation [121]. An extensive research has been done in this thesis to recognize the optimal number of branches.

Let us define 'aging degree' which means how long samples are aged and this term will be higher for aged samples compare to conditioned samples.

As discussed in the measurement of the Polarization-Depolarization Currents, a DC Voltage is applied across the Oil Impregnated Paper Insulation, which can be viewed as a predominant capacitor, creating a field strength. The following mathematical expressions help us analyze how we arrive to the equations for the two currents.

For a geometrical capacitance C_0 and field strength $E(t)$ due to the external voltage $U(t)$, the current through a homogeneous dielectric can be written as follows[122]:

$$i(t) = C_0\left[\frac{\sigma_0}{\varepsilon_0}U(t) + \varepsilon_\infty\frac{\mathrm{d}U(t)}{\mathrm{d}t} + \frac{\mathrm{d}}{\mathrm{d}t}\int_0^t \varphi(t-\tau)U(\tau)\mathrm{d}\tau\right]$$

where, ε_∞ denotes relative permittivity at power frequency, $\varphi(t)$ represents dielectric response function at time t. The measured polarised current in this period contains absorption and conduction components and thus can be represented as [122]:

$$i_\mathrm{p}(t) = C_0U_0\left[\frac{\sigma_0}{\varepsilon_0} + \varepsilon_\infty\delta(t) + \varphi(t)\right]$$

where, $\delta(t)$ is the impulse voltage, U_0 is the applied HV DC voltage.

After the polarisation period, the applied DC source is removed, and the test object is short circuited. This short circuit allows the depolarisation current $i_\mathrm{d}(t)$ to build up which measures only the absorption current without the conduction part and thus can be revealed as [122]:

$$i_\mathrm{d}(t) = -C_0U_0\left[\varphi(t) - \varphi\left(t + T_\mathrm{p}\right)\right]$$

According to the extended Debye model, the depolarization current can be fitted by the equation below [114]:

$$I_d = \sum_{i=1}^{n}\alpha_i e^{-\frac{t}{\tau_i}}$$

$\alpha_i e^{-\frac{T}{\tau_i}}$ stands for i^{th} polarization process. α_i is the coefficient and τ_i means relaxation time constants which are product of the corresponding resistance and capacitance. Then using the α_i and τ_i, we can calculate the R_i and C_i in the model using the equation below [114]:

$$R_i = U_0\left(1 - e^{-\frac{t}{\tau_i}}\right)/\alpha_i$$

$$C_i = \tau_i/R_i$$

The R_0, which is the insulation resistance can be calculated by the following way [114]:

$$R_0 \approx \frac{U_0}{i_\mathrm{p}\left(t_\mathrm{m}\right) - i_\mathrm{d}\left(t_\mathrm{m}\right)}$$

where, $i_p(t_m)$ & $i_d(t_m)$ are the polarization and depolarization current values after a very long time when it becomes almost constant.

C_0 is the geometric capacitance which has been calculated by measuring the value of the capacitance at 50 Hz using the IDAX 300 and then dividing by the real part of the permittivity (ϵ') [118].

Thus, firstly, α_i and τ_i are evaluated by fitting the depolarization current consisting of 'n' number of branches. Then R_i,C_i are evaluated from the above obtained values. Finally, R_0 & C_0 is calculated and compared for different temperatures.

8.3. Capturing the PDC and Post Processing

Step 1: Acquiring the Unfiltered Polarization Depolarization Current Curves:

After exporting the CSV from MATLAB to Python, the first 10 values for each process is eliminated owing to the transient due to the switching of the circuit. The unfiltered I_p and absolute value of I_d are depicted in Figure 8.7(a) and (b). It is observed that the polarization current has more noise when compared to the unfiltered depolarization curve. The reason may be due to some noises induced from the D.C. source during the polarization phase imparting noises in the I_p signal, but in the depolarizing phase, the sample is shorted and thus, there is no noise from the source and the curve looks very smooth. Also, the I_d is negative since it flows in the opposite direction, but the absolute value is used for analyzing the data. 3 samples are taken for each temperature and each degree of aging, and the average of the values are taken which are then passed through a filter.

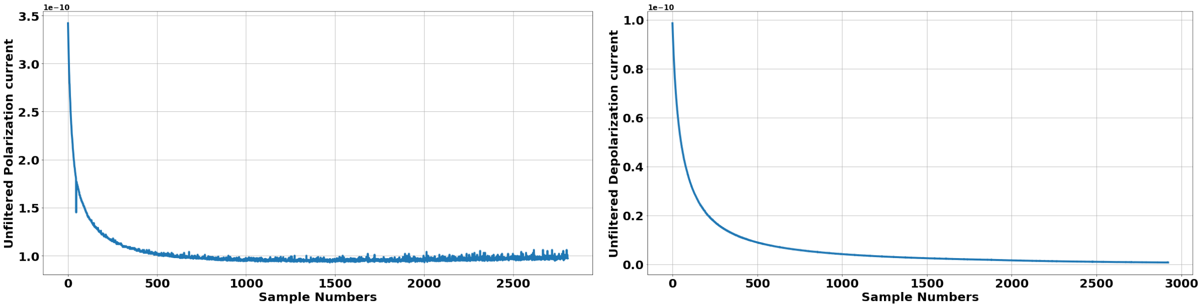

(a) Polarization Current Measured before Filtering

(b) Absolute Depolarization Current Measured before Filtering

Figure 8.7: PDC Currents Measured without application of Filters

Step 2: Filtering the Signals:

In the next stage, the signals are passed through a Butterworth filter coded in python using Scipy. The major parameters for designing the filter are the order number, critical frequency and the type of the filter. Since, we want to eliminate the high frequency components, hence a Low Pass Filter (LPF) is chosen whose frequency and phase response looks like Figure 8.8. Regarding the order number and the critical frequency, a double loop is run such that the absolute error between the filtered and unfiltered data is minimized and we obtain a relatively smooth signal. In majority of cases, a 2^{nd} order filter was sufficient. Thus, the following nature of residual errors were obtained as seen in Figure 8.9(a) for I_p Residual and (b) for I_d Residual which was less than 1% and the signal obtained was smooth as well devoid of high frequency components.

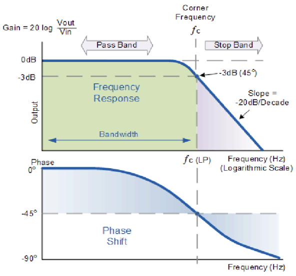

Figure 8.8: LPF Frequency and Phase Response

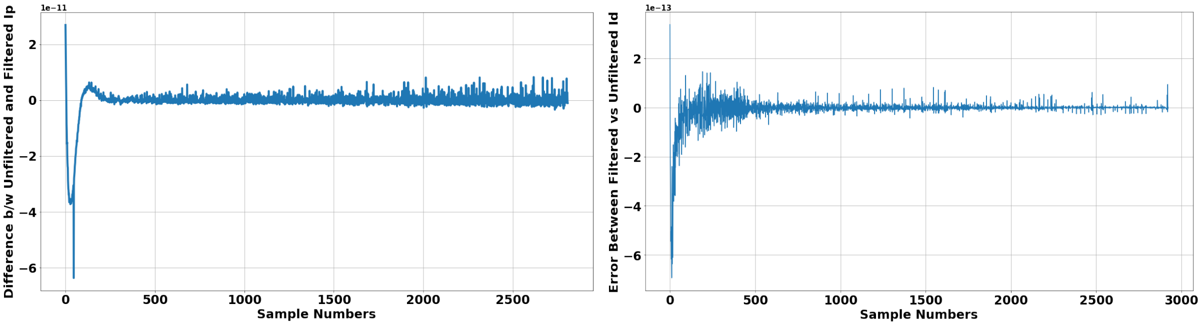

(a) Residual Error in I_p between Measured and Filtered Values

(b) Residual Error in I_d between Measured and Filtered Values

Figure 8.9: Residual Errors for Polarization and Depolarization Currents

Step 3: Comparing the Unfiltered and Filtered Currents:

Now, the filtered and unfiltered currents are depicted in Figure 8.10. Both visually and statistically, it is observed to have excellent goodness of fit. The purpose of the filtering is to fit the Extended Debye Model well on the depolarization current values. Having high frequency components would add outliers in data biasing the goodness scores, thereby causing a problem in choosing the best 'n' branch model. Figures 8.10(a) and (b) represent the measured and filtered polarization and depolarization currents respectively.

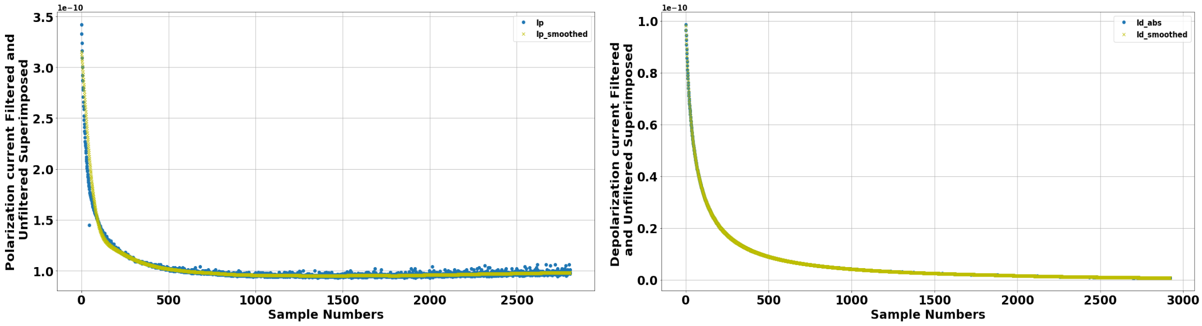

(a) Measured and Filtered Polarization Current

(b) Measured and Filtered Depolarization Current

Figure 8.10: Deviation between Measured and Filtered Currents

Step 4: Fitting the Model on Depolarization Smoothed Curve:

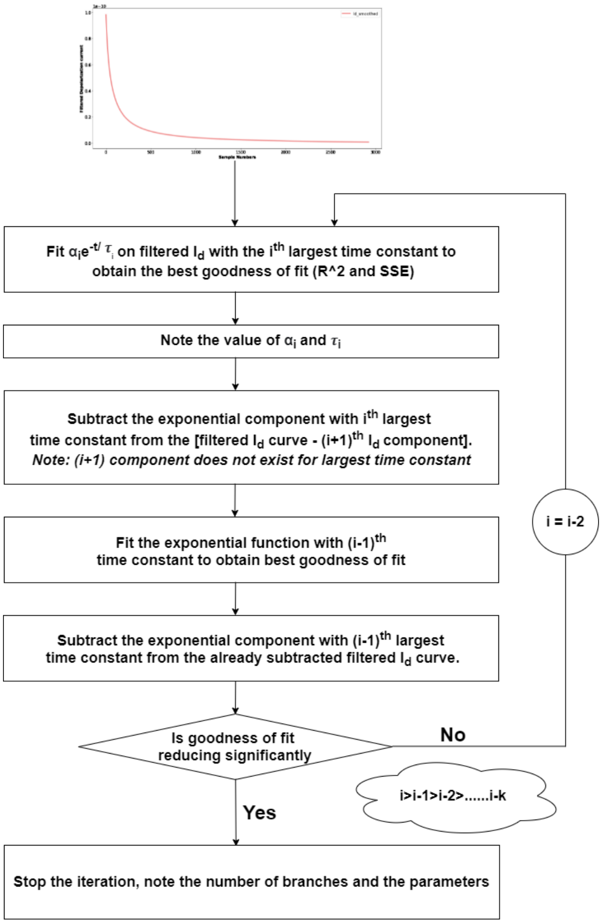

Figure 8.11: Algorithm of extracting polarization parameters from measured PDC

Non Linear Squares with Levenberg-Marquardt Algorithm is used for optimum curve fitting [118]. This curve-fitting method is a combination of two other methods: the gradient descent and the Gauss-Newton. Both the Gradient Descent and Gauss-Newton methods are iterative algorithms, which means they use a series of calculations (based on guesses for x-values) to find a solution. The gradient descent differs in that at each iteration, the solution updates by choosing values that make the function value smaller. More specifically, the sum of the squared errors is reduced by moving toward the direction of steepest descent.
Also, the LAR robust method is used to find the most optimal fit. The LAR method finds a curve that minimizes the absolute difference of the residuals, rather than the squared differences. Therefore, extreme values have a lesser influence on the fit [123]. Since, the dataset obtained has very few abnormalities due to filtering, LAR is better suited over Bisquare in this case.

8.3.1. Case 1: Aged Samples

For T = 45^{o}C:

For the aged samples, at T = 45^{o}C, the depolarization currents are fitted with the Extended Debye Model with number of branches varying from 1 to 6. Beyond 6 branches, the goodness of fit, R^2 and SSE reduces significantly, hence, the iteration is stopped at the last 6^{th} branch. From the fitting, it can be observed that the first and the second branch is unable to completely model all the polarization processes in spite of having high goodness of fit. But from 3^{rd} to 6^{th} branch, the modelling shows quite a good fit, as shown in Figures 8.12. The blue line represents the fitted model and the black curve represents the filtered depolarization current obtained after filtering of the experimental data.

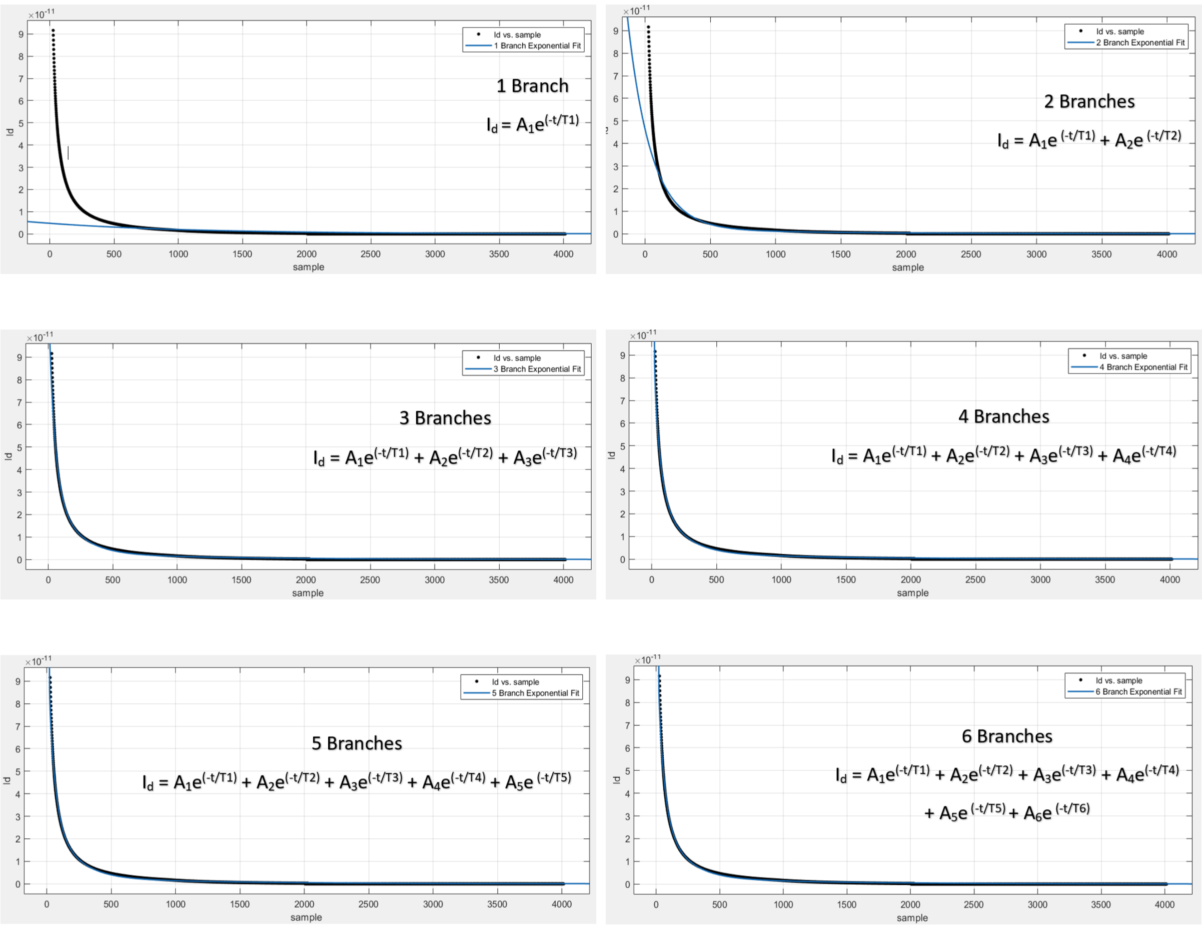

Figure 8.12: Exponential Modelling of 1-6 Branches to obtain the best fitting

The statistic scores for fitting are observed in Figure 8.13. It often becomes difficult to choose the best model, since some may have lower SSE, but higher R^2 and vice versa. The variation in these scores for 1-6 branches can be seen in Figure 8.14. Also, too less branches might not accurately model all the polarization events, and too many might lose the physics based interpretation. From literature the best fit is 2-6 branches [124].

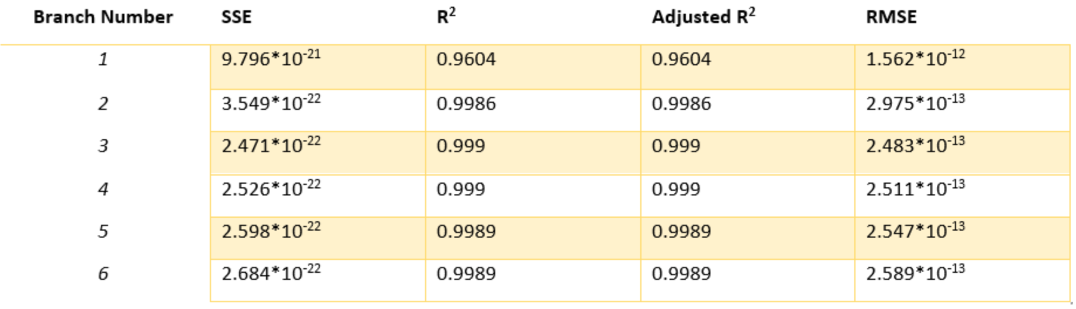

Branch Number	SSE	R^2	Adjusted R^2	RMSE
1	$9.796*10^{-21}$	0.9604	0.9604	$1.562*10^{-12}$
2	$3.549*10^{-22}$	0.9986	0.9986	$2.975*10^{-13}$
3	$2.471*10^{-22}$	0.999	0.999	$2.483*10^{-13}$
4	$2.526*10^{-22}$	0.999	0.999	$2.511*10^{-13}$
5	$2.598*10^{-22}$	0.9989	0.9989	$2.547*10^{-13}$
6	$2.684*10^{-22}$	0.9989	0.9989	$2.589*10^{-13}$

Figure 8.13: Statistical Scores of each branch after fitting 1-6 Branches

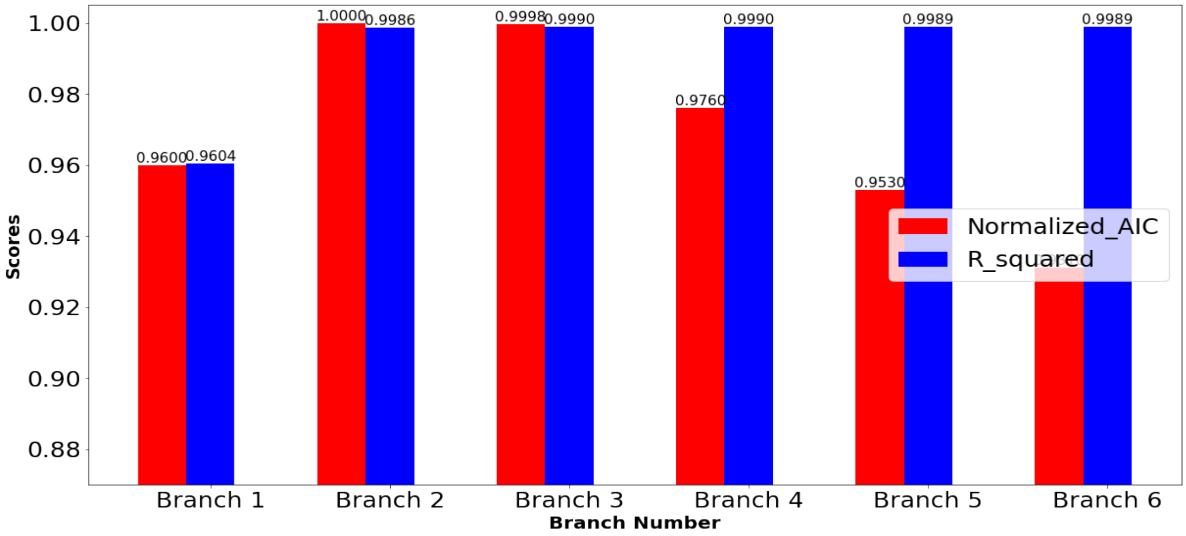

Figure 8.14: Normalized AIC and R^2 scores for each modelled branch

A new statistical parameter named Adjusted Akaike Information Criterion (Adjusted AIC) has been devised here. The advantage of AIC (Figure 8.15) over other parameters is that in parallel to finding the best model, it penalizes the models which has a lot of parameters but do not significantly improve the fitting score. Here, the $-2ln(L)$ chooses the model with the best accuracy and the $2K$ term adding to the negative likelihood penalizes models with a lot of parameters. In our case, since we are dealing with regression models, hence instead of maximizing the log likelihood, we are maximizing the inverse of Squared Sum of Errors (SSE), since Likelihood is inversely proportional to SSE. Now after finding the $Adjusted\ AIC = 2K - 2ln(1/SSE)$, lower is this value, the better is the model. Then, we divide all the Adjusted AIC Scores for each branch by the minimum one to obtain the Normalized AIC which is <= 1. Also, the Adjusted R^2 <=1. Thus, now we define

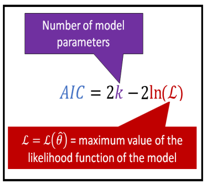

Figure 8.15: AIC Formulation

$$Error\ Function = (1 - Normalized\ AIC) * 100\% + (1 - Adjusted\ R^2) * 100\% \tag{8.1}$$

The Error Function is thus calculated for all the branches for 45^oC as observed in Figure 8.16. The trend seems to be be like the error function is monotonically decreasing until it hits a minima and then monotonically increases.

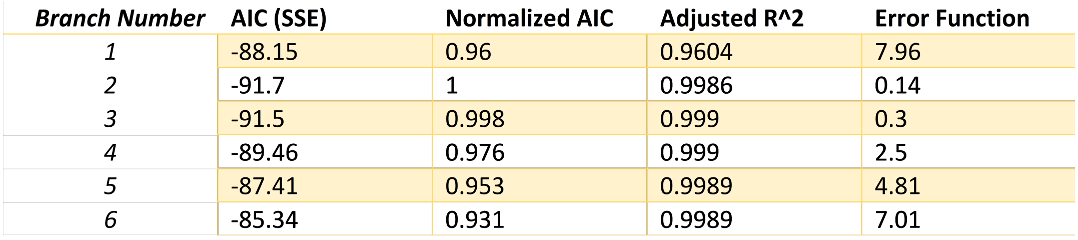

Branch Number	AIC (SSE)	Normalized AIC	Adjusted R^2	Error Function
1	-88.15	0.96	0.9604	7.96
2	-91.7	1	0.9986	0.14
3	-91.5	0.998	0.999	0.3
4	-89.46	0.976	0.999	2.5
5	-87.41	0.953	0.9989	4.81
6	-85.34	0.931	0.9989	7.01

Figure 8.16: Evaluation of Error Function for each branch at 45^{o}C

As observed from Figure 8.17, for 45^{o}C, the best model is for 2 branches, but conclusion can be made only after analyzing all the temperatures. Thus, the objective is to minimize the error function which gives the best model i.e. high goodness of fit without overly complicating the model. But, to obtain the optimal number of branches, the error scores for all temperatures are calculated and then visualized in a stacked bar in Figure 8.18. By analyzing the trend, it is evident that the best model is the one with 3 branches having the lowest Error Function. The result is perfectly in line with literature where they have considered 2-6 branches [124], predominantly 3. But this new method justifies the choosing of the 3-Branch Debye Model. Now, the next questions remains, what polarization processes does each of the 3 branches possibly represent?

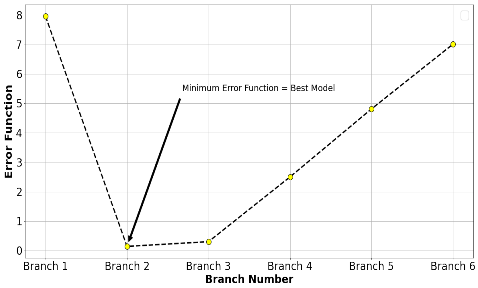

Figure 8.17: Error Function variation with Branches for 45^{o}C

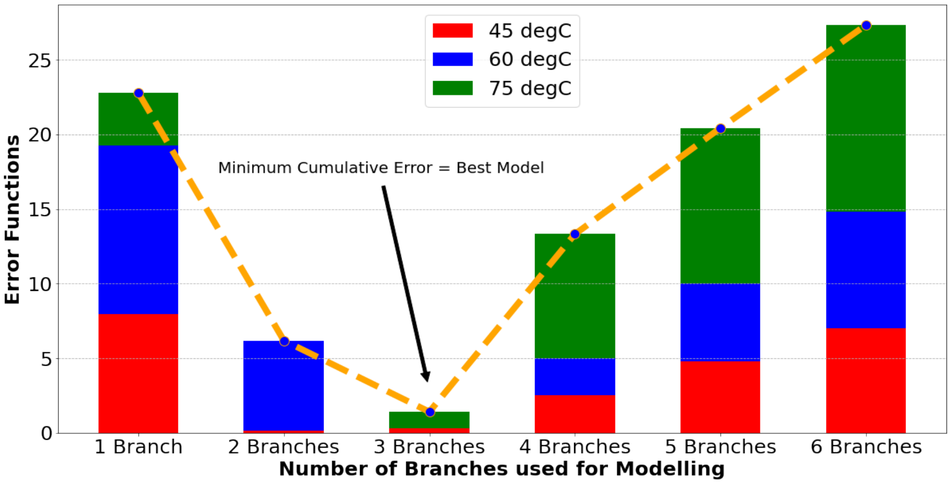

Figure 8.18: Stacked Error Functions for Aged Samples for all Temperatures vs Number of Branches

The electrical parameters as mathematically represented in Section 8.2.1 is coded in Python, where the parameters from the Curve Fit is input to obtain all the resistances and the capacitance in the 3 Debye branches and the 2 main branches as observed in Figure 8.19. As observed, the relaxation time constants are represented in a decreasing order according to the algorithm mentioned in Step 4 of Section 8.3. The resistances are in TeraOhms and capacitance in picofarads. These parameters would be compared to see if they vary with different aging temperatures in the subsequent sections.

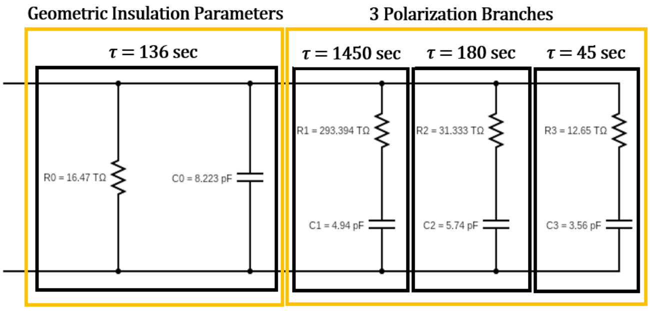

Figure 8.19: Modelling of Electric Equivalent Circuit at 45^{0}C

For T = 60^{o}C:

The same procedure as used for 45^{o}C is also used for 60^{o}C and the Extended Debye Model is fitted. The statistic has been obtained and represented in Figure 8.21. The Error Function has been calculated which shows same trend as discussed for the composite model, where the error function reduces monotonically, hits a minimum at 3 branches and then it increases strictly for higher number of branches. Thus, now the branch parameters are calculated and the corresponding resistances and capacitance have been reported in the electrical equivalent dielectric circuit as seen in Figure 8.20. The variation of these parameters with temperature has been discussed in the end of the chapter.

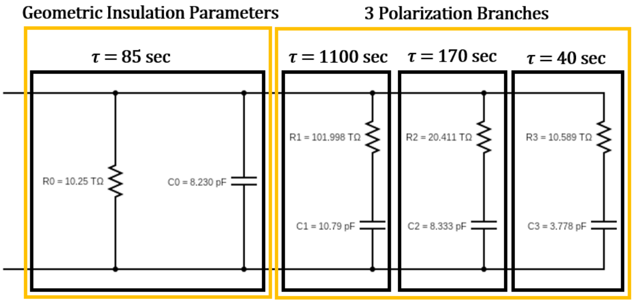

Figure 8.20: Modelling of Electric Equivalent Circuit at 60^{0}C

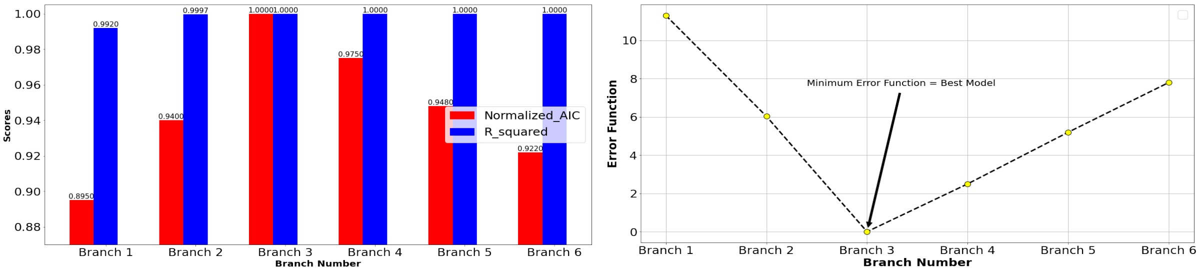

Figure 8.21: AIC and R^2 scores with Branch Number and trend in Error Function at 60^{0}C

For T = 75^{o}C:

After filtering the measured depolarization current at 75^{o}C using a 2nd order filter, the non linear model fit is performed. For this case, the 2 Branch model seemed to perform better, but not significantly more than the 3 Branch one as observed in Figure 8.23. But as discussed earlier from the stacked Error Function Model, the 3 Branch Model is the best fit. The Branch parameters have been obtained after inserting the coefficients from the Non Linear Fit into the Python Code and the resultant electrical circuit is shown in Figure 8.22. It is worthy to note that the R^2 fit for all branches at all temperatures has been significantly high, proving how good the model fits into the measured current.

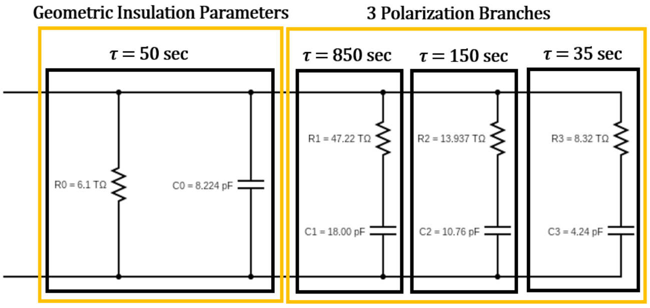

Figure 8.22: Modelling of Electric Equivalent Circuit at 75^{0}C

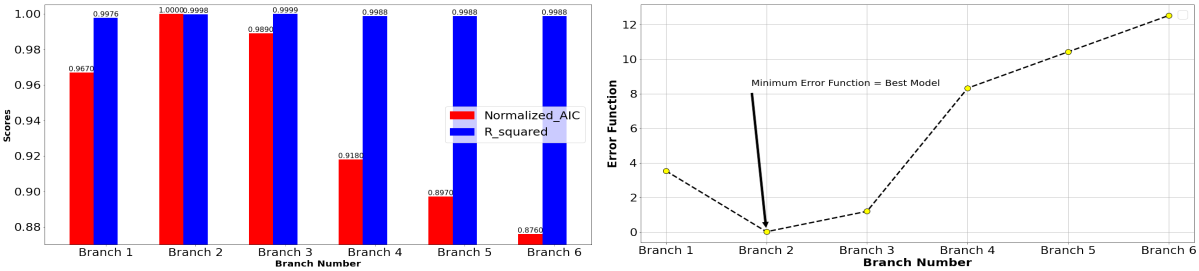

Figure 8.23: AIC and R^2 scores with Branch Number and trend in Error Function at 75^{0}C

8.3.2. Case 2: Temperature Conditioned Samples

For T = 45^{o}C:

For Case 2, the samples are conditioned to 45^{o}C. Then the measured data is filtered by a 2^{nd} order low-pass Butterworth Filter. The dataset is in accordance to the temperature aged samples, as in the polarization current filtering, the initial filtering upto 25 seconds have a higher error between the unfiltered and filtered signal. This is the basis in which for all the measurements, the first 12 samples are eliminated because of the initial transient. After that both the polarization and depolarization current has error almost equal to 0 with some small outliers, depicted as spikes in Figures 8.24(b) and 8.25 (b). The same procedure is again followed to obtain the equivalent electrical circuit and validate which branch gives the most optimal fit.

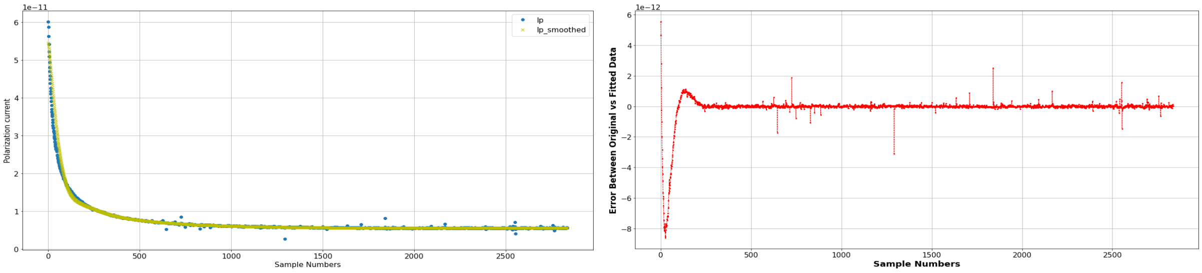

(a) Measured and Filtered I_p at 45^{o}C for Conditioned Samples

(b) Residual Error between Measured and Filtered I_p

Figure 8.24: Measured and Filtered I_p with Residual Plot

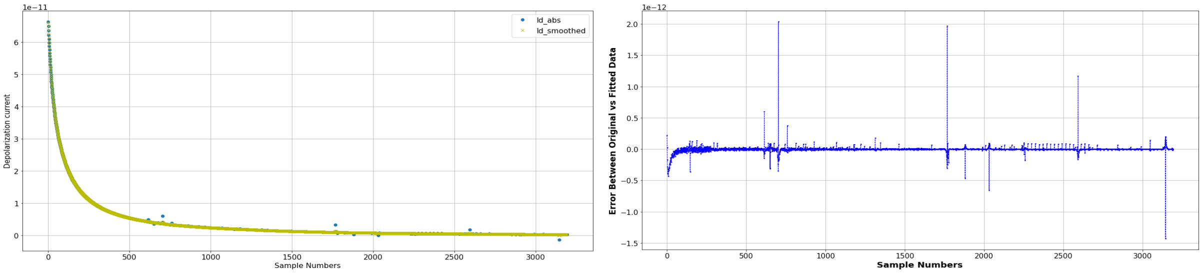

(a) Measured and Filtered I_d at 45^{o}C for Conditioned Samples

(b) Residual Error between Measured and Filtered I_d

Figure 8.25: Measured and Filtered I_d with Residual Plot

The Error Function has been evaluated for 45^{o}C samples and the best model is obtained for the 3 Branch Fitting (Figure 8.26(b)). Then the coefficients of the fit are extracted and inserted as the input array in the Python code to obtain the respective values of resistance and capacitance as shown in Figure 8.26(a). A strong change can be observed between the 2 cases of aged and conditioned samples which will be discussed in the conclusions of this chapter.

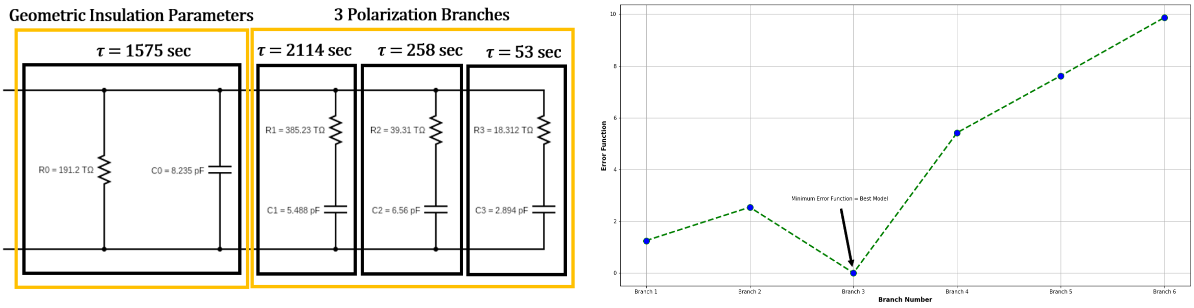

(a) Electrical Equivalent Circuit at 45^{o}C for Conditioned Samples

(b) Trend of Error Function with Branch

Figure 8.26: Electrical Representation with respective errors with branches at 45^{o}C for Conditioned Samples

The Error Functions for all the temperature conditioned samples have been stacked and exactly similar trend is observed where the function reduces to a minimum in 3^{rd} branch and then increases as seen in Figure 8.27. This does validate how good the 3 branch fit is for the provided HPGC to illustrate the polarization processes.

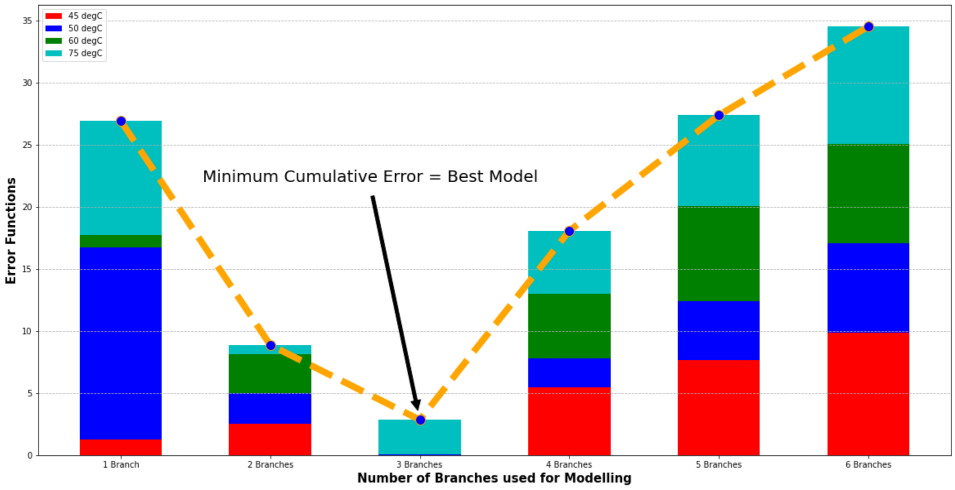

Figure 8.27: Stacked Error Functions for Conditioned Samples for all Temperatures vs Number of Branches

For T = 50^{o}C, 60^{o}C and 75^{o}C:

In the case of conditioned samples, an additional temperature of 50^{o}C was also tested. This is because one of the trend was not very clear, which would be discussed in the comparative study. For 50^{o}C and 60^{o}C, the 3 Branch Model again had the best score but for 75^{o}C, the 2 Branch is better. The 3 sub-figures in Figure 8.28 represent the change in the electrical parameters for conditioned samples at elevated temperatures. The trends would be discussed in details in the conclusion at the end of this chapter.

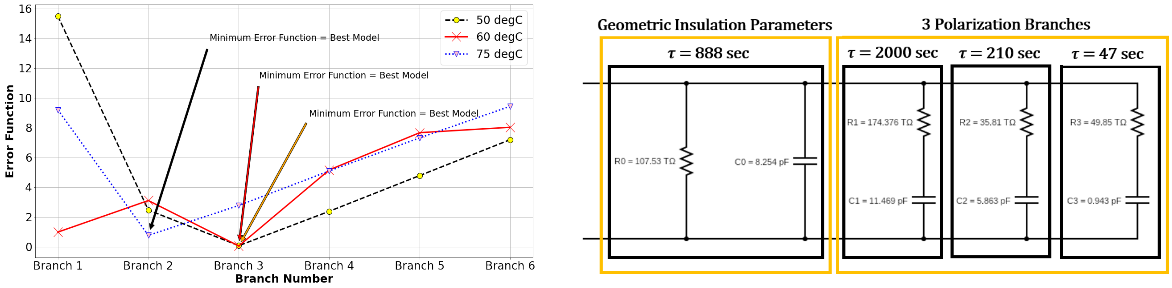

(a) Error Function vs Branch Number for 50,60 and 75^{o}C for Conditioned Samples

(b) Electrical Representation of Conditioned Sample at 50^{o}C

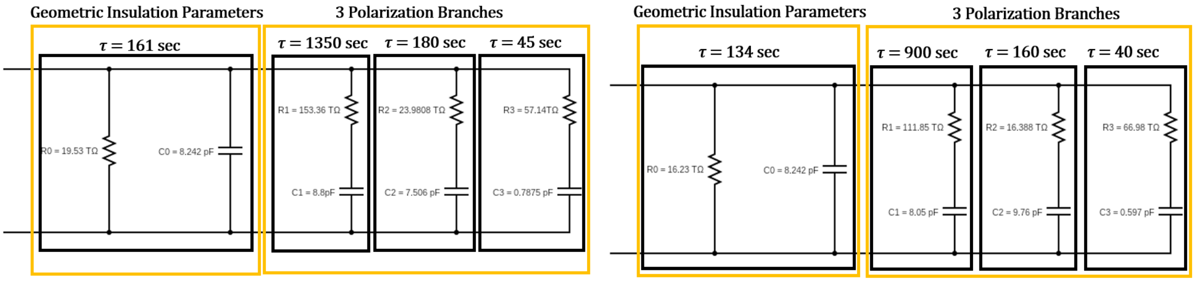

(c) Electrical Representation of Conditioned Sample at 60^{o}C

(d) Electrical Representation of Conditioned Sample at 75^{o}C

Figure 8.28: Electrical Representation and Error Scores of Conditioned Sample at 50, 60 and 75^{o}C

8.4. Trends in OIP Insulation Parameters

As discussed in last section, the polarization current is the sum of the conduction current and the absorption current whereas the depolarization current represents the absorption current which are represented as [122]:

$$i_{\mathrm{p}}(t) = C_0 U_0 \left[\frac{\sigma_0}{\varepsilon_0} + \varepsilon_\infty \delta(t) + \varphi(t)\right]$$

$$i_{\mathrm{d}}(t) = -C_0 U_0 \left[\varphi(t) - \varphi\left(t + T_{\mathrm{p}}\right)\right]$$

Since, the short circuit is made for 1.5 hours, which is a considerably long time for depolarization, hence $\varphi\left(t + T_{\mathrm{p}}\right) \simeq 0$. Hence, the conduction current can be expressed as $i_{\mathrm{c}}(t) = i_{\mathrm{p}}(t) - i_{\mathrm{d}}(t)$.

The DC conductivity of the dielectric material can be formulated as [114]:

$$\sigma_0 \simeq \frac{\varepsilon_0}{C_0 U_0}\left[i_{\mathrm{p}}(t) - i_{\mathrm{d}}(t)\right]$$

8.4.1. Trend in DC Conductivity (κ) Variation:

Case 1: Aged Samples:

The filtered polarization and depolarization currents are subtracted which is again filtered to produce a smooth conduction current. This is then multiplied by the constant $\frac{\varepsilon_0}{C_0 U_0}$. In Figure 8.29(a), it can be observed that there is a slight variation in the initial part, because of the variations in the polarization and depolarization currents which after a certain period almost becomes constant; thereby giving a constant DC Conductivity, which has been zoomed and being shown in Figure 8.29(b), for all temperatures.

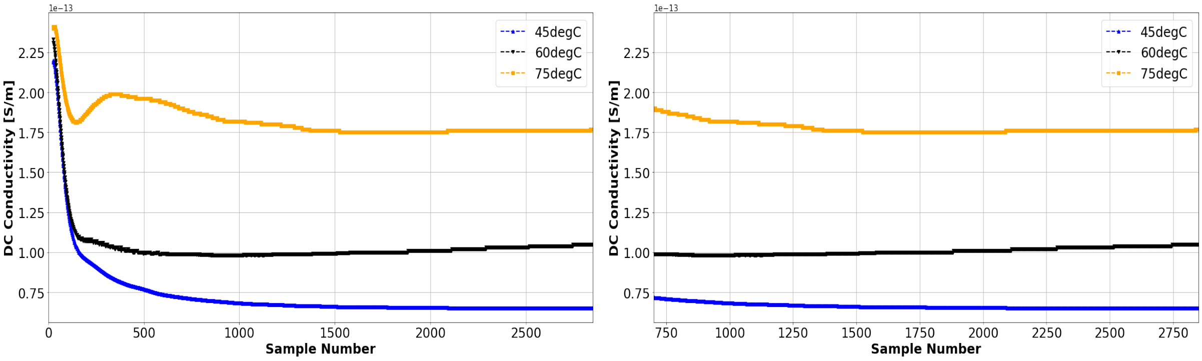

(a) Percentage (b) Percentage

Figure 8.29: Comparison between Extruded or Paper Cables

To quantify the DC Conductivity, the mean is calculated for the constant part and the values at the 3 different temperatures have been reported in the table below:

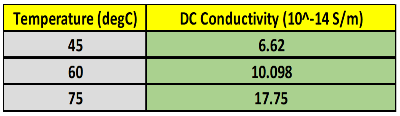

Temperature (degC)	DC Conductivity (10^-14 S/m)
45	6.62
60	10.098
75	17.75

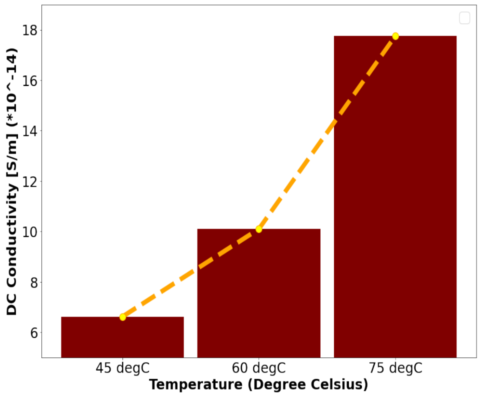

Figure 8.30: Change of DC conductivity with Temperature for Aged Samples

It is observed that with increase in temperature causing different rates of aging, the DC Conductivity also increases (Fig 8.30). This is because in case of insulators, the valence band is fully occupied with electrons due to covalent bonds. With increase in temperature, considerable energy is provided causing the electrons to overcome the band gap and migrate from valence to conduction band, increasing the conductivity due to availability of free electrons in the conduction band. In the OIP samples, the conductivity of insulating oil depends exponentially on temperature, described as [125]:

$$\kappa = \kappa_0 \exp(-F/k_B.T)$$

Where κ is electrical conductivity, κ_0 and F are material constants, k_B is Boltzmann constant $(k = 8.61733.10^{-5}\mathrm{eV/K})$ and T is the absolute temperature. The material constant F represents the energy which is required for moving the space charges in the oil-paper interface [125].

Thus, explicitly, form the formula it is evident that for the OIP dielectric, the conductivity is directly proportional to the temperature. Thus, with aging due to elevated temperatures, the DC Conductivity can be observed to have an increasing trend [124].

Case 2: Temperature Conditioned Samples:

For the temperature conditioned samples at 4 different temperatures, the value of conductivity follows a similar trend where it increases with temperature as observed in Figure 8.31(b). But the κ value for the conditioned samples are much lesser than the prolong aged samples, which means with aging, the DC conductivity increases significantly. This may be due to that the internal structure of the paper is changed by thermal oxidative aging (discussed in section 7.3) , which enhances the conductivity [125]. But this can be validated as a future scope using FTIR Analysis to check the oxidative breakdown at elevated temperature.

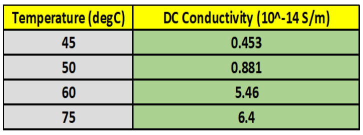

Temperature (degC)	DC Conductivity (10^-14 S/m)
45	0.453
50	0.881
60	5.46
75	6.4

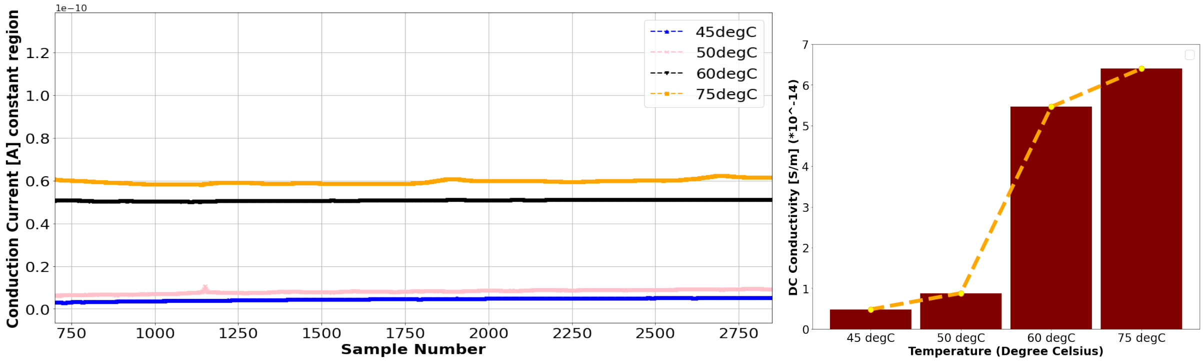

(a) Measured DC Conductivity during constant phase for Conditioned Samples

(b) Change of DC Conductivity with Temperature for Conditioned Samples

Figure 8.31: Change in DC Conductivity for Conditioned Samples

8.4.2. Trend in Conduction Current (I_c) Variation:

Case 1: Aged Samples:

The nature of the conduction current follows similar to the DC Conductivity. The conduction current arises due to the κ of the OIP and thus, since conductivity is proportional to temperature as discussed in the previous section, hence the same nature is observed for the conduction current which is shown in Figure 8.32(a) and the constant region is zoomed in Figure 8.32(b). So, in the analysis during field measurement, either conduction current or DC Conductivity is sufficient to predict the trend.

Case 2: Temperature Conditioned Samples:

Similar trend is also observed for these samples as seen in Appendix. The current saturates at a lower value as compared to the aged samples [124]. This is reflected directly from the change in conductivity from the aged to the conditioned samples. Since $\kappa_{aged} > \kappa_{conditioned}$, hence $I_{c-aged} > I_{c-conditioned}$.

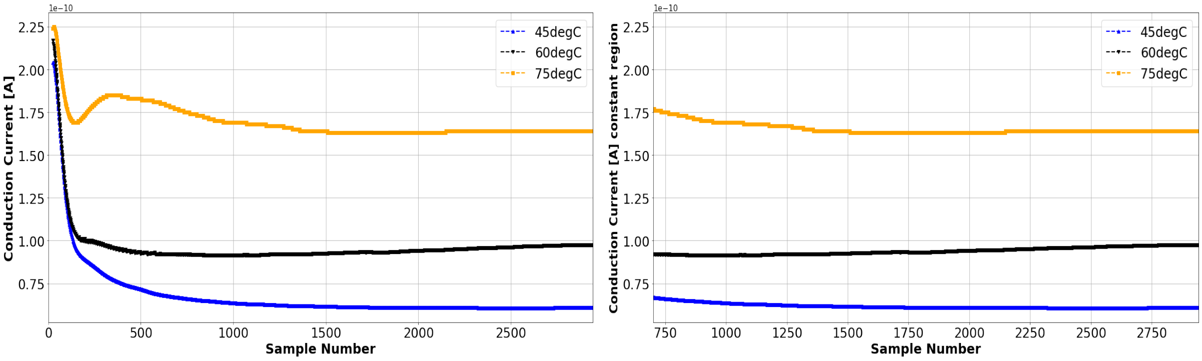

(a) Change in Conduction Current with time

(b) Zoomed constant section of Conduction current

Figure 8.32: Change of Conduction Current for Aged Samples

8.4.3. Trend in Polarization Current (I_p) Variation:

Case 1: Aged Samples:

Polarization current is given by [122]:

$$i_{\mathrm{p}}(t) = C_0 U_0 \left[\frac{\sigma_0}{\varepsilon_0} + \varepsilon_\infty \delta(t) + \varphi(t) \right]$$

Thus with increase in temperature, the DC Conductivity should increase as discussed in the previous section. Also, the real permittivity also increases with temperature (Discussed in the Chapter 9, Subsection 9.0.3). Since two factors are directly proportional to temperature, hence with increase in temperature, the polarization current settles at a higher value as shown in Figure 8.33(a) [124][126].

Case 2: Temperature Conditioned Samples:

The trend is exactly similar as the former case. But the rate of thermal oxidative aging varies and the conductivity increases according to the aging degree. Also, the rate of relative permittivity changes at a slower rate if the aging degree is low (Discussed in the Chapter 9, Subsection 9.0.3). Thus, together, the effect causes the polarization current to settle at a lower value for the conditioned samples (due to lower degree of aging) as seen in Figure 8.33(b). This phenomenon seems to be related to the loss of linearity at higher temperature. Spontaneous polarization is to be known as temperature dependent. Any change in temperature causes a change of the dipole moments, measurable as a change of electric charges at both ends of the polar axis [126].

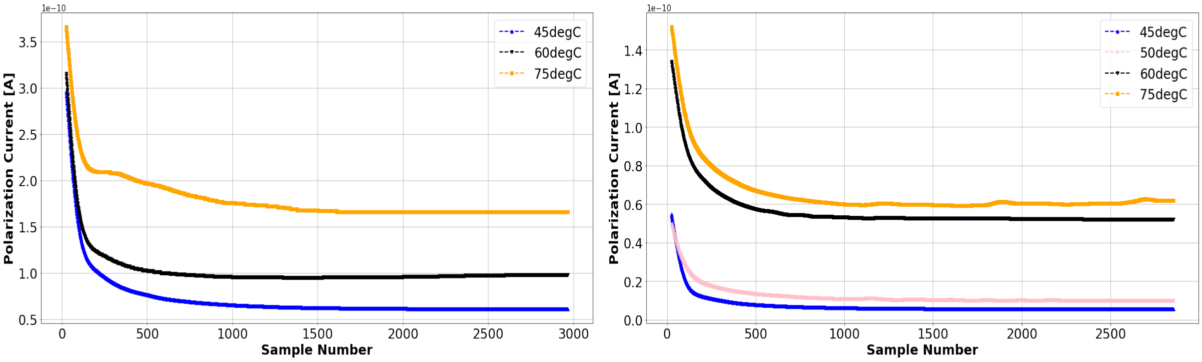

(a) Change in Polarization Current for Aged Samples

(b) Change in Polarization Current for Conditioned Samples

Figure 8.33: Comparison between Polarization current for Aged and Conditioned Samples

The polarization currents for different temperatures have been plotted for Aged and Conditioned Samples. As discussed before, for all of them, the I_p saturates to a constant value after some time. But it can be observed in Figure 8.34(a), that the polarization current for the aged samples is higher compared to the conditioned samples, indicating that with aging the polarization current magnitude increases. This means that the conductivity also increases with aging which is the case as observed in Figure 8.34(b), since with aging the breakdown of cellulose and hemicellulose in paper becomes more intense, affecting the conductivity. This can be a good aging indication before we discuss about the parameters obtained from analyzing the depolarization current.

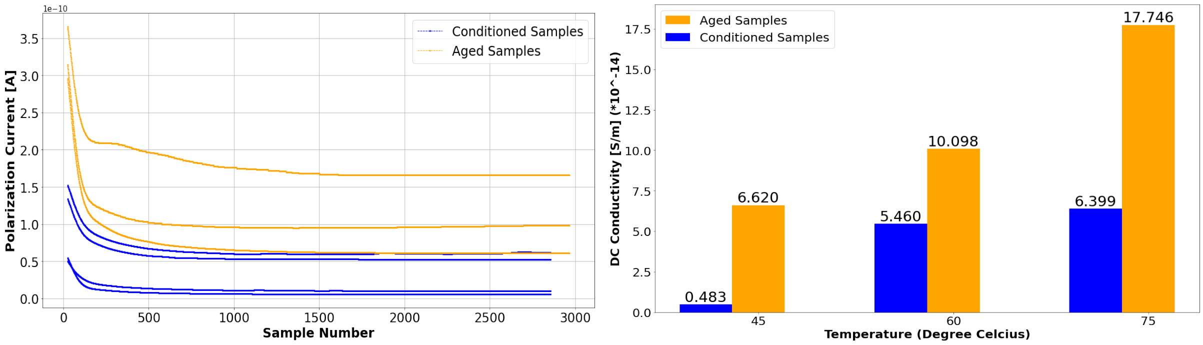

(a) Polarization Current for aged and conditioned samples

(b) DC Conductivity for aged and conditioned samples

Figure 8.34: Polarization current and DC Conductivity variation for aged and conditioned samples

8.4.4. Trend in Depolarization Current (I_d) Variation:

Case 1 and 2: Aged Samples and Temperature Conditioned Samples:

For Depolarization current[122]:

$$i_{\mathrm{d}}(t) = -C_0 U_0 \left[\varphi(t)\right]$$

Since, $\varphi\left(t+T_{\mathrm{p}}\right) \simeq 0$ as it is short circuited for 1.5 hours. The Dielectric Response Time ($\varphi(t)$), varies continuously but after a long time, when the discharging occurs completely, they settle down at similar values irrespective of temperature. The absolute values of I_d have been plotted in Figure 8.36 (a) and (b) to demonstrate the effect of temperature. When two different periods of aging is considered as in Figure 8.35, similar conclusions can be drawn. The noticeable change is that the rate of decay for aged sample is much slower compared to conditioned ones, but in the end, they settle almost at similar magnitudes

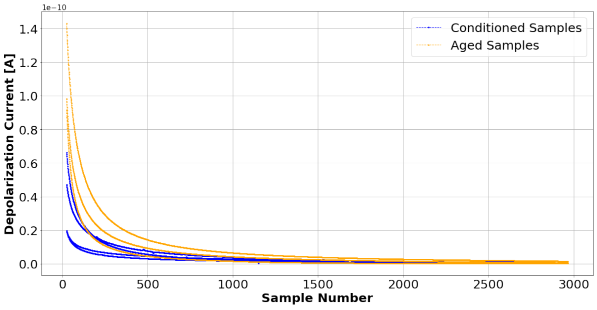

Figure 8.35: I_d for Aged and Conditioned Sample

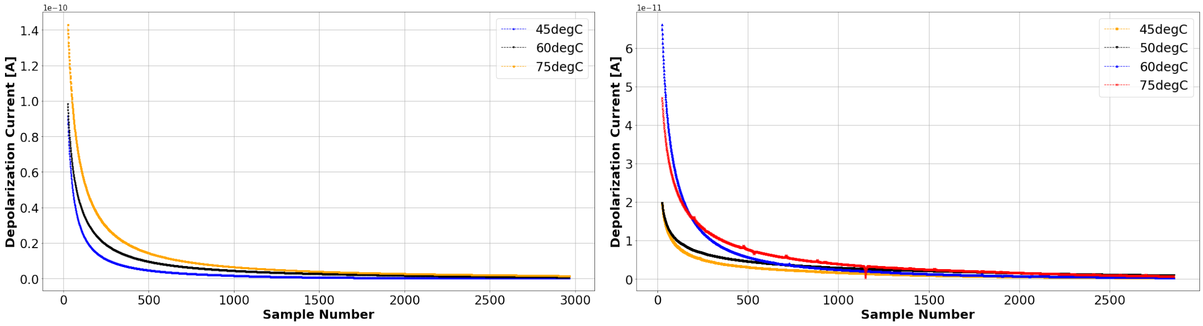

(a) Variation of I_d for Aged Samples

(b) Variation of I_d for Conditioned Samples

Figure 8.36: Comparison of I_d between Aged and Conditioned Samples

8.4.5. Trend of Branch Relaxation Times with Temperature and Aging:

τ The time constant of each polarization branch that can be calculated by $\tau_i = R_i C_i$ is given and sorted in descending order in Table 8.1. It can be observed that all the 3 time constants reduce with increase in temperature. The physical significance of the relaxation time constants is interpreted as the time taken for the dipole groups to establish the polarization. Mathematically, it can be expressed as [121]:

$$\tau = \pi \exp(\frac{U}{kT})/\omega_0 \tag{8.2}$$

where U is the barrier height in double-well potential; and ω_0 is the angular frequency of particle vibration. Equation 8.2 indicates that the time constant decreases exponentially as the temperature increases[127]. In Figures 8.37, the relaxation time constants can be seen to decrease exponentially with increase in temperature. Also, with aging, the chemical degradation is higher due to oxidation of cellulose, the reaction kinetics change, thereby shortening the polarization processes [121]. So, it is observed that the blue stacks for Aged samples are always lower than the red stacks for Conditioned Samples. The parameters derived from the time constants in next section would be an accurate measure for degradation with temperature and degree of aging. It should be mentioned that for Conditioned Samples, the 50^{o}C were measured to validate the model which has not been done for the Aged Samples, thus, there are no time constant bars for Aged Samples at 50^{o}C.

Temperature	**Branch Number**	$\tau_{Conditioned}$ **(sec)**	τ_{Aged} **(sec)**
45^{o}C	Branch 0	1575	135
	Branch 1	2114	1450
	Branch 2	258	180
	Branch 3	53	45
60^{o}C	Branch 0	161	85
	Branch 1	1350	1100
	Branch 2	180	170
	Branch 3	45	40
75^{o}C	Branch 0	134	50
	Branch 1	900	850
	Branch 2	160	150
	Branch 3	40	35

Table 8.1: Relaxation Time Constants for different branches and temperatures

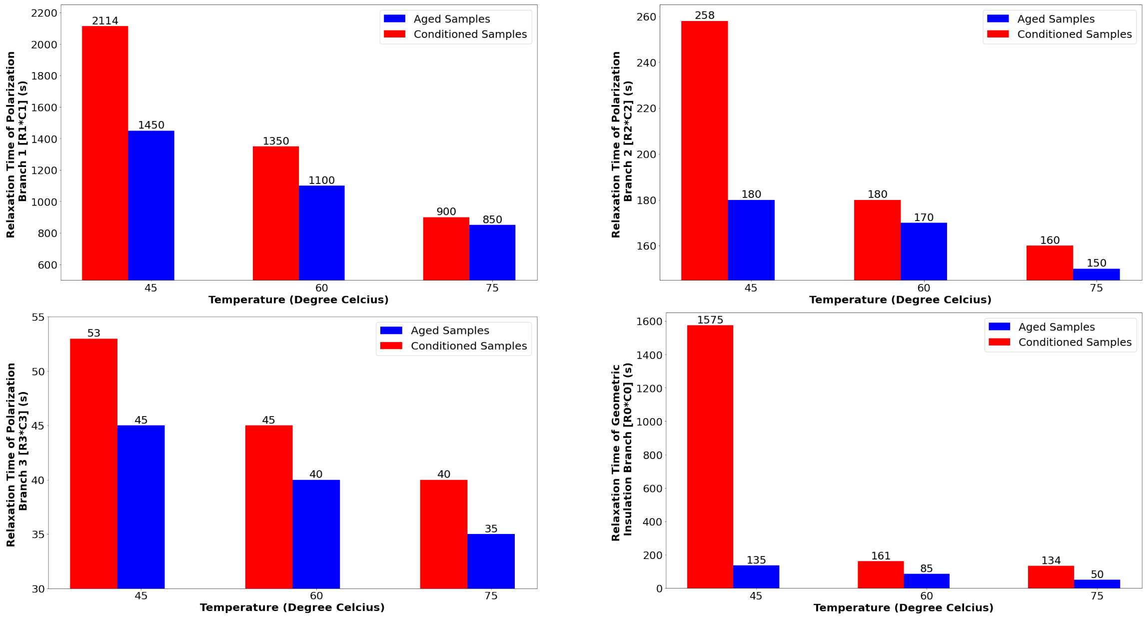

Figure 8.37: Relaxation Time Constants for different branches and temperatures

8.4.6. Trend of Insulation and Branch Resistances(R_i) and Capacitance(C_i):

The resistance and capacitance for each branch are derived from the fitting parameters by loading them in the Python Code for both aged and conditioned samples. Table 8.2 shows the change in these values for different temperatures and at different rates of aging.

Temperature	Branch Number	R$_{Conditioned}$ (TΩ)	R$_{Aged}$ (TΩ)
45^{o}C	Branch 0	191.2	16.5
	Branch 1	385	293
	Branch 2	39.3	31.3
	Branch 3	18.3	12.7
60^{o}C	Branch 0	19.5	10.3
	Branch 1	153	102
	Branch 2	23.9	20.4
	Branch 3	57.1	10.6
75^{o}C	Branch 0	16.2	6.1
	Branch 1	112	47.2
	Branch 2	16.4	13.9
	Branch 3	67	8.32

Table 8.2: Change of Resistance with Temperature for different branches

A.1. Change of Resistance with Temperature:

As indicated by the low frequency dispersion (LFD) theory developed by Jonscher [42], as the temperature decreases, the average kinetic energy of charge carriers contained in the OIP system also declines; thus, the relaxation time rises and the LFD frequency descends. Therefore, the fitted insulation resistance R_0 is observed to decrease with the increase of temperature. This phenomenon can be formulated by the well-known Arrhenius relationship [121]:

$$\mu = \mu_0 \exp\left(-E_\mu / k_B T\right) \tag{8.3}$$

where μ is the mobility; E_μ is the activation energy; k_B is the Boltzmann constant and T is absolute temperature. The reduction in insulation resistance with increasing temperature is due to increased mobility of the charge carriers inside the insulation at higher temperatures. Thus, prolonged exposure to elevated temperatures, causes irreversible damage which is reflected in the reduction of the resistances [121]. The trend in reduction of the resistances is very prominent for insulation, maximal and submaximal polarization branches (Branch 1 and 2). The trend does not follow in Branch 3 for conditioned samples (Fig 8.38(b)) and the change is not too significant (almost constant) for aged samples (Fig 8.38(a)). This is because, for modelling the Debye model, the smaller time-constant branches (specially from Branch 3 onwards) are found to be more related to the condition of the oil—whereas the condition of the paper insulation is found to be responsible for affecting the higher time-constant branches (Branch 1 and 2) [126][118].

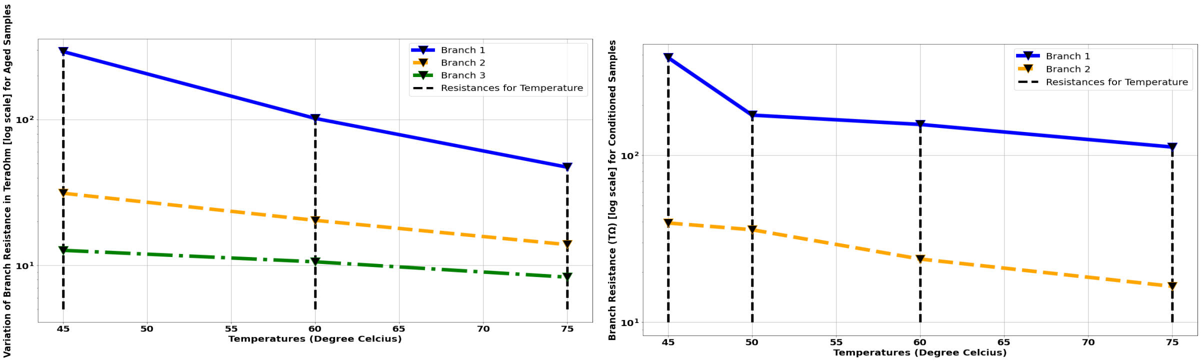

(a) Change in Resistance for different temperatures and branches in Aged Samples

(b) Change in Resistance for different temperatures and branches in Conditioned Samples

Figure 8.38: Comparison between Aged and Conditioned Samples with change in Resistance with temperatures and branches

A.2. Change of Resistance with Increase in Aging Condition:

The insulation resistance provides information about the overall condition of the insulation. A higher value of indicates better condition of resistance insulation whereas a lower value corresponds to moist insulation or high temperature. Thus, for the insulation and maximal and submaximal branch resistances, it can be observed that the magnitude of the resistance is higher for conditioned sample and lower for aged sample. But for the 3^{rd} branch, there is no specific trend and the reasoning is well defined in the last discussion. Thus, with higher degree of aging the resistance reduces, indicating degraded condition of insulation. Figure 8.39 (a),(b) represents the variation of resistance in tera-ohms for maximal and submaximal branch (1 and 2) whereas Figure 8.39(c) and (d) shows the resistance in Branch 3 and 0.

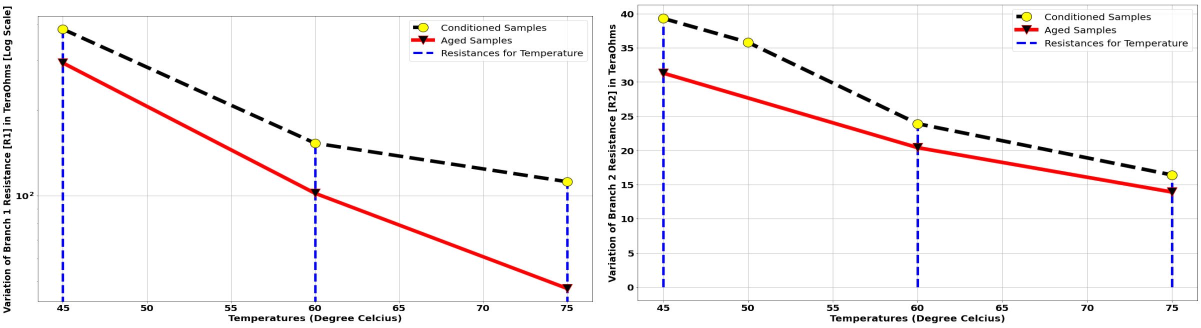

(a) Variation in Branch 1 Resistance for Conditioned and Aged

(b) Variation in Branch 2 Resistance for Conditioned and Aged

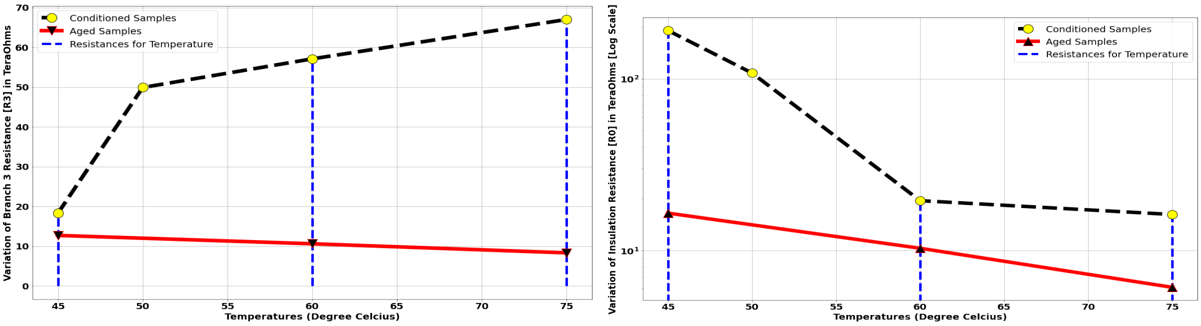

(c) Variation in Branch 3 Resistance for Conditioned and Aged

(d) Variation in Branch 0 Resistance for Conditioned and Aged

Figure 8.39: Variation in Branch Resistances for Conditioned and Aged

B.1. Change of Capacitance with Temperature:

Temperature	Branch Number	$C_{Conditioned}$ (pF)	C_{Aged} (pF)
45^oC	Branch 0	8.24	8.22
	Branch 1	5.49	4.94
	Branch 2	6.56	5.74
	Branch 3	2.89	3.56
60^oC	Branch 0	8.24	8.23
	Branch 1	8.8	10.8
	Branch 2	7.52	8.33
	Branch 3	0.788	3.78
75^oC	Branch 0	8.24	8.22
	Branch 1	8.05	18
	Branch 2	9.76	10.8
	Branch 3	5.97	4.24

Table 8.3: Variation of Capacitance across branches and temperatures

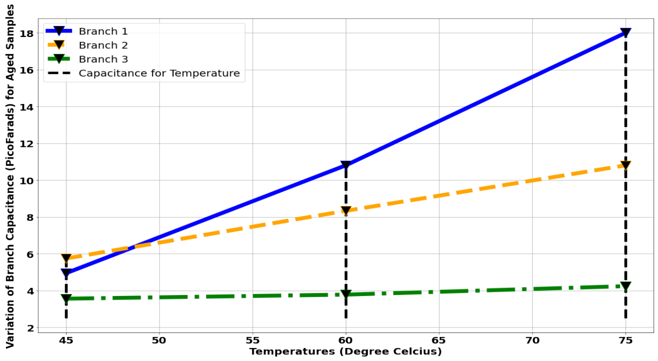

Figure 8.40: Variation of Branch Capacitance with Temperature for Aged Samples

It is observed that as the temperature decreases, the capacitance in the maximum and submaximal time constant branches significantly decreases. This is because the mobility of charge and polar particles as well as the relaxation of dipole groups are retarded, which reduces the stored energy in the dipole, shown as a decline of capacitance in the polarization branches [121]. But the reduction of stored energy is not very high, as a result of which the reduction of capacitance is not very significant, but it is definitely lower. But for Conditioned Samples, there is no specific trend observed since the temperature condition for such a short time is not sufficient to retard the dipoles and thus there is no significant change observed in the capacitance values. As the degree of aging gets high, the change in capacitance with temperature becomes more prominent. As it can be seen from Figure 8.40, in the aged samples as temperature reduces, the capacitance in Branch 1 and 2 reduces and vice-versa, but for the 3^{rd} branch, it is almost constant.

B.2. Change of Capacitance with Increase in Aging:

The capacitance of the maximal and submaximal branches are observed to increase as the aging degree increases. Thus, the values of capacitance for aged samples are seen to be higher than the conditioned samples (with some values very close to one another), which is an indication of a stronger polarization behavior attributed to the ageing by-products such as water, organic acid, and furan inside the cellulose insulation [121]. For the insulation capacitance, which is measured from the IDAX at 50 Hz and then divided by the real part of permittivity ($C_0 = \frac{C_{50}}{k'}$), the value is found to be constant and same for both Aged and Conditioned Samples. More insight about this would be discussed in the Chapter 9 Subsection 9.0.3. Figure 8.41 represent the value of capacitance in the main insulation branch and 3 polarization branches.

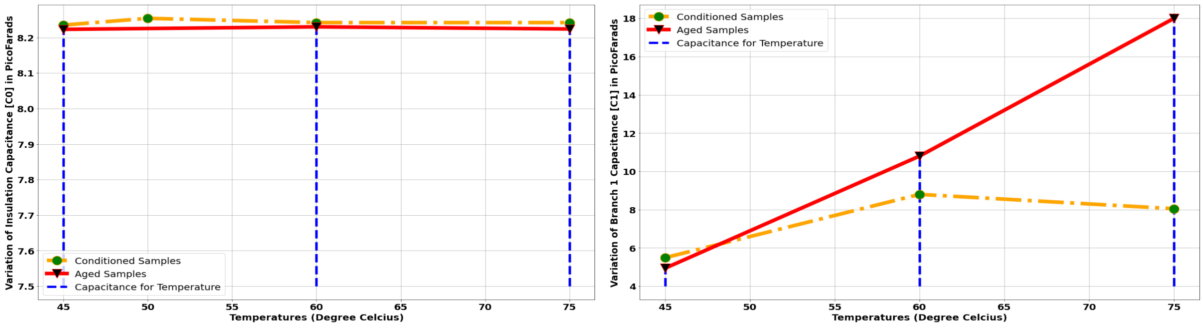

(a) Variation of C0 for Aged and Conditioned Samples

(b) Variation of C1 for Aged and Conditioned Samples

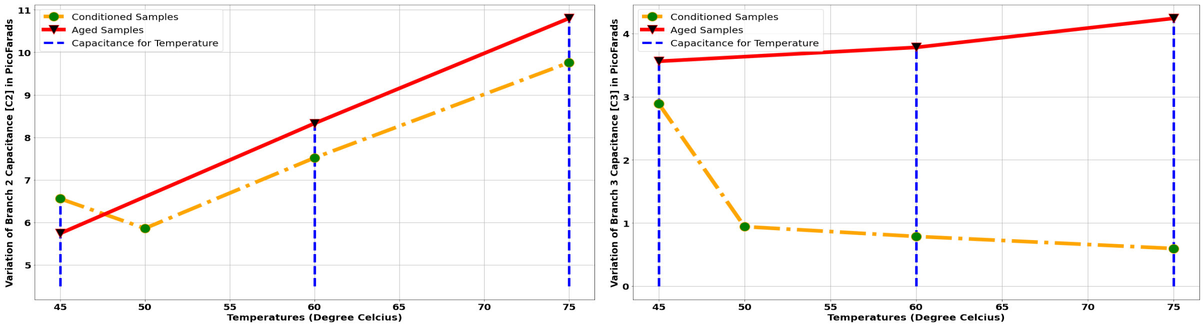

(c) Variation of C2 for Aged and Conditioned Samples

(d) Variation of C3 for Aged and Conditioned Samples

Figure 8.41: Variation of C in different branches for Aged and Conditioned Samples

8.4.7. Conclusion from PDC Measurements:

Case A: With Increase in Insulation Temperature:

- The DC Conductivity of the insulation increases,
- The Conduction Current (I_c) saturation magnitude increases,
- The Polarization Current (I_p) settling value increases,
- The Depolarization Current (I_c) saturation value is unaffected, but the rate of decay varies for different temperature,
- The Electrical Equivalent Circuit Resistances for Branch 0,1 and 2 reduces significantly,
- The Capacitance for Branch 0 remains almost unaffected by temperature and is constant, while for Branches 1 and 2, their values increase,
- The Relaxation Time constants corresponding to the 3 main polarization processes educe.

Case B: With Increase in Aging Degree:

- The DC Conductivity of the insulation increases significantly,
- The Conduction Current (I_c) saturation magnitude increases,
- The Polarization Current (I_p) settling value increases,
- The Depolarization Current (I_c) decays at a slower rate for aged samples over conditioned ones, but eventually settle at same final values after a long time (1.5 hours),
- The Electrical Equivalent Circuit Resistances for Branch 0,1 and 2 reduces significantly,
- The Capacitance for Branch 0 remains similar with aging, while for Branches 1 and 2, their values increase but not very significantly,

Future Research Scope:

The trends should be validated for higher aging periods of 2,3,4,5 and 6 months to see if the trends are maintained which are expected due to the fact that property of insulation is related to thermal aging. Also, as an additional interest, same experiments can be done with oil, paper separately and oil-paper composite together to see if the individual trends are reflected in the combination.

9

Frequency Domain Dielectric Spectroscopy Characterization

Chapter 9 discusses about extracting indication parameters of thermal aging for OIP samples by developing an experimental setup for it. A model would be formulated to calculate real permittivities at very low and high frequencies and all the pre measured data would be fitted in a Cole-Cole Model to extract parameters indicating temperature effect and aging on insulation as shown in the flowchart below. Also, a novel procedure is proposed to extract these parameters using a short duration off-line measurement in the grid which can be applied on the field aged cables for monitoring and diagnostics.

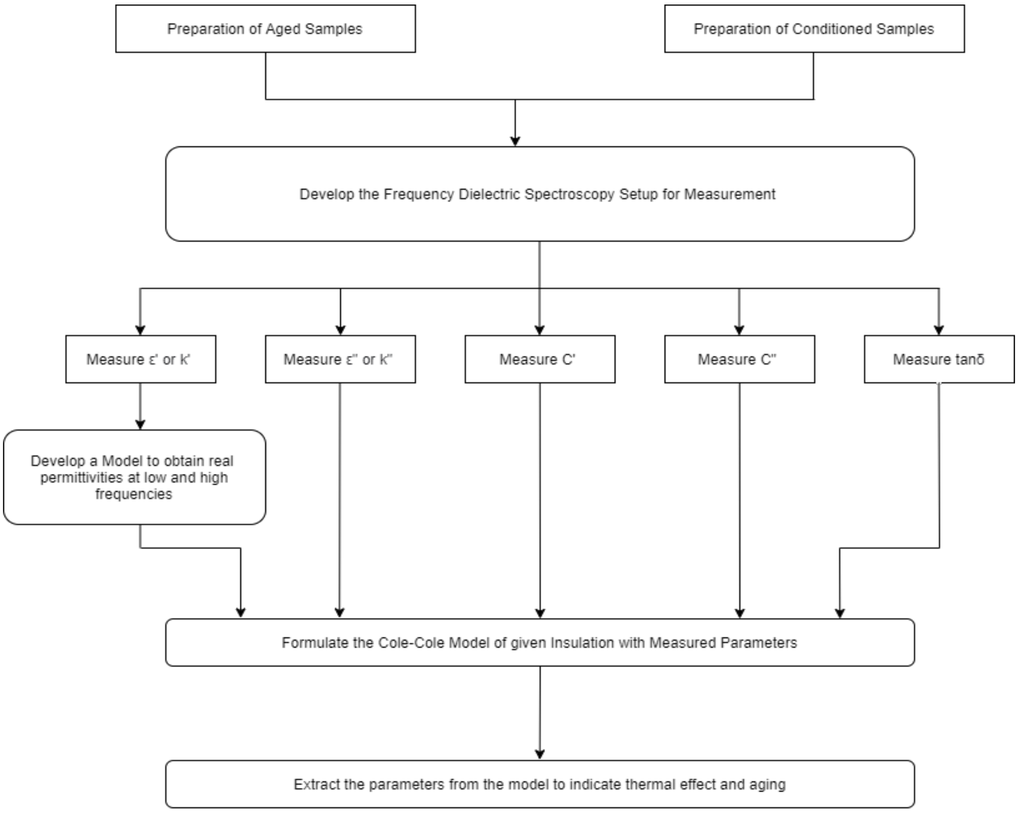

ε' and k' are same and refer to real part of permittivity

ε'' and k'' are same andrefer to imaginary part of permittivity

Flow of Research in Chapter 9:

Chapter 9 discusses the preparation of the samples in the exactly similar way as in Chapter 8 used for the tests. Firstly, the Frequency Dielectric Spectroscopy Measurement Setup is built enclosed by a Faraday Cage. The different dielectric parameters are obtained from the samples prepared at three temperatures. The main objective of this section is to develop a test for the shortest duration which provides maximum information about insulation degradation. So, a model is prepared from one of the measured parameters (ϵ') from which the whole trend of the parameter is determined for very low and high frequencies from a short range frequency sweep. Using all the parameters obtained from the 6-minute test, Cole-Cole model was fitted to extract indicators of aging and elevated temperature. So, the test can be either used separate or in combination with the setup mentioned in Chapter 8, to extract maximum parameters required to build a robust model. The next chapter discusses the possibility of incorporating Partial Discharge Measurements in the designed model.

9.1. FDS Measurement Setup:

The setup with all the detailed parts, shows the experimental implementation for measurement of tan-delta and the capacitance which have been discussed in details in this chapter.

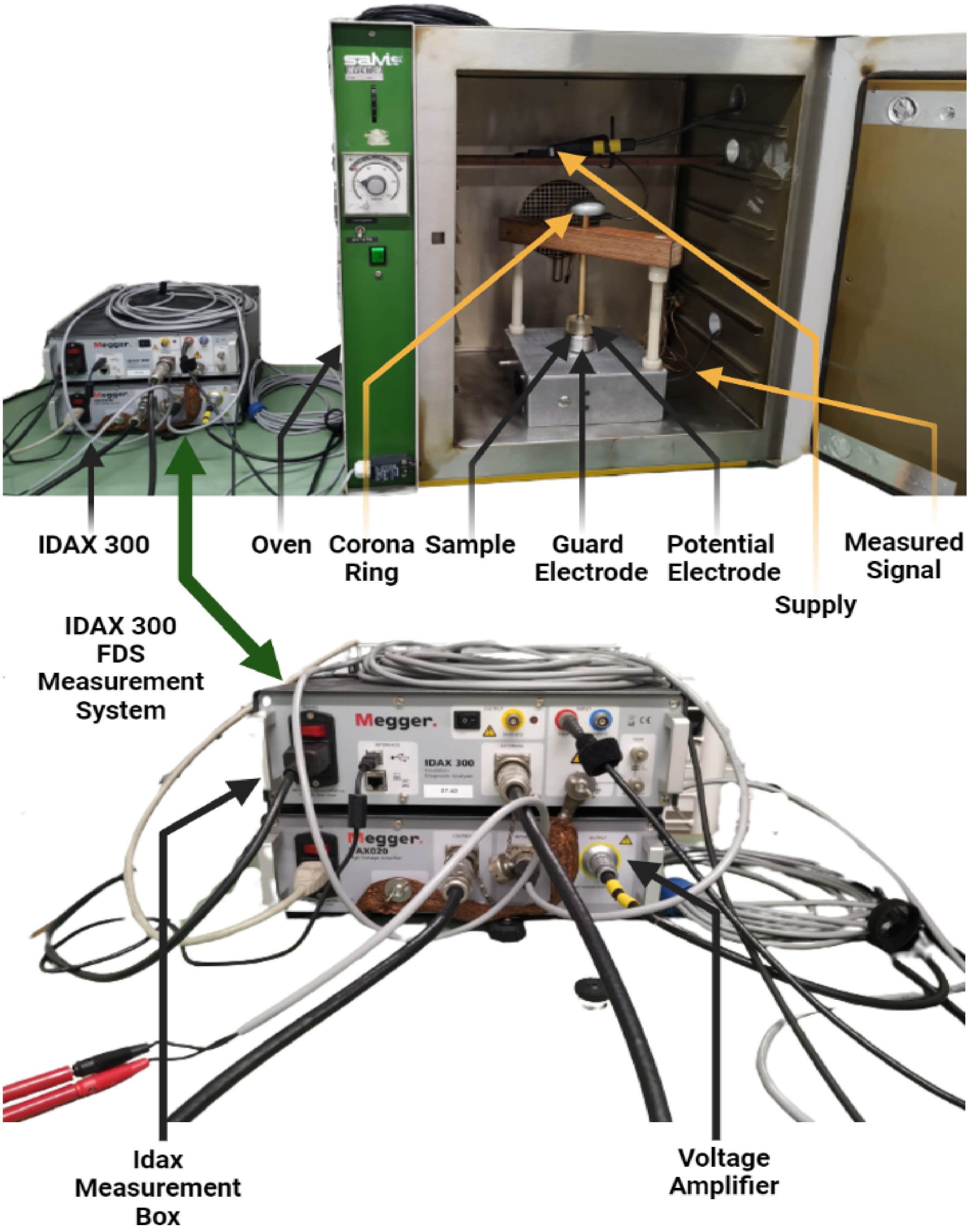

Experimental Setup Description:

The sample are conditioned or aged as discussed in Chapter 8. Then they are transferred to the setup where it is placed between the Guard electrode and the Potential Electrode. The reason for using the guard electrode is to bypass all the leakage currents and measure the current through the sample to give accurate measurements. The IDAX 300 supplies a 200V rated to the sample and thus due to application of the voltage a current flows through the sample which are transferred to the IDAX setup as shown in Figure 9.1. The entire setup is placed inside the oven which acts like a Faraday Cage and eliminates interference.
The impedance is calculated using Ohm's law:

$$Z = \frac{U}{I}$$

where Z, U and I are complex entities.

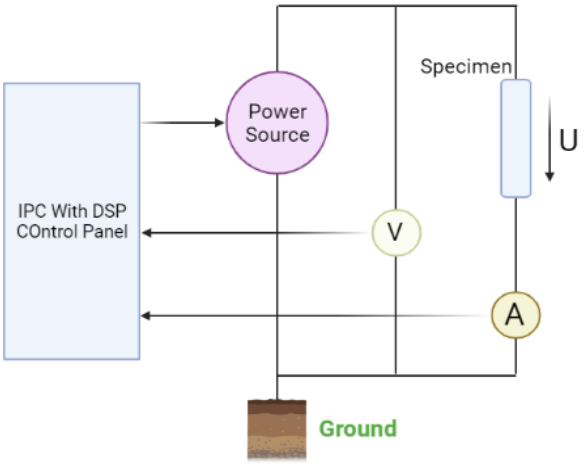

Figure 9.1: FDS Graphical Setup

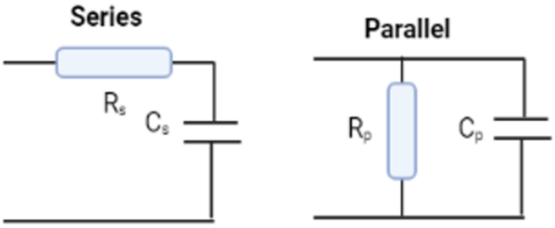

Figure 9.2: Series and Parallel Modelling

Two simple models which are usually used in circuit analysis, although more seldom in insulation analysis, are capacitance, C, and resistance, R. The equivalent RC circuit models available are series and parallel models as seen in Figure 9.2, calculated as follows [128]:

Parallel:

$$Z_p = \frac{R_p}{1 + j\omega R_p C_p} \tag{9.1}$$

$$C_p = \mathrm{Re}\left\{\frac{1}{j\omega Z}\right\} \tag{9.2}$$

$$R_P = \frac{1}{\mathrm{Re}\left\{\frac{1}{Z}\right\}} \tag{9.3}$$

Series:

$$Z_s = R_S + \frac{1}{j\omega C_s} \tag{9.4}$$

$$C_s = -\frac{1}{\omega\,\mathrm{Im}\{Z\}} \tag{9.5}$$

$$R_s = \mathrm{Re}\{Z\} \tag{9.6}$$

where $\omega = 2\pi f$ and f is frequency.

Another model more often used in insulation diagnostics, is the complex capacitance model describing the insulation impedance as a complex capacitance, where the imaginary part of the capacitance represents the losses. The complex capacitance model is defined as follows[128]:

$$Z = \frac{1}{j\omega C} \quad \text{where} \quad C = C' - jC'' \tag{9.7}$$

Complex C:

$$C' = \mathrm{Re}\left\{\frac{1}{j\omega Z}\right\} \tag{9.8}$$

$$C'' = -\,\mathrm{Im}\left\{\frac{1}{j\omega Z}\right\} \tag{9.9}$$

A model, very often used in insulation diagnostics, is a description of the insulation impedance as a capacitance combined with a dissipation factor, $tan\delta$, or a power factor (PF or $\cos\varphi$). The capacitance, tan δ and $\cos\varphi/\mathrm{PF}$ are defined as follows [128]:

$$\begin{aligned} C' &= \mathrm{Re}\left\{\frac{1}{j\omega Z}\right\} \\ PF &= \cos\varphi = \frac{\mathrm{Re}\{Z\}}{|Z|} \\ \tan\delta &= -\frac{\mathrm{Re}\{Z\}}{\mathrm{Im}\{Z\}} \end{aligned}$$

Dielectric Loss, Tan Delta Calculation:

Due to application of AC Voltage, losses occur inside the insulation resulting in a resistive current component, I_r as shown in Figure 9.3, that makes an angle δ with the purely capacitive current, I_c. So, $I_r = I_c tan\delta$ as seen from the Phasor Diagram in Figure 9.3.

The tangent of the angle basically measure's the dielectric losses, W, given by:

$$W = UI_c tan\delta = U^2\omega C tan\delta \tag{9.10}$$

where, C is the capacitance of insulation and U is the phase voltage.

The losses are proportional to the loss tanδ,

$$tan\delta = \frac{I_r}{I_c} = \frac{1}{\omega RC}$$

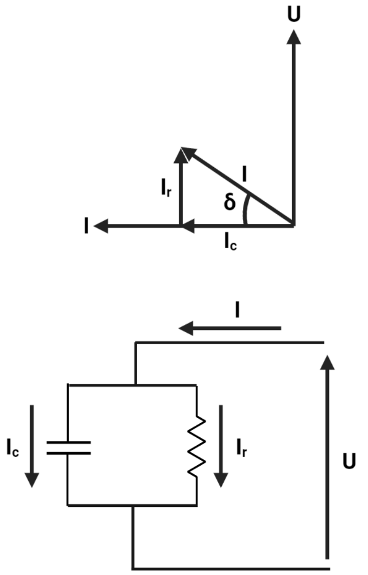

Figure 9.3: Phasor and Equivalent Circuit of Dielectric

Figure 9.3 represents the phasor diagram of the cable dielectric with the resistive and capacitive branch phasor currents, giving the equivalent total current through the dielectric phasor. The other diagram shows the electrical equivalent circuit of the dielectric with the capacitive and resistive branches with their respective currents, flowing due to application of AC Voltage.

9.2. FDS Parameters for Aged and Conditioned Samples:

Case A: Variation of Real Permittivity (ϵ') with Temperature for Aged and Conditioned Sample:

Trend with Frequency: The real part of permittivity ($\epsilon'(\omega)$) increases as the frequency decreases. This phenomenon is well explained by the theory proposed by Debye-Huckel-Falkenhagen [129][130], which states that in disordered systems (OIP system here), the charge transport takes place because of hopping conduction. Also, the motion of charge in the system is accompanied by electrical relaxation where an ionic or electronic charge is surrounded by negative or positive counter charges. The hop of a charge carrier to a new site will lead to successful charge transport if the polarization cloud also follows. The theory also specifies that there is no requirement to treat AC and DC conductivity as separate processes in such case. In Figures 9.4(a) and (b), it can be well observed that with increase in frequency, ϵ' reduces.

Trend with Increase in Temperature: As the temperature increases, the Degree of Polymerization for OIP samples reduce (as discussed in subsection 7.4.3) and that alters the dielectric characteristics. With reduction in cellulose polymer chain length in oil impregnated paper, the real part of permittivity increases [131]. Thus, with higher temperature, the real part of the permittivity shifts upward. For both aged and conditioned samples, it can be observed that with increase in temperature, ϵ' shifts upwards. There is a greater shift for 60 and 75 ^{o}C compared to 45 and 50 ^{o}C observed in both the cases (See Figure 9.4).

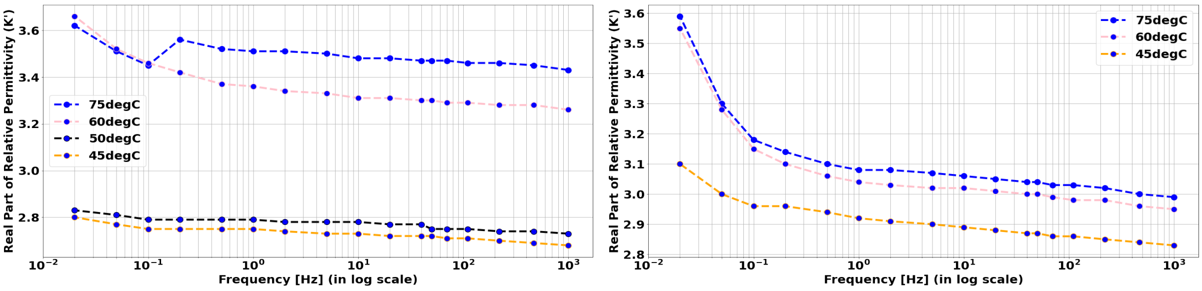

(a) Variation of Real Permittivity for Conditioned Samples

(b) Variation of Real Permittivity for Aged Samples

Figure 9.4: Comparison of Real Permittivity between Aged and Conditioned Samples

Case B: Variation of Real Capacitance (C') with Temperature for Aged and Conditioned Sample:

Trend with Frequency: The real capacitance curve (C'), shows that with increase in frequency the value of C' decreases. The reason is that in lower frequency, since the time is higher, more polarization processes can be completed [131]. When the frequency increases, some slower polarization processes do not have enough time to set up in the fast varying electric field. The real part of complex dielectric permittivity $\epsilon'(\omega)$ reduces and thus the real capacitance will decrease, as shown in Figure 9.5(a),(b).

Trend with Increase in Temperature: With temperature rising, conductivity of the oil impregnated paper sample increases, and induces stronger dispersion effect. It gives rise to an increase of C'. Since C' is proportional to the real permittivity, hence its increase (reasons discussed above) leads to an increment in C'. Thus, with increase in temperature, C' increases and the curve shifts up.

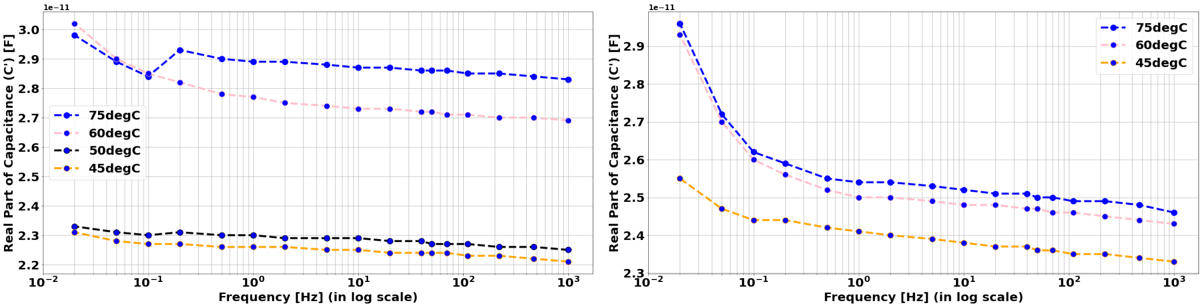

(a) Variation in Real Capacitance for Conditioned Samples

(b) Variation in Real Capacitance for Aged Samples

Figure 9.5: Comparison of Real Capacitance between Aged and Conditioned Samples

Case C: Imaginary Permittivity (ϵ”) Change with Temperature for Aged and Conditioned Sample:

Trend with Frequency: The imaginary part of permittivity ϵ” is observed to first decrease and then increase as the frequency increases for both conditioned and aged samples as seen in Figure 9.6. The low frequency (0.01-1 Hz) and high frequency region (2 - 10^3Hz) for the conditioned samples have been separately addressed in Figures 9.7(a) and (b) where the trend is very clearly observed. This is because as frequency increases, more polarization processes evolve and the frequency dependence of the conductivity is less, which means that dielectric loss is caused by both the conductivity contribution and relaxation process [132]:

$$\tan\delta = \frac{\sigma_0/\omega\varepsilon_0 + \varepsilon''(\omega)}{\varepsilon'(\omega)}$$

Where, $\varepsilon'(\omega)$ is the real part of the complex dielectric permittivity $\varepsilon^*(\omega)$, and $\varepsilon''(\omega)$ is the imaginary part, while σ_0 represents the conductivity of the dielectric.
Thus, higher imaginary permittivity can be observed at lower frequency range due to higher conduction and polarization losses.

Trend with Temperature: ϵ” represents the loss component of the dielectric. As temperature increases, the losses increase and thus with higher temperature, the curve is expected to shift upwards which is observed in both Figures 9.6(a) and (b). Also, the losses are not proportional to temperature, thus, the shift of the curves are not equidistant, and it can be observed that ϵ” for 45 and 50 ^{o}C is much lesser than for 60 and 75 ^{o}C. Also, at high frequencies, where the electric field is changing very rapidly, the effect of temperature is almost not noticeable.

The relation of ϵ” with ϵ' has been discussed in subsection 9.0.4 along with the correlation between log(ϵ”) with log(f) establishing the physical phenomena happening.

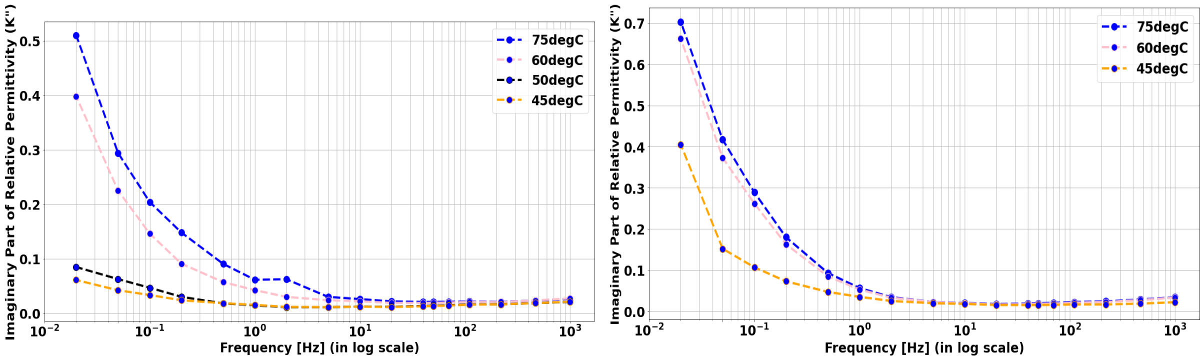

(a) Variation of Imaginary Permittivity for Conditioned Samples

(b) Variation of Imaginary Permittivity for Aged Samples

Figure 9.6: Variation of Imaginary Permittivity for Aged vs Conditioned Samples

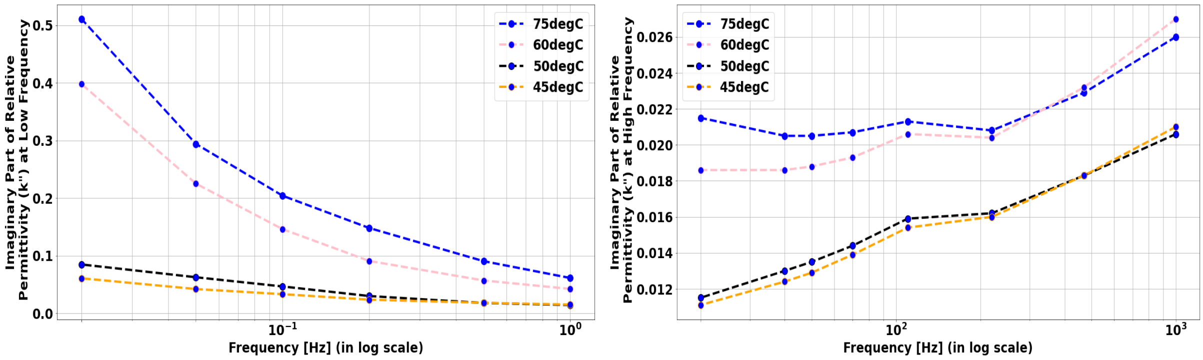

(a) Variation of Imaginary Permittivity for Conditioned Samples at low frequency range

(b) Variation of Imaginary Permittivity for Conditioned Samples at high frequency range

Figure 9.7: Variation of Imaginary Permittivity for Conditioned Samples at low and high frequency range

Case D: Imaginary Capacitance (C'') Variation for Aged and Conditioned Sample:

Trend with Frequency: The imaginary part of capacitance (C”) is proportional to $(\sigma_0/\omega\varepsilon_0 + \varepsilon''(\omega))$ [132]. Since ϵ” decreases to a minimum and then increases (see Figure 9.6), the imaginary capacitance also follows the trend as observed in Figure 9.8.

Trend with Temperature: With increment in temperature, the C” curves shift upwards in lower frequency upto 5 Hz, whereas they exhibit slight changes in higher frequencies. This is caused by the increase in the conductivity of the sample with temperature. In the lower frequency range, $(\sigma_0/\omega\varepsilon_0 + \varepsilon''(\omega))$ increases due to higher conductivity, so C” increases. The trend is observed in both aged and conditioned samples. Additionally it is observed that C” increases for aged samples more than conditioned ones, indicating a degradation of insulation causes higher losses which has been discussed in 7.2.1.

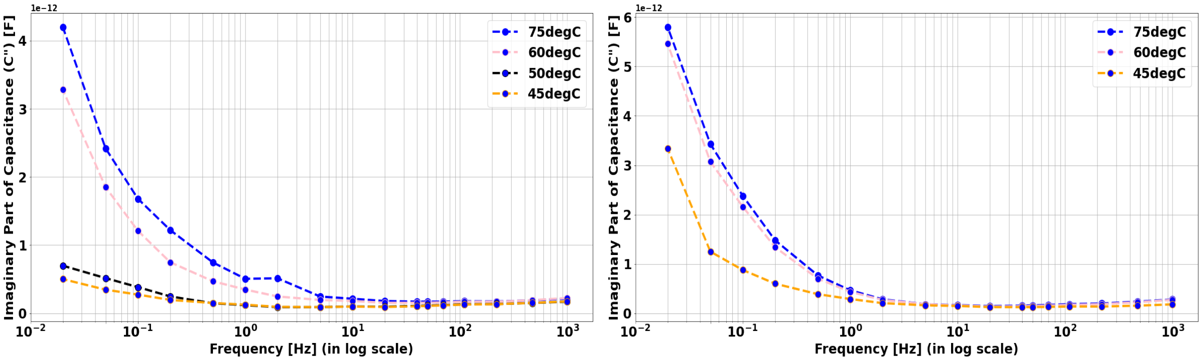

(a) Variation of Imaginary Capacitance for Conditioned Samples

(b) Variation of Imaginary Capacitance for Aged Samples

Figure 9.8: Variation of Imaginary Capacitance for Aged vs Conditioned Samples

9.2.1. Relationship between Imaginary Part of Dielectric Permittivity and Polarization:

In Figures 9.9 (a) and (b), the variation of ϵ' and ϵ” is shown with frequency for conditioned samples at 45 & 50 ^{o}C respectively, yet it also follows for all temperatures and for the aged samples and thus they are not shown again. For very low frequencies (< 0.1 Hz for this case), the complex permittivity, consisting of both real and imaginary parts, increases strongly with decreasing frequencies up to significantly high values, which is a clear indication of electrode polarization [131]. This will mask the dielectric response of the sample and give rise to unwanted parasitic effect during dielectric measurements. Electrode polarization may be due to conductivity of sample, ambient temperature, frequencies but they cannot be explained by molecular relaxation processes. At slightly higher frequencies, 0.1-1 Hz, ϵ' remains almost constant whereas ϵ” reduces as frequency increases, which means that dielectric loss is mainly due to conductivity contribution.

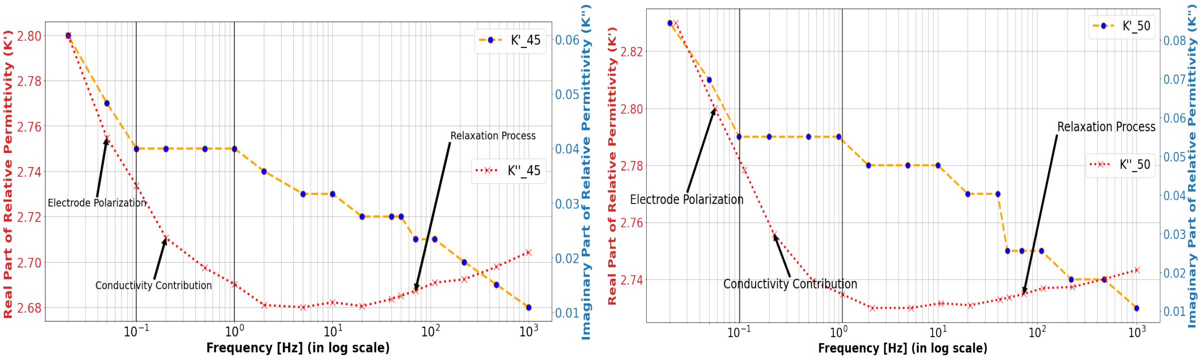

Figure 9.9: Variation of ϵ' and ϵ” with log(f) for Conditioned Samples at 45^{o}C and 50^{o}C showing 3 distinct phases

When log(ϵ”) and log(f) are plotted as in Figure 9.10, it is observed that they have a linear relationship whose slope is affected by Maxwell/Wagner process [133]. Beyond 1 Hz, ϵ” is observed to increase, whereas, ϵ' reduces with increase in frequency [131]. This is the relaxation process generated by the polarization of the dipole and separation of charges at interfaces of oil and paper. Thus, the whole frequency domain dielectric permittivity at constant temperature can be divided into the mentioned 3 parts [131]. With change in temperature, it is expected that the polarization processes and conductivity would be affected, and thus, the Cole-Cole Model would help us in identifying the aging degree in oil impregnated paper cables. For Figure 9.9, if the measurements are taken at close frequencies, then a more smoothed curve could have been obtained. But the three processes are clearly visible which will later enable to model the insulation aging.

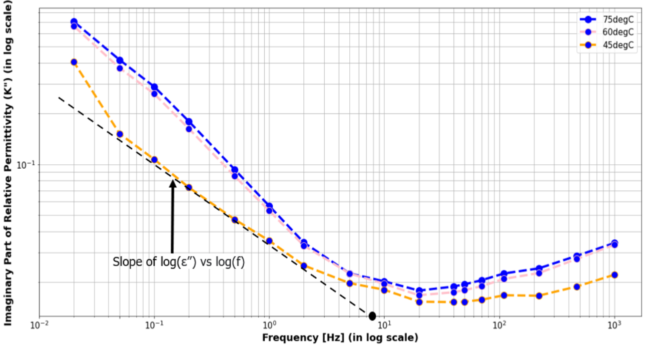

Figure 9.10: Slope of linear region in low frequency range of log(ϵ”) vs log(f) curve

Case D: Tangent Delta (tanδ) Variation for Aged and Conditioned Sample:

Trend with Frequency: In a practical dielectric, which is oil impregnated paper insulation in this case,the dissipation factor $\tan\delta$ should be expressed as [132]:

$$\tan\delta = \frac{\sigma_0/\omega\varepsilon_0 + \varepsilon''(\omega)}{\varepsilon'(\omega)}$$

Where $\varepsilon'(\omega)$ is the real part of the complex dielectric permittivity $\varepsilon^*(\omega)$, and $\varepsilon''(\omega)$ is the imaginary part, while σ_0 represents the conductivity of the dielectric. Now, tan delta depends majorly on the loss component, ϵ”. Previously, from Figure 9.4, it is evident that the change of ϵ' is not significant with frequency at a single temperature, whereas ϵ” decreases first to a minimum and then increases as frequency increases. Thus, the tan delta follows this trend too.

Trend with Temperature:

Tanδ_{min} is the minimum value of tanδ at different temperature which shows an increasing trend with temperature increment as shown in Figure 9.11. It is also possible to correlate the minimum dissipation factor (tanδ_{min}) with moisture content in oil paper samples with a logarithmic relationship [134] but that remains as a future scope to investigate it by validating with chemical tests. Figure 9.12 represents the variation of tanδ with frequency and temperature for conditioned and aged samples. It can be observed that for both sample types, temperature has a significant impact on the dissipation factor. With the increment of temperature, all tanδ curves shift upward in lower frequency range up to 100 Hz. This shift is due to increase in the conductivity of sample which appears in the numerator for tanδ expression. As the temperature rises, the quantity of moving charge carriers and the average kinetic energy of these charge carriers will increase, thereby increasing the conductivity [134]. With increasing the frequency, the conductivity contribution to tanδ reduces gradually. Thus, at higher frequencies the curves are not equidistant. This is evident from the tanδ vs frequency plots dissected into lower and higher frequencies for aged samples in Figure 9.13. Thus, with increase in temperature, the losses increase and the curves shift up for aged samples. For conditioned ones, the same trend is followed, but at very high frequencies (>400 Hz), the conductivity contribution reduces and converge to similar values.

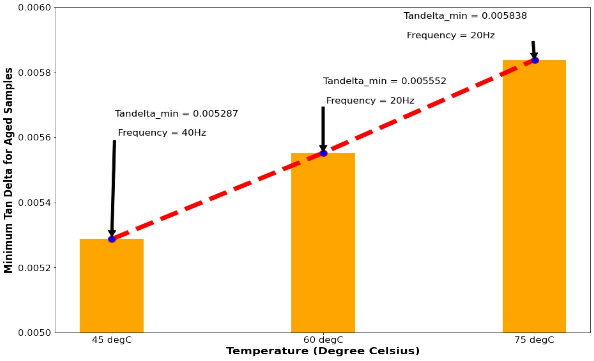

Figure 9.11: Minimum value of tan delta with temperature

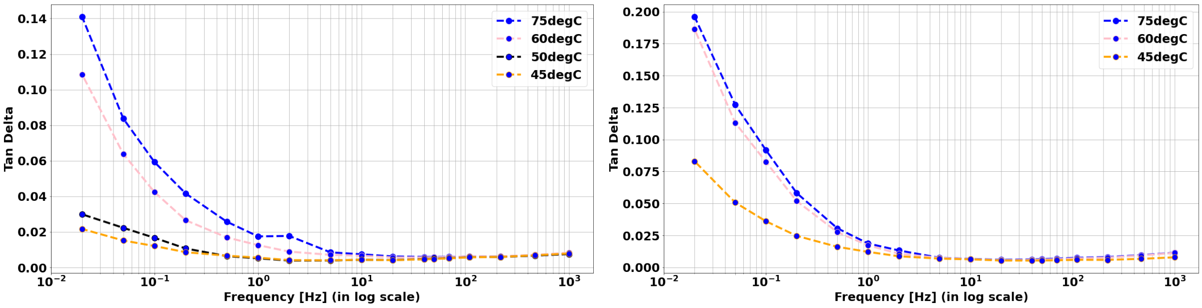

(a) Variation of tanδ vs frequency for Conditioned Samples

(b) Variation of tanδ vs frequency for Aged Samples

Figure 9.12: Variation of tanδ vs frequency for Aged and Conditioned Samples

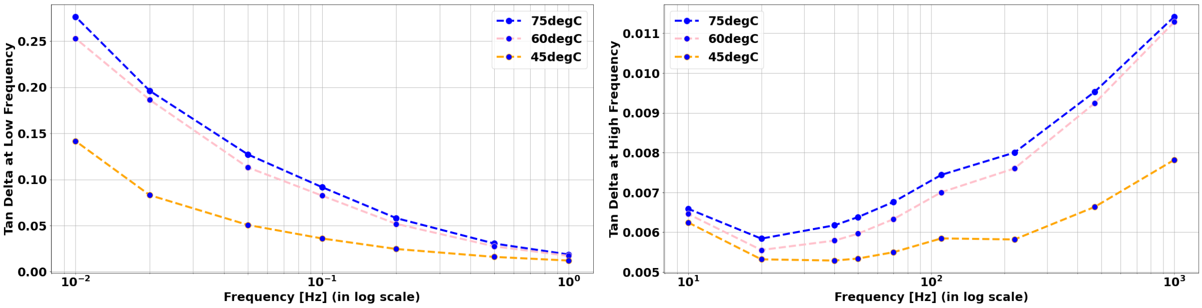

Figure 9.13: Variation of tanδ vs frequency for Aged Samples in low and high frequency range

In Figure 9.14(a),the solid lines represent the aged samples where as the dashed lines are the conditioned ones; moreover the ones at same temperature of each kind are marked with same colours. With increase in the aging degree, it is observed that the tan delta increases because the ionic mobility increases and influences the conductivity level in the OIP sample. This increases tanδ till 100 Hz, after which there is not significant difference in the values as they converge to very close values in an increasing trend. This is because at higher frequencies the contribution of conduction process reduces as discussed before. The value of tanδ at 50 Hz has been plotted in Figure 9.14(b), the operating frequency of the HPGC, which clearly signifies that tan delta increases with aging degree[131][134].

But tan delta increment alone is not sufficient to indicate the degree of aging. So we will analyze the Cole-Cole Model of the insulation. Since the rule of thumb is that if the value of tan delta rises very ”high”, losses would be higher and the chances of failure in future for such cables would be higher. But it is difficult to predict what is a ”high” value, so it has to be coupled with some other derived parameters to have a robust model.

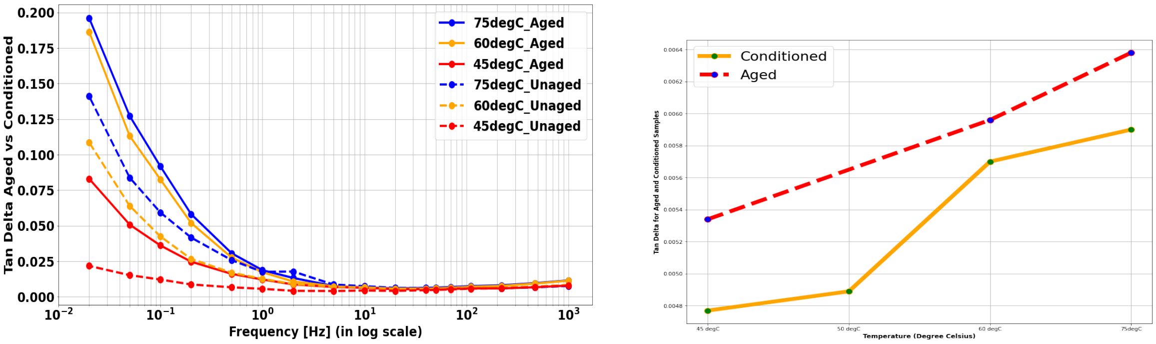

(a) Variation of tanδ vs frequency for Aged Samples and Conditioned Samples

(b) Variation of tanδ vs temperature at 50 Hz

Figure 9.14: Variation of tanδ for Aged vs Conditioned and at 50 Hz

9.3. Deriving Cole-Cole Model for the OIP Samples

Consider the impedance of an insulation is Y(s) in s-domain which can be represented according to equation 9.11, where C_s is the capacitance at very low frequency and C_∞ is the capacitance at very high frequency. With some mathematical conversions, the formula for characteristic impedance Z_a can be determined by removing capacity C_∞ and $(C_s - C_\infty)$ from the admittance operator given by Equations 9.12 and 9.13. The electric equivalent circuit of the dielectric built on the basis of the Cole-Cole model is represented in Figure 9.15(b) with the following governing equations [135]:

$$Y(s) = sC_\infty + \frac{(C_s - C_\infty)\, s}{1 + (s\tau)^{1-\alpha}} = sC_\infty + \frac{1}{Z_1(s)} \tag{9.11}$$

$$Z_1(s) = \frac{(s\tau)^{\alpha} + s\tau}{(C_s + C_\infty)\,(s\tau)^{\alpha_s}} = \frac{1}{(C_s - C_\infty)\, s} + Z_a(s) \tag{9.12}$$

$$Z_a(s) = \frac{\tau}{(C_s + C_\infty)\,(s\tau)^{\alpha}} \tag{9.13}$$

The characteristic impedance $Z_a(s)$ describes relaxation properties of a dielectric. Since the operator s is usually in the fractional power $(0 < \alpha < 1)$ as shown in Figure 9.15(a), determining the equivalent circuit of impedance Z_a is possible only through approximation.

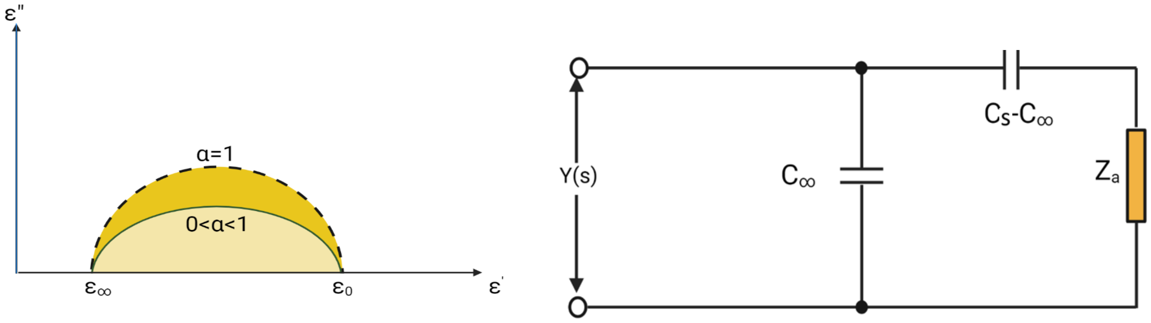

(a) Cole-Cole Circle

(b) Electrical Equivalent Model of Cole-Cole Model

Figure 9.15: Cole-Cole Model Representations

In order to properly determine the formula for the characteristic impedance Z_a for a given dielectric, it is necessary to get to know the parameters of the Cole-Cole model $(C_s, C_\infty, \tau, \alpha)$ [136]. In the case of paper-oil insulation samples, C_s is the capacitance at very low frequency (DC is the most ideal case) whereas C_∞ is the measurement of capacitance at high frequency of measurement voltage. In order to determine the characteristic impedance Z_a, it is still necessary to determine properly the value of time constant τ and parameter α. This can be done only based on the data from experimental measurements. For this purpose, the Frequency Dielectric Spectroscopy (FDS) method can be used, based on which the Cole-Cole characteristics of the complex permittivity $(\varepsilon' - \varepsilon'')$ will be obtained [137].

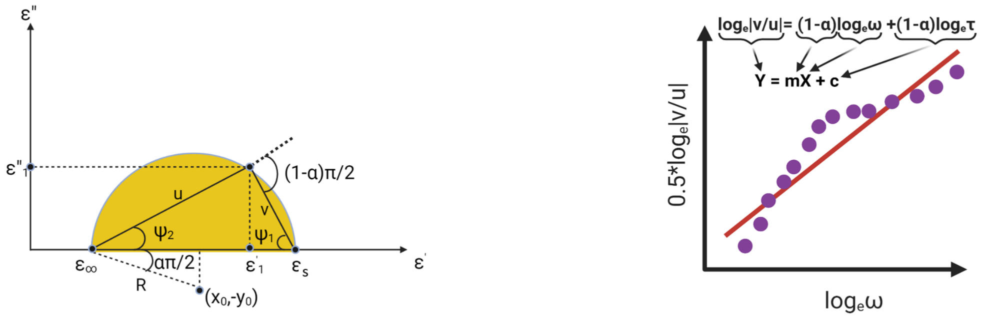

(a) Geometrical Interpretation of Cole-Cole Model

(b) Fitting a linear regression

Figure 9.16: Cole Cole Model Derivation and Fitting Model

The aim of the experimental investigations was to determine the influence of the temperature on the parameters of the Cole-Cole model. Based on the measurements obtained from the FDS test, the complex permittivities ε' and ε'' can be calculated according to:

$$\varepsilon' = \frac{C'}{C_0} \tag{9.14}$$

$$\varepsilon'' = \varepsilon' \cdot tan\delta \tag{9.15}$$

After calculating the value of the complex permittivity $(\varepsilon', \varepsilon'')$, the time constant τ and coefficient α can be determined based on the characteristics from Figure 9.16(a) and the following equations [137]:

$$u = \sqrt{\left(\varepsilon_1' - \varepsilon_\infty\right)^2 + \varepsilon_1''^2} \tag{9.16}$$

$$v = \sqrt{\left(\varepsilon_s - \varepsilon_1'\right)^2 + \varepsilon_1''^2} \tag{9.17}$$

$$\left|\frac{u}{v}\right| = (\omega\tau)^{1-\alpha} \tag{9.18}$$

$$\mathrm{Arg}(v) - \mathrm{Arg}(u) = (1-\alpha)\frac{\pi}{2} \tag{9.19}$$

where, v and u are the side lengths of triangle in Figure 9.16(a)

$$\alpha = 1 - \frac{2}{\pi}(\psi_1 + \psi_2) = 1 - \frac{2}{\pi}\left(tg^{-1}\frac{\varepsilon_1''}{\varepsilon_s - \varepsilon_1'} + tg^{-1}\frac{\varepsilon_1''}{\varepsilon_1' - \varepsilon_\infty}\right) \tag{9.20}$$

$$\tau = \frac{1}{\omega}\left[\frac{\left(\varepsilon_s - \varepsilon_1'\right)^2 + \varepsilon_2''^2}{\left(\varepsilon_1' - \varepsilon_\infty\right)^2 + \varepsilon_2''^2}\right]^{\frac{1}{2(1-\alpha)}} \tag{9.21}$$

Equation 9.21 can also be written as:

$$\tau\omega^{(1-\alpha)} = \left[\frac{\left(\varepsilon_s - \varepsilon_1'\right)^2 + \varepsilon_2''^2}{\left(\varepsilon_1' - \varepsilon_\infty\right)^2 + \varepsilon_2''^2}\right]^{\frac{1}{2}} \tag{9.22}$$

Now, taking logarithm on both sides, and substituting values of u and v from Equations 9.16 and 9.17, we obtain,

$$(1-\alpha)\log_e(\tau\omega) = 0.5\log_e\frac{|v|}{|u|} \implies (1-\alpha)\log_e\tau + (1-\alpha)\log_e\omega = 0.5\log_e\frac{|v|}{|u|} \tag{9.23}$$

Now, by defining the following:

$$Y = 0.5\log_e\frac{|v|}{|u|}$$

$$m = (1-\alpha)$$

$$X = \log_e\omega$$

$$c = (1-\alpha)\log_e\tau$$

Equation 9.23 yields a line graph, $Y = mX + c$ that can be fitted on data points as shown in Figure 9.16(b).

A sample calculation has been done in details to explain the whole process in Section 9.1.

9.4. Deriving the Cole-Cole Model Parameters for OIP Insulation:

Here the procedure is explained using data of conditioned samples at 45^{o}C. The similar procedure is followed at other temperatures for both Aged and Conditioned Samples and it is not repeated.

The following steps are undertaken to extract the aging parameters from the FDS measurements [137]:

Step 1: Acquiring the Real Part of Permittivity (ϵ') at 45^{o}C:

The frequency sweep for FDS Measurement using IDAX 300 is made from 0.01-10^3 Hz. Thus, the sum of all the time is 6 minutes for the whole sweep. The Real Part of Permittivity (ϵ') is extracted for the short sweep and then plotted in MATLAB for the measured frequency range as shown in Figure 9.17.

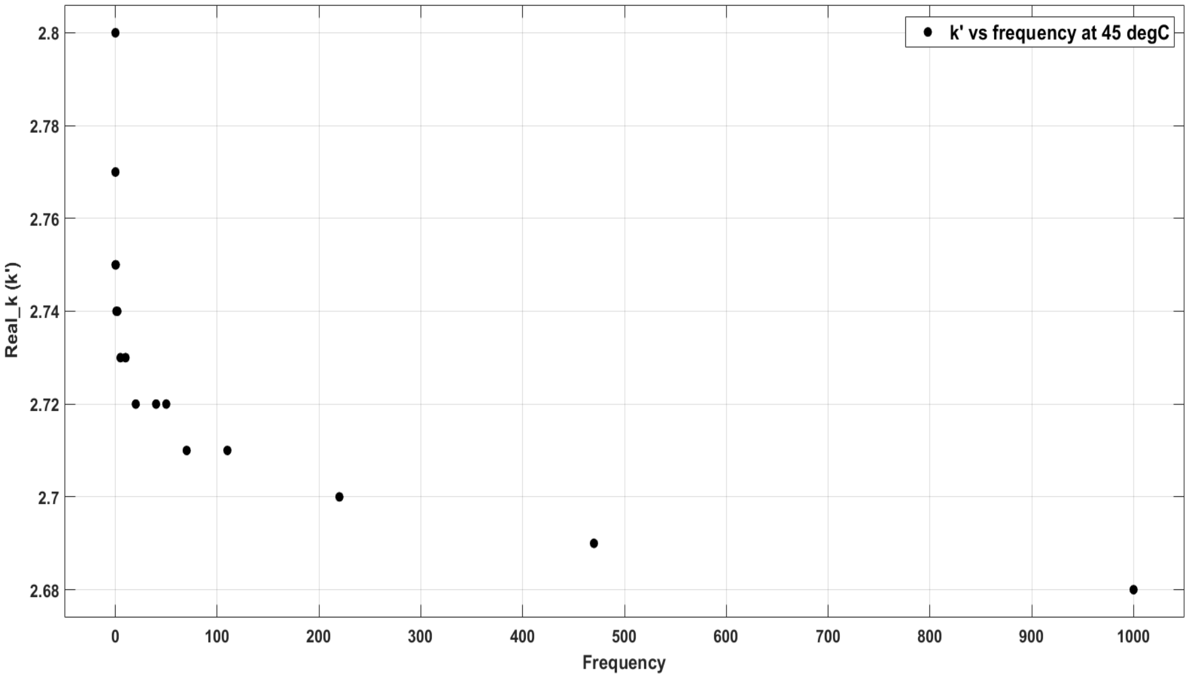

Figure 9.17: Measured value of ϵ' vs Frequency

Step 2: Mathematical Model to Predict ϵ_s and ϵ_∞:

For the model, ϵ_s corresponds to the real permittivity at very low frequency and ϵ_∞ corresponds to one at very high frequency (ϵ_s>ϵ_∞). With tanδ measuring commercial instruments discussed in Section 2.5, the lowest measured frequency is 1μHz, thus also for the model, the same low frequency is considered. For high frequency, it is possible to go to 1 kHz with the commercial device, so in this research, 1 kHz is measured with IDAX. Beyond that frequency, the change in the electric field is so rapid that the polarization processes can not be further modelled (t < 10^{-3} sec). So we consider the range of frequency from 1μHz-1kHz. A best fit power model [138] has been fitted using MATLAB, by minimizing the Residual Errors and having the best R^2 score. The power curve is fitted since it has been discussed in subsection 9.2 Case A. It has been demonstrated that as frequency reduces, ϵ' increases significantly and for high frequencies it saturates mostly and does not change. This fits perfectly for a power law when plotted against frequency in a non-logarithmic scale as shown in Figure 9.18.

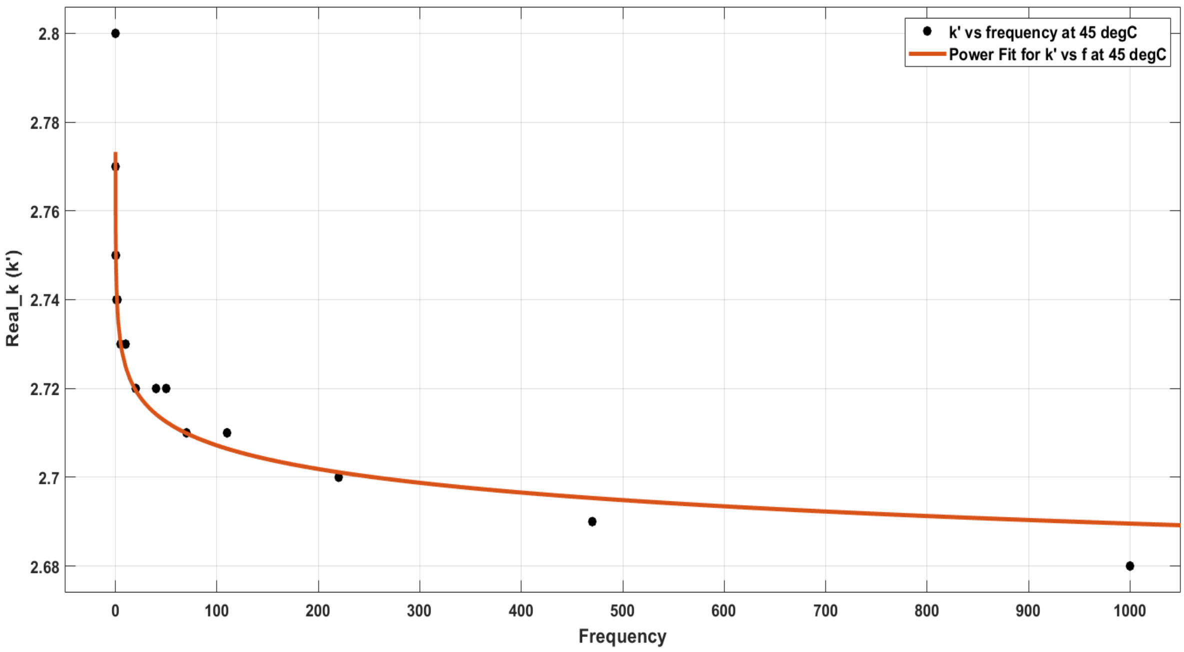

Figure 9.18: Fitting of Power Model in ϵ' vs f for measured data

The power relation between ϵ' and f is :

$$\epsilon' = 2.747f^{-0.003223} \tag{9.24}$$

which gives us, ϵ_s= 2.87 for 1μHz and ϵ_∞=2.685 for 1kHz from the power model.
The value at f=1kHz is almost same as the IDAX measured value of 2.68 validating the accuracy of the model. All the goodness of fit scores for conditioned and aged samples have been reported later in the chapter in Subsection 9.4.1. Due to some different physical phenomena occurring at such low frequencies [131], ϵ_s is higher in measurements but this model gives a good estimation for short time measurements.

Step 3: Fitting the Cole-Cole Model to Extract the Parameters:

For fitting the Model as derived and physically explained in Section 9.3, the following Linear Equation 9.23 derived should be used for the measured points. Now substituting $\omega = 2\pi f$ and by rule of logarithm, $\log_e(\omega) = \log_e(2\pi) + \log_e(f)$.

So, the plot is now $\log_e(f)$ vs $0.5\log_e\frac{|v|}{|u|}$ giving the overall equation:

$$0.5\log_e\frac{|v|}{|u|} = (1-\alpha)\log_e(f) + (1-\alpha)\log_e(\tau) + (1-\alpha)\log_e(2\pi)$$

u and v are calculated from Equations 9.16 and 9.17 in Section 9.3.

Now, after fitting $0.5\log_e\frac{|v|}{|u|}$ vs $\log_e(f)$,

(i) the slope becomes $(1-\alpha)$, and

(ii) the intercept becomes $(1-\alpha)\log_e(\tau) + (1-\alpha)\log_e(2\pi)$.

With mathematical calculations, the value of α and τ can be extracted for each temperature for conditioned and aged samples and then compared. Figures 9.19 shows the linear fit of the measured points and 9.20 represents the residuals of fit (the lower, the better). It can be observed that the fit at very low frequency have larger residues due to the steep rise as justified by the power fit in Step 2.

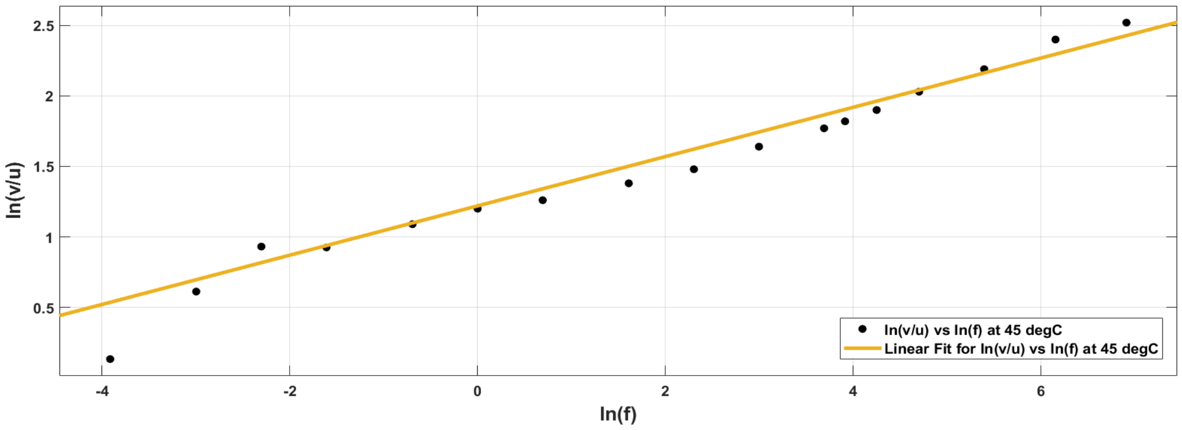

Figure 9.19: Linear Regression fitting on Cole-Cole Model scatter plot

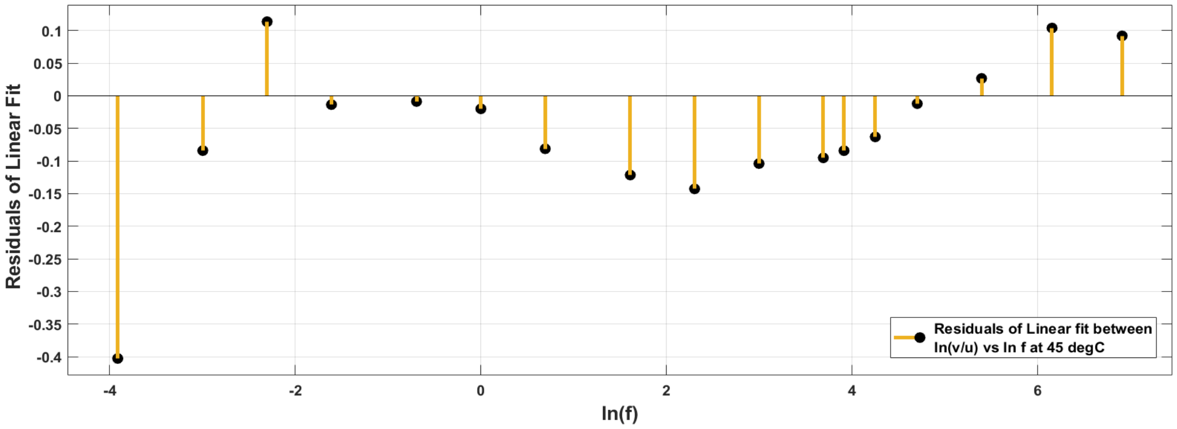

Figure 9.20: Linear Regression Fitting with Residuals

9.5. Scores to Evaluate Goodness of Fit

To evaluate the goodness of fit, commonly used metrics have been used which are R^2 score and Squared Sum of Errors. For Conditioned Samples, log(SSE) is calculated to fit it in the same graph with R^2 scores. So, lower is the SSE or log(SSE) and higher the R^2 score, better is the fit. For small datasets, if one point is an outlier, the R^2 is heavily affected and the SSE also increases [139]. So, the measurements need to be accurate to prevent any form of inaccuracy. This is not faced if the dataset is sufficiently large.

9.5.1. Goodness of Fit for Conditioned and Aged Samples vs Temperature:

Conditioned Samples

Temperature	Power Curve Fit for ϵ'	Linear Fit for Cole-Cole Model
45^{o}C	R^2= 0.9526 SSE= 0.000663 ϵ_s= 2.87 ϵ_∞= 2.68	R^2= 0.97 SSE= 0.1955 Slope= 0.1659 Intercept= 1.232
50^{o}C	R^2= 0.9317 SSE= 0.0008183 ϵ_s= 2.96 ϵ_∞= 2.73	R^2= 0.9222 SSE= 0.6432 Slope= 0.1752 Intercept= 1.197
60^{o}C	R^2= 0.91 SSE= 0.01232 ϵ_s= 3.96 ϵ_∞= 3.26	R^2= 0.9532 SSE= 0.8012 Slope= 0.26 Intercept= 1.705
75^{o}C	R^2= 0.40 SSE= 0.014 ϵ_s= 3.85 ϵ_∞= 3.43	R^2= 0.971 SSE= 0.3198 Slope= 0.278 Intercept= 1.68

Table 9.1: Fitting statistics for power curve and linear fit

From Table 9.1, the goodness of fit from the power curve reflects that the R^2 score is well above 0.9 for the 3 temperatures indicating a very good fit for conditioned samples. For 75^{o}C, the score is low. This is because in the low frequency region one of the points do not follow the trend, which maybe due to noise introduced during measurement creating the deviation. As a result of which the score is affected. Removing this point would increase the R^2 score above 0.9, but that is not done to keep all the measured values intact.

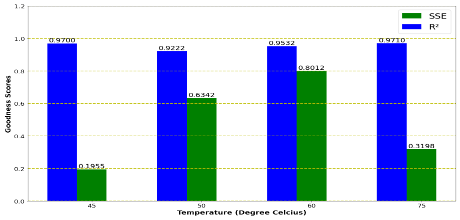

Figure 9.21: Goodness Scores for Linear Fit of Cole-Cole Model

Also, the sum of squared errors are very low and to accommodate them in the same scale, log(SSE) is taken and plotted as shown in Figure 9.22(a). So, higher the R^2 and lower the log(SSE), better is the fitting. Overall, it indicates that the power law is a very optimal fit for predicting ϵ_0 at very low frequencies. Also, after obtaining the parameters it can be seen that as temperature increases, the ϵ'_0 and ϵ'_∞ also increases as seen in Figure 9.22(b). This follows from the variation of ϵ' as discussed before in this chapter. For the linear fit, all the R^2 values are more than 0.9 with small SSE Values indicating that the model is a very good fit for the FDS measurements obtained for the OIP samples as shown in Figure 9.21. The exact same conclusions are also drawn for the aged samples with better fitting and more prominent right shift of the Cole-Cole Circles with increasing temperatures.

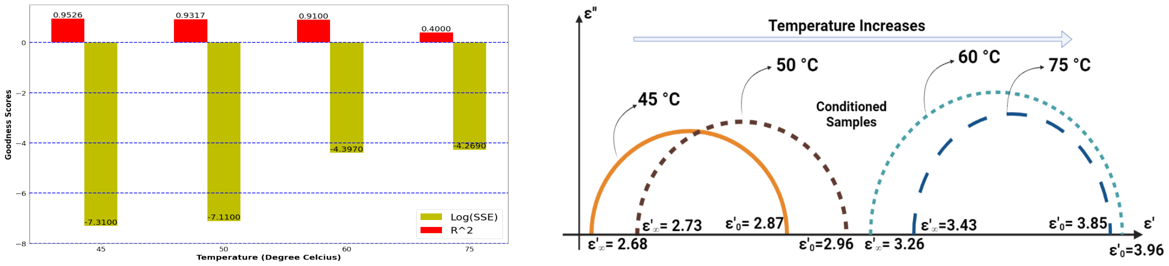

(a) Goodness Scores for Power Fit of ϵ'

(b) Cole-Cole Circles Plotted vs Temperature

Figure 9.22: Curve Fittings leading to geometric construction of circles using Cole Cole Model

9.5.2. Trends of FDS Model Parameters: Time Constant and Alpha

Trend of Time Constant:

The time constant decreases with increase in temperature for both Aged and Conditioned Samples as seen in 9.23(a). This is because increasing temperature interferes with the ordering of the dipole hereby decreasing the value of time constant [135][136][140].

Observations: 1) The relaxation time for FDS Measurement is quite smaller than PC Measurement even though the samples have been Aged and Conditioned for same time. This is because the PDC was carried for 3 hours allowing the slow polarization processes to complete and reflect on the output currents. But the whole point of the research in this chapter is to devise a short term measurement method. Thus, the FDS Measurement was carried for 6 minutes, and thus not all the polarization processes are accommodated in the relaxation time constants. But even for such a short time it is evident that with increase in temperature, the dipoles are affected reducing τ [135]. The next step remains to find an optimal time of FDS Measurement that can be generalized for oil impregnated paper cables. This duration should be sufficient to model certain polarization which can be used to distinguish change in temperatures.
2) The Cole Cole Model treats all the parallel branches as a whole system and thus, it is not possible easily to extract the electrical equivalent parameters which actually reflect on insulation condition. Relaxation time itself is not sufficient to detect the degree of aging.

Trend of α:

In the derivation of the Cole-Cole Model, the coefficient α depends on the structure of the dipole particles participating in polarization. With variation in temperature, the orientation polarization and others take place, changing the structure. Thus, with increase in temperature, the coefficient is observed to decrease [135] as seen in Figure 9.23(b). Note: The disorientation phenomenon with temperature should be investigated for different types of oil paper cables to validate the phenomenon as future research scope. The influence of thermal degradation degree of cellulose on α by shortening the length of cellulose chain and changing the dielectric structure also remains an open question which can be investigated alongside [140].

Temperature	Tau (sec)	Alpha
45^{o}C	268	0.8341
50^{o}C	148	0.8248
60^{o}C	113	0.74
75^{o}C	67	0.722

Temperature	Tau (sec)	Alpha
45^{o}C	99	0.79
60^{o}C	79	0.7481
75^{o}C	28	0.6971

Table 9.2: Change in Cole Cole Parameters for (a) Conditioned (b) Aged Samples

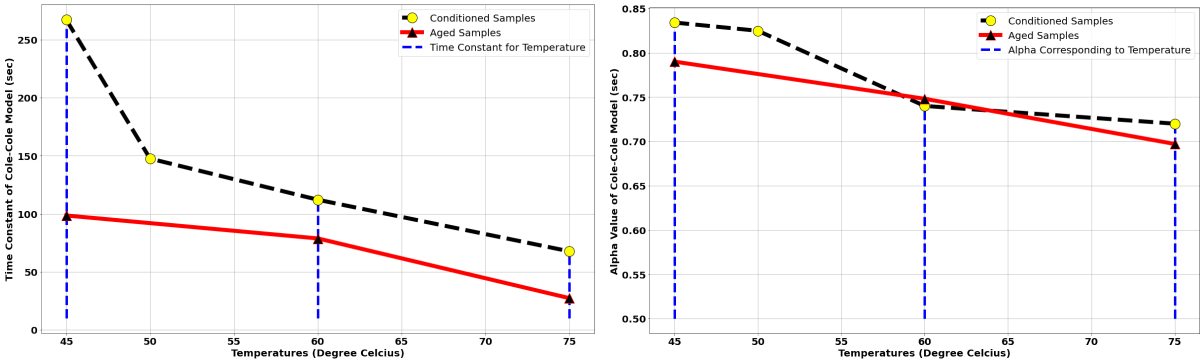

(a) Time Constant for Cole-Cole Model with Temperature

(b) Alpha Value of Cole-Cole Model with Temperature

Figure 9.23: Cole-Cole Parameter Detection and variation with temperature and aging

10

Partial Discharge Characterization

This chapter discusses about the selection of the sample: short length cables or paper insulation? Once decided, the samples are aged at different temperatures. Also, a PD Setup is built to characterize the discharges accurately. Finally some parameters are calculated to observe changes in insulation due to elevation in temperature. Further research needs to be carried out for this section as it gives us an initial path with some positive conclusions.

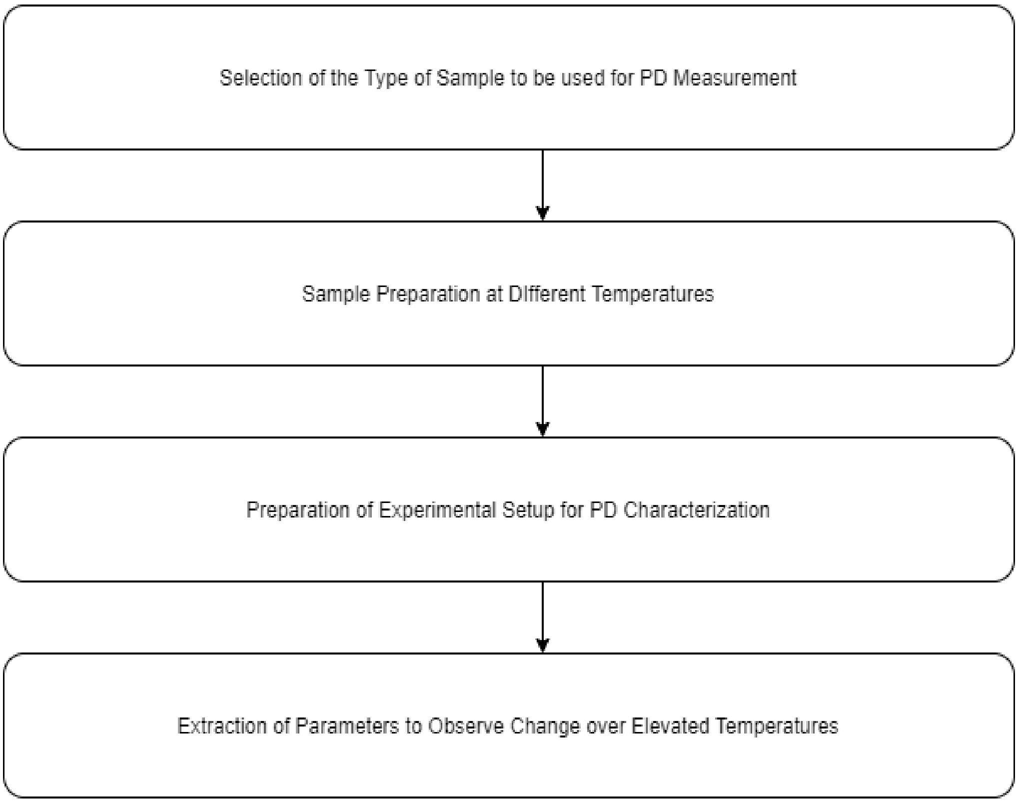

Flow of Research in Chapter 10:

Chapter 10 discusses the incorporation of Partial Discharge Characterization in the aging model. A preliminary study has been performed where the samples are aged at different temperatures and different sample types have been tried before finalizing. Then, a PD Setup was built which was tested to be free from any other discharges occurring due to sharp edges in the setup. After testing that the whole setup was discharge free, the actual experiments was carried out. Parameters were extracted from this test to indicate the degradation of insulation with temperature. Though future research is required to to investigate how PD Characterization can be incorporated in the aging detection model, this research sets the foundation of the possibility for such kind of insulation.

10.1. PD Measurement Setup:

The following setup shows the experimental implementation for measurement of partial discharges, which have been discussed in details in this chapter.

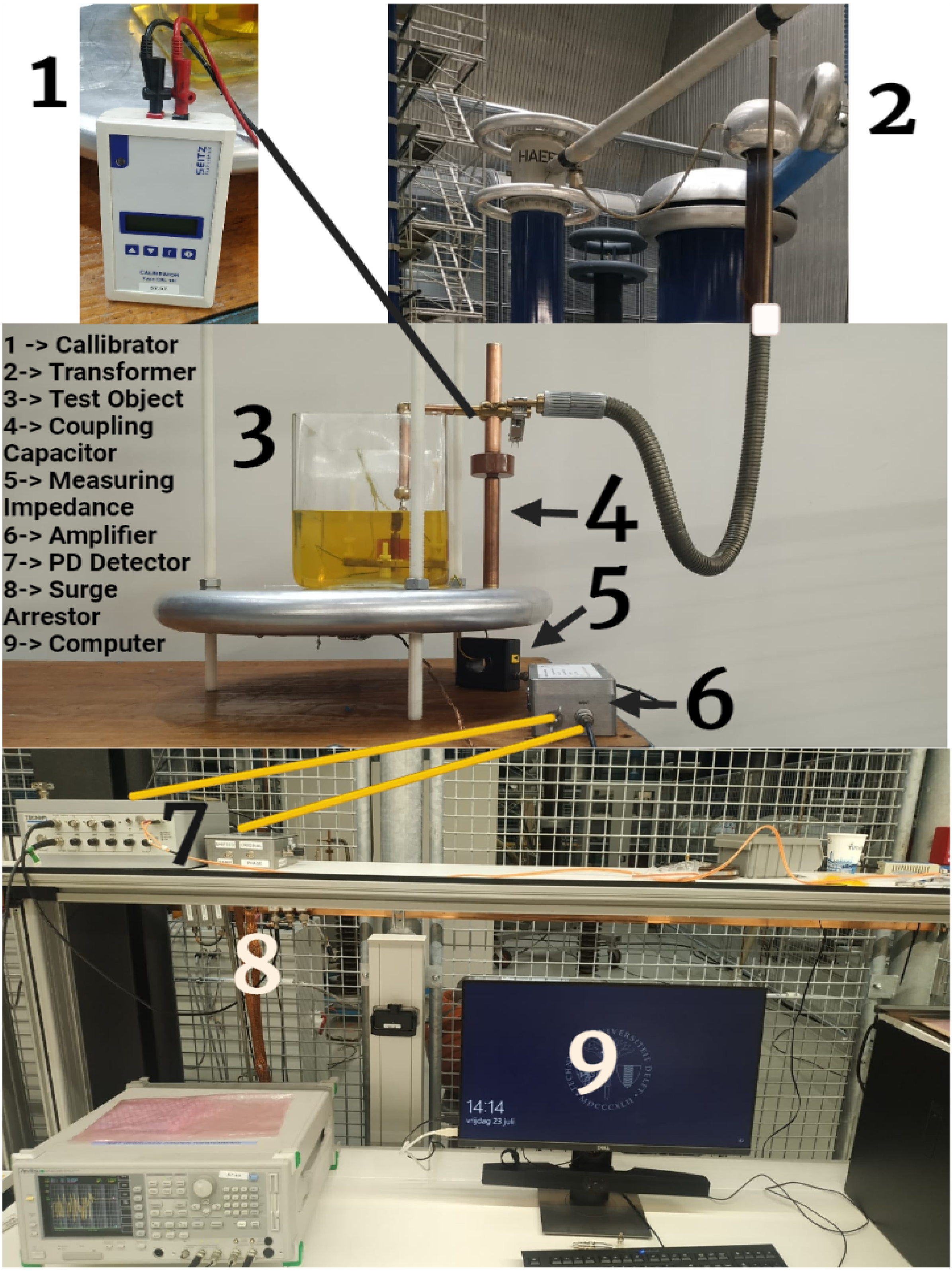

Explanation of the Setup:

The experimental implementation of the partial discharge setup for measuring the PD has been shown. The PD Measurement has been done in accordance to IEC 60270, inspite of having optical, acoustic PD Measurement units, because of the reliability and the repeatability of the robust setup. The HV Source for providing the voltage is given from a transformer, which has been prechecked and found to be PD-Free and without any noise and interference. The standard recommends to use a H.V. Filter but it appeared to be more of an overkill since, the transformer was already checked to be free from producing any noise or interference. Also, it is highly recommended to use the filter when we are performing the tests close to the maximum voltage rating of the transformer. Discharges are more likely at that voltage, but it is not the case for us. The maximum measurement voltage never exceeded 10 kV for the OIP Samples, whereas the transformer rated voltage is 200 kV. A shielded connection is made between the HV Source and the sample, placed between the HV and the ground electrode as seen in Figure 10.1. The setup is made inside a glass jar where the ground electrode is placed on the flat surface. The H.V. Electrode is casted in epoxy as discussed in Chapter 3, to prevent any floating electrode due to small rounded surface area of H.V. Electrode and also to prevent any surface discharges [141].

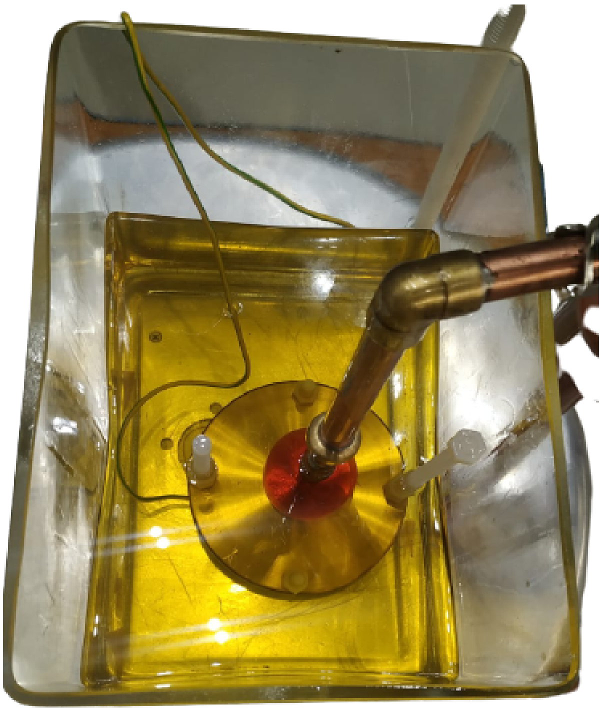

Figure 10.1: Electrode-Sample Setup for PD Measurement

The oil used is different to the oil impregnated in the cable sample. But the sample is kept in the oil for such a short time that it does not interfere with the material properties of the OIP sample. The purpose of the oil is to prevent any surface flash-over which was happening without it in air. The samples were kept in oil for 15 hours, which was not sufficient for the oil to penetrate the paper and affect the chemical properties.

The PD signal generated from the sample is in form of a current. This flows in form of a loop connecting the sample, measuring impedance and the coupling capacitor as seen in Figure 10.3. The coupling capacitor is 1 nF and is much higher than the insulation capacitance, in the range of 10’s of pF. The coupling capacitor basically provides a low impedance path for the HF discharge current to circulate. The ratio of coupling capacitance to the test object capacitance determine the sensitivity of PD measurement. However, increasing the capacitance also necessitates higher power supply to provide greater load current, which is not an issue in this case. A large coupling capacitor also increases time constant, thereby increasing the width of discharge pulses. The measuring impedance, which is basically a current transformer is connected in series to the coupling capacitor converts the input current signal of the partial discharge to an output voltage signal but blocks the power frequency signal. This ensures no 50 Hz signal or harmonics in the measured PD voltage signal. The signals are very low in magnitude and they are amplified with a ratio of 25.3 dB. The measuring impedance has to be equipped with surge over voltage protection devices in case of component breakdown or short circuit. This PD voltage signal is detected by the PD Detector, which serves as the signal acquisition unit. The filter ranges have to be precisely implemented in the detector. Also, selecting the right frequency band for PD Measurement is very vital, which is done using ”Trigger by Level” or ”Trigger by Position” . These signals are then observed in the PDBase Software running in the computer, which distinguishes noise, internal and surface discharges, corona and invalid signals.

Care should also taken to ensure all the parts are grounded properly. After each test, the H.V. Source is grounded to ensure there is no residual charge remaining, which can be detrimental for the working personnel. At the beginning of the PD Measurements, the system has to be calibrated with a known pulse as shown in Figure 10.2 so as to quantify the amount of charge observed in picoCoulomb (pF). It has to be removed after calibration before starting the test.

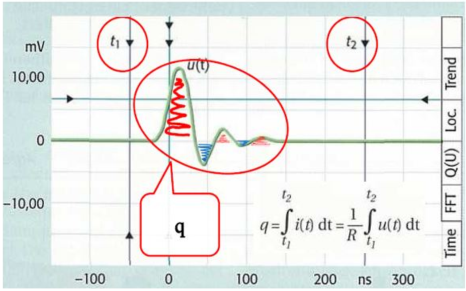

Figure 10.2: Calibration with a known Pulse

The following steps are followed while measuring the PD from the software:

Step 1: Checking the noise spectrum: Noise comes from the three main categories: random noise, switching noise and sinusoidal noise. So, the triggering is made in such a way that it is always above the noise level. Also, before starting the experiment, the setup was checked to ensure that the background noise was low.

Step 2: Checking the calibration Spectrum: The linearity of the calibration was checked by injecting multiples of the originally injected charge value. Also, one has to make sure to remove the ground rod from the circuit to avoid calibration errors.

Step 3: Analyzing the PD Patterns: The filter bars should be placed properly in the software to eliminate any noise and focus on the PD patterns, else, it would be rendered as invalid signal. Also, the test needs to be carried out for multiple samples to validate any trends.

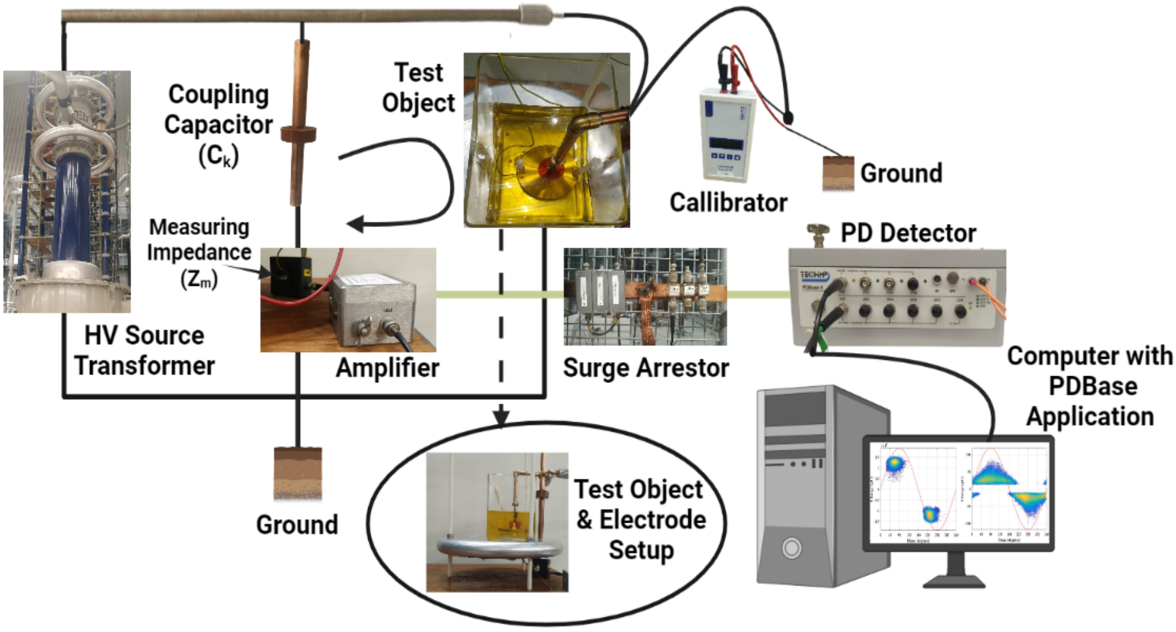

Figure 10.3: Schematic of PD Measurement

Preparation of Samples: For the PD Test, the cable has been cut open vertically and the insulation is removed like a book. 3 layers are removed from each of these cut sections. Then all the samples are kept at 75^{o}C for 1 week just as the preparation during PDC or FDS Tests. Then 10 samples were shifted to 45^{o}C and the rest were kept at 75^{o}C for 2 more weeks. Thus, the samples are aged and kept at different temperatures which mimic similar aging procedure as for the Aged Samples prepared for the Tests in Section 8 & 9. Before the test, the samples were shifted in transformer oil, and kept for a very short duration such that it does not interfere with the properties of OIP samples.

10.2. PD Patterns for Samples at 75^{o}C:

6 sample patterns have been demonstrated below in Figure 10.6 out of all the samples, to give an overall understanding of the shape of the PD Pattern at that temperature. Before starting the test, the setup was tested without any sample at very high voltage to check if there is a discharge from any part of the setup. Luckily, no such discharge was detected and thus, we proceeded with the experiments.

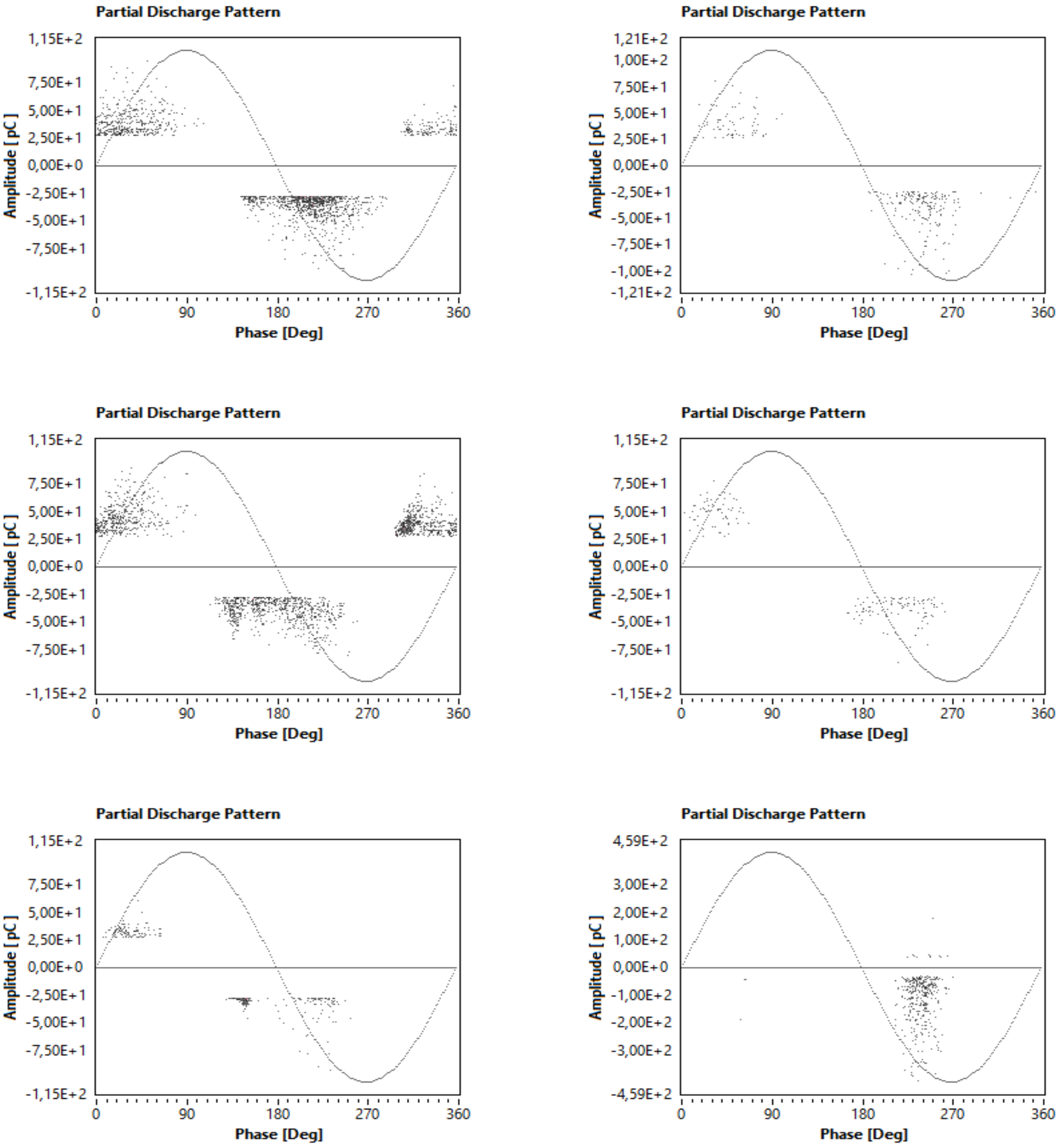

Figure 10.4: PD Patterns for 75^{o}C

It can be observed that all the PD Patterns are concentrated near the zero-crossings of the sinusoidal wave with a definite circular dome pattern. This refers to internal discharges in the OIP samples which occurs at zero-crossing. Except for one of the samples as observed in last sub-plot in Figure 10.4, the discharges are mostly concentrated in the negative peak yet it is not corona discharge since it is not near the negative peak and neither does it have a circular dome like structure. It would mean there are positive discharges but they are below the threshold, hence they are not reflected in the diagram. The rest of the plots are very similar with prominent internal discharge patterns.

10.3. PD Patterns for Samples at 45^{o}C:

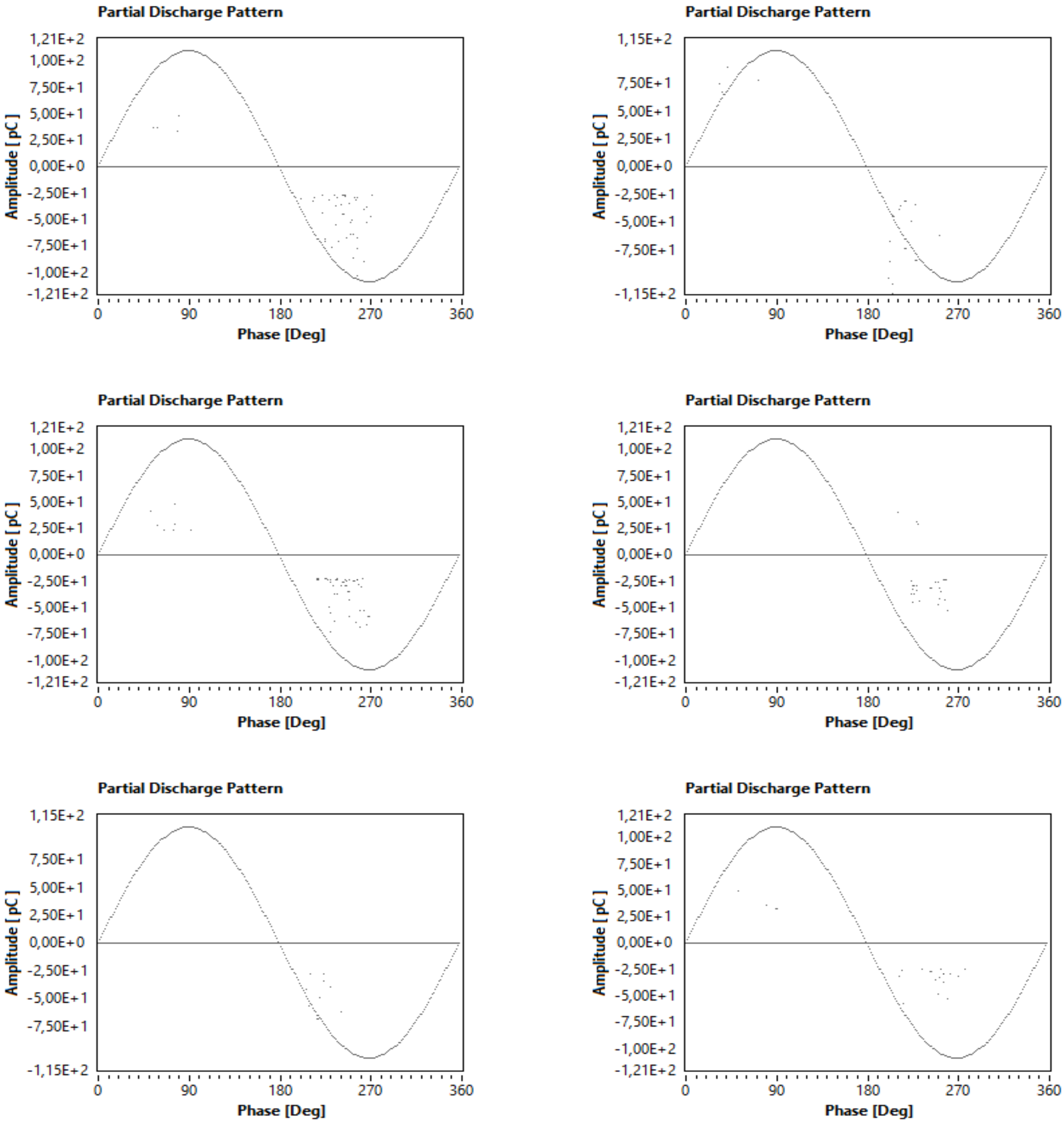

Figure 10.5: PD Patterns for 45^{o}C

For 45^{o}C, PD are observed in positive and negative peaks but they are very few in number as seen in Figure 10.5. For both the temperatures, 10 kV is applied, a voltage substantially higher than the PD Inception Voltage, on the 3 OIP stack for measurement. The captures are taken after 5 minutes of stabilizing in each case so that the repetition frequency is on the same time scale.

In a previous attempt, 0.5 m of cable samples were taken for testing, but because of unavailability of bushings, there was a lot of surface discharges from the terminations, so high that it was visual. Thus, it had to be replaced with samples. An interesting observation is that even though the cables are old, the impregnation coefficient is still very high as a result of which the discharge is quite low. The next section focuses on the comparison in the change of the PD Activity due to change of temperature.

10.4. Change in PD Pattern with Temperature

The study aimed at seeing the correlation of temperature with PD Activity which requires more future work to develop a good understanding.

PD Repetition Rate reflects the intensity and degradation level of OIP samples. The parameter expresses number of partial discharges per minute. Although number of negative pulses were more than positive pulses in all cases, Figure 10.6 (a) and (b) represents the sum of both polarity pulses repetition rate at 75 and 45 ^{o}C at 10 kV RMS, at which the discharging process intensifies but is not sufficient to breakdown. The blue line and yellow lines represent the median and mean values of raw data. To have a better estimate the repetition frequency at two temperatures are fitted with Weibull and the correlation coefficient of 0.946 and 0.878 show how good fit the distribution is. The scale parameter basically reflects the repetition rate which is basically the value for 63.2% samples. Different distributions were fitted and it was observed that Weibull distribution was the best fit with maximum correlation coefficient and interpretability. Thus, 2 parameter Weibull was chosen as the distribution to fit the data as seen in Figure 10.7 for the 2 temperatures. For 75^{o}C, the rate is 618 /s whereas for 45^{o}C, it is only 28 /s. This striking difference shows that with increase in 30^{o}C, temperature, repetition rate is almost 22 times higher. At lower temperature, there is very low PD (in one case it was just 1), whereas for higher temperatures, PD Rate went as high as 1736, and the growth with temperature seems to increase it exponentially [142].

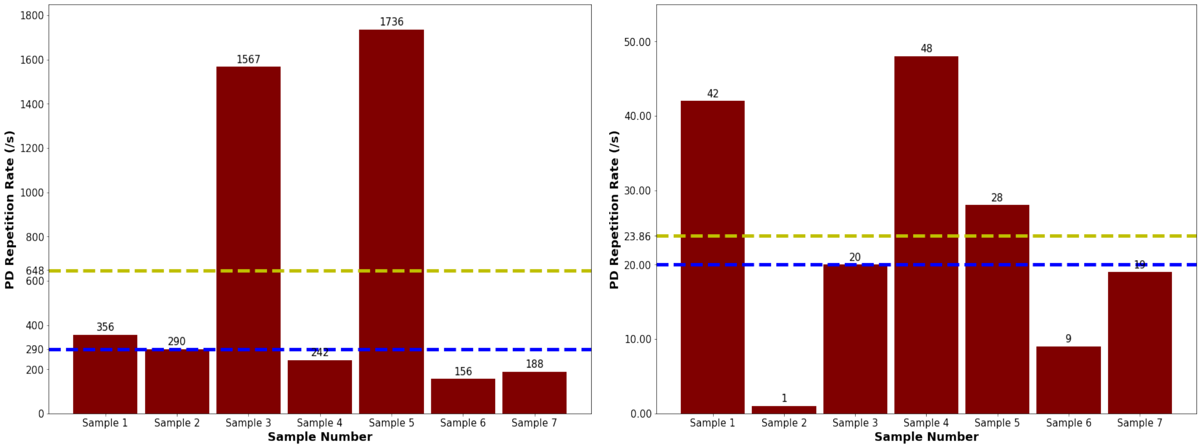

Figure 10.6: PD Repetition Rate for 75^{o}C and 45^{o}C

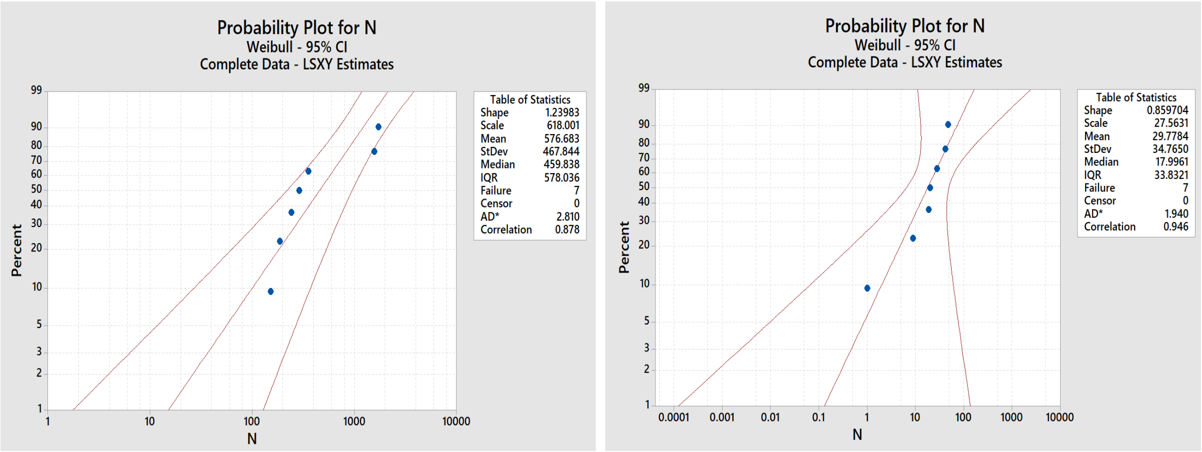

Figure 10.7: 2-parameter Weibull to fit PD Repetition Rate Data at 75^{o}C and 45^{o}C

The phenomenon is considered to be due to change in conductivity of oil and paper with increase in temperature during the lab aging phase. The cellulose chains break down at higher temperature lowering the mechanical strength of paper creating voids which is not perfectly replenished by oil and those weak spots become the hub of PD activities [143]. At lower temperature, impregnation is not affected much and possibility of voids remain only if they are already present during manufacturing. This gives an indication about how PD can be utilized for detecting temperature changes on samples derived from actual cable pieces and not impregnated artificially at lab, giving a more close-to-real case.

Readers might wonder why inception voltage is not compared. It is seen that the diameter and corner curvatures of the electrode actually affected the inception voltage. The PD test was performed for different types of electrodes on the sample. It was seen that the repetition rate was similar for all types, but inception voltage varied. In an extension of future work, it remains an open question as to how the electrodes can be optimized which can be used for samples taken from cable, which can produce repeatable results.

The other important feature, after repetition rate and inception voltage is the mean charge. Though the maximum and minimum charge may vary due to sudden occurrence of a PD which is mostly an outline, the mean of them would give somewhat an average of the sample set. Figures 10.8(a) and (b) represents the mean charge for 75 and 45^{o}C respectively. The anomaly in the last bar at 75^{o}C is due to the scattered PD structure discussed in Figure 10.4 (Last Sub figure). Except for that, there is not much deviation in the mean charge and thus, temperature deviation actually does not affect the pulse magnitudes. Infact, the data is so close that there is small difference between the mean and median as visible from the 2 horizontal lines. Thus, it cannot be used as an basis of distinction for elevated temperatures [144][142].

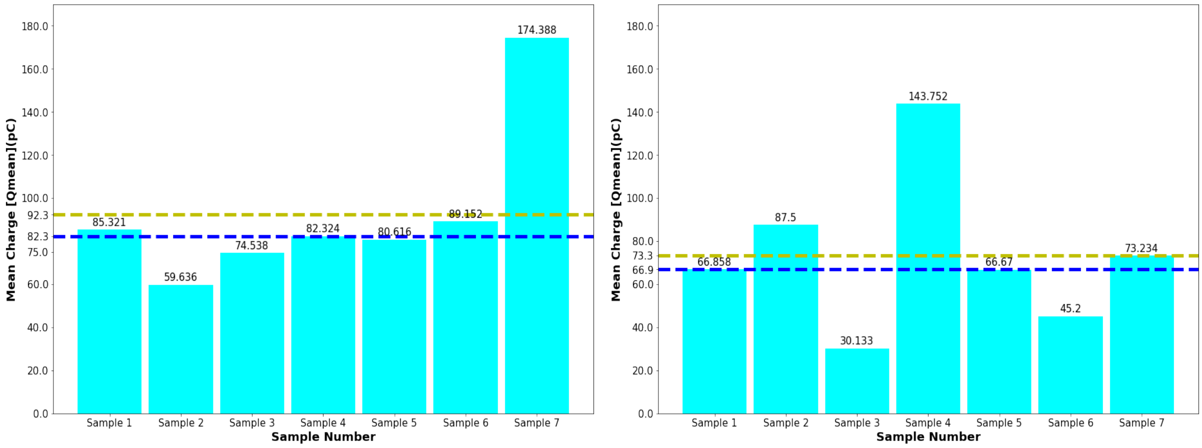

Figure 10.8: PD Mean Charge for 75^{o}C and 45^{o}C

Further research needs to be done to analyze, how to recreate the experiment with high repeatability with electrodes of different diameters and curvatures producing similar PDIV. Also, there needs to be further investigation if the experiment could be one without using the external oil, without creating any surface discharges. But the clear indication of increase in PD with temperature for HPGC is established.

11

Conclusion & Future Scope

Chapter 11 discusses about all the observations drawn from the previous chapters 5-10 to answer the questions formulated in Chapter 1, Section 1.3 as Research Questions. It also introduces to the Future Scope of the research that can be extended for validation. The structure of this Chapter can be summarized by the following flowchart.

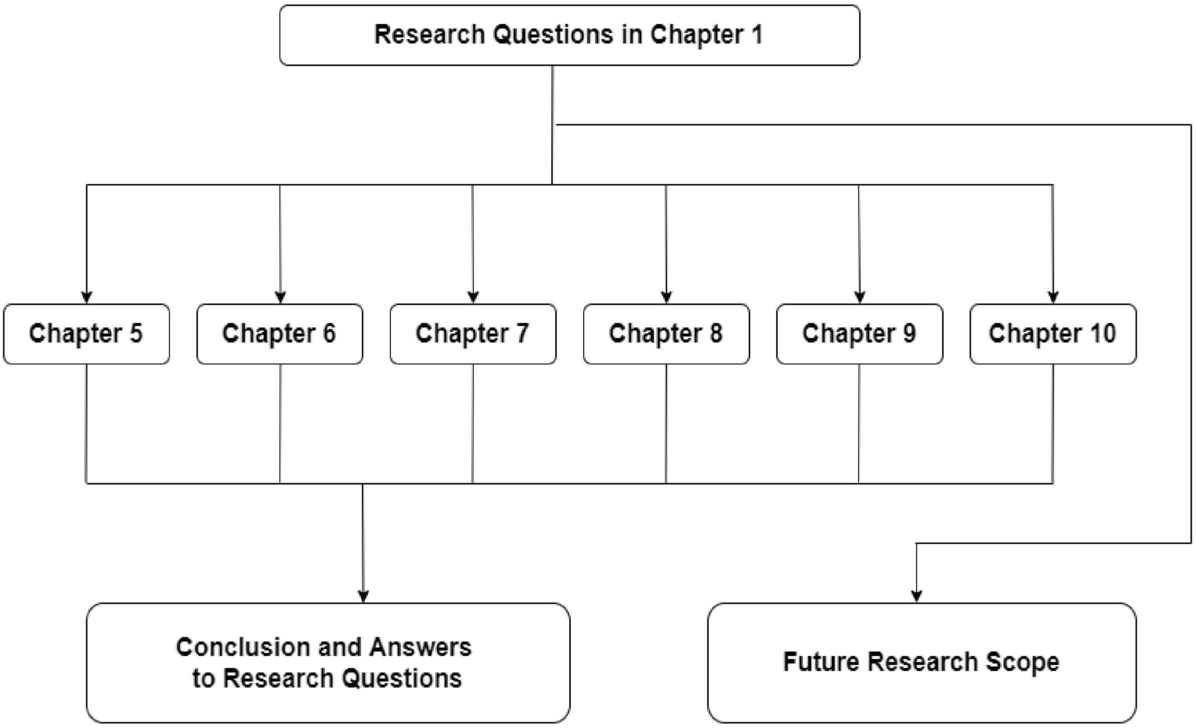

11.1. Conclusions from the Research

The research questions have been answered and the conclusions are reported with the explanation of the phenomena in the respective chapters.

1) How does the electrothermal combined effect age the insulation at different temperatures and how to model the lifetime from limited failure data using advanced statistical analysis?

In Chapter 6, Fast Ramped Breakdown Tests were used to determine the breakdown voltage of the OIP samples which gave us the first observation that as temperature increases, the breakdown voltage reduces as seen in Figure 6.33(a). This can be explained since the temperature is already high, say for 75^{o}C, a smaller magnitude voltage would be required to cause the damage in the OIP to break it down. With the evaluation of the BDV at different temperatures, the steps were designed for the long term step stress tests. From chapter 7, the failure data was fitted into Weibull distribution with the power law model and solved using Maximum Likelihood Estimation method which enabled us to find the parameters for the model. It was observed that the β value was always constant at 1.5 which signifies that the failure rate behaviour at all temperatures is same and is on the same region of the wear-out phase. The important finding was that the non-linear reduction in the value of the exponent for power law, n, with increase in temperature as:

	45^{o}C	60^{o}C	75^{o}C
n-parameter	13.61	10.81	7.38

Table 11.1: Reduction of n with Increase in Temperature

The power-law as introduced in Chapter 7 is given by: $L(s) = \frac{1}{KS^n}$. Now, the constant, 1/K is often replaced by D_{tot} called the damage or ageing dose at failure which affects the lifetime of the sample [145]. So, the power law can be re written as: $L(s) = \frac{D_{tot}}{S^n}$. Taking logarithm on both sides, we arrive to the following equation:

$$log(S) = \frac{1}{n}log(D_{tot}) - \frac{1}{n}log(L(s)) \tag{11.1}$$

which represents a line with negative slope if we take Y = log(S) and X = log(L(s)) giving a slope of $-\frac{1}{n}$, which are represented by Lines L1, L2 and L3 for 3 temperatures as seen in Figure 11.1. Now as 1/n increases the slope increases and the line becomes steeper or equivalently if n decreases the lines become steeper. L3 represents the power law for 75^{o}C, L2 for 60^{o}C and L1 for 45^{o}C.

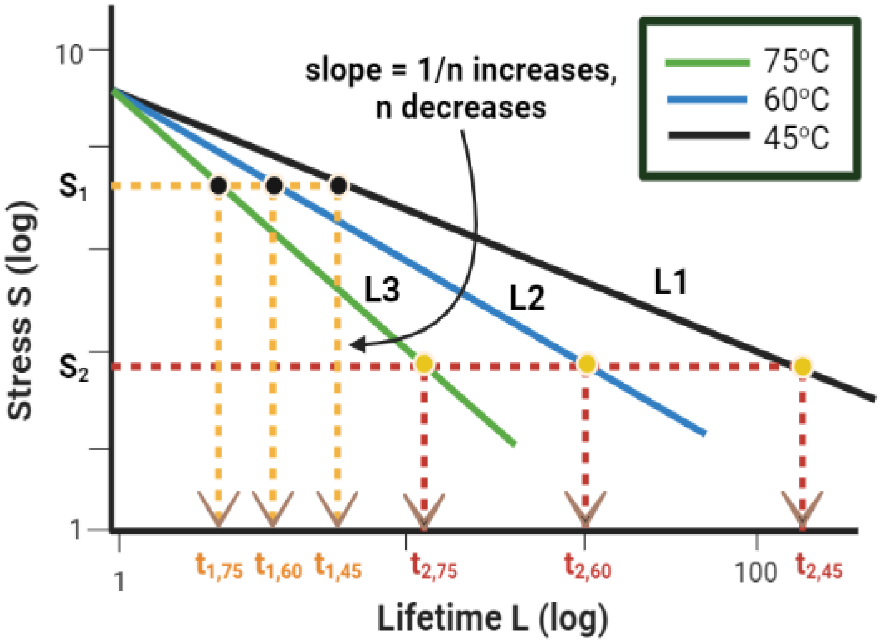

Figure 11.1: Variation of Time to Failure with Temperature

This is due to the trends in the n resulting in the lines in the log-log plot. Now, the cable under research is already field aged for 44 years and the first question addresses how long it would survive at a given stress field for different temperatures. From the contour plots in Figure 7.26, it is possible to estimate the value of n and K-parameter and construct the linear model.

An instance has been discussed to explain how the research question has been tackled. If a field stress of S_2 kV/mm is applied, it is observed that L3 breaks down fastest at time equalling $t_{2,75}$ followed by L2 and L3. This clearly indicates that temperature rise clearly degrades the samples faster and also the breakdown times are not proportional to the change in temperature as discussed in Section 7.4. Now, if the field applied stresses are increased due to increase in loading, and say the stress goes to S_2 kV/mm (S_2>S_1), we see that the cables breakdown at a faster rate because of higher stress but the trend follows and accordingly we can find the remaining lifetime of the cable given a field stress. So, if we want to keep the cable in operation for ”x” more years, from the model we know what can be our limiting temperature and accordingly we can change the loading from the present scenario. Thus, with advanced statistical formulation and aging model, even though the previous 44 years remain a black box, but the future life-time of the cable can be predicted and needs to be validated on field to check the accuracy and robustness of the model.

2) Can diagnostic tests be developed or modified focusing on the material physics inside the insulation that can be performed on the cable alongside tan delta at 50 Hz and Partial Discharge Measurements, that is viable in field with least offline time?

A novel method of measuring FDS at very low frequencies with cable off-service time of 6 minutes has been discussed in Chapter 9. Chapter 8 discusses about an electronic circuit developed to measure polarization and depolarization currents. Advanced physical and mathematical models have been extended to these concepts and parameters have been extracted which indicates thermal degradation and aging related to elevated thermal limits. Thus, in addition to the present online tanδ at 50 Hz and Partial Discharge measurements, the two researched methods can be used either together or separately to gain more insights about the insulation material characteristics. Partial discharge dependence on temperature has been established in Chapter 10 for the given sample material yet further studies need to be conducted to correlate these findings with other parameters. The methods and calculations for modelling have been discussed in depth in Chapters 8 and 9.

3) What parameters can be extracted from measurements to develop a robust model that determines the degradation of HPG cable insulation with temperature and aging?

Different parameters have been extracted from the developed models for OIP samples. They are Tau$_0$, Tau$_1$, Tau$_2$, Tau$_3$, R$_0$, R$_1$, R$_2$, R$_3$, C$_0$, C$_1$, C$_2$, C$_3$, conductivity, I$_p$, I$_c$ from PDC Measurements (Refer to Section 8.4) and C’$_{50Hz}$, C”$_{50Hz}$, tan$_{50Hz}$, Tau$_{cole}$, alpha$_{cole}$ from FDS Measurements (Refer Chapter 9). Parameters like real and imaginary parts of permittivities (ϵ' and ϵ”) and others are not considered since they are already correlated with respective capacitance and thus, it would increase unnecessary variables. Each of their Pearson’s Correlation Coefficient is evaluated with each other for Aged as well as Conditioned Samples as seen in Correlation Heat Map in Figure 11.2. The most important correlation is with temperature and rest of the parameters to understand their trends with varying thermal stress as observed in Figure 11.3. For both aged and conditioned it is observed that most variables are correlated with values close to 1 which means a positive trend and shown by the darker colour shade or close to -1 which refers to negative trend shown by the light colour shade. Values close to 0 would mean there is no correlation at all as seen for C_0 for aged samples. Also, for the aged samples, the correlation values become more extreme which means with aging, the trend is more intensely observed over conditioned ones. Since the reasons for each of the trends have been discussed in depth in respective chapters, here it will be concluded with supporting graphs.

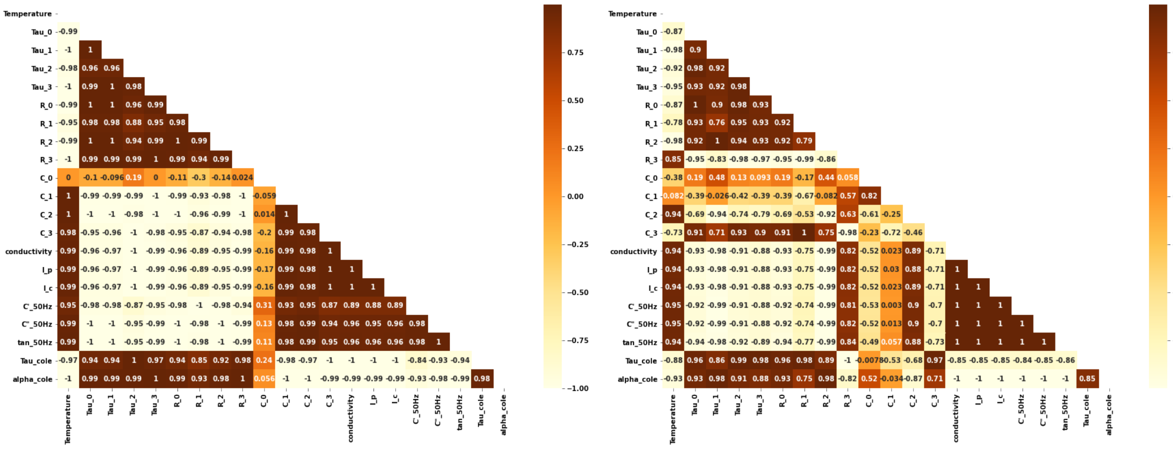

Figure 11.2: Pearson's Correlation Coefficients for Each Extracted Parameters for (a) Aged and (b) Conditioned

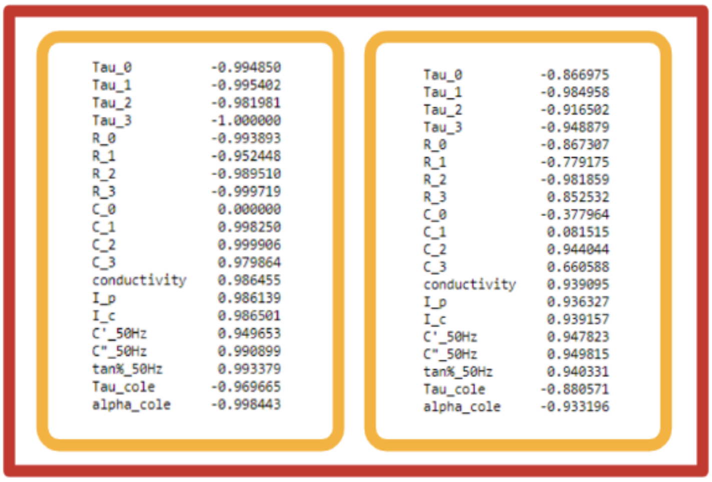

```
Tau_0          -0.994850
Tau_1          -0.995402
Tau_2          -0.981981
Tau_3          -1.000000
R_0            -0.993893
R_1            -0.952448
R_2            -0.989510
R_3            -0.999719
C_0             0.000000
C_1             0.998250
C_2             0.999906
C_3             0.979864
conductivity    0.986455
I_p             0.986139
I_c             0.986501
C'_50Hz         0.949653
C"_50Hz         0.990899
tan%_50Hz       0.993379
Tau_cole       -0.969665
alpha_cole     -0.998443
```

```
Tau_0          -0.866975
Tau_1          -0.984958
Tau_2          -0.916502
Tau_3          -0.948879
R_0            -0.867307
R_1            -0.779175
R_2            -0.981859
R_3             0.852532
C_0            -0.377964
C_1             0.081515
C_2             0.944044
C_3             0.660588
conductivity    0.939095
I_p             0.936327
I_c             0.939157
C'_50Hz         0.947823
C"_50Hz         0.949815
tan%_50Hz       0.940331
Tau_cole       -0.880571
alpha_cole     -0.933196
```

Figure 11.3: Correlation of Temperature with other parameters for (a) Aged and (b) Conditioned

Relaxation Times: For both conditioned and aged samples, the relaxation times reduce for each branch 0-3 with increase in temperature for the PDC measurements. Also, from the Cole-Cole Model, the cumulative relaxation time reduces with temperature. Due to a result of aging, when the aged samples are compared to conditioned ones, the relaxation time reduces due to aging which is a good indication. These trend can be observed across all branches as seen in Figure 11.4.

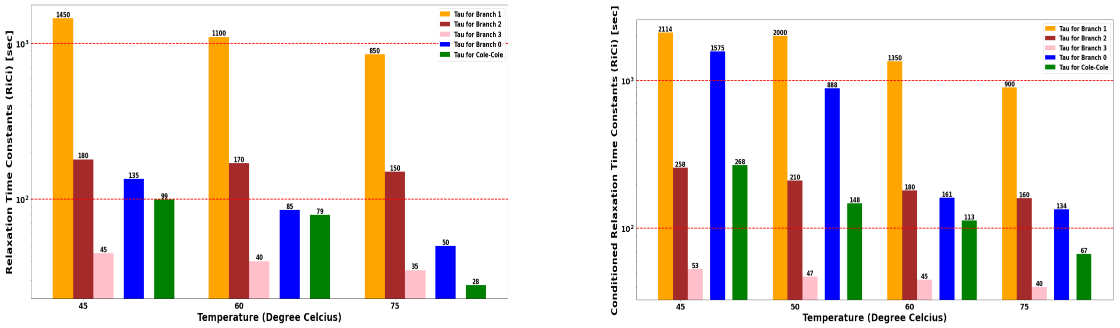

Figure 11.4: Relaxation Time Constants for Aged (left) and Conditioned Samples (right)

Insulation and Branch Resistance:

For both aged and conditioned samples, with increase in temperature, the branch and insulation resistances reduce, indicating degradation. This reduction is more prominent for aged samples as seen in Figure 11.5. The resistances across the branches can be seen to reduce but this is due to fitting of the Extended Debye Model on the Depolarization current with reducing values of relaxation times according to algorithm discussed in Step 4 of Subsection 8.4. When aging degree is compared it can be seen that the resistance values are much lower for aged over conditioned samples.

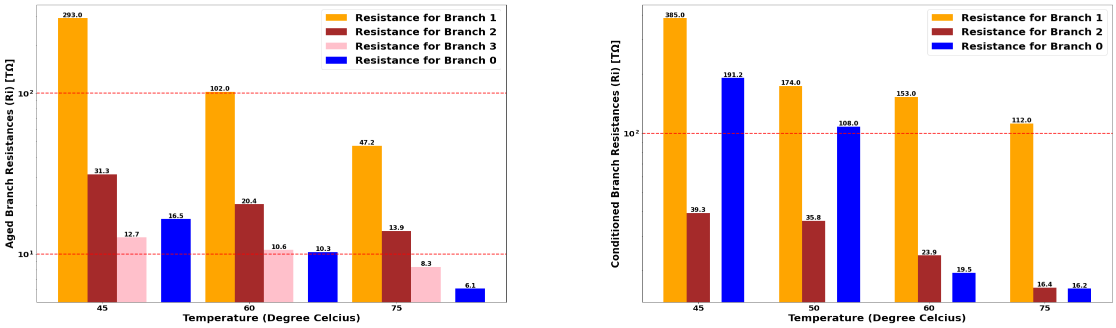

Figure 11.5: Insulation and Branch Resistance for Aged (left) and Conditioned Samples (right)

Insulation and Branch Capacitance:

For Aged Samples, it can be clearly seen that the capacitance increases with temperature but for conditioned samples the trend is not very monotonic. The insulation capacitance remains constant and is uncorrelated with temperature for both the cases. With aging it can be observed that the capacitance for aged samples are generally higher than conditioned ones indicating aging, and is very prominent in the maximal branch capacitance which has the maximum change and can be observed in Figure 11.6.

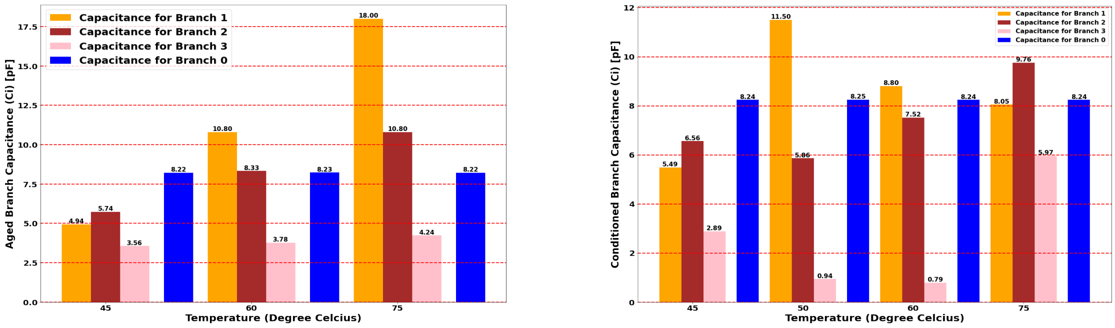

Figure 11.6: Insulation and Branch Resistance for Aged (left) and Conditioned Samples (right)

Polarization, Conduction current and DC Conductivity:

For both conditioned and aged samples, with increase in temperature, the Polarization, Conduction current and DC Conductivity increases monotonically as seen in Figure 11.7. Since the depolarization current saturates at a low value after 1.5 hours of PDC test, there is not much variation with temperature but the rate of decay of depolarization current is very different at different temperatures, giving different resistance and capacitance values as seen in the previous observations. Also, with temperature, the DC conductivity increases. As the aging degree is more, it can be observed that the magnitude of the currents and conductivity increases significantly indicating aging.

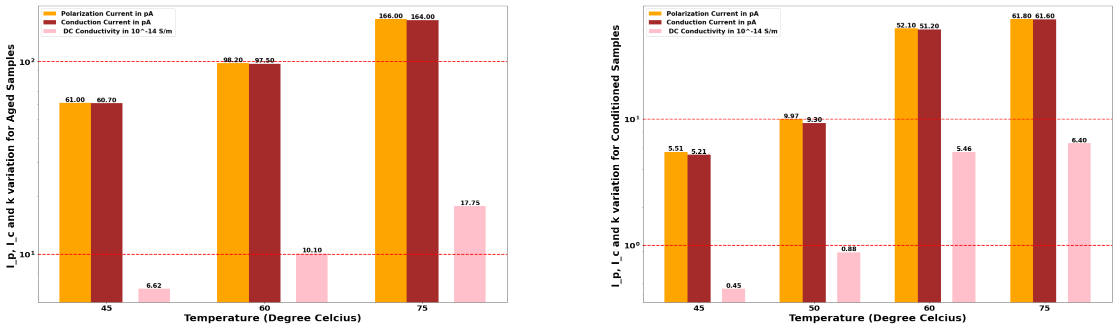

Figure 11.7: Polarization, Conduction current and DC Conductivity variation for Aged (left) and Conditioned Samples (right)

Real and Imaginary part of Capacitance and Tan Delta % at 50 Hz:

For the Aged and Conditioned Samples, near 50 Hz region, the real and imaginary part of capacitance increases with temperature but there is not a significant change. This is reflected in the tan delta value which increases with temperature indicating more losses. When the aging degree is compared between the two, instead of comparing the capacitance, the tan delta has a more profound change as tanδ increases with aging. Also, from fitting the Cole-Cole Model on FDS Measurements, it was already observed that relaxation time and alpha value reduces with temperature and degree of aging.

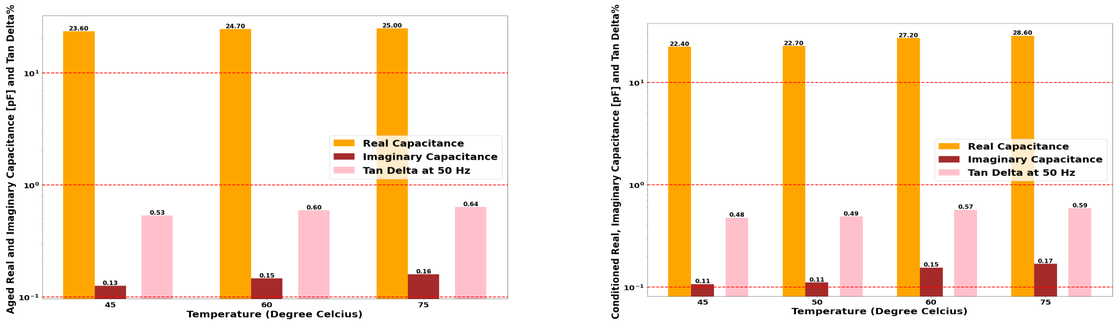

Figure 11.8: Polarization, Conduction current and DC Conductivity variation for Aged (left) and Conditioned Samples (right)

Therefore, with all the parameters extracted from the research conducted, the aging model has been constructed with varying temperature. And as the cable samples age, the material characteristics have been identified which show a strong trend (monotonically increase or decrease) that can be used as an indication of degradation. In field measurements, the values would differ compared to lab results, but the trends are expected to be maintained and so, prolonged period of measurement would help us analyze how the cables are degrading with aging or due to temperature elevation.

11.1.1. Future Research Scope:

A vast range of research topics have been explored in the thesis, yet more areas remain as scope for future research.

1) The tests have been conducted under thermal and different degree of aging, so it has to be extended with both electro-thermal stresses to validate that similar effect and trends are also observed for combined stresses.

2) Instead of putting electrical stress steps, temperature steps should be applied to obtain failure data and verify it with Arrhenius law to observe the similar change in alpha as obtained in this research.
2) For aging related to temperature, measuring Tensile strength using Universal Tensile Machine is very important. So, the mechanical strength should also be measured after the tests and correlated with the obtained parameters.

3) The moisture content of the paper sample should be varied to study its effect, specially since moisture is observed due to breaking of cellulose chains at higher temperatures. Thus, this domain also remains as an extended study.

4) The Partial Discharge Measurement can be more researched into about how to carry the experiment without introduction of oil and also not causing surface discharges for varying temperature. If all the parameters can be combined, then the model would become even more robust.

5) Lastly, since a single type of cable sample was provided, the research has been done on one type of OIP cables only. The next work would be to validate the research results for different types of cables (provided by TenneT). The lab results can be coupled with field data of PD and tan delta, if possibly provided by TenneT to validate the research results.

12

Acknowledgement

And it finally comes down to the Chapter where I will introduce you to the people who have been instrumental in developing my profound interest in research. If you are reading this chapter, chances are high that you have found the thesis so interesting that you read it whole, or you jumped all the chapters in the middle. It was like a journey for last 10 months from experiments, to simulations and algorithms and I have been blessed to have some wonderful people during the journey. The thesis started at the time, when times were uncertain and taking an experimental thesis was not the best of choices. But with the support of some wonderful people, it was not only possible but perhaps the best time I have had in my research experience.

Firstly, I would like to thank TenneT TSO for giving me the opportunity to do this research project and the wonderful team under **Amy Slootweg**, which I have been a part. A big shout-out to every colleague in Asset Management Team, where the meetings have been quite an eye opener for me. Specially to **Ranjan**, for providing the cable samples when the world was stagnant amidst the pandemic. I would take the opportunity to thank **Prof. dr. Rob Ross**, who has been my main supervisor and chair of defence. The weekly meetings are something I looked forward to and being a person who loves statistics, the conversations with Rob are something I would treasure from this journey. In spite of his busy schedule, Rob always had time for my smallest and silliest of questions and the half hour meetings would go for hours. Coming to my supervisor from Tennet, **Dr. Shima Mousavi Gargari**, she used to be the life of the meetings. Apart from helping me with all the technical details, her discussions would keep us giggling throughout. It is because of her that she gave me the liberty to carry my independent research and answer TenneT's questions at the same time. I would like to thank **Luis, Paul, Wim and Radek** for their help every time I needed to set up an experiment. Without them, I could have never finished my research. Those discussions with Luis and Wim over building a new experiment would be something I would definitely miss here. A big thanks to **Dr. M. Ghaffarian Niasar** for clarifying every doubt I had and staying late in lab which enabled the students to work till late. His jokes and willingness to always help, clearly makes him stand out from everyone else. These 10 months gave me some wonderful research mates as **Weichuan** and **Christian** and those long lunch time fun, frustrations and talks about life would be definitely missed. I would love to thank **Dr.ir. JL (Jose) Rueda Torres** for accepting my request of being the committee member. But our relation goes long back, and I have had some wonderful experience while being the TA for his 2 courses during the last 10 months, which enriched my love for teaching and redesigning the courses. Finally coming to **Dr. B. Gholizad**, who was my daily supervisor for the research. But in reality, he broke down all the boundaries of a student teacher as he supported me like a friend, guide as well as a professor. He gave me the liberty to take the research according to my own imaginations, at the same time kept me inline with the research objectives. From staying back with me in the lab during experimental phase till late night to answering my silliest questions over Whatsapp, it has been a tremendous journey having him as my guide. Not only technically, but he was there as an emotional support, specially during periods of my outburst. Be it about superconductors or Dutch language, he has always entertained my doubts and that has made the journey even more fulfilling. To me, it has been a privilege to have all of them as my supervisors. Coming here 2 years back, hardly did I know what was awaiting me here. I would also like to thank **Dr.**

Armando Rodrigo Mor and **Prof. Peter Vassen** for their valuable inputs during HV Research Group Meetings.

During this period, Anjali, Shreya and Gourab has also been a support system. Whenever I was down or bored, their company would always cheer me up no matter what. A special thanks to my roommates, Tadej and Tanko for those academic discussions to cooking specialities. Finally, no amount of thanks can justify the support that I received from my parents and sister during this time. From listening to my rants at midnight to breakdowns, they have always stood by me through thick and thin. This month is indeed special as I defend my Master Thesis and my sister has been conferred with the ”Doctor” title; She has been my inspiration always. The list goes on but a heartful gratitude to everyone who believed me and inspired me, no matter how small their role has been. As I start my new journey from September, I wish that I get a research group as strongly bonded as this and wonderful people like them around me.

Bibliography

[1] Jos van Rossum et al. 'development hv external gas pressure cable systems retrofit'. *CIGRE Session 48*, 2020.

[2] Shuai Han, Qingmin Li, Chengrong Li, and Jiangyan Yan. Electrical and mechanical properties of the oil-paper insulation under stress of the hot spot temperature. *IEEE Transactions on Dielectrics and Electrical Insulation*, 21:179–185, 02 2014.

[3] Caiming Tang, Ruting Liao, F. Huang, Lijun Yang, and Meng-Zhao Zhu. The breakdown voltage of power transformer insulation paper after thermal aging. *Diangong Jishu Xuebao/Transactions of China Electrotechnical Society*, 25:1–8, 11 2010.

[4] Muhammad Rafiq, Muhammad Shafique, Anam Azam, and Muhammad Ateeq. Transformer oil-based nanofluid: The application of nanomaterials on thermal, electrical and physicochemical properties of liquid insulation-a review. *Ain Shams Engineering Journal*, 12, 09 2020.

[5] S Mousavi Gargari. Pattern recognition and knowledge extraction for on-line partial discharge monitoring with defect location. 2012.

[6] Rob Ross. Lecture 6: Aging of cable systems and cable testing. 2020.

[7] John Densley. Ageing mechanisms and diagnostics for power cables-an overview. *IEEE electrical insulation magazine*, 17(1):14–22, 2001.

[8] Seiichi Kagaya, Takeo Yamamoto, and Akiji Inohana. Aging of oil-filled cable dielectrics. *IEEE Transactions on Power Apparatus and Systems*, (7):1420–1428, 1970.

[9] FM Clark. Factors affecting the mechanical deterioration of cellulose insulation. *Electrical Engineering*, 61(10):742–749, 1942.

[10] John Kuffel and Peter Kuffel. *High voltage engineering fundamentals*. Elsevier, 2000.

[11] Main page, Feb 2021.

[12] Hassan Mashad Nemati, Anita Sant'Anna, and Sławomir Nowaczyk. Reliability evaluation of underground power cables with probabilistic models. In *The 11th International Conference on Data Mining (DMIN'15), Las Vegas, Nevada, USA, July 27-30, 2015*, pages 37–43, 2015.

[13] RA Jongen, PHF Morshuis, E Gulski, JJ Smit, J Maksymiuk, and ALJ Janssen. Application of statistical methods for making maintenance decisions within power utilities. *IEEE electrical insulation magazine*, 22(6):24–35, 2006.

[14] Paul Barringer. Predict failures: crow-amsaa 101 and weibull 101. *Proceedings of IMEC*, page 11, 2004.

[15] H Paul Barringer. Use crow-amsaa reliability growth plots to forecast future system failures. 2006.

[16] Larisa Mariut and Elena Helerea. Multiple stress life analysis on underground power cables from distribution networks. In *Doctoral Conference on Computing, Electrical and Industrial Systems*, pages 275–282. Springer, 2012.

[17] EA Feilat, S Grzybowski, and P Knight. Electrical aging models for fine gauge magnet wire enamel of flyback transformer. In *Proceedings of the IEEE SoutheastCon 2000.'Preparing for The New Millennium'(Cat. No. 00CH37105)*, pages 146–149. IEEE, 2000.

[18] S Grzybowski and S Bandaru. Effect of multistress on the lifetime characteristics of magnet wires used in flyback transformer. In *Conference Record of the 2004 IEEE International Symposium on Electrical Insulation*, pages 200–203. IEEE, 2004.

[19] B Fallou, C Burguiere, and JF Morel. First approach on multiple stress accelerated life testing of electrical insulation. *CEIDP Annual Report*, pages 621–8, 1979.

[20] Gian Carlo Montanari and Luciano Simoni. Aging phenomenology and modeling. *IEEE Transactions on Electrical Insulation*, 28(5):755–776, 1993.

[21] TS Ramu. On the estimation of life of power apparatus insulation under combined electrical and thermal stress. *IEEE Transactions on Electrical Insulation*, (1):70–78, 1985.

[22] Gian Carlo Montanari and Luciano Simoni. Aging phenomenology and modeling. *IEEE Transactions on Electrical Insulation*, 28(5):755–776, 1993.

[23] Eyad A Feilat. Lifetime assessment of electrical insulation. *Electric Field*, 2018.

[24] Jerald F Lawless. Observation schemes, censoring, and likelihood. *Statistical Models and Methods for Lifetime Data, 2nd ed.; John Wiley & Sons, Inc.: New York, NY, USA*, pages 49–78, 2002.

[25] WB Nelson. Accelerated testing: Statistical models, test plans and data analysis. *John Wiley & Sons, Inc.: New York, NY, USA*, pages 49–78, 2008.

[26] Nancy R Mann, Ray E Schafer, and Nozer D Singpurwalla. Methods for statistical analysis of reliability and life data(book). *Research supported by the U. S. Air Force and Rockwell International Corp. New York, John Wiley and Sons, Inc., 1974. 573 p*, 1974.

[27] William Q Meeker and Luis A Escobar. *Statistical methods for reliability data*. John Wiley & Sons, 2014.

[28] Yan Wang, Jian Li, Youyuan Wang, and Stanislaw Grzybowski. Electrical breakdown properties of oil-paper insulation under ac-dc combined voltages. pages 115–118, 05 2010.

[29] Roberts Neimanis and R. Eriksson. Diagnosis of moisture in oil/paper distribution cables—part i: Estimation of moisture content using frequency-domain spectroscopy. *Power Delivery, IEEE Transactions on*, 19:9 – 14, 02 2004.

[30] Danyu Jiang, Guangning Wu, Xian Yang, and Qingkai Hao. The research of connection between degree of polymerization and frequency domain dielectric spectroscopy characteristics during oil-paper insulation aging. *Energy and Power Engineering*, 09:667–674, 01 2017.

[31] Jeongtae Kim, Woobin Kim, Hung-Sok Park, and Ji-Won Kang. Lifetime assessment for oil-paper insulation using thermal and electrical multiple degradation. *Journal of Electrical Engineering and Technology*, 12:840–845, 03 2017.

[32] Peter Werelius, Jialu Cheng, Matz Ohlen, and D.M. Robalino. Dielectric frequency response measurements and dissipation factor temperature dependence. pages 296–300, 06 2012.

[33] Mohamad Ghaffarian Niasar. *Mechanisms of electrical ageing of oil-impregnated paper due to partial discharges*. Electrical engineering, KTH Royal Institute of Technology, 2015.

[34] Antonio Mandala, Zhang Tao, Jiang Shiejie, and Zhang Ning. Analysis of dielectric response measurements for condition assessment of oil-paper in power transformer insulation. *International Journal of Scientific and Research Publications (IJSRP)*, 11:145–151, 04 2021.

[35] Abi Munajad, Cahyo Subroto, et al. Study on the effects of thermal aging on insulating paper for high voltage transformer composite with natural ester from palm oil using fourier transform infrared spectroscopy (ftir) and energy dispersive x-ray spectroscopy (eds). *Energies*, 10(11):1857, 2017.

[36] Nick Lelekakis, Jaury Wijaya, Daniel Martin, and Dejan Susa. The effect of acid accumulation in power-transformer oil on the aging rate of paper insulation. *Electrical Insulation Magazine, IEEE*, 30:19–26, 05 2014.

[37] Sayidul Morsalin, Animesh Sahoo, and Bao Toan Phung. Recovery voltage response of xlpe cables based on polarisation and depolarisation current measurements. *IET Generation, Transmission & Distribution*, 13(24):5533–5540, 2019.

[38] Wolfgang Hauschild and Eberhard Lemke. *High-voltage test and measuring techniques*, volume 1. Springer, 2014.

[39] Gusztav Csepes, Istvan Hamos, Roger Brooks, and Volker Karius. Practical foundations of the rvm (recovery voltage method for oil/paper insulation diagnosis). In *1998 Annual Report Conference on Electrical Insulation and Dielectric Phenomena (Cat. No. 98CH36257)*, volume 1, pages 345–355. IEEE, 1998.

[40] Hari Charan Verma, Arijit Baral, Arpan K Pradhan, and Sivaji Chakravorti. Condition assessment of various regions within non-uniformly aged cellulosic insulation of power transformer using modified debye model. *IET Science, Measurement & Technology*, 11(7):939–947, 2017.

[41] PQ Mantas. Dielectric response of materials: extension to the debye model. *Journal of the European Ceramic Society*, 19(12):2079–2086, 1999.

[42] Kenneth S Cole and Robert H Cole. Dispersion and absorption in dielectrics i. alternating current characteristics. *The Journal of chemical physics*, 9(4):341–351, 1941.

[43] SN Al-Refaie and HSB Elayyan. Modelling and simulation of knbo3 ceramics dispersion. *IET science, measurement & technology*, 1(3):133–137, 2007.

[44] Graham Williams. Molecular aspects of multiple dielectric relaxation processes in solid polymers. In *Electric phenomena in polymer science*, pages 59–92. Springer, 1979.

[45] Graham Williams. Dielectric properties of polymers. *Materials Science and Technology*, 2006.

[46] HG David, SD Hamann, and JF Pearse. The dielectric constant of ethylene at high pressures. *The Journal of Chemical Physics*, 19(12):1491–1495, 1951.

[47] John G Kirkwood. On the theory of dielectric polarization. *The Journal of Chemical Physics*, 4(9):592–601, 1936.

[48] A Pradhan, C Koley, B Chatterjee, and S Chakravorti. Non-linear modeling of oil-paper insulation for condition assessment using non-sinusoidal excitation. *IEEE Transactions on Dielectrics and Electrical Insulation*, 22(4):2165–2175, 2015.

[49] Wong Jee Keen Raymond, Hazlee Azil Illias, Hazlie Mokhlis, et al. Partial discharge classifications: Review of recent progress. *Measurement*, 68:164–181, 2015.

[50] Binu Melit Devassy, Sony George, and Peter Nussbaum. Unsupervised clustering of hyperspectral paper data using t-sne. *Journal of Imaging*, 6(5):29, 2020.

[51] Seiya Masuda, Tadahiro Fujimura, Yusuke Nakano, Masahiro Kozako, Masayuki Hikita, Hiroshi Haruyama, Kazunori Miyazaki, Hideaki Sato, and Fumiyasu Aono. Discussion on partial discharge measurement technique of cable joint in three phase high voltage overhead transmission line. In *2018 Condition Monitoring and Diagnosis (CMD)*, pages 1–4, 2018.

[52] E Gulski, JJ Smit, FJ Wester, and JW Van Doeland. Condition assessment of high voltage power cables. In *2004 International Conference on Power System Technology, 2004. PowerCon 2004.*, volume 2, pages 1661–1666. IEEE, 2004.

[53] Adrianus J Dekker. *Electrical engineering materials*. Prentice-Hall, 1959.

[54] Ronald Pethig, Ying Huang, Xiao-Bo Wang, and Julian PH Burt. Positive and negative dielectrophoretic collection of colloidal particles using interdigitated castellated microelectrodes. *Journal of Physics D: Applied Physics*, 25(5):881, 1992.

[55] Carl Johan Friedrich Böttcher and Paul Bordewijk. *Theory of electric polarization*, volume 2. Elsevier Science Limited, 1978.

[56] Xu Yang, Shawn Nielsen, and Gerard Ledwich. Investigations of dielectric monitoring on an energised transformer oil–paper insulation system. *IET Science, Measurement & Technology*, 9(1):102–112, 2015.

[57] S Ochiai, M Ito, T Mizutani, and M Ieda. Interface traps and swelling of polypropylene films immersed in silicone oils. *IEEE transactions on electrical insulation*, (3):575–580, 1985.

[58] GM Tsangaris, GC Psarras, and N Kouloumbi. Electric modulus and interfacial polarization in composite polymeric systems. *Journal of materials science*, 33(8):2027–2037, 1998.

[59] H Fröhlich. Theory of dielectrics, clarendon, 1958.

[60] Graham Williams. Molecular aspects of multiple dielectric relaxation processes in solid polymers. In *Electric phenomena in polymer science*, pages 59–92. Springer, 1979.

[61] Fabio Bruni, Giuseppe Consolini, and Giorgio Careri. Temperature dependence of dielectric relaxation in h2o and d2o ice. a dissipative quantum tunneling approach. *The Journal of chemical physics*, 99(1):538–547, 1993.

[62] NR Tu and KC Kao. High-field electrical conduction in polyimide films. *Journal of applied physics*, 85(10):7267–7275, 1999.

[63] ‘cable diagnostics’. available at https://www.baur.eu/products/cable-testingand- diagnostics/vlf-testing-and-diagnostic, accessed april 2018.

[64] ‘tan delta’. available at http://power.sebakmt.com/bg/products/power networks/diagnosis/dielectric-diagnosis/tan-delta.html, accessed april 2018.

[65] ‘vax/230/214 high voltage amplifier’. available at http://www.intylerfimaco. com/vax-230-214dsenv01.pdf, accessed april 2018.

[66] ‘tettex products’. available at http://www.maceyselectrical.com.au, accessed april 2018.

[67] ‘tan delta cable diagnostics’. available at https://hvdiagnostics.com/ products/td, accessed april 2018.

[68] ‘dirana sys.’. available at https://www.omicronenergy.com/en/products// dirana, accessed april 2018.

[69] ‘dissipation/power factor measurement’. available at https:// www.omicronenergy.com/en/applications/power-transformer-testing/diagnosis-dissipationpower-factor-measurement-tan-delta-on-powertransformers/,accessed april 2018.

[70] J Lansley et al. ’update of service experience of hv underground and submarine cable systems’. *CIGRE*, September 2020.

[71] ’update of service experience of hv underground and submarine cable systems’. *CIGRE B1*, September 2007.

[72] Qing Yang, Yang Jin, Wenxia Sima, and Mengna Liu. Effect of the electrode material on the breakdown voltage and space charge distribution of propylene carbonate under impulse voltage. *AIP Advances*, 6(4):045215, 2016.

[73] F. Guerbas, M.Mohamed Zitouni, Ahmed Boubakeur, and Abderrahmane Beroual. Barrier effect on breakdown of point-plane oil gaps under alternating current voltage. *Generation, Transmission Distribution, IET*, 4:1245 – 1250, 12 2010.

[74] Bjoern Mieller. Influence of test procedure on dielectric breakdown strength of alumina. *Journal of Advanced Ceramics*, 8(2):247–255, 2019.

[75] Puchong Praekhaow. Determination of trading points using the moving average methods. 06 2010.

[76] Eva Ostertagova and Oskar Ostertag. The simple exponential smoothing model. 09 2011.

[77] Kuljeet Singh, Sourabh Shastri, Arun Bhadwal, Paramjit Kour, Monika Kumari, Anand Sharma, and Vibhakar Mansotra. Implementation of exponential smoothing for forecasting time series data. 01 2019.

[78] Thitima Booranawong and Apidet Booranawong. Double exponential smoothing and holt-winters methods with optimal initial values and weighting factors for forecasting lime, thai chili and lemongrass prices in thailand. *Engineering and Applied Science Research*, 45:32–38, 02 2018.

[79] A. Sarvani, B. Venugopal, and Nagaraju Devarakonda. *Anomaly Detection Using K-means Approach and Outliers Detection Technique: Proceedings of SoCTA 2017*, pages 375–385. 01 2019.

[80] Zhiguo Ding and Minrui Fei. An anomaly detection approach based on isolation forest algorithm for streaming data using sliding window. *IFAC Proceedings Volumes*, 46(20):12–17, 2013. 3rd IFAC Conference on Intelligent Control and Automation Science ICONS 2013.

[81] Junshui Ma and S. Perkins. Time-series novelty detection using one-class support vector machines. volume 3, pages 1741 – 1745 vol.3, 08 2003.

[82] Mohammad Braei and Sebastian Wagner. Anomaly detection in univariate time-series: A survey on the state-of-the-art. 04 2020.

[83] yu yf, Yuelong Zhu, Shijin Li, and Dingsheng Wan. Time series outlier detection based on sliding window prediction. *Mathematical Problems in Engineering*, 2014, 10 2014.

[84] Zakia Ferdousi and Akira Maeda. Anomaly detection using unsupervised profiling method in time series data. 01 2006.

[85] Guilherme Barreto and Leonardo Aguayo. Time series clustering for anomaly detection using competitive neural networks. pages 28–36, 06 2009.

[86] Nethal Jajo and K. Matawie. Outlier detection using modified boxplot. *International Journal of Ecology and Development*, 13:116–122, 01 2009.

[87] Electric cables - calculation of the current rating - part 1-1: Current rating equations (100 % load factor) and calculation of losses - general. *IEC 60287-1-1:2006*, 41(3):65, 2006-12-13.

[88] Electric cables - calculation of the current rating - part 2-1: Thermal resistance - calculation of the thermal resistance. *IEC 60287-2-1:2015*, 3(3):84, 2015-04-09.

[89] Herbert Bristol Dwight. Skin effect and proximity effect in tubular conductors. *Journal of the American Institute of Electrical Engineers*, 41(3):203–209, 1922.

[90] Nkf kabel delft, type ep-splkugd. *NKF Datasheet*, 1(3):13, 1979.

[91] 3 - power cables. In Jan de Kock and Kobus Strauss, editors, *Practical Power Distribution for Industry*, pages 30–68. Newnes, Oxford, 2004.

[92] Y. Zhou, J. Huang, Y. Sha, F. Jin, M. Huang, and Z. Li. Effect of kraft paper's thickness on electrical properties of oil-paper insulation. 41:3014–3020, 09 2015.

[93] Mahdi Rasekhi, Mohamed Zayed, and Haitham M. Yousof. A new two-parameter weibull distribution with variable shapes for the hazard rate. *Journal of modern applied statistical methods: JMASM*, 11 2017.

[94] Survival models.

[95] Stanislaw Weglarczyk. Kernel density estimation and its application. *ITM Web of Conferences*, 23:00037, 01 2018.

[96] Frank J Massey Jr. The kolmogorov-smirnov test for goodness of fit. *Journal of the American statistical Association*, 46(253):68–78, 1951.

[97] Runs test of randomness in python, Jun 2020.

[98] Lukasz Chmura, DVD Boorn, PHF Morshuis, and JJ Smit. Life curves for new and thermally aged oil-impregnated paper insulation. In *2013 IEEE Electrical Insulation Conference (EIC)*, pages 45–48. IEEE, 2013.

[99] Mohammad Modarres, Mehdi Amiri, and Christopher Jackson. *Probabilistic Physics of Failure Approach to Reliability: Modeling, Accelerated Testing, Prognosis and Reliability Assessment*. John Wiley & Sons, 2017.

[100] Survival models.

[101] LA Chmura, PHF Morshuis, E Gulski, and JJ Smit. Time-to-breakdown and breakdown voltage for oil-impregnated insulation subjected to thermal aging. In *2012 International Conference on High Voltage Engineering and Application*, pages 233–236. IEEE, 2012.

[102] Emilia Vänskä, Tuomas Vihelä, Maria Soledad Peresin, Jari Vartiainen, Michael Hummel, and Tapani Vuorinen. Residual lignin inhibits thermal degradation of cellulosic fiber sheets. *Cellulose*, 23(1):199–212, 2016.

[103] Paul Jusner, Elisabeth Schwaiger, Antje Potthast, and Thomas Rosenau. Thermal stability of cellulose insulation in electrical power transformers–a review. *Carbohydrate Polymers*, page 117196, 2020.

[104] Thomas A Prevost. Thermally upgraded insulation in transformers. In *Proceedings Electrical Insulation Conference and Electrical Manufacturing Expo, 2005.*, pages 120–125. IEEE, 2005.

[105] Antje Potthast, Thomas Rosenau, Paul Kosma, Anna-Maija Saariaho, and Tappani Vuorinen. On the nature of carbonyl groups in cellulosic pulps. *Cellulose*, 12(1):43–50, 2005.

[106] Deng Wang, Zhiping Zhu, Li Zhang, Yihua Qian, Wei Su, Tiansheng Chen, Shengping Fan, and Yaohong Zhao. Influence of metal transformer materials on oil-paper insulation after thermal aging. *IEEE Transactions on Dielectrics and Electrical Insulation*, 26(2):554–560, 2019.

[107] Chao Tang, Song Zhang, Qian Wang, Xiaobo Wang, and Jian Hao. Thermal stability of modified insulation paper cellulose based on molecular dynamics simulation. *Energies*, 10(3):397, 2017.

[108] A V Schijndel. Power transformer reliability modelling. *Technische Universiteit Eindhoven, Eindoven, Denmark*, 2010.

[109] John R Sans, K Muge Bilgin, and Joseph J Kelly. Large-scale survey of furanic compounds in operating transformers and implications for estimating service life. In *Conference Record of the 1998 IEEE International Symposium on Electrical Insulation (Cat. No. 98CH36239)*, volume 2, pages 543–553. IEEE, 1998.

[110] Barry Lennon. Dielectric relaxation analysis to assess the integrity of high voltage dc cables of the mass impregnated type. 2009.

[111] Antti Paajanen and Jukka Vaari. High-temperature decomposition of the cellulose molecule: a stochastic molecular dynamics study. *Cellulose*, 24(7):2713–2725, 2017.

[112] Robert Ross. *Reliability Analysis for Asset Management of Electric Power Grids*. John Wiley & Sons, 2019.

[113] Tian Li, WD Griffiths, and J Chen. Weibull modulus estimated by the non-linear least squares method: a solution to deviation occurring in traditional weibull estimation. *Metallurgical and Materials Transactions A*, 48(11):5516–5528, 2017.

[114] Xing Zhang, Long Xu, Aixuan Zhao, Yanbo Wang, Xue-Feng Zhao, Lu Pu, Junbo Deng, and Guanjun Zhang. Research on conversion of polarization/depolarization current and frequency domain spectroscopy for xlpe cable. In *2017 1st International Conference on Electrical Materials and Power Equipment (ICEMPE)*, pages 452–456. IEEE, 2017.

[115] Issouf Fofana, H Hemmatjou, F Meghnefi, M Farzaneh, A Setayeshmehr, H Borsi, and E Gockenbach. Low temperature and moisture effects on oil-paper insulation dielectric response in frequency domain. In *2009 IEEE Electrical Insulation Conference*, pages 368–372. IEEE, 2009.

[116] F Gülşen Erdinç, Ozan Erdinç, Recep Yumurtacı, and João PS Catalão. A comprehensive overview of dynamic line rating combined with other flexibility options from an operational point of view. *Energies*, 13(24):6563, 2020.

[117] Y Wang, A Zhao, X Zhang, Y Shen, F Yang, J Deng, and G Zhang. Study of dielectric response characteristics for thermal aging of xlpe cable insulation. In *2016 International Conference on Condition Monitoring and Diagnosis (CMD)*, pages 602–605. IEEE, 2016.

[118] Tapan K Saha, Prithwiraj Purkait, and Frank Muller. Deriving an equivalent circuit of transformers insulation for understanding the dielectric response measurements. *IEEE Transactions on Power Delivery*, 20(1):149–157, 2005.

[119] G Frimpong, U Gafvert, and J Fuhr. Measurement and modeling of dielectric response of composite oil/paper insulation. In *Proceedings of 5th International Conference on Properties and Applications of Dielectric Materials*, volume 1, pages 86–89. IEEE, 1997.

[120] AK Jonscher. Dielectric relaxation in solids (chelsea dielectrics press, london, 1983).

[121] Feng Yang, Lin Du, Lijun Yang, Chao Wei, Youyuan Wang, Liman Ran, and Peng He. A parameterization approach for the dielectric response model of oil paper insulation using fds measurements. *Energies*, 11(3):622, 2018.

[122] C Stancu, PV Notingher, and LV Badicu. Dielectric response function for nonhomogeneous insulations. In *2011 Annual Report Conference on Electrical Insulation and Dielectric Phenomena*, pages 97–100. IEEE, 2011.

[123] József Valyon and Gábor Horváth. A sparse robust model for a linz-donawitz steel converter. pages 1–6, 06 2007.

[124] Sayidul Morsalin, Animesh Sahoo, and Bao Toan Phung. Recovery voltage response of xlpe cables based on polarisation and depolarisation current measurements. *IET Generation, Transmission & Distribution*, 13(24):5533–5540, 2019.

[125] Farzaneh Vahidi, Stefan Tenbohlen, Michael Rösner, Christophe Perrier, and Harald Fink. The investigation of the temperature and electric field dependency of mineral oil electrical conductivity. *ETG-Fachbericht-Grenzflächen in elektrischen Isoliersystemen, Dresden*, 2013.

[126] XU Jiquan, Yang Lijun, LI Bin, Liao Ruijin, HE Yunhua, and Guo Pei. Study on assessing the ageing condition of oil-paper insulation by polarization/depolarization current. In *2013 Annual Report Conference on Electrical Insulation and Dielectric Phenomena*, pages 617–621. IEEE, 2013.

[127] X. Zhongnan. Study on simulation and experiment of polarization and depolarization current for oil-paper insulation ageing. *Master's Thesis*, 2011.

[128] Idax 300 user manual.

[129] Jeppe C Dyre. The random free-energy barrier model for ac conduction in disordered solids. *Journal of Applied Physics*, 64(5):2456–2468, 1988.

[130] Andrew K Jonscher. Dielectric relaxation in solids. *Journal of Physics D: Applied Physics*, 32(14):R57, 1999.

[131] Ming Dong, Ming Ren, Fuxin Wen, Chongxing Zhang, Jialin Liu, Christof Sumereder, and Michael Muhr. Explanation and analysis of oil-paper insulation based on frequency-domain dielectric spectroscopy. *IEEE Transactions on Dielectrics and Electrical Insulation*, 22(5):2684–2693, 2015.

[132] Issouf Fofana, H Hemmatjou, F Meghnefi, M Farzaneh, A Setayeshmehr, H Borsi, and E Gockenbach. Low temperature and moisture effects on oil-paper insulation dielectric response in frequency domain. In *2009 IEEE Electrical Insulation Conference*, pages 368–372. IEEE, 2009.

[133] Chuanhui Cheng, Kai Wu, Mingli Fu, YanPeng Hao, Shuangzan Ren, Jingfeng Wu, and Hao Wu. Interface charge barrier between oil and oil immersed paper. *IEEE Transactions on Dielectrics and Electrical Insulation*, 28(2):390–397, 2021.

[134] Chun-she Xu, Shi-Qiang Wang, Hao Xu, and Guan-Jun Zhang. Temperature effect on frequency domain spectroscopy characteristics of oil impregnated pressboard. In *Proceedings of 2011 International Symposium on Electrical Insulating Materials*, pages 197–200. IEEE, 2011.

[135] Stefan Wolny, Artur Adamowicz, and Marek Lepich. Influence of temperature and moisture level in paper-oil insulation on the parameters of the cole-cole model. *IEEE Transactions on Power delivery*, 29(1):246–250, 2013.

[136] Patrick J Baird, Henryk Herman, Gary C Stevens, and Paul N Jarman. Spectroscopic measurement and analysis of water and oil in transformer insulating paper. *IEEE Transactions on Dielectrics and Electrical Insulation*, 13(2):293–308, 2006.

[137] Samiha T Bishay. Numerical methods for the calculation of the cole-cole parameters. *Phypics department, AimShams University, Cairo, Egypt*, 2000.

[138] Quanmin Dai, Yanxia Liu, and Guang Cheng. The mathematical model of dissipation factor with temperature–frequency effect for oil-impregnated paper bushings. *AIP Advances*, 10(11):115112, 2020.

[139] David G Jenkins and Pedro F Quintana-Ascencio. A solution to minimum sample size for regressions. *PloS one*, 15(2):e0229345, 2020.

[140] S Wolny and M Zdanowski. Analysis of recovery voltage parameters of paper-oil insulation obtained from simulation investigations using the cole-cole model. *IEEE Transactions on Dielectrics and Electrical Insulation*, 16(6):1676–1680, 2009.

[141] Petr Mraz, Saliha Abdul Madhar, Patrick Treyer, and Urs Hammer. Guidelines for pd measurement according to iec 60270. In *21st International symposium on high voltage engineering, Budapest, Hungary*, 2019.

[142] Yuan Li, Qiaogen Zhang, Yi Zhao, Tonglei Wang, Guangqi Liu, and Ke Wang. The influence of temperature on partial discharges and wormhole effect of oil-paper insulation under dc voltage. In *2017 IEEE Electrical Insulation Conference (EIC)*, pages 100–103. IEEE, 2017.

[143] R.H. Khawaja and Trevor Blackburn. Partial discharge patterns in oil-impregnated paper and pressboard insulation at high temperature. pages 1 – 5, 01 2009.

[144] Weizheng Zhang, Zhimin Li, Guojian Ji, Jumei Guo, and Yongbo Yang. Partial discharges behaviors of internal void in the oil-paper insulation and its effect on the material. In *International Conference on Applied Science and Engineering Innoation (ASEI 2015)*, 2015.

[145] Robert Ross. *Reliability Analysis for Asset Management of Electric Power Grids*. John Wiley & Sons, 2019.